Experimental and Quantum-Mechanical Approaches to Explore Oxide, Phosphate, and Sulfate Minerals as Redox Catalysts, Geochemical Probes, and the Stability of Their Solid Solutions

by

YoungJae Kim

A dissertation submitted in partial fulfillment
of the requirements for the degree of
Doctor of Philosophy
(Earth and Environmental Sciences)
in the University of Michigan
2019

Doctoral Committee:

Professor Udo Becker, Chair
Associate Professor Rose Cory
Assistant Professor Brian R. Ellis
Professor Adam Simon

YoungJae Kim

youngjkm@umich.edu

ORCID iD: 0000-0003-0712-3794

Acknowledgements

At this moment, I recall the statement from the Old Testament and feel like a “truly happy person” who resembles the “tree replanted by streams of water, which bears fruit” on just right time. My life is about to bear this dissertation, but owes it to people who have been the streams of water.

I thank my adviser, Dr. Udo Becker ever so much. He listened to me, understood me and knew what I wanted and needed throughout the course of my dissertation research. I was very lucky to attend his class “determinative methods in mineralogical and inorganic materials” (Earth 455, fall 2014) where he led me to the world of electrochemistry and its application to studying mineral redox catalyst. As such, the seed of Chapter II was made from his advice while we were in this class. In the fall of 2015, he taught class “computational mineralogy” (Earth 429) that gave me the unforgettable chance to start my career on atomistic modeling applied to mineralogy and geochemistry. When consulting on my term project, he suggested to give it a shot for Cr-S solid solution in jarosite. He kept encouraging me to research on this and related solid solution subjects and the project ended up with Chapter V. While interacting with him, I have always found him very enthusiastic about education and research, which has inspired me to dream about the future being such a great scientist. Special thanks goes to Dr. Maria Marcano for advising and teaching me ever with many research seeds and ensuring my lab safety. Especially, I would have had a tough time on the photochemical experiments (Chapter III) if it were not for her keen insights and warm cares.

I am so grateful to Dr. Rose Cory, Dr. Brian Ellis, Dr. Adam Simon, and who have provided great advice and valuable feedback on my research during last 5 years. They allowed me to interrupt their daytime work and chat about research but also my future career. Not only did they support me mentally, but also their supports and encouragements helped me publish the research works in this dissertation. Many thanks to Dr. Rose Cory. I was so lucky to take her class

"Geochemistry of natural waters (Earth 478, fall 2014). I was able to establish those concepts (acid/base, complexation, and redox chemistry) very clearly in my mind and brain thanks to her well-organized and thoughtful way of teaching. This class is a real core that became a large proportion of the background of this dissertation (especially, Chapter II and III). During winter 2015, I luckily had a chance to do an independent study on Chapter II with Dr. Brian Ellis. He and I had fruitful discussions on redox chemistry of selenium throughout the semester. Our discussion was further extended to the projects regarding photocatalytic reduction of uranium (Chapter III), full of his warm cares and advice. Dr. Adam Simon has been leading a new paradigm on S oxidation states in apatite and supported me to computationally simulate some part of the system (Chapter IV). It was a great experience that I learned how my computational skill can meet experiments/field observations in the field of geosciences. Special thanks to his student as well as my first-year graduate friend, Brian Konecke who discovered such interesting sulfur data from XANES analysis. He and Dr. Adam Simon sacrificed their busy times to meet me and chat whenever I requested and our discussion made substantial improvements on the computational work. Special thanks to Dr. Aaron Wolf who did not hesitate to devote his time and effort to working on the solid solution project (Project V). There could not be such great improvements on the phase diagrams if it were not for his incredibly valuable ideas and knowledge.

Many thanks to Dr. Jackie Li who was my special instructor during my GSI activity in Earth materials (Earth 315). I am very impressed with her rich and creative class design and truly want to be a teacher like her if I have a chance to teach mineralogy in the future. Many thanks to Dr. Joel Blum, Dr. Youxue Zhang, Dr. Jena Johnson for teaching me valuable knowledge on environmental and high-temperature geochemistry and geomicrobiology.

I am grateful so much for the friends that I found in Udo's group. I spent the first year of my UM life having warm chat and advice from Sandy Taylor and Ke Yuan. Ke Yuan taught me how to work on electrochemical experiments that was very useful to complete Chapter II. Peter Cook was always humorous and helped me learn and experience American culture. I had a great time and a lot of fun with Ben Gebarski sharing our office (Rm 3021) and doing on outdoor activities together. Sarah Walker helped me a lot when having difficulties on experiments and computing. Will Bender always listened to me and I deeply appreciated that he shared with me his experience and wisdom on teaching, research, and life. Sooyeon Kim was my kind-hearted friend who listened to me when I needed to brainstorm my research and have some worries. I shared great moments

of our group with Yingwei since he joined the group. Dr. Jerry Li, Dr. Owen Neil, and Dr. Gordon Moore have provided tremendous support with my analyses EMAL, and thank you to Dr. Greg Dick for the generous use of his lab. Thank you to Mike Messina of all assistance on computing resources.

Many thanks to Anne Hudon and Paula Frank for answering all my questions and chatting with me about my US life as well as to Nancy Kingsbury, Stacy Wilkin, Julie Haggerty, Craig Delap, Dale Austin for supporting my department affair and making things run smoothly.

Thank you so much to my first-year graduate office friends, Adrianna, Alex, Brian, Hong, Katy, Laura, Meg, Meredith, Sam, Sharon, Tristan who spent the longest time in the department, cheered me up, and shared happy and sad moments together including the Prelim exam in 2015 (in a harsher version than now) and defenses of our own as well as to other graduate friends, Allison, Cameron, David, Elizabeth, Forrest, Guolei, Jackie, James, Jenny, Juliana, Junjie (at Harvard), Madelyn, Maria, Mark, Nikita, Peng, Phoebe, Sae, Sha, Tao, Xiaofei, Xiaojing, Yanhan, Yi (Niu), Yi (Wang), and to undergraduate friends (Earth 315), Alex, Anne, Ariana, Celeste, Jamie, Monique, Pete, Zach for sharing time, ideas and funs.

I was very lucky to meet other Korean graduate students who have shared great times, funs, and motivations since 2014, Jaeho, Jeonghyo, Jongchan, JunHyuk and friends in the KU-Michigan society. I deeply appreciate their supports and encouragements. I am also grateful to my former advisor, Dr. Young Jae Lee who greatly influenced my academic performance and motivated me to pursue my PhD degree. Thank you to my former teachers Dr. Ho Young Jo and Dr. Mee Hye Lee for advising me and sharing their wisdom during my master program that I recalled whenever I had tough time during my PhD program.

Last, but not least, I owe much of my achievement to my loving parents. Thank you for all your efforts on our family and for always supporting me. Thank you to Young-Il, Sun-Hee, Ji-Su and the rest of my family for their unconditional love, encouragement, and support.

Table of Contents

List of Tables

List of Figures

Abstract

In this dissertation, the role of mineral catalysis for redox reactions, and the thermodynamics, mechanism, and atomic and electronic structure of ionic substitution in minerals are investigated using experimental and computational approaches.

There has been an increasing understanding in the literature and from our group's previous work that semiconducting minerals catalyze otherwise-slow redox reactions in the environment, either by partially dehydrating the reactants or by shuttling electrons from the reductant to the oxidant. In this context, Chapter II investigates redox transformation of selenium (Se) catalyzed by magnetite (Fe_3O_4). A novel electrochemical setup using a powdered mineral as the working electrode and catalytic surface was applied to measure the redox thermodynamics and to identify the reaction mechanisms as a function of speciation, pH, and Eh. We find direct evidence of a multi-electron transfer process for Se reduction and nucleation mediated by magnetite. This study advances our understanding of Se oxidation state changes and catalytic effects of Fe-bearing minerals in subsurface environments.

Chapter III investigates mineral catalysis further by adding photons as the main driving force of the electron transfer. The photocatalytic reactivity of anatase (TiO_2) indicates interaction between uranyl (as an electron acceptor), organic ligands (electron acceptor and ligand), catalytic surfaces, and UV light at different wavelengths, all of which are necessary to promote the redox kinetics. Uranyl removal was almost independent of wavelength for acetate- and oxalate-containing solutions whereas greater removal was observed for EDTA (using UV-C) and

hydroquinone (UV-A) solutions. Our results suggest that formation of uranium-ligand complexes plays a critical role in controlling the reactivity of uranyl species and the stability of reduced uranium species in the course of the photoreaction.

In Chapters IV and V, quantum-mechanical modeling has been applied to simulate ionic substitution in minerals and establish the thermodynamic basis for using these incorporated phases as a geochemical probe and the structural stability of solid solutions in the environment. Chapter IV addresses the energetic stability and geometry of sulfur (S) in multiple oxidation states in apatite [$Ca_5(PO_4)_3(F,OH,Cl)$]. These properties of S-incorporated apatite vary depending on (1) the major/minor ions in apatite and their site preferences, and (2) the molecular geometry and orientation of S oxyanions in the structure. These new computational results provide the thermodynamic framework required to investigate the potential role of S in apatite as a proxy to trace redox conditions in hydrothermal-magmatic systems.

In Chapter V, thermodynamic mixing properties of sulfate-chromate (S-Cr) and sulfate-selenate (S-Se) solid solution and of sulfate-phosphate-arsenate (S-P-As) solid solutions in alunite supergroup minerals are investigated. This work includes the first geochemical application that combines first-principles calculations, statistical thermodynamic analysis, and the convex hull method to derive phase diagrams of binary and ternary solid solution. S-Cr and S-Se solid solutions in alunite [$KAl_3(SO_4)_2(OH)_6$] and jarosite [$KFe_3(SO_4)_2(OH)_6$] tend to be complete at room temperature and no ordering is acquired at or above ambient conditions. Our computed phase diagrams of S-P-As mixing suggest that binary solid solutions between pairs of sulfate, phosphate, and arsenate in alunite-like minerals scarcely occur below 100 °C, are limited to temperatures from 100 to 300 °C, and become extensive or complete above 300 °C. Our computational model demonstrates the potential role of alunite and jarosite as an indicator for the equilibrium

temperature on magmatic-hydrothermal processes as well as in controlling toxic elements for long-term immobilization.

Chapter I. Introduction

While traditionally, mineralogists have focused on the structural, physical, and chemical properties of bulk minerals, minerals in natural systems (especially, nano-sized minerals due to the large specific surface areas and reactivity) can play a central role in environmentally-relevant reactions, such as crystal growth/dissolution, ion exchange with the aqueous phase, and redox transformation catalysis. In addition, the thermodynamics, as well as the atomic and electron structure of foreign elements or molecules present within the mineral structure have led to understanding of using natural minerals as geochemical probes such as a geothermometer and an (oxy)barometer in a variety of geological systems. Fundamental investigations on these subjects have been made possible by the refinement and widespread use of spectroscopic and microscopic techniques as well as fast development in computational methods.

The semiconducting properties of transition metal oxides and sulfides have recently gained attention because of their geochemical and environmental implications (e.g., Renock et al., 2013; Yuan et al., 2015). Semiconducting minerals have been identified as catalysts that facilitate otherwise slow redox reactions in natural environments and engineered systems designed to degrade hazardous chemicals (Xu and Schoonen, 2000). While, conventionally, the bandgaps of semiconducting minerals are measured using UV-vis spectra (López and Gómez, 2012), novel electrochemical techniques have been proposed to directly measure the electron transfer capability

of semiconducting oxide/sulfide minerals and Fe-bearing clay minerals (Tratnyek et al., 2011; Renock et al., 2013; Yuan et al., 2015).

Upon the process of crystallization, the mineral structure determines how (trace) elements partition between the mineral and the reaction media such as melt and aqueous phases. Since elements contained in the structure behave as passive tracers of these processes, their distribution can yield process-specific information, for example, change in temperature, pressure, and oxygen fugacity in magmatic evolution (Allan et al., 2001). Spectroscopic techniques (XANES, EXAFS, SIMS, LA-ICPMS, XPS, and XAS, to name a few) have been employed to determine (trace) elements contained in minerals and their chemical characteristics (e.g., coordination geometry and oxidation state; Henderson et al., 2014). In addition, computational approaches (e.g., density functional theory (DFT) and classical force field modeling) are useful in predicting the atomistic/electronic structures and thermodynamics of chemical species in or on mineral phases. A combined approach of experimental and computational methods is often needed when a mechanistic and thermodynamic understanding cannot be fully obtained from experiments alone.

This dissertation explores (i) the role of mineral catalysis for redox reactions based on redox chemistry experiments and (ii) the thermodynamics, atomic/electronic structures and mechanisms of ionic substitution in minerals by employing DFT calculations. The following sections of Chapter I describe the background of these research objectives and methods in details as well as introductions to Chapters II to V.

1. Minerals as redox catalysts in geochemical reactions and environmental treatments

There has been an increasing awareness that electron transfer processes can be mediated by semiconducting minerals. Mineral-catalyzed redox reactions can be sped up by orders of magnitude compared to their analogous reaction in solution. Since the toxicity and mobility of chemical species in the environment are highly dependent on their oxidation state, the kinetics of redox processes has been considered an important contribution to control the fate and transport of organic and inorganic species in natural environments (Xu and Schoonen, 2000; Tratnyek et al., 2011). The role of the catalyzing mineral can be dehydrating the reactants to make them more amenable to electron shuttling or aiding in the actual electron transfer process. If it is the latter, one has to understand a complicated pathway from the electron donor into the catalyst, electronic changes in the catalyst, and finally the shuttling of electrons from the catalyst towards the oxidant. In order to understand this process of electron transfer through the catalyst, using an electronic energy diagram can be helpful. In the energy diagram of a semiconducting solid (Figure 1-1A), the conduction band (CB) is mostly empty and the valence band is the pool of electrons that can hop into the CB when excited by energy or photons. There are two mechanistic processes to explain abiotic redox transformation. One process is that the energy level of the conduction band of a mineral phase is lower than that of the electron donor but higher than that of the electron acceptor, such that an electron is transferred from the electron donor into the conduction band of the catalyst and then into the electron acceptor (Figure 1-1A). The main driving force is the redox potential gradient between the donor (has to be higher) and acceptor (lower). However, if the energy level of electron donor is lower than the CB of a mineral phase (Figure 1-1B), an external photon of sufficient energy can provide the energy needed to lift the electron to the CB of the

catalyzing mineral. In this case, the driving force is photons with wavelengths that match the band gap in the semiconducting mineral.

Although some naturally occurring minerals (e.g., magnetite, hematite, ilmenite, anatase, pyrite, and sphalerite) are known to be semiconducting, our understanding about catalytic redox properties of semiconducting minerals is limited in most (bio-)geochemical and environmental processes. In this context, this dissertation explores the properties of mineral catalysis (Chapters II and III) upon redox transformation of chemical elements in geochemical systems and environmental treatments.

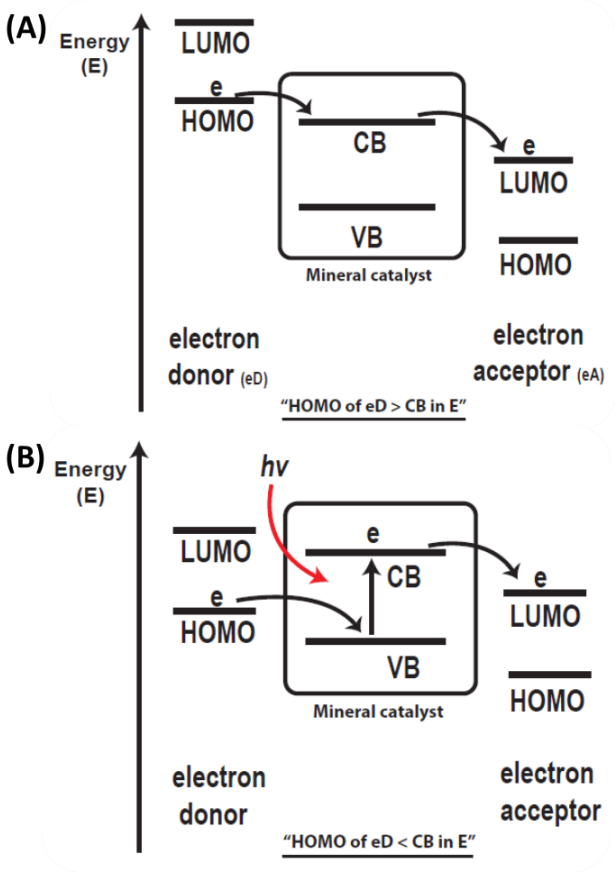

Fig. 1. 1. Mechanistic schematic of electron transfer mediated by semiconducting minerals. The main driving force is (A) the redox potential gradient in the non-photolytic process and (B) the electromagnetic radiation whose wavelength matches the band gap between the bottom of the conduction band (CB) and the top of the valence band (VB) in the photolytic process.

1.1. Can Fe-bearing mineral minerals in the environment catalyze redox reactions of trace elements?

In Chapter II, the redox chemistry is investigated as a function of pH and Eh as well as the influence of the catalyzing mineral. This experimental work has focused on redox transformations of selenium (Se) as catalyzed by magnetite (Fe_3O_4).

While Se is an essential nutrient at micromole concentrations, it becomes toxic at higher concentrations. Its mobility, toxicity, and bioavailability are greatly influenced by its redox chemistry. Se is present in natural environments in +6, +4, 0, and –2 oxidation states in dissolved or solid form, and at the –1 oxidation state in some pyrite-like solids (e.g., ferroselite ($FeSe_2$); Williams and Byers, 1934).

In order to achieve fast and controlled variation in the redox conditions in solution and controlled determination of the resulting electron transfer between the mineral catalyst and the respective Se species, I have used a novel electrochemical setup that involves the use of powdered mineral as the working electrode. This approach measures the thermodynamics (from peak positions in a current vs. redox potential diagram) and kinetics (peak area per time) of redox processes catalyzed by natural minerals. This procedure helps in identifying relevant reaction mechanisms mediated by minerals as a function of pH and Eh. A combined approach between electrochemical experiments and X-ray photoelectron spectroscopy analysis is applied to determine whether Se reduction and nucleation are mediated by magnetite.

1.2. How do organic molecules act as ligands and electron donors upon the photocatalytic reduction of uranyl? Does the energy (or wavelength) of UV light matter upon the photoreduction?

In Chapter III, the photocatalytic reactivity of the semiconducting mineral has been investigated and key reaction parameters have been identified upon the process of electron transfer

between the organic electron donor and the metal ion. This investigation focuses on the photochemical reduction of uranyl (UO_2^{2+}) as catalyzed by anatase (TiO_2).

The uranyl ion is the most stable form of uranium with the oxidation number VI in natural settings such as soils and groundwater, and in waste mixtures (for example, in nuclear waste disposal sites). Although the mobility of uranyl can be retarded by sorption onto mineral and solid-waste surfaces as well as secondary mineralization (Yang and Davis, 2000; Kim et al., 2015), remobilization may occur due to complexation with dissolved ligands, thereby potentially spreading pollution.

There is a general consensus that the heterogeneous photoreduction of uranyl with organic compounds is hindered in the presence of dissolved oxygen and that in anoxic solutions, uranyl can be reduced and precipitated as U(IV)-bearing oxides. In spite of this knowledge, it is not clear how organic molecules influence this photochemical reaction as they act as not only electron donors but also ligands. In addition, more electrons will overcome the bandgap of semiconductors as the wavelength of UV radiation becomes shorter. One question to be answered in Chapter III is whether UV radiation with shorter wavelengths and thus creating more electron-hole pairs in the anatase catalyst will be either cooperative or inhibitive to uranyl photoreduction. Chapter III is the first investigation demonstrating the oxidation of oxalate and hydroquinone as coupled with photocatalytic uranyl reduction. The three subclass regions of the UV spectrum, UV-A, B, and C, are used to examine how uranyl photoreaction with varying organic ligands responds to these regions of UV light. XPS analysis and its ability to discern oxidation states of adsorbed species were adopted to obtain direct evidence for U photoreduction as catalyzed by the irradiated mineral catalyst. Based on the uranium speciation with the organic ligand, reaction mechanisms and effects of organic ligands and UV wavelengths on photocatalytic reduction of uranyl are discussed. In

addition, quantum-mechanical calculations were performed to visualize where on the uranyl-organic complex a nucleophilic attack would be most likely to occur.

2. Ionic substitution in minerals as an indicator for physical and chemical constraints in geochemical systems and atomistic modeling of their thermodynamic properties.

Ion substitution is a spontaneous reaction when minerals form with coexisting foreign elements. From a thermodynamic point of view, energy is required for ionic substitution ($\Delta H_{inc} > 0$), i.e., a trace-element bearing mineral is less stable than the corresponding pure mineral (Figure 1-2). However, since the contributions of disorder to the total entropy ($T\Delta S > 0$) lower the total Gibbs free energy ($G=H-TS$), trace ions replacing a major ion in a mineral is energetically favorable to a certain extent at finite temperatures; the more unfavorable ΔH_{inc}, the smaller the proportion of incorporation will be. Upon the growth of minerals in fluids (e.g., melt and water), partitioning of (trace) elements to the mineral phase determines the proportion of ions as a result of ionic substitution and is often termed as incorporation and solid solution.

Incorporation and solid solution of foreign elements in minerals enable isotopic dating of geological events from natural samples, unearth valuable metals from ores, and sequestrate contaminants such as heavy metals for long time scales. For instance, uranium (U) and thorium (Th) readily substitute for zirconium in zircon ($ZrSiO_4$) (Ferriss et al., 2010). Radiogenic isotopes of U and Th in zircon are measured to date geological processes, which is known as U-Th-Pb geochronology (Schoene, 2014). Monazite, with the general formula [(Ce, La, Nd, Th)(PO_4, SiO_4)], forms solid solutions to limited or extensive degrees at the cation and the anion sites and thus becomes an important ore for thorium and rare earth elements. For example, the Th content

of monazite is variable and can be up to 30 %. Accommodating contaminants in sparingly soluble minerals is considered a promising approach for environmental treatment. In the context of nuclear waste disposals, incorporation of radioactive elements in stable structures of carbonate and sulfate minerals has been studied computationally and experimentally (Walker and Becker, 2015).

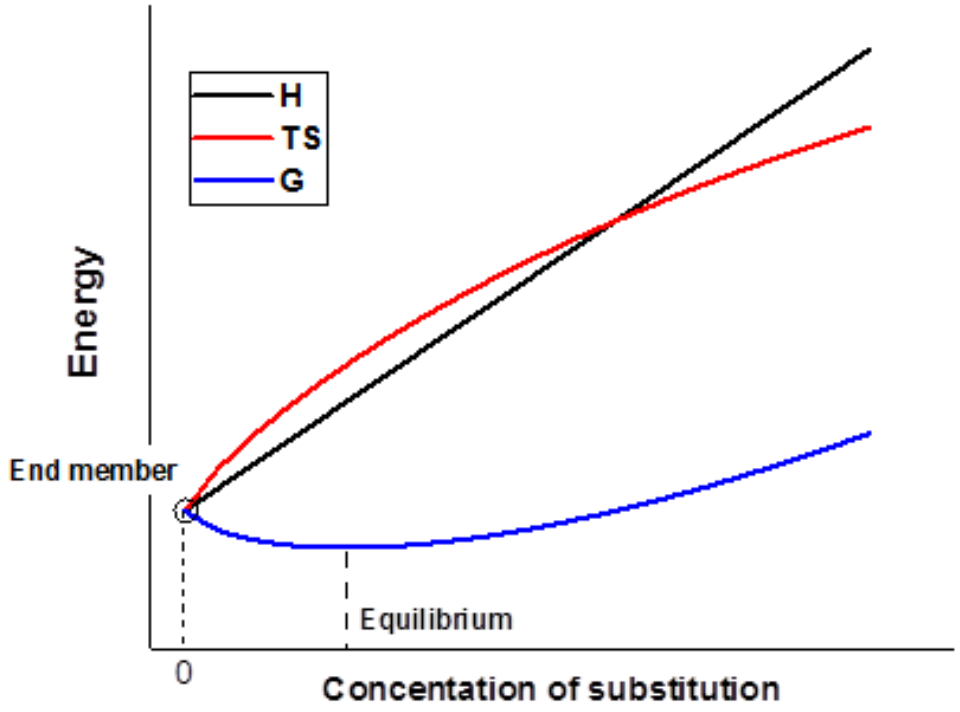

Fig. 1. 2. Schematic diagram of thermodynamic variables as a function of the extent of ionic substitution in the mineral phase.

In Chapters IV and V, quantum-mechanical modeling has been applied to simulate ionic substitution in minerals and establish the thermodynamic basis for using this system as geochemical probes. The first step of this computational procedure is to establish reaction equations of ionic substitution in the mineral of interest (Fig. 1-3). For example, the formation of olivine solid solution with a composition of [$MgFeSiO_4$] can be evaluated from an equation describing mixing between two end members, forsterite (Mg_2SiO_4) and fayalite (Fe_2SiO_4). The

next step is to run density functional theory (DFT) modeling to evaluate energies of individual reactants and products species and ultimately the reaction energy of ionic substitution such as incorporation of trace elements and binary/ternary solid solutions. If needed, thermodynamic analysis or frequency/phonon calculation is performed to obtain thermodynamic variables such as Gibbs free energy, enthalpy, and entropy. While frequency/phonon calculations allow for the analysis of the vibrational part of the entropy, the configurational entropy, which deals with the number of configurations that can be generated for a given concentration of substituting ions, and the loss of entropy due to ordering of the solid solution are calculated using statistical thermodynamic integrations.

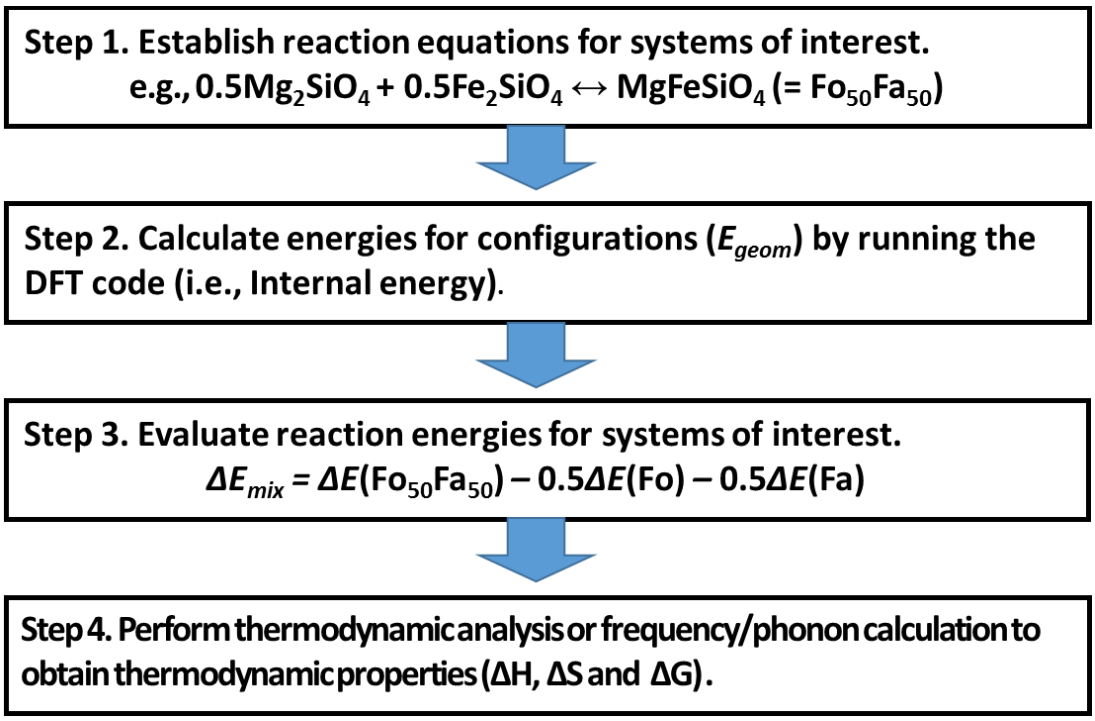

Fig. 1. 3. Schematic diagram of the computational approach applied to subjects regarding ionic substitution.

2.1. Applying quantum-mechanical modeling to simulate sulfur incorporated into apatite and establishing the thermodynamic basis for using this system as an oxybarometer.

In Chapter IV, the thermodynamics and geometry of S incorporation into apatite [$Ca_5(PO_4)_3(F,OH,Cl)$] were investigated based on the computational approach described above. Despite previous studies demonstrating the evolution and variation of S recorded in apatite phases from igneous systems (Peng et al., 1997; Streck and Dilles, 1998; Parat et al., 2002; Parat and Holtz, 2004; Parat and Holtz, 2005), little is known about the structure and thermodynamic stability of S in apatite. The recent study by Konecke et al. (2017) is the first to show semi-quantitatively that variable abundances of S^{6+}, S^{4+}, and S^{2-} are incorporated into apatite as crystallized from a mafic silicate melt under varying oxygen fugacity (fO_2) conditions. The new experimental data on S redox chemistry in apatite highlight the need for a theoretical understanding of the structural incorporation of different S species into apatite in order to understand the thermodynamics of incorporation as well as changes in the atomistic and electronic structure.

The relative stability of S with different oxidation states (S^{6+}, S^{4+}, and S^{2-}) in apatite is calculated with reference to common solid source phases for S (e.g., gypsum for SO_4^{2-} and troilite for S^{2-}) and sink phases that accommodate the replaced anions from apatite (e.g., monazite for PO_4^{3-}). This computational approach permits the determination of the energetic favorability of S incorporation into apatite depending on the occupancy of the column anion or cation impurities favorable for coupled substitution and the electronic structure and structural distortion of the incorporation site upon S incorporation. Based on the results of this computational study along with the published experimental data (Konecke et al., 2017), the potential role of S-in-apatite as a proxy to trace redox in magmatic systems is discussed.

2.2. Thermodynamic mixing properties of alunite supergroup minerals: Quantum mechanical modeling and statistical thermodynamic analysis

In Chapter V, thermodynamic mixing properties of sulfate-chromate (S-Cr) and sulfate-selenate (S-Se) solid solution and of sulfate-phosphate-arsenate (S-P-As) solid solution in alunite supergroup minerals are computationally investigated. In various geological settings, alunite supergroup minerals including the end members alunite [$KAl_3(SO_4)_2(OH)_6$] and jarosite [$KFe_3(SO_4)_2(OH)_6$] occur in extensive solid solution on both the cation and anion sites, enabling them to accommodate a variety of elements. Jarosite is known for scavenging heavy metals on the K site (e.g., Pb in solid solution between jarosite and plumbojarosite) in acid mine drainage settings; in addition, both jarosite and alunite can be important in controlling toxic anions such as selenate, chromate, or arsenate. However, there is no thermodynamic information on the solubility of these important cations and anions as a function of temperature, in part because this information is difficult to obtain experimentally.

Prior to performing the actual DFT calculations, possible configurations of ion arrangements within each solid solution are created to represent intermediate compositions between the end-member species. DFT modeling is performed to estimate the corresponding excess energy of configurations with respect to a physical mixing of end-members. The enthalpy of mixing can be derived using statistical thermodynamic analysis and assuming a Boltzmann distribution of energies. Thermodynamic integration then allows for the derivation of Gibbs free energies and configurational entropies of mixing for respective solid solution series. This work is the first to evaluate the solid solution limit of alunite supergroup minerals as a function of temperature. Our computed data are revisited to compare with previous experimental and field observations on alunite supergroup minerals. This computational work evaluates the significance of solid solution formation of alunite supergroup minerals in controlling toxic elements for long-term

immobilization in aqueous and subsoil environments and in estimating the equilibrium temperature of their formations in magmatic-hydrothermal systems.

3. Scientific contributions of the dissertation.

The experimental and computational works described in Chapter II to V have been published and other manuscripts for extended projects are in preparation and briefly introduced in Chapter VI.

- Chapter II: Kim Y., Yuan K., Ellis B. R. and Becker U. (2017) Redox reactions of selenium as catalyzed by magnetite: Lessons learned from using electrochemistry and spectroscopic methods. *Geochimica et Cosmochimica Acta* **199**, 304-323.

- Chapter III: Kim Y., Marcano M. C., Ellis B. R. and Becker U. (2018) Photocatalytic reduction of uranyl: Effects of organic ligands and UV light wavelengths. *American Journal of Science* **318**, 949-968.

- Chapter IV: Kim Y., Konecke B., Fiege A., Simon A. and Becker U. (2017) An ab-initio study of the energetics and geometry of sulfide, sulfite, and sulfate incorporation into apatite: The thermodynamic basis for using this system as an oxybarometer. *American Mineralogist: Journal of Earth and Planetary Materials* **102**, 1646-1656.

- Chapter V: Kim Y., Wolf A. S. and Becker U. (2019) Thermodynamic mixing properties of alunite supergroup minerals: Quantum-mechanical modeling and thermodynamic analysis of sulfate, chromate, selenate, phosphate, and arsenate solid solutions, as well as uranyl incorporation. *Geochimica et Cosmochimica Acta* **248**, 138-160.

- (Chapter VI): Kim Y. and Becker U. (2019, in prep) Imaging the reduction of uranyl on Fe-bearing minerals surfaces using in situ electrochemical AFM. *ACS Earth and Space Science*.

- (Chapter VI): Kim Y., Konecke B., Fiege A., Simon A. and Becker U. (2019, prep) An ab-initio study of the energetics and geometry of disulfide and bisulfide incorporation into apatite. *American Mineralogist*.

References

Allan N., Blundy J., Purton J., Lavrentiev M. Y. and Wood B. (2001) Trace element incorporation in minerals and melts. *EMU Notes in Mineralogy* **3**, 251-302.

Ferriss E., Ewing R. and Becker U. (2010) Simulation of thermodynamic mixing properties of actinide-containing zircon solid solutions. *Am. Mineral.* **95**, 229-241.

Henderson G., Neuville D. and Downs R. (2014) *Spectroscopic methods in mineralogy and material sciences*. Walter de Gruyter GmbH & Co KG.

Kim Y., Seo J., Kang S.-A., Choi S.-G. and Lee Y. J. (2015) Geochemistry and uranium mineralogy of the black slate in the Okcheon Metamorphic Belt, South Korea. *Geochem. J.* **49**, 443-452.

Konecke B. A., Fiege A., Simon A. C., Parat F. and Stechern A. (2017) Co-variability of S6+, S4+, and S2− in apatite as a function of oxidation state: Implications for a new oxybarometer. *Am. Mineral.* **102**, 548-557.

López R. and Gómez R. (2012) Band-gap energy estimation from diffuse reflectance measurements on sol–gel and commercial TiO 2: a comparative study. *J. Sol-Gel Sci. Technol.* **61**, 1-7.

Parat F., Dungan M. A. and Streck M. J. (2002) Anhydrite, pyrrhotite, and sulfur-rich apatite: tracing the sulfur evolution of an Oligocene andesite (Eagle Mountain, CO, USA). *Lithos* **64**, 63-75.

Parat F. and Holtz F. (2004) Sulfur partitioning between apatite and melt and effect of sulfur on apatite solubility at oxidizing conditions. *Contrib. Mineral. Petrol.* **147**, 201-212.

Parat F. and Holtz F. (2005) Sulfur partition coefficient between apatite and rhyolite: the role of bulk S content. *Contrib. Mineral. Petrol.* **150**, 643-651.

Peng G., Luhr J. F. and McGee J. J. (1997) Factors controlling sulfur concentrations in volcanic apatite. *Am. Mineral.* **82**, 1210-1224.

Renock D., Mueller M., Yuan K., Ewing R. C. and Becker U. (2013) The energetics and kinetics of uranyl reduction on pyrite, hematite, and magnetite surfaces: A powder microelectrode study. *Geochim. Cosmochim. Acta* **118**, 56-71.

Schoene B. (2014) 4.10-U–Th–Pb Geochronology. *Treatise on geochemistry* **4**, 341-378.

Streck M. J. and Dilles J. H. (1998) Sulfur evolution of oxidized arc magmas as recorded in apatite from a porphyry copper batholith. *Geology* **26**, 523-526.

Tratnyek P. G., Grundl T. J. and Haderlein S. B. (2011) *Aquatic redox chemistry*. American Chemical Society.

Walker S. M. and Becker U. (2015) Uranyl (VI) and neptunyl (V) incorporation in carbonate and sulfate minerals: Insight from first-principles. *Geochim. Cosmochim. Acta* **161**, 19-35.

Williams K. T. and Byers H. G. (1934) Occurence of selenium in pyrites. *Industrial & Engineering Chemistry Analytical Edition* **6**, 296-297.

Xu Y. and Schoonen M. A. (2000) The absolute energy positions of conduction and valence bands of selected semiconducting minerals. *Am. Mineral.* **85**, 543-556.

Yang J.-K. and Davis A. P. (2000) Photocatalytic oxidation of Cu (II)− EDTA with illuminated TiO_2: Kinetics. *Environ. Sci. Technol.* **34**, 3789-3795.

Yuan K., Renock D., Ewing R. C. and Becker U. (2015) Uranium reduction on magnetite: Probing for pentavalent uranium using electrochemical methods. *Geochim. Cosmochim. Acta* **156**, 194-206.

Chapter II. Redox reactions of selenium as catalyzed by magnetite: Lessons learnt from using electrochemistry and spectroscopic methods

Abstract

Although previous studies have demonstrated redox transformations of selenium (Se) in the presence of Fe-bearing minerals, the specific mechanism of magnetite-mediated Se electron transfer reactions are poorly understood. In this study, the redox chemistry of Se on magnetite is investigated over an environmentally relevant range of Eh and pH conditions (+0.85 to –1.0 V vs. Ag/AgCl; pH 4.0–9.5). Se redox peaks are found via cyclic voltammetry (CV) experiments at pH conditions of 4.0–8.0. A broad reduction peak centered at –0.5 V represents a multi-electron transfer process involving the transformation of selenite to Se(0) and Se(–II) and the comproportionation reaction between Se(–II) and Se(IV). Upon anodic scans, the oxidation peak centered at –0.25 V is observed and is attributed to the oxidation of Se(–II) to higher oxidation states. Deposited Se(0) may be oxidized at +0.2 V when pH is below 7.0. Over a pH range of 4.0–8.0, the pH dependence of peak potentials is less pronounced than predicted from equilibrium redox potentials. This is attributed to pH gradients in the microporous media of the cavity where the rate of proton consumption by the selenite reduction is faster relative to mass transfer from the solution. In chronoamperometry measurements at potentials ≥ –0.6 V, the current–time transients

show good linearity between the current and time in a log–log scale. In contrast, deviation from the linear trend is observed at more negative potentials. Such a trend is indicative of Se(0)

nucleation and growth on the magnetite surface, which can be theoretically explained by the progressive nucleation model. XPS analysis reveals the dominance of elemental selenium at potentials ≤ –0.5 V, in good agreement with the peak assignment on the cyclic voltammograms and the nucleation kinetic results.

1. INTRODUCTION

Magnetite (Fe_3O_4) is one of the most common ferrous oxide minerals in the Earth's crust (Ronov and Yaroshevsky, 1969). It occurs in diverse geological settings including igneous, metamorphic, and sedimentary units (Grant, 1985). Magnetite has unique ferromagnetic properties and contains both ferric and ferrous iron in its structure. As a result, it plays a unique role in catalytically promoting redox reactions that may affect the short- and long-term geochemical cycles of iron and trace metals, such as Cr, As, or U, where the redox state sensitively affects the environmental behavior. In oxic aqueous environments, the ferrous iron (Fe^{2+}) present in magnetite may serve to reduce other redox-sensitive species in solution and form ferric oxyhydroxides (White et al., 1994). The magnetite surface also provides specific adsorption sites for other solutes, which accounts for an interdependence of the iron geochemical cycle with that of many other elements (Stumm and Sulzberger, 1992). Gorski et al. (2012) recently reported that exchange of iron between the magnetite bulk structure and the aqueous phase is much more dynamic than previously believed and may be an important process in the sequestration and release of structurally incorporated trace metals.

While selenium (Se) is an important micronutrient for most life forms, it can be toxic at high concentrations. Its mobility, toxicity, and bioavailability are greatly influenced by its redox chemistry. Se is present in natural environments at +6, +4, 0, and –2 oxidation states in dissolved or solid form, and at the –1 oxidation state in some pyrite-like solids (e.g., Williams and Byers, 1934). Se(VI) and Se(IV) (selenate and selenite, respectively) tend to be more soluble and toxic than Se(0) and Se(–II). Under highly reducing conditions in natural environments, Se(–II) is stable in solution as HSe^- and Se^{2-} or in solid phase metal selenides. H_2Se is stable only in highly acidic solutions.

The redox state of selenium can be influenced by microbial and abiotic processes in natural environments. The reduction of oxidized Se species to Se(0) is induced by microorganisms that metabolize organic matter in subsurface and aqueous environments (Lovley, 1993). Such microorganisms use oxidized selenium species as a terminal electron acceptor during the oxidation of organic matter. Analogous abiotic reduction of Se can be facilitated or catalyzed on mineral surfaces. The mechanisms for Se reduction by Fe-containing minerals are well described (Myneni et al., 1997; Bruggeman et al., 2005). Myneni et al. (1997) reported that reduction of Se(VI) to Se(0) occurs in the presence of green rust at rates comparable to those found in sediments. Green rust was demonstrated to mediate the reduction of Se(VI) via a heterogeneous process that includes adsorption or co-precipitation. The kinetics of Se reduction depends on the type of selenium species and mineral. For example, the reduction of oxidized Se to Se(0) by green rust or pyrite is slow whereas selenite is rapidly reduced by nanoparticles of magnetite and mackinawite (Scheinost and Charlet, 2008). These studies demonstrate that abiotic redox transformation mediated by Fe-bearing minerals can be an important process in the geochemical cycling of selenium in natural environments.

There have been attempts to adopt electrochemistry to investigate geochemical redox processes involving minerals. White et al. (1994) studied the dissolution kinetics of magnetite and observed the formation of an oxidized layer and the release of Fe(II) from the mineral structure into solution. A related study examined the reductive dissolution of magnetite in the presence of dissolved transition metals through use of potential dynamic voltammetry and found that the reduction of dichromate can suppress the reductive dissolution of magnetite (White and Peterson, 1996). The powder microelectrode (PME) method is commonly used to investigate electroactive materials and technological applications such as battery materials and fuel cells. So far, the application of the

PME to study naturally occurring minerals has been limited but promising for the investigation of redox kinetics on surfaces (mainly oxides and sulfides).

Renock et al. (2013) employed a standard three-electrode system equipped with PME to evaluate the thermodynamics and kinetics of U(VI) reduction by Fe oxides and sulfides. Yuan et al. (2015a) and Yuan et al. (2015b) used a PME in concert with cyclic voltammetry experiments to discover that the disproportionation reaction mediated by U(V) is predicated upon the redox transformation of U(VI) on magnetite. Far fewer studies have addressed abiotic redox transformations of selenium mediated or catalyzed by magnetite (Scheinost and Charlet, 2008). The redox chemistry of Se has been examined for industrial purposes. For example, Se thin films are semiconducting and light sensitive such that they can be applied to devices such as solar cells, biological sensors, and light-emitting diodes (Lai et al., 2010; Saji and Lee, 2013). Although similar redox transformations may proceed upon interaction of Se with natural minerals, it is expected that specific mechanisms of Se redox behavior on minerals can be distinguished from those of industrially relevant materials (Saji and Lee, 2013). Moreover, little is known about Se electrochemistry over environmentally relevant pH value ranges because previous experiments have typically been performed in very acidic solutions (pH < 2) pertinent to technical applications (Saji and Lee, 2013).

The goal of this investigation is therefore to use electrochemical techniques to identify and quantify reaction mechanisms and kinetics of the redox transformation of selenium mediated by magnetite at pH and Eh values commonly encountered in natural aqueous environments. The range of pH investigated was from 4.0 to 9.5 and the Eh range from +1.1 to –0.77 V (+0.85 to –1.0 V vs. Ag/AgCl). Cyclic voltammetry and chronoamperometry were performed using the magnetite electrode and collected data were analyzed to identify specific redox species responsible for

electrical signals at given pH and Eh. X-ray photoelectron spectroscopy (XPS) was adopted to obtain direct evidence for Se redox reactions catalyzed by the magnetite electrode. In the discussion section, some of the results are revisited and discussed with quantitative evaluation including possible effects of solution chemistry on the Se redox transformation, mechanisms of Se nucleation derived by the magnetite electrode, and the catalytic role of magnetite in aqueous environments. By evaluating mechanisms and kinetics of heterogeneous redox reactions involving a mineral, this study intends to advance our understanding of the selenium redox transformation and catalytic effects of Fe-bearing minerals in subsurface environments.

2. MATERIALS AND METHODS

2.1. Magnetite electrodes

The powder microelectrode (PME) was prepared by conventional glass-blowing techniques with a Pt wire (100 lm in diameter) sealed in the center of the glass tube. In order to create the powder-filling cavity, the tip of the Pt wire was digested in aqua regia for 3 h at 80℃. Further details about the PME preparation and usage can be found in the literature (Cha et al., 1994; Cachet-Vivier et al., 2001; Renock et al., 2013; Yuan et al., 2015a; Yuan et al., 2015b). Although most experiments were performed using the PME, a bulk magnetite electrode (10–30 mm^2 in cross-sectional area) was prepared for specific experiments such as nucleation chronoamperometry and X-ray photoelectron spectroscopy (XPS). The preparation procedure for the bulk magnetite electrode was adopted from methods described by White et al. (1994) and Yuan et al. (2015b). Magnetite crystals (<5 mm in dimension) were polished with sand paper and thoroughly rinsed with Milli-Q water in order to remove any contaminants introduced through polishing. The samples were attached to copper wires using conducting silver paste and subsequently sealed,

except for the exposed mineral surface, with an electronic-grade insulating epoxy. Natural magnetite (Mineville, New York) was used for all experiments. X-ray diffraction (XRD) analysis confirmed that magnetite is the primary phase in the specimen. No treatment of the magnetite powder was performed to remove potential impurities prior to experiments. Although magnetite is a semiconductor, impurities can lead to a decrease in its conductivity. In order to ensure stable electrochemical signals for the PME, the natural magnetite was mixed with a graphite additive (10:1 magnetite/graphite ratio in mass) and ground using mortar and pestle. Such use of graphite to improve conductivity in PME experiments is well documented by Yuan et al. (2015b). The microcavity was packed with the magnetite powder by tapping the electrode cavity into the powder. The powder stayed in contact with the Pt wire during the experiment and was subsequently removed by sonication in 0.1 M $HClO_4$ solution after completion of each experiment.

2.2. Electrochemical experiments

In addition to the magnetite PME as the working electrode, a Pt wire served as the counter electrode and Ag| AgCl|1 M KCl (+0.235 V vs. standard hydrogen electrode, SHE, at 25 ℃) was employed as a reference to compose a standard three-electrode cell. In the cyclic voltammetry (CV) measurements, voltammetric cycles were repeated until steady-state voltammetric responses were obtained. The potential range at which experiments can be performed without reducing or oxidizing the solvent differs between the electrode materials. The effective potential range for the Pt electrode in water is approximately –1.0 to +1.0 V *vs.* Ag/AgCl (Nurmi and Tratnyek, 2011). This range was used for all magnetite PME experiments. The scan rate for voltammetry experiments was set at 50 mV/s unless stated otherwise. Scanning at a higher rate was avoided because the irreversibility of Se redox reactions on magnetite increases with increasing scan rate,

whereas scanning at lower rates leads to a decrease in the ratio of peak current to magnetite background current (see Section 3.1.2). For electrochemical experiments, the Se(IV) solution was prepared by dissolving Na_2SeO_3 (Sigma Aldrich) in Milli-Q water with sodium perchlorate added as a background electrolyte to make solutions sufficiently conductive. The solutions were initially adjusted to the desired pH (4.0–9.5) by adding concentrated $HClO_4$ or NaOH. Prior to voltammetric scans, the solutions were purged with argon gas for 30 min to minimize the presence of dissolved oxygen and an argon headspace was maintained throughout each experiment. All electrochemical experiments were carried out at room temperature and atmospheric pressure.

2.3. XPS analysis

XPS spectra were collected using an Axis Ultra spectrometer (Kratos Analytical UK). A monochromic and focused Al Ka radiation (1486.6 eV) was used for the excitation of samples. All measurements were performed in hybrid mode which employs both electrostatic and magnetic lenses. Survey and core scans were acquired at the constant pass energies of 160 and 20 eV, respectively. Measurements were performed under vacuum lower than 10^{-8} Torr. All spectra reported were calibrated using the position of the C 1s peak (286.4 eV) from adventitious carbon at the surface. Spectra analysis and calibration were performed using the CASA XPS software (version 2.3.16, www.casaxps.com).

3. RESULTS

3.1. Electrochemical characterization of selenium redox transformation

Magnetite behaves like a capacitor and typically exhibits a capacitance one or two orders of magnitude greater than electric double-layer capacitance (EDLC). Its pseudocapacitance arises

mainly from Faradaic reactions involving surface or adsorbed species in aqueous electrolytes and is highly dependent on the type of aqueous electrolyte (Wu et al., 2003; Wang et al., 2006). Since the pseudocapacitance of magnetite results in large currents, electrochemical measurements were performed with the blank (i.e., $NaClO_4$ only) and selenium solutions (Se(IV) + $NaClO_4$), separately, and the data were compared to distinguish electric signals of redox-active species from those of magnetite.

3.1.1. Cyclic voltammetry of magnetite microelectrode

The cyclic voltammetry of the magnetite PME was performed to examine current and electrochemical features of magnetite in blank solutions ($NaClO_4$ only) (Fig. 2.1). The cyclic voltammetry of magnetite was run at different pH values for 25 cycles (Fig. 2.1A). Since new magnetite samples were tested at each pH value, there was variation in current between the experiments. Nevertheless, the general patterns of the voltammograms are comparable between all magnetite PMEs.

The complete voltammetric cycle shows a broad reduction shoulder centered near –0.3 V and two anodic peaks at –0.15 V and +0.4 V in agreement with previous reports on magnetite electrochemistry (Renock et al., 2013; Yuan et al., 2015b). For the anodic peak at +0.4 V, Yuan et al. (2015b) found that the peak potential and current increased when Fe(II) was added to the solution and proposed that the peak is attributed to the oxidation of ferrous to ferric iron. The cyclic voltammetry as a function of scan range is shown in Fig. 2.1B. The currents measured from cathodic and anodic scans increase with increasing negative switching potential. The anodic peak at +0.4 V appears at switching potential lower than –0.7 V, indicating the occurrence of magnetite dissolution.

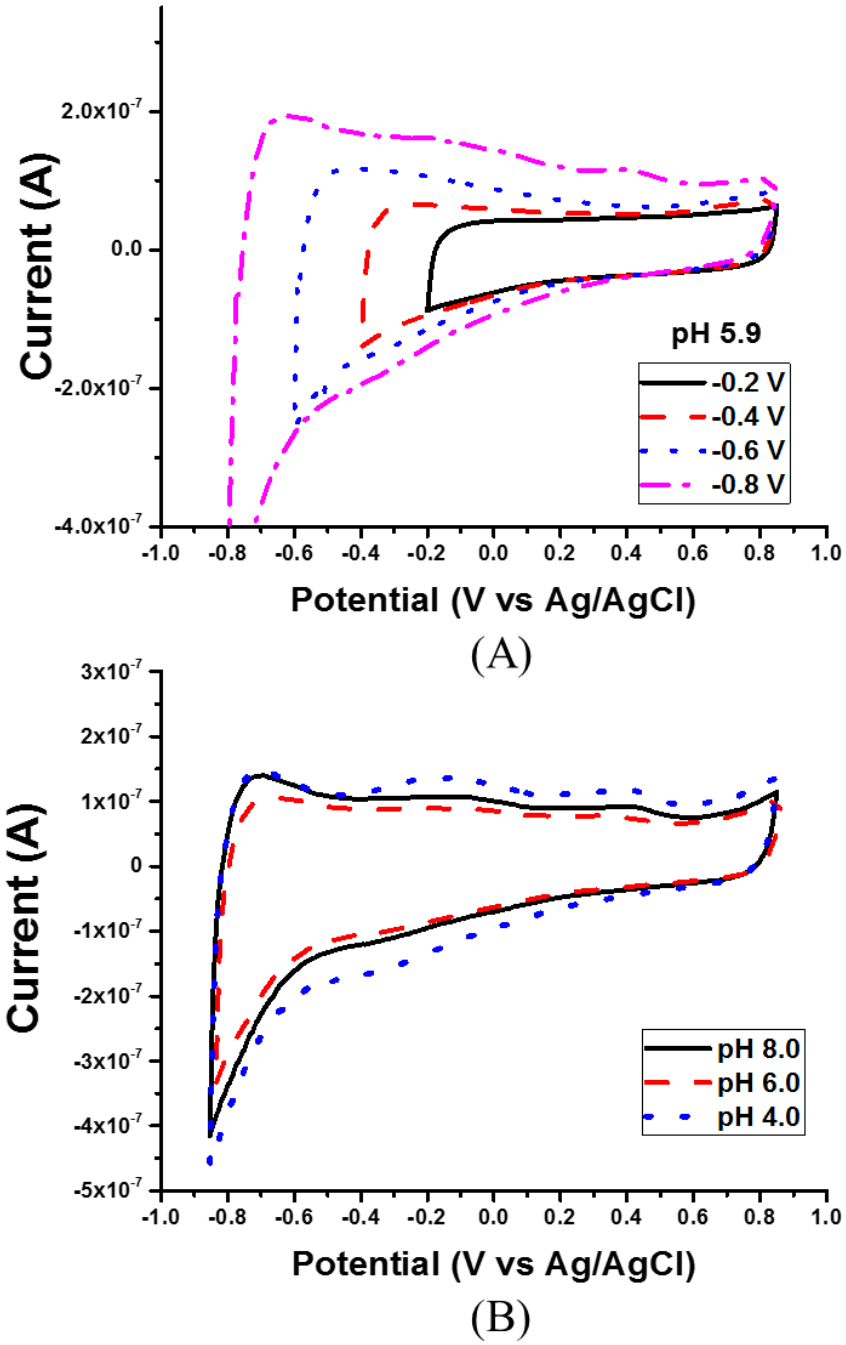

Fig. 2. 1. Cyclic voltammograms of the magnetite PME in 0.05M $NaClO_4$ (A) at the whole scan range with different pH values and (B) as a function of scan range at pH 5.9. Scan ranges are denoted by the negative switching potential values (–0.2 to –0.8 V) in the legend.

3.1.2. Cyclic voltammetry of selenium using a magnetite electrode

The cyclic voltammogram of Se(IV) as a function of pH and concentration is shown in Fig. 2.2. At pH 9.5, variations in Se(IV) concentration have little influence on the voltammogram, indicating no significant change in Se redox characteristics on magnetite (Fig. 2.2A). The voltammograms evidently evolve as the selenium concentration varies at pH values ≤ 8.0. At pH 8.0, cathodic and anodic peaks are centered at about –0.5 and –0.25 V, and denoted by C1 and A1, respectively (Fig. 2.2B). Under acidic conditions (pH 4.0–6.0), there is only a small change in the peak position of C1 (–0.5 to –0.45 V). Upon anodic scans, peak A1 shows only a slight variation in potential (within a range of –0.3 to –0.2 V) and a new anodic peak, A2, develops near +0.2 V. At the pH range of 4.0–8.0, the anodic curves of different Se concentrations (1–25 mM) intersect with each other and the background curve (i.e., [Se] = 0 mM) at about –0.6 V. The intersection can be interpreted as a potential where a transition between reductive and oxidative processes occurs as redox potential changes on the magnetite electrode. The total current measured on the magnetite electrode is a combination of the current rising from magnetite, which is the observed current in the background curve, and the current generated from Se redox transitions. The total current is lower than the background current in the anodic potential region <–0.6 V, because electron-accepting processes of the electroactive species continue even upon anodic scanning. The total current is higher than the background current at potentials >–0.6 V where the electron-donating processes proceed. For all CV curves between pH 4.0–8.0, the peak currents of A1, A2, and C1 increase as the concentration of Se(IV) increases from 1 to 25 mM, confirming that the peaks are mainly due to redox processes involving Se during the positive and negative-going scans.

Cyclic voltammetry was performed at varying scan range in order to help identify individual redox peak pairs (Fig. 2.3). The aim of voltammetry using a narrow electrochemical potential range

is to assign peaks describing corresponding redox couples observed upon cathodic and anodic scans. Coupling peaks may be obscured when scanning over a wide range of potentials if more than two peaks are produced as a result of cyclic voltammetry. This method of incrementally increasing scan ranges can be advantageous to resolve the CV curves where cathodic scans produce a broad peak region (i.e., peak C1 in Fig. 2.2). In Fig. 2.3, the growth of anodic peaks A1 and A2 becomes pronounced as the switching potential increases. At pH 4.0–7.9, peak A1 starts to appear upon scans recorded at the switching potentials of –0.5 V and its peak current is further enhanced at more negative switching potentials. At pH 5.9 and 4.0, peak A2 begins to rise above background signals at a scan between –0.4 and +0.85 V. The switching potentials of –0.5 V for A1 and –0.4 V for A2, are both close to the peak potential of C1, thus implying that peak C1 is responsible for both peak A1 and A2. In this case, more than one reduction process takes place and the reduction products are oxidized at peaks A1 and A2. This explanation is plausible because the slow redox kinetics of selenium can cause multiple peaks to overlap and to be seen as a single broad peak (Renock et al., 2013). In summary, although peak C1 is centered at about –0.5 V, the peak is broad, ranging from –0.2 to –0.8 V (Fig. 2.2) and is likely the result of multistep charge transfer and slow Se redox chemistry.

The kinetics of selenium transformation on the magnetite surface is further examined by performing cyclic voltammetry at varying scan rates (Fig. 2.4). The small size of the microcavity electrode (100 μm in diameter and a few tens of μm deep) in this study allows performing cyclic voltammetry over a large range of scan rates (25–250 mV/s). The CV curves remain stable at rates ≤250 mV/s. The peak currents increase with increasing scan rate and the least-square fits show excellent linearity ($R^2 > 0.98$) between the current and the the current and the square root of the scan rate (Fig. 2.4C). Upon increasing the scan rate, the cathodic and anodic peaks are shifted by

about 0.1 V to more negative and positive potentials, respectively (Fig. 2.4D). Irreversibility of Se redox processes on magnetite is indicated by the fact that the positions of cathodic and anodic peaks are highly dependent of the scan rate (Nurmi and Tratnyek, 2011). The role of slow kinetics in Se redox irreversibility is further substantiated by other features from the cyclic voltammetry results such as the broad peak widths and deviation of the peak potentials from the corresponding equilibrium reduction potentials (Fig. 2.2 and Section 3.1.3) (Bard and Faulkner, 1980).

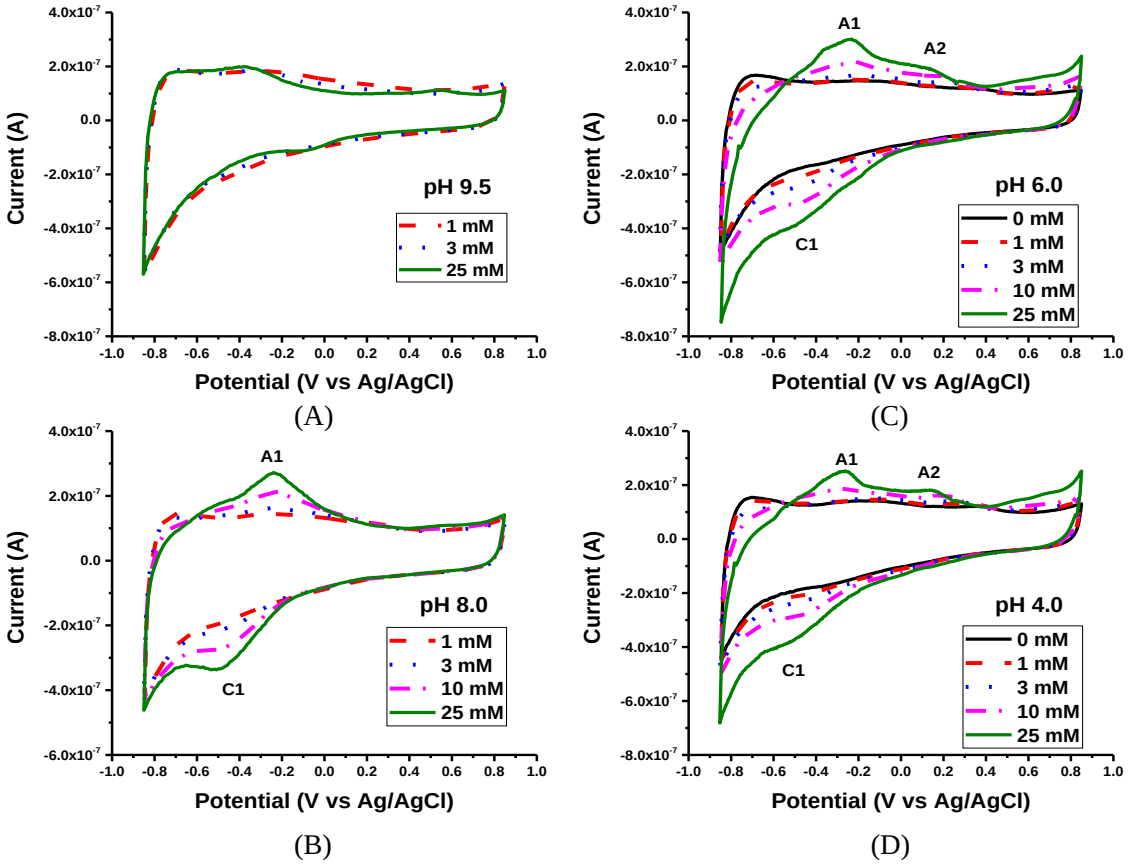

Fig. 2. 2. Cyclic voltammograms for Se(IV) with the magnetite PME as a function of pH and the Se(IV) concentration (pH 4.0 to 9.5; [Se(IV)] = 1–25 mM). The solution contained 0.05 M $NaClO_4$ as a background electrolyte.

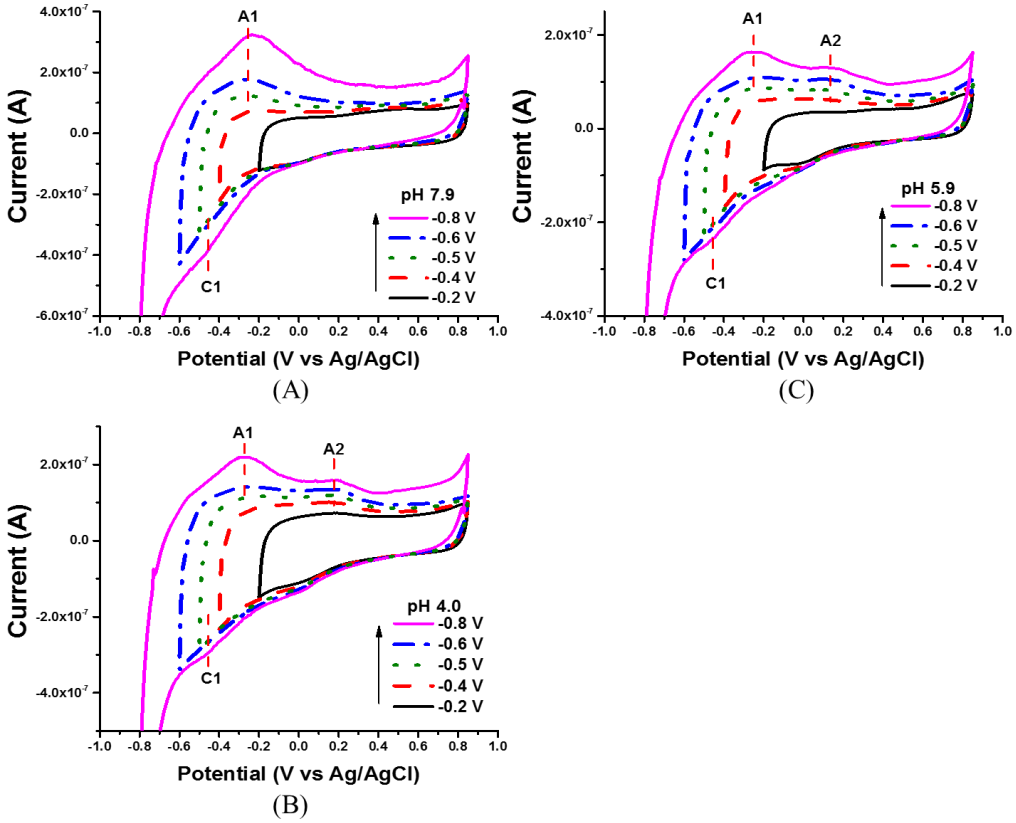

Fig. 2. 3. Cyclic voltammograms for Se(IV) with the magnetite PME as a function of scan ranges. The scans were performed in a solution containing 10 mM Se(IV) and 0.05 M $NaClO_4$.

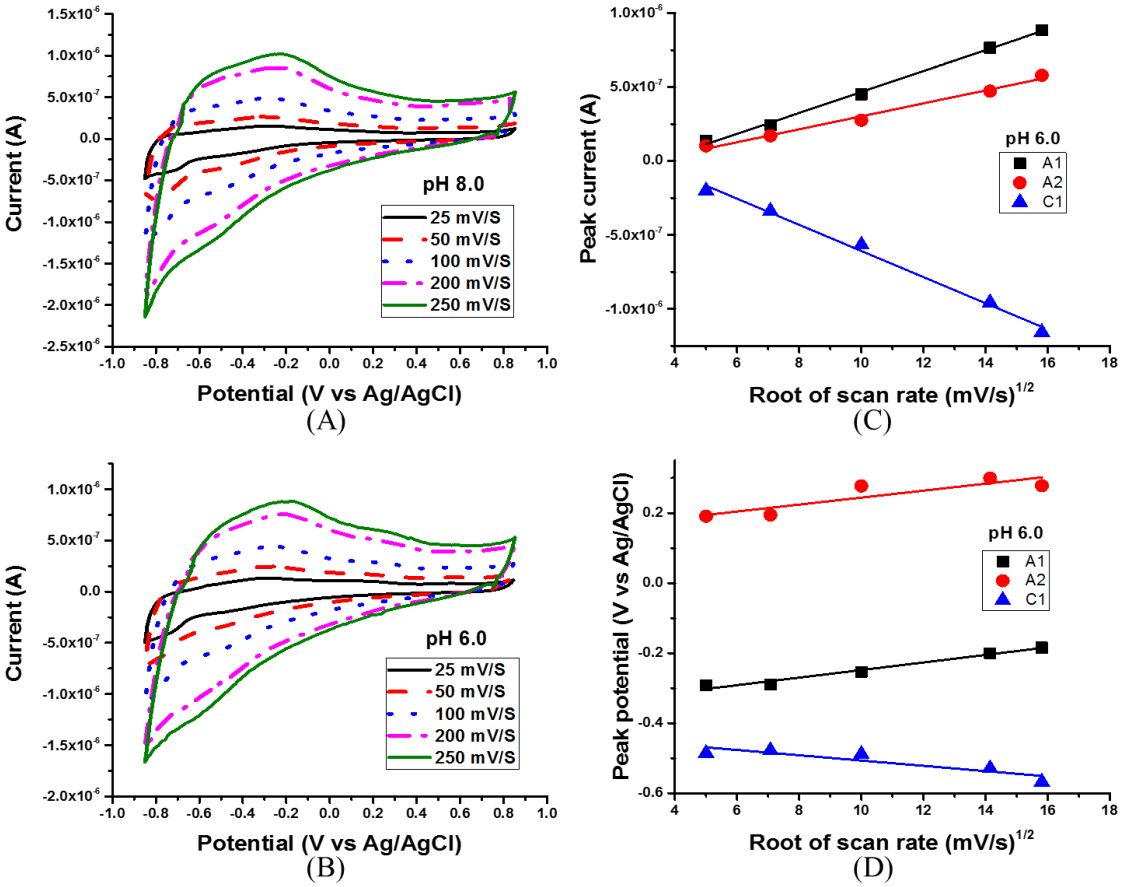

Fig. 2. 4. Cyclic voltammograms as a function of scan rate (25 to 250 mV/s) (A) at pH 8.0 and (B) at pH 6.0. For pH 6.0, (C) peak currents and (D) potentials were plotted and the linear least-square fits were added to show their trends. The scans were performed in a solution containing 10 mM Se(IV) and 0.05M $NaClO_4$.

3.1.3. Redox transformation of selenium on magnetite

Se(IV) in the bulk solution can be converted into Se(VI), Se(0), and Se(–II) during cyclic voltammetry scans. To investigate Se redox transformations on the magnetite surface, possible selenium redox reactions and their reduction potentials were considered (Table 2.1 and Fig. 2.5). The Se(IV) speciation (protonation stage) was calculated for pH 2–12 as shown in Fig. 2.6. Biselenite ($HSeO^{3-}$) and biselenide (HSe^{-}) are the dominant selenium species between pH 4.0–8.0 where electrochemical peaks indicating selenium redox transformation are found (Figs. 2.2 and 2.6). The oxyanion of Se(VI), selenate is a very weak base (pK_{a2} = 1.7) and is present mainly as a deprotonated species, SeO_4^{2-} at pH>2. Based on this speciation, half reactions of the dominant Se species as reactants or products were derived as a function of pH (Table 2.1).

Table. 2. 1. Reduction potential equations for possible redox reactions of selenite as a function of pH. The reactions I to IV are denoted in text by abbreviated forms indicating the oxidation state, Se(IV)/Se(0), Se(IV)/Se(-II), Se(0)/Se(-II) and Se(VI)/Se(IV), respectively.

	Standard reduction potential* (*vs.* Ag/AgCl)
I) $HSeO_3^- + 5\ H^+ + 4e^- = Se(s) + 3H_2O$ $E = 0.54 - 0.074\ pH + 0.015\ \log[HSeO_3^-]$	$E^0 = 0.54$ V
II) $HSeO_3^- + 6\ H^+ + 6e^- = HSe^- + 3H_2O$ $E = 0.11 - 0.059pH + 0.010\ \log[HSeO_3^-]/[HSe^-]$	$E^0 = 0.11$
III) $Se(s) + H^+ + 2e^- = HSe^-$ $E = -0.75 - 0.030\ pH - 0.030\ \log\ [HSe^-]$	$E^0 = -0.75$
IV) $SeO_4^{2-} + 3H^+ + 2e^- = HSeO_3^- + H_2O$ $E = 0.84 - 0.089\ pH + 0.030\ \log\ [SeO_4^{2-}]/[HSeO_3^-]$	$E^0 = 0.84$

* adopted from Bouroushian (2010).

The half reactions of these redox couples indicate that the reduction of selenium species is thermodynamically favored under acidic conditions. The equilibrium reduction potential (E_{eq}) equation of each half reaction was calculated from the Nernst relation (Eq. (1)) to identify the redox processes responsible for the observed CV peaks (Table 2.1).

$$E_{eq} = E^0 + \frac{RT}{nF} ln \frac{a_O}{a_R} \quad (1)$$

where E_{eq} is the equilibrium reduction potential, E^0 the standard reduction potential, R the universal gas constant, T the temperature in Kelvin, n the stoichiometric number of electrons involved in an electrode reaction, F the Faraday constant, and a_O and a_R, the product of activities of all oxidants and reductants, respectively.

Although the standard potential may serve as a similar indicator, the equilibrium reduction potential is suitable in this study where the solution chemistry departs from the standard state (i.e., the concentrations of solutes and proton ≤ 1 M). It is a reasonable assumption that the initial Se(IV) concentration (0.01 M) is approximately equal to [$HSeO_3^-$] at a pH range of 4.0–8.0. In the bulk solution (50 mL in this study), other selenium species can only be produced from the Se(IV) redox reactions in the microcavity and therefore, their concentrations would be minute. In Fig. 2.5, the reduction potential lines are where [$HSeO_3^-$] is 10^{-2} M and the concentrations of other selenium species are from 10^{-4} to 10^{-8} M. All four redox couples considered show a decrease in their equilibrium reduction potentials with increasing pH.

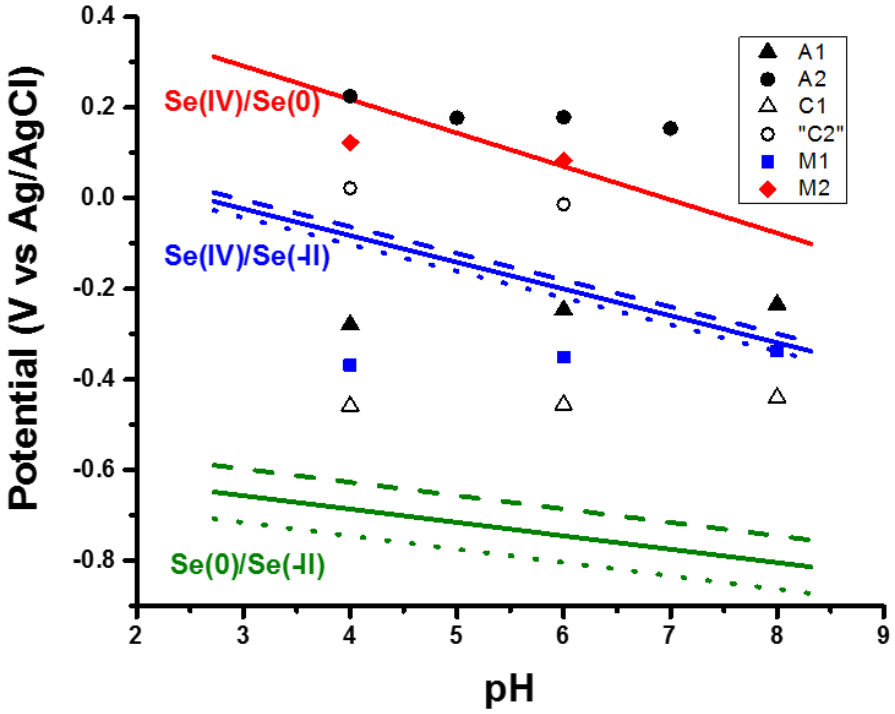

Fig. 2. 5. pH dependence of observed CV peaks and theoretical equilibrium reduction potentials for selenium redox transformation. The peak potential data were collected from the cyclic voltammetry performed in solution containing 10 mM Se(IV) and 0.05 M NaClO4. Lines are equilibrium reduction potentials of the redox couples, Se(IV)/Se(0) (red), Se(IV)/Se(–II) (blue) and Se(0)/Se(–II) (green) where $[HSeO_3^-]$ = 0.01 M and $[HSe^-] = 10^{-4}$–10^{-8}M (dashed, 10^{-4} M; solid, 10^{-6} M; dotted, 10^{-8} M). (For interpretation of the references to color in this figure legend, the reader is referred to the web version of this article.)

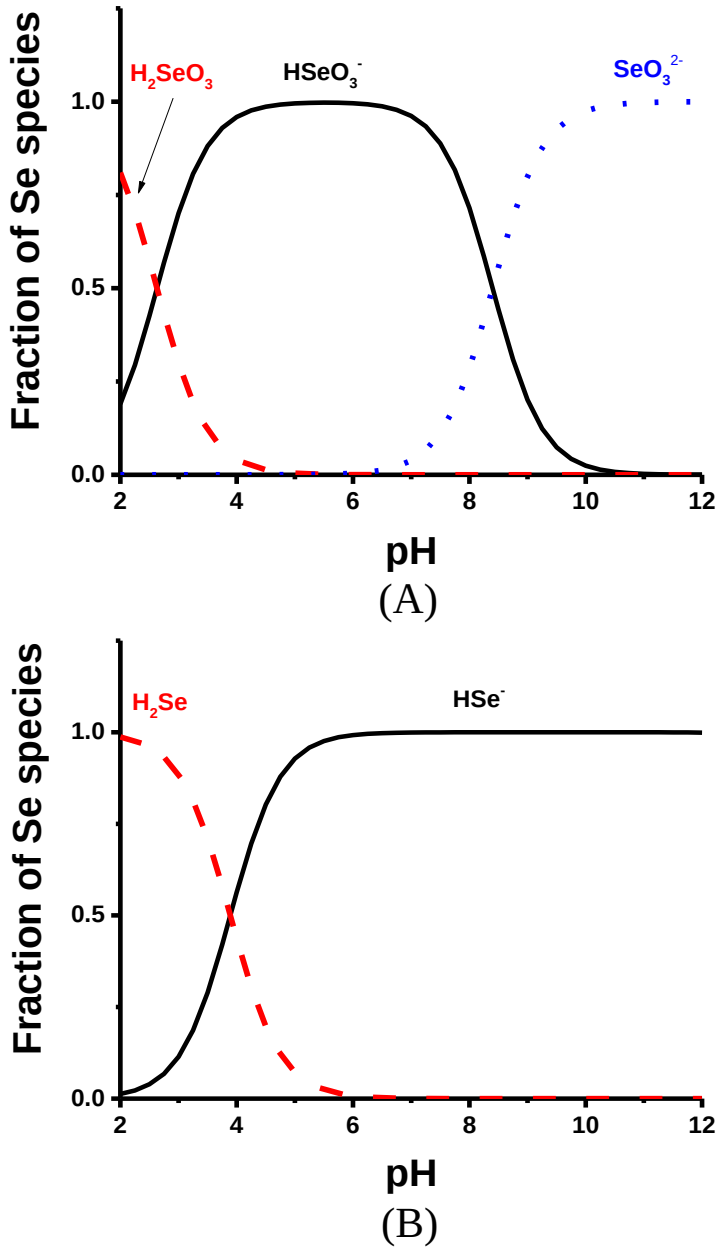

Fig. 2. 6. Speciation of (A) Se(IV) and (B) Se(–II) as a function of pH ([Se] = 0.01 M). It is noted that biselenite ($HSeO_3^-$) and biselenide (HSe^-) are the most dominant species over a range of solution pH 4.0–8.0.

When comparing reduction potentials measured using CV curves with theoretical equilibrium reduction potentials, determination of the midpoint potentials, i.e., the average of cathodic and anodic peak potentials ($E_{mid} = (E_{cath} + E_{anod})/2$) is typically used because the mid potential is approximately equal to the equilibrium reduction potential for reversible redox couples (Renock et al., 2013; Yuan et al., 2015b). This means that for both anodic peaks (A1 and A2), corresponding cathodic peaks have to be identified. Accurate measurements of reduction potentials using mid peak potentials are obscured by the fact that cathodic peaks, especially the ones corresponding to A2, cannot be clearly identified in all CV curves, partly because they are less sharp than the anodic ones. Nevertheless, for the sake of comparing theoretical reduction potentials with measured midpoint potentials, some data points ‘‘C2” (the quotation marks indicating the caveats described above), and the corresponding midpoint potentials are given in Fig. 2.5. The midpoint potentials of pairs A1/C1 and A2/‘‘C2” are close to the theoretically-derived reduction potentials of the Se(IV)/Se(–II) and Se(IV)/Se(0) couples, respectively, but the association of the peaks with the selenium redox couples can be more complicated (Table 2.1).

First, one needs to consider if either of the trends for Al and A2 peaks can be associated with the Se(VI)/Se(IV) couple. Alanyalioglu et al. (2004) reported that a pair of peaks corresponding to Se(VI)/Se(IV) redox pair was not observed when a scan range is made more negative than +0.3 V because of the formation of elemental Se from adsorbed selenite ions. Such a tendency of the Se(VI)/Se(IV) pair is contrasted with the trend for peak A1 and A2 in this study where an increase of peaks A1 and A2 with scanning at more negative potentials was observed (Fig. 2.3). Since the initial solution is prepared with sodium selenite, reduced species Se(0) or Se(–II) are likely to form under negative potentials and oxidation of Se(IV) to Se(VI) can be excluded as a peak assignment for these two anodic peaks. Since the peak potential values of A2 are comparable to reduction

potentials of the Se(IV)/Se(0) couple, it may be tentatively assigned to the oxidation of Se(0) to Se(IV) (Fig. 2.5). Lai et al. (2010) studied electrodeposition of Se(IV) onto the SnO_2 electrode using cyclic voltammetry in an acidic solution (pH ≈ 2). The oxidation peak at +0.25 V (vs. Ag/AgCl) was assigned to the oxidation of Se(0) to Se(IV). Although the electrode material and solution chemistry differed, the values reported by Lai et al. (2010) are comparable to the A2 peak potential of this study (+0.2 V at pH 4.0). Although peak C1 is centered at –0.5 V, the peak is very broad (from –0.2 to –0.8 V) and can reflect multistep charge transfer on the electrode (Section 3.1.2). The potential of –0.5 V is more negative than the equilibrium reduction potentials of the Se(IV)/Se(0) and Se(IV)/Se(–II) couples (Table 2.1 and Fig. 2.5). Despite no further thermodynamic evidence, the comparison with the equilibrium reduction potentials supports the peak potential of C1 accounting for the formation of Se(0) and Se(–II) over the pH range of this study. An analogous interpretation was made in a previous study for selenite reduction on a gold electrode (Wei et al., 1994), which assigned a peak at –0.5 V to a combination of Se bulk deposition and Se(–II) formation. There is an overall consensus that Se(–II) species are produced from the reduction of Se(IV) (e.g., Wei et al., 1994; Santos and Machado, 2004; Lai et al., 2010; Saji and Lee, 2013). Two different mechanisms have been proposed for the formation of Se(–II) (Lai et al., 2010; Saji and Lee, 2013). The first one is that Se(–II) is produced from further reduction of deposited Se(0). This can be described for our solution chemistry as a two-step process, equation I followed by equation III in Table 2.1. The second scheme is the formation of Se(–II) directly from Se(IV) as seen from equation II in Table 2. 1. As the potential goes more negative than –0.5 V, the direct conversion from Se(IV) to Se(II) becomes more likely, but the production of Se(–II) from Se(0) may also proceed at very negative potentials (<–0.7 V). When Se(–II) is produced from

either process, a subsequent comproportionation reaction can proceed in Se(IV)-containing solutions (Wei et al., 1994; Santos and Machado, 2004):

$$2\,HSe^- + HSeO_3^- + 3\,H^+ \leftrightarrow 3\,Se^0 + 3\,H_2O \quad \text{or} \quad 2\,HSe^- + HSeO_3^- \leftrightarrow 3\,Se^0 + 3\,OH^- \quad (2)$$

The broad cathodic peak at C1 can explain different Se redox transformation processes: Se(IV) → Se(0) (→ Se(-II)), Se(IV) → Se(-II), and Se(-II) → Se(0). Therefore, the observed cathode peak broadening may reflect that the selenium redox transformation on magnetite occurs through multiple processes.

The oxidation of Se(–II) and Se(0) may occur more and more as the anodic scan proceeds. The cyclic voltammetry as a function of scan range reveals that the peak current of A1 is associated with the species produced at C1 (Fig. 2.3). The equilibrium reduction potential data suggest that the peak potential of Al (–0.2 to –0.25 V) may account for the oxidation of Se(–II) to Se(IV) or to Se(0) (Fig. 2.5). In a similar manner, it is inferred that the oxidation of Se(0) may proceed at the potential corresponding to peak A2 as the scan goes more positive. Although our peak assignment based on the thermodynamic data is consistent with previous studies and spectroscopic data (Section 3.2), the pH dependence of the CV peaks measured using a PME is less pronounced than that expected from the corresponding half reactions (Fig. 2.5). This may be caused by the pH in the microcavity continuously changing during potential scans whereas the bulk solution pH (that is used to calculate expected peak positions from half reactions) is almost invariable throughout the experiment. This pH gradient between the bulk solution and pores in the powder where redox transitions (and implicit pH changes) take place, leads to a peak broadening and potential shift of peaks relative to peak positions when the bulk solution pH is applied. Such considerations are revisited and discussed further in Section 4.1.

3.1.4. Chronoamperometry and nucleation kinetics

The kinetic aspects of selenium reduction processes on magnetite were examined using chronoamperometry over a negative potential range (0.0 to –1.0 V). Chronoamperometry measures current as a function of transient time when a potential is stepped between potentials on the working electrode. Two different solutions were prepared to differentiate the current from electroactive species and the capacitance current from electrolyte species acting on the magnetite surface: a selenium solution (10 mM Na_2SeO_3 + 0.1 M $NaClO_4$) and a blank solution (0.1 M $NaClO_4$). Current–time transients were recorded after stepping a potential from +0.25 V to various final potentials ranging from 0.0 to –1.0 V. Current–time transients are plotted on a log–log scale (Fig. 2.7A and B) and indicate a continuous decrease in current with time. The general trend is that the logs of measured currents are linearly dependent on the log of time throughout the measurement time (50 s). For the current–time data in the first second, the coefficient of determination (R^2) was calculated using the least-squares method and exhibits good linearity ($R^2 > 0.90$) for all potentials tested (Table 2. 2). Such linearity can be formulated as presented in Eq. (3).

$$log\ (-I\ /\ A)\ =\ m\ log\ (t\ /\ s)\ +\ k, and\ thus\ I(t)\ =\ -\ (10^k)t^m \qquad (3)$$

where *m* and *k* are the slope and intercept, respectively, measured in the log-log plots. The *k* value is proportional to current measured on the magnetite electrode, and the time dependence of the currents can be determined from the *m* value. The *k* value is greater in the selenium solution than in the blank solution for potentials between -0.1 and -1.0 V. The difference in the *k* value between the two solutions increases at more negative potentials. This implies that the contribution of selenium to the total electrical signal is enhanced as the potential decreases. There is no monotonic trend (*i.e.*, increase or decrease) in the *m* value for the blank solution as the potential varies. The *m* value averages to -1.1$\pm$ 0.1 over a potential range from 0 to -1.0 V and thus the current-time transient, I (t) is approximately proportional to 1/t. At potentials $\geq$ -0.6 V, the selenium solution shows comparable values of *m* to those of the blank solution whereas there are

appreciable differences in the *m* value between the solutions at more negative potentials. Such differences account for chemical processes involving the electroactive species on the electrode surface which can be observed within the initial 1 s.

Table. 2. 2. Chronoamperometry (during the first second of measurement) data linear-fitted in a log-log scale using the least square method.

	0.1M ClO_4			**10 mM Se(IV) + 0.1M ClO_4**		
Potential	***m***	***k***	R^2	***m***	***k***	R^2
0.0	-1.08	-7.57	0.998	-1.06	-7.58	1.000
-0.1	-1.07	-7.44	0.999	-1.08	-7.39	1.000
-0.2	-1.17	-7.38	0.999	-1.10	-7.23	1.000
-0.3	-1.18	-7.23	0.999	-1.08	-7.01	0.999
-0.4	-1.19	-7.09	0.998	-1.07	-6.76	0.997
-0.5	-1.17	-6.93	0.999	-1.08	-6.56	0.994
-0.6	-1.16	-6.76	0.997	-1.09	-6.41	0.993
-0.7	-1.13	-6.56	0.996	-0.87	-6.11	0.997
-0.8	-1.07	-6.34	0.996	-0.76	-5.87	0.988
-0.9	-0.99	-6.14	0.993	-0.76	-5.71	0.960
-1.0	-0.96	-5.99	0.988	-0.76	-5.55	0.944
Average	-1.11					
STDEV	0.08					

Although the information from chronoamperometry is limited because of the pseudo-capacitance of the magnetite electrode, it is possible to distinguish the currents generated by magnetite from the total currents (Vielstich and Xia, 1995; Öznülüer and Demir, 2002). The current-time curves of the blank solution (*i.e.*, $NaClO_4$ only) were subtracted from those of the selenium solution (Se(IV) + $NaClO_4$) for each potential and are shown in Fig. 2.7C. The resulting curves show increments in the measured current as a potential becomes more negative. At potentials ≥ -0.6 V, the cathodic currents rapidly decay within the first few seconds, but a significant change in the curve pattern is observed at potential ≤ -0.7 V. Specifically, the peak or shoulder-shaped pattern is developed within the first second. The dependence of curve shape on the potential is also consistent with the interpretation on the *m* value described above. The time at which

the center of the peak or shoulder shape appears (t_{max}) is measured within 0.15 to 0.7 s and becomes shorter with decreasing potential. Such patterns and time ranges of the current-time transients at the initial stage match well with a nucleation and growth process of selenium and other metals, which is recorded on the current-time curve in the first few hundred milliseconds to few seconds (Hölzle et al., 1994; Lai et al., 2010; Bougouma et al., 2013). The increase in peak current (I_{max}) and the decrease in peak time (t_{max}) indicate that the kinetics of Se deposition becomes faster as overpotential increases (Bougouma et al., 2013).

Experiments on metal electrodeposition are typically carried out using macroelectrodes (a few mm to a few cm in dimension). Therefore, chronoamperometry was also run using a bulk magnetite electrode in order to compare with the results from the magnetite PME. The experiments were performed with the selenium and blank solutions described above, and background curves were subtracted from total current curves. The resulting current-time curves are shown in Fig. 2.7D. At potentials ≤ -0.8 V, the current density ($J = I$/A, a current per unit area) exhibits the peak- or shoulder-shaped pattern and the maximum values (J_{max}) are recorded between 0.35 and 2 s (t_{max}). The features on the observed curves are similar to those of the PME, although a longer time is needed for a peak or shoulder to appear on the curves. This delay indicates slower kinetics for Se deposition on the bulk electrode versus the PME. The shoulder-shaped pattern shown at potentials of -0.7 and -0.8 V for both the powder and bulk electrodes can be considered the current-time transient from the crystallization process superimposed on a falling transient at short times after double-layer charging (Hölzle et al., 1994). In the discussion section, the deposition of selenium on magnetite is examined theoretically and a possible nucleation mechanism is suggested.

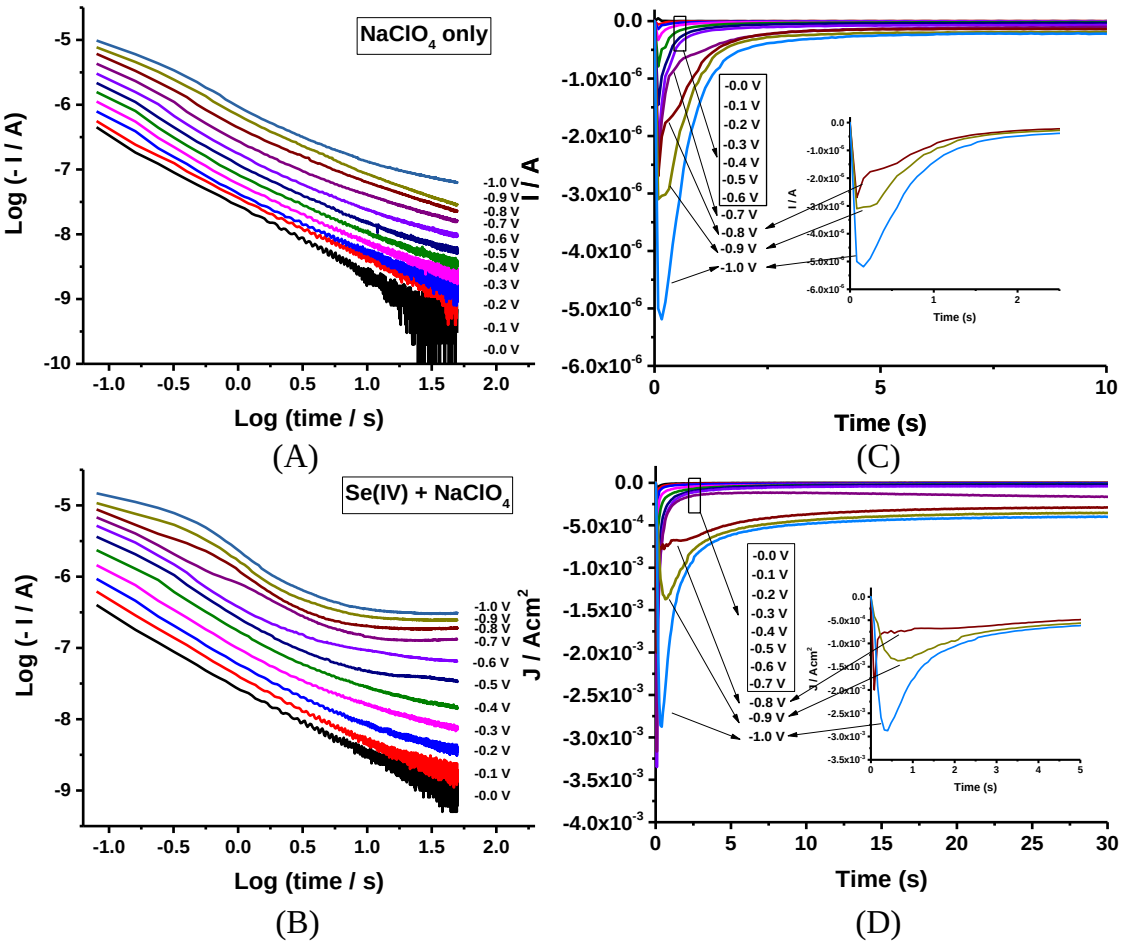

Fig. 2. 7. Speciation of (A) Se(IV) and (B) Se(–II) as a function of pH ([Se] = 0.01 M). It is noted that biselenite ($HSeO_3^-$) and biselenide (HSe^-) are the most dominant species over a range of solution pH 4.0–8.0.

3.2. XPS analysis for selenium redox chemistry on magnetite

XPS analysis was performed to examine redox chemistry of selenium on the magnetite electrode. The chemical reactions that represent the peaks observed on the CV curves can be related to specific selenium species produced at the peak potentials. Due to the geometry of the PME not being suitable for XPS analysis, all XPS samples were prepared from the bulk electrodes. The sample preparation was made at pH 6 using a solution containing 25 mM Na_2SeO_3 + 0.1 M $NaClO_4$.

3.2.1. Cyclic voltammetry of bulk magnetite electrode prior to XPS analysis

Prior to the XPS analysis, the cyclic voltammetry was run using the bulk magnetite electrode and the electrochemical features were compared with the PME (Fig. 2.8). In the blank solution ($NaClO_4$ only), continuous increase in negative currents on the cathodic scan and small variation in positive currents on the anodic scan are similar to the background curves of the PME (Fig. 2.1A). In the presence of selenite (Se(IV) + $NaClO_4$), the cathodic currents begin to rise above the background signals at a potential below -0.1 V. A broad shoulder develops at potentials ≥ -0.6 V where a peak C1 is pronounced on the cyclic PME voltammograms. The negative currents drastically increase at potentials < -0.6 V where the nucleation and growth process of selenium is promoted by large overpotentials. Upon anodic scanning, a single peak positioned at -0.25 V is produced which corresponds to peak A1 of the PME and the anodic current gradually decreases at more positive potentials. There is no observed CV peak or shoulder in the potential region where peak A2 is located in the PME results. Selenium redox transformation mediated by magnetite is greatly influenced by kinetic parameters and so the observed differences between the bulk electrode and PME may be due to the influence of the electrode properties on the redox kinetics. In particular, the bulk magnetite exhibits slower kinetics than the PME as evidenced by the nucleation and growth of selenium (section 3.1.4). The surface reactivity of solid materials as electrochemical catalysts is highly dependent on particle size. Smaller catalyst particles have higher density of reactive sites and thus typically exhibit greater rates of reaction with dissolved species (Nurmi et al., 2005; Peng et al., 2008; Yuan et al., 2015a; Yuan et al., 2015b). Nevertheless, the potential dependence of the cathodic and anodic currents (*i.e.*, the shape of

CV curves) is comparable between the bulk electrode and PME (Fig. 2.2 and 2.8) which suggests similar redox transformation processes occur on the two electrode surfaces.

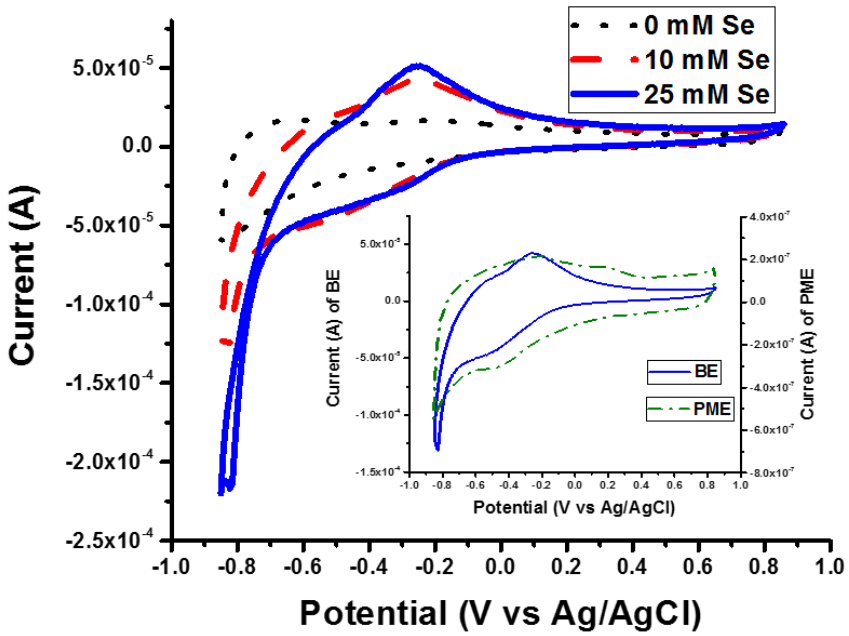

Fig. 2. 8. Cyclic voltammograms for Se(IV) using the bulk magnetite electrode at pH 6.0 (scan rate = 50 mV/s; a scan range, –0.85 to +0.85 V). The scans were performed in solutions containing Se(IV) (10 and 25 mM) and 0.1M NaClO4. Inlet: Comparison of CV patterns measured (pH = 6.0 and [Se(IV)] = 10 mM) using the bulk electrode (BE) and the powder microelectrode (PME) of magnetite.

3.2.2. XPS results for selenium redox transformation

For the sample preparation, potential values were selected on the basis of the cyclic voltammograms at pH 6 (Fig. 2.2 and 2.8). Potentials of -0.5 and -0.2 V are where peaks C1 and A1 are approximately positioned, respectively, and -0.85 V corresponds to the switching potential in the voltammetry cycles performed in this study. A potential of +0.6 V was selected to examine possible redox reactions under very oxidizing conditions. Each potential was kept constant on a bulk electrode for 30 min. For the potential of -0.5 V, two additional samples were potential held and subsequently stepped to +0.2 and +0.6 V, respectively. These samples are intended to investigate any oxidation of selenium species produced at peak C1.

Survey scans on the magnetite electrodes are shown in Fig. 2.9. Observed peaks are labeled according to the corresponding orbitals of elements. The main peaks associated with Fe (Fe 2p and LMM) are clearly seen for all the magnetite electrodes. Two Auger peaks, $L_2M_{45}M_{45}$ and $L_3M_{45}M_{45}$ (denoted LMM and LMM' in Fig. 2.9, respectively) and three XPS peaks, Se 3s, 3p, and 3d are associated with selenium on the electrode surface. The survey spectra show the presence of Se, Na, and Cl for all potentials tested, which are adsorbates from the background solution.

Core scans for the Se 3d peak are presented in Fig. 2.10A. The scan range also covers the binding energy corresponding to the Na 2p orbital (~ 63 eV) as shown in the Se 3d spectra for all potentials tested. This orbital peak does not interfere with the Se 3d peak whose binding energies typically range from 62 to 53 eV (Wagner et al., 1979). Over such an energy range, two different peaks centered at about 55.5 and 58.5 eV are observed for all the potential-held electrodes. Sodium selenite was core-scanned as a reference material, which shows Se 3d peaks centered at 58.4 eV (Fig. 2.10A). Therefore, the XPS peak at ~58.5 eV found from the electrode samples can be mainly attributed to Se(IV) despite the fact that there might be a minor contribution of Se(VI) if produced during the voltammetry scan on a positive potential range (*e.g.*, Alanyalioglu et al., 2004). Decrease in the oxidation state of an element leads to decrease in the electron binding energy of its orbitals. Therefore, the Se 3d peak centered at 55.5 eV, compared to the one at 58.5 eV, can indicate the presence of selenium with a lower valence state such as Se(0) or Se(-II). Bulk magnetite

was analyzed as a reference sample and revealed a Fe 3p peak centered at about 55.5 eV. Interference of the Fe 3p peak with the Se3d peak also made it difficult to interpret the core-level spectra of selenium in previous studies (Liu et al.; Hamdadou et al., 2002). To resolve this issue, the Se 3p peak was core scanned and compared with the Se 3d peak (Fig. 2.10B). Whereas of lower signal-to-noise ratio than the Se 3d spectra, the Se 3p spectra can be analyzed without the interference of the Fe orbitals. Peaks centered at 161.5 eV are found on the spectra of the electrodes held at -0.85 and -0.5 V and can be assigned to Se(0) and/or Se(-II) (Mandale et al., 1984). In contrast, there are no observed peaks at 161.5 eV for the electrode of +0.6 and -0.2 V. The Se 3d spectra of these electrodes, therefore, should be identified as belonging to Fe 3p. It is also important to note that the peak at 55.5 eV appears as a doublet for the electrodes at -0.85 and -0.5 V and as a singlet for those at +0.6 and -0.2 V. The doublet feature is evidently different from the singlet feature observed on the Fe 3p of the magnetite reference.

For the Se 3d XPS peak, the binding energy between 56 and 55 eV is a commonly reported value for Se(0) (Wagner et al., 1979; Shenasa et al., 1986; Tang et al., 1996). The doublet appears at 55.0/55.8 eV, which is very close to the values for Se(0) reported from a previous study (Babu et al., 2007). In addition, a reddish deposit was observable by the naked eye on the magnetite electrode after it was held at a potential of -0.85 V for 30 min. This macroscopic observation indicates formation of elemental selenium on an electrode surface at a negative potential (Tang et al., 1996). The binding energy of Se(-II) 3d reported from many selenide compounds ranges from 55 to 53 eV depending on the nature of its coordinated atoms (Wagner et al., 1979; Shenasa et al., 1986; Hamdadou et al., 2002; Wu et al., 2007; Golovchak et al., 2013). As these ranges are close to the Se 3d peaks found in the present study, the minor presence of Se(-II) cannot be excluded. Se(0) is believed to dominate over Se(-II) given that at the high Se(IV) concentration of this study, Se(-II) produced at negative potentials can react with Se(IV) in solution to form elemental selenium in a comproportionation reaction (Wei et al., 1994) (Eq. 2).

The spectroscopic results provide supportive evidence for the peak assignments on the cyclic voltammograms. There is no detected selenium species other than Se(IV) at the potential of -0.2 V. The

reduction to elemental selenium is confirmed from the magnetite electrode held at -0.5 V. These results support the assignment of the broad C1 peak to the formation of Se(0). The predominance of elemental selenium on the electrode of -0.85 V is also in good agreement with the results of chronoamperometry that showed how nucleation and growth mechanisms govern the selenium redox transformation under very reducing conditions (< -0.6 V). Elemental selenium is detected even if the electrode is stepped from -0.5 V to +0.2 or to +0.6 V (Fig. 2.10). Although the thermodynamic interpretation suggests that elemental selenium can be oxidized to Se(IV) at positive potentials, the interpretation for the selenium oxidation is limited from the XPS results because Se(IV) was detected in all the electrodes tested. The electrode held at +0.6 V shows no evidence for oxidation of Se(IV) to Se(VI). This may be due to the fact that Se(VI) formed at high potentials is immediately released into solution. If this was the case, only a minute amount of selenate could be retained on the electrode and would be undetectable by XPS. No clear indication is found for the transformation of selenite to selenate based on the electrochemical and spectroscopic approaches used in this study. Future research could be aimed at systematic investigation on the oxidation of Se(0) and Se(IV).

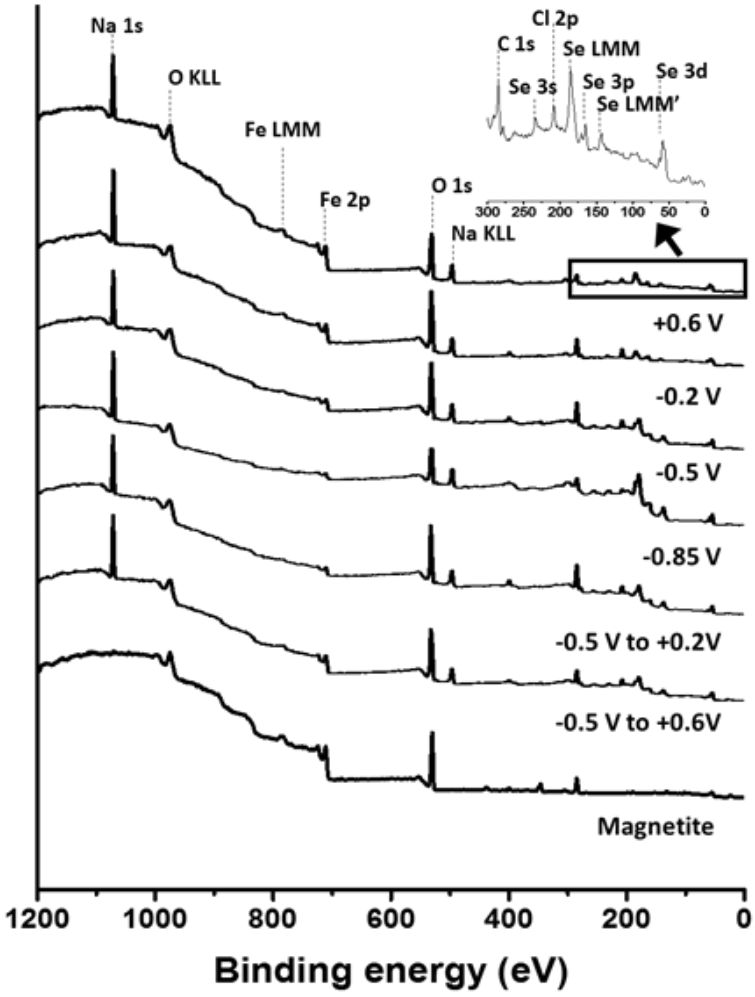

Fig. 2. 9. XPS survey scans on the magnetite electrodes potential-held at various potentials. For the electrode at _0.5 V, two additional samples were stepped to positive potentials, +0.2 and +0.6 V, respectively, to re-oxidize the reduced products.

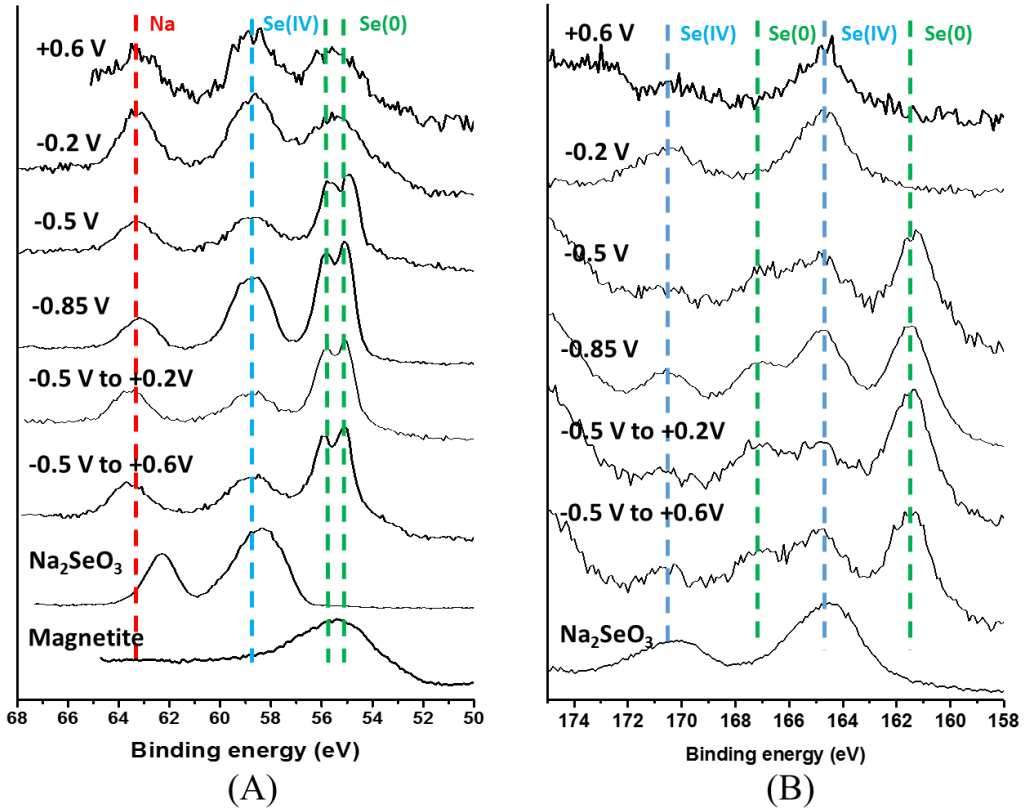

Fig. 2. 10. XPS core scans for (A) Se 3d and (B) Se3p on the magnetite electrodes potential-held at various final potentials.

4. DISCUSSION

4.1. Possible effects of solution chemistry on Se redox transformation

CV peaks indicating selenium redox transformations on magnetite are evident at pH 4.0 to 8.0 but are of limited intensity at pH 9.5 (Fig. 2.2). Such pH dependence of the Se redox sensitivity is closely associated with the variation of Se solution chemistry. The speciation calculations demonstrate that Se(IV) is mainly present as biselenite ($HSeO_3^-$) at pH 3.0 to 8.0 whereas selenite (SeO_3^{2-}) is predominant at pH $\geq$ 9.0 (Fig. 2.6) It is thus inferred that biselenite is redox-active on magnetite in weak acids and bases (i.e. circumneutral pH values) whereas magnetite catalysis of selenite redox transformation is limited under high pH conditions (where SeO_4^{2-} is the dominant species). One speculation to explain this relationship between redox sensitivity and Se speciation is that the affinity of a given selenium species for the magnetite surface changes as a function of pH (Martinez et al., 2006; Rovira et al., 2008) and this may impact the surface concentration of Se available to participate in magnetite-mediated redox transformations. The point of zero charge of magnetite is near a pH of 7 (Tewari and McLean, 1972), which implies that positively and negatively charged species can be retained on its surface at basic and acidic solutions, respectively. It follows that adsorption of Se(IV) on magnetite, as SeO_3^{2-} or $HSeO_3^-$ decreases with increasing pH as the magnetite surface becomes more negative (Martinez et al., 2006; Jordan et al., 2009; Missana et al., 2009). This may explain the absence of observable Se redox transformation at pH 9.5 in this study.

In comparison to thermodynamic data, the peak potentials fall into equilibrium reduction potential regions that correspond to the redox couples of interest (Fig. 2.5). However, the pH dependence of peak potentials is less pronounced than that predicted from equilibrium reduction potentials. For example, peak A2 was assigned to oxidation of Se(0) to Se(IV); therefore, from the ratio of the protons consumed *vs.* electrons accepted, a pe/pH slope of -5/4 (Eqn. 4a) is expected, resulting in a slope of -74 mV (5/4·59 mV, which is the Nernstian slope) per pH unit (Table 2.1). The observed slope of the potential change is ca. -21 mV per pH unit, or nearly three times lower. This reduction reaction can be written in two ways:

$$HSeO_3^- + 4\,e^- + 5\,H^+ \leftrightarrow Se(s) + 3\,H_2O \quad (4a)$$

$$HSeO_3^- + 2\,H_2O + 4\,e^- \leftrightarrow Se(s) + 5\,OH^- \quad (4b)$$

In the following, we discuss two explanations:

1. In the theoretical derivation, one underlying assumption is that the pH does *not* change significantly as a result of the reaction, but due to the small reaction volume (*i.e.*, the pore volume in the PME could be considered the reaction volume) the number of protons consumed per volume may be high.
2. Since the slope of Eqn. 4a is -5/4, and the numerator is the number of protons consumed, if there is also a source that releases protons as a result of the reaction, or consumes hydroxide ions (Eqn. 4b), the slope of the reduction potential *vs.* pH would be diminished.

Quantification of explanation 1: In order to estimate the amount of protons released or consumed, the number of electrons can be calculated from the CV curves and converted to the number of protons. The proton concentration is obtained by either considering the pore volume of the mineral powder or the entire volume of the reacted solution. The consumption of protons during reduction may increase pH and lead to the difference in pH between the cavity and bulk solution. Although protons are exchanged between the pore and bulk solutions by mass transfer, the effect of proton consumption may be important under our experimental conditions where solution pH is weakly acidic to basic and the total selenium concentration exceeds the proton concentration.

The electronic charge transferred at peak C1 was calculated from a CV curve in Fig. 2.2 (pH 6.0 and 10 mM [Se]) as an example and the value is 1.07×10^{-6} C. This value was obtained by integrating the current peak over the voltage and dividing this value by the scan rate of, in this case, 50 mV/s. By dividing the charge value by the electron charge, one obtains 6.7×10^{12} electrons to be transferred. According to Eqn. 4a, this value has to be multiplied by 5/4 to obtain the number of protons being consumed, which is 8.3×10^{12} protons or 1.4×10^{-11} mol of H^+. The *concentration* of protons consumed by the reduction can be evaluated considering the total volume of the microcavity (~1.2×10^{-10} L; radius of the cavity ≈50 μm,

depth ≈30 μm, porosity about 0.5). The calculated charge is equivalent to a proton concentration of 0.12 M in reference to the microcavity volume. This value is five orders of magnitude greater than the solution proton concentration (10^{-6} M) indicating that the cavity proton concentration is decreased by selenite reduction. An easier way to interpret this process is using Eqn. 4b which states that an equivalent amount of OH^- would be produced and would push the pH to high values. The minimum *concentration* change of protons can be estimated if one assumes that the reaction volume mixes with the entire volume of the vessel (50 ml). This would result in a proton concentration change of 1.4×10^{-11} mol/0.05 L = 2.8×10^{-10} mol/L, which is essentially no change in pH. Any local pH change induced by this reduction would be between these two extreme values due to the exchange of liquid between the microcavity pores and the bulk solution. This indicates that anyone performing redox reactions in a porous medium in contact with an aqueous solution may have a significant pH gradient between the medium and bulk solution; the same is true for a microporous soil with redox activity in contact with solution flowing through larger cracks. Due to the interdependence of pe and pH, there may also be a wide range of redox potentials for a specific redox transition in porous media where the water does not mix well.

Quantification of explanation 2: as Se(IV) is reduced to Se(0), the produced Se(0) is adsorbed or precipitated on the magnetite surface, thereby replacing protons from the mineral surface. The net loss in proton per reaction step in Eqn. 4a is thus less than 5. Whereas it is possible to lessen the pe/pH slope, it would be difficult to imagine that one Se(0) sorbed releases one proton, but five protons are consumed (Eqn. 4b) contributes largely to the observed reduction in slope.

As known from macroscopic examples, *e.g.*, as in acid mine drainage, redox reactions can have a significant influence on pH and vice versa. Here, we demonstrate the potential for creating a pH gradient of several pH units at the interface between small redox-active micropores and larger, at least ml-sized volumes of water. This is not only the case in an experimental setup like the one at the interface of a powder microelectrode but also in redox active environments (e.g., soils) where microporous clay aggregates are in contact with flow-through macro cracks. Since the potential of

a redox transition is typically pH-dependent, this means, in turn, that the pH gradient also leads to a peak broadening with more solution-like pH values right at the interface and higher/lower pH values further away for reduction/oxidation reactions while the magnitude of the gradient is dependent on pore size and diffusion times (Barth et al., 2009; Borch et al., 2009). It would be challenging to measure and quantify those pH gradients that take place at a micrometer scale in a total volume on the order of tens of microns across, which is even below the size and resolution of pH microelectrodes.

4.2. Mechanism of selenium nucleation on magnetite

As shown from the electrochemical and spectroscopic measurements, selenite can be reduced to elemental selenium at a negative potential (< –0.2V). The next challenge is to determine, in a more mechanistic and quantitative way, how Se(0) precipitation starts and crystal growth progresses. The XPS spectra denoting a predominance of elemental selenium on the electrode of -0.85 V is in good agreement with the results of chronoamperometry that the nucleation and growth mechanism governs the selenium redox transformation under those negative potentials.

For theoretical considerations, the current-time curves in Fig. 2.7C and D were fitted to the nucleation and growth model proposed by Scharifker and Hills (1983) (Fig. 2.11). The model suggests two kinetic mechanisms, *i.e.*, instantaneous and progressive nucleation to address the nucleation properties such as the nuclear number density and the nucleation rate. Instantaneous nucleation describes the process by which the nuclei are formed at the onset of the electrochemical current, while progressive nucleation describes the process where the nuclei are continuously formed during the crystal growth (Bijani et al., 2011). These two nucleation processes are classically described by equations 5a and 5b.

$$Instantaneous: (I/I_{max})^2 = 1.95(t/t_{max})^{-1}\{1 - exp[-1.26(t/t_{max})]\}^2 \quad (5a)$$

$$Progressive: (I/I_{max})^2 = 1.23(t/t_{max})^{-1}\{1 - exp[-2.34(t/t_{max})^2]\}^2 \quad (5b)$$

The experimental transients in Fig. 2.11 all (examples chosen are -1.0 V for PME and -1.0 and -0.9 V for the bulk electrode) show a peak in redox current at a certain time of the chronoamperometry experiment (t_{max}). The current and time values of the data were normalized to the current and time at each peak (I_{max} and t_{max}), respectively, and were compared with the multiple nucleation model (Fig. 2.11). The experimental curves fall closer to the theoretical model for the progressive nucleation (average residual $(I/I_{max})^2$ of 0.1) than to that for the instantaneous nucleation (average residual $(I/I_{max})^2$ of 0.2). On the rising portion of the curves ($t < t_{max}$), the slower increase in current for progress nucleation (compared to the instantaneous one) implies greater increment in the number of nuclei with time and slower nucleation than instantaneous nucleation (Scharifker and Hills, 1983).

There are, however, similarities and differences between the experimental data and theoretical progressive nucleation. The small positive deviation from the progressive model is observed on the rising portion of the fitting curves. This may be explained by contributions of other processes such as double layer charging and possibly adsorption-desorption processes (Scharifker and Hills, 1983; Hölzle et al., 1994). Based on the assumptions of the model, a diffusion-controlled behavior is expected for long times and was evaluated on our data using the Cottrell relation (Eq. 6).

$$I = \frac{zAFD^{1/2}c}{\pi^{1/2}t^{1/2}} \qquad (6)$$

where I is the current, A the area of the electrode, z the number of electrons transferred on the reduction, F the faraday constant, D the diffusion coefficient, c the bulk concentration, and t the time. The relation implies that the current is proportional to $t^{-1/2}$. In this application, caution should be taken since a planar electrode and unstirred solution are presumed for the strict application of the Cottrell relation. The bulk electrode used in this study is planar (section 2.1) while the powder microelectrode obeys the Cottrell

relation if the time of experiment is short (Yang et al., 1999; Zuleta et al., 2003). Thus the Cottrell relation was applied to the two types of electrode for a limited period of time (from 2 t_{max} to 10 t_{max}).

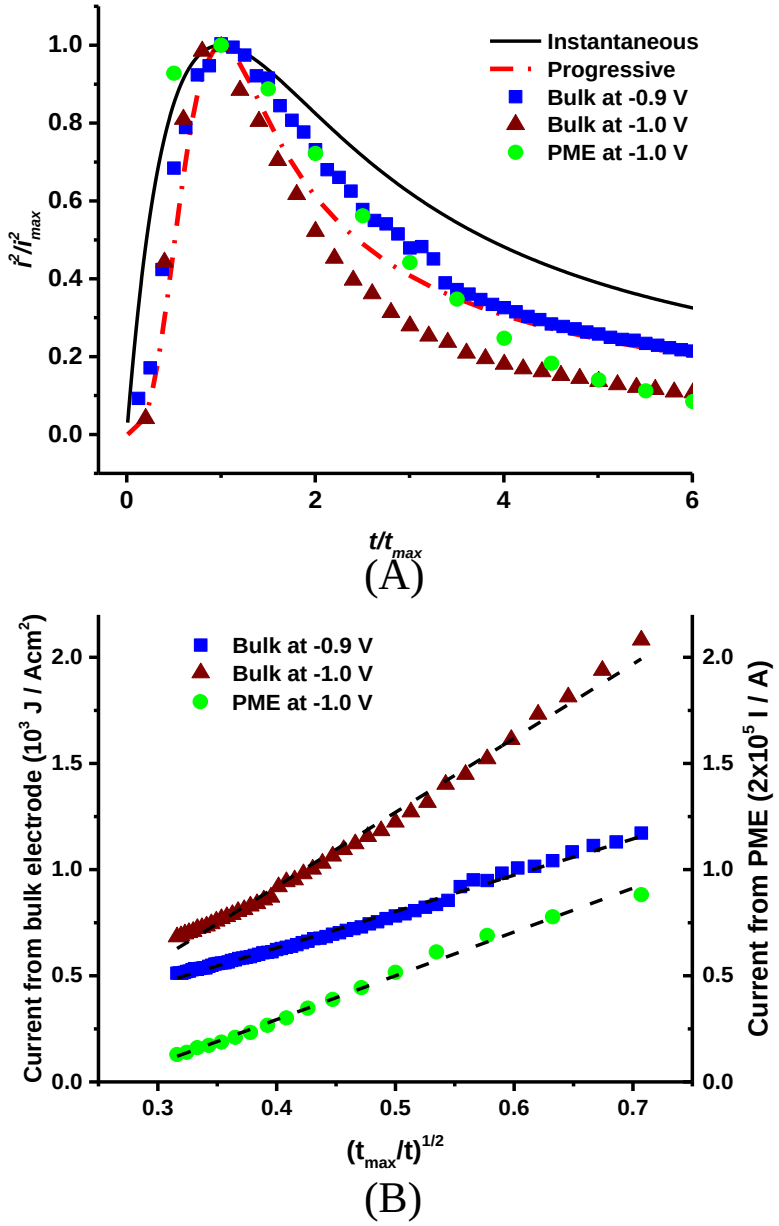

Fig. 2. 11. Comparison between the experimental transients (symbols) and the theoretical nucleation models (lines) in the dimensionless plot and (B) linear dependence between current and $t^{-1/2}$ for the falling portions of the transients over a time interval from $2t_{max}$ to $10t_{max}$.

For better illustration, I and $t^{-1/2}$ were multiplied by large numbers and t_{max}, respectively (Fig. 2.11B). The resulting current-time transients show excellent linearity (R^2 > 0.99), indicating nucleation as a diffusion-controlled process over the time range of interest. For the bulk electrodes, the diffusion coefficient was calculated from the Cottrell equation with the measured cross-sectional area (A) and the number of electrons transferred during the nucleation (z = 4 for selenite reduction to Se(0)). The values for the diffusion coefficient are 4.1×10^{-7} cm^2s^{-1} for -0.9 V and 10×10^{-7} cm^2s^{-1} for -1.0 V. Alternatively, the diffusion coefficient can be derived from the nucleation model and the expression for progressive nucleation is presented in Eq. 7.

$$J_{max}{}^2 t_{max} = 0.2598 \cdot (zFc)^2 D \quad (7)$$

The calculated values are 3.1×10^{-7} cm^2s^{-1} and 8.6×10^{-7} cm^2s^{-1} for -0.9 and -1.0 V, respectively, comparable to the diffusion coefficients from the Cottrell equation. For both approaches, the diffusion coefficient observed at -1.0 V is about 2.5 times as great as that at -0.9 V which is at odd with the prediction from the multiple-nucleation model. Specifically, Scharifker and Hills (1983) suggested that for a given bulk concentration of electroactive species (10 mM Se(IV) in that case), the diffusion constant (*D)* should not vary with the potential. The inconsistency with the model is also seen on the falling portion of the curves where the experimental transients deviate negatively from the model for longer times ($t > 4t_{max}$). One possible source of the deviation from the theoretical model can be the morphology of the nuclei because the nuclei are considered hemispherical in the model (Grujicic and Pesic, 2002). The growth of nuclei under other mechanisms was postulated from a study regarding Rn deposition on a gold electrode (Schrebler et al., 2001). Another possibility is the beginning of H_2Se evolution followed by the comproportionation reaction with Se(IV) or hydrogen evolution at very negative potentials (Schrebler et al., 2001; Steponavičius et al., 2011). In summary, the interpretation of Se nucleation with the ideal model is limited as the reaction

proceeds for long times. Nevertheless, in this study, the early stage of the peak-shaped current-time transients can be explained with the progressive 3-D nucleation model.

There have been a few studies adopting the multiple-nucleation model to investigate the mechanisms on electrodeposition of selenium on the various electrodes. Lai et al. (2010) examined selenium deposition on a tin oxide electrode over a potential range of –0.4 to –0.6 V where a good agreement with progressive nucleation is observed. Glassy carbon was tested as a substrate for selenium deposition and revealed consistency with the progressive nucleation mechanism (Steponavičius et al., 2011). Although these reports employed aqueous solvents at room temperature, the instantaneous nucleation may occur under other physicochemical settings. Bougouma et al. (2013) suggested that the Se deposition kinetics is largely dependent on temperature and that slower progressive nucleation is favored at ambient temperature, whereas instantaneous nucleation is likely at higher temperatures (*e.g.*, 110 ℃ in a non-aqueous solvent). Our data support the progressive nucleation as a dominant mechanism for selenium deposition under ambient temperature and highly reducing conditions.

4.3. Catalysis of magnetite in geochemical systems

In natural environments, the abiotic reduction of trace elements can be mediated by a mineral surface when the reduction is coupled with the oxidation of other species on the surface. Dissolved Fe(II), for instance, does not seem to act as a reductant, but Fe(II) involved in a heterogeneous system enables trace elements to be reduced (Charlet et al., 2007; Taylor et al., 2015). Charlet et al. (2007) demonstrated the role of Fe(II) adsorbed by clay minerals in reducing selenium and helping form nanoparticulate Se(0). Selenium reduction can also be facilitated by oxidation of iron mineral surfaces and gives rise to products such as elemental selenium and iron selenides (Myneni et al., 1997; Scheinost and Charlet, 2008).

Our results from electrochemical experiments show that magnetite can act as a good substrate for selenite reduction and elemental selenium is formed as a primary product. While, in the electrochemical part of this study, electron transfer is triggered by applying an electrical potential, the mineral surface

oxidation or the adsorption of reductants from solution to the surface can play an equivalent role in natural systems (Renock et al., 2013; Yuan et al., 2015b). Under a range of environmental conditions (pH 1 to 7 and 2 to 65 ℃), the oxidation of magnetite can be promoted in the presence of proton (H^+) or redox active metal species (M^{z+}) dissolved in water and cause the formation of maghemite (γ-Fe_2O_3) (Eq. 8a and b) (White et al., 1994; White and Peterson, 1996).

$$\left[Fe^{2+}Fe_2{}^{3+}\right]O_4 \; + \; 2H^+ \leftrightarrow \gamma - Fe_2O_3 \; + \; Fe^{2+} \; + \; H_2O \tag{8a}$$

$$3\left[Fe^{2+}Fe_2{}^{3+}\right]O_4 \; + (\frac{2}{n})M^{z+} \leftrightarrow 4\gamma - Fe_2O_3 \; + \; Fe^{2+} + \; (\frac{2}{n})M^{(z-n)+} \tag{8b}$$

As a result, the metal species can be reduced by participating in the surface oxidation process or subsequent heterogeneous reactions involving ferrous iron (Fe^{2+}) released from the process. The formation of maghemite can passivate the magnetite surface, resulting in two important effects: 1) magnetite, which is thermodynamically unstable in most soil environments, can persists over geological time scales and 2) the redox-catalytic ability of magnetite is limited by passivation of the oxidized surface (Peterson et al., 1997). It is also likely that the redox-catalysis rate of magnetite becomes slower as Se(0) is deposited on the mineral surface due to a similar passivation effect. Peterson et al. (1997) studied reduction of Cr(VI) in the presence of magnetite and calculated the thickness of the maghemite layer (T_{mh}, in nm) formed as a result of electron transfer from Fe^{2+} in magnetite to an oxidized species in solution and the formula can be written for the reduction of Se(IV) to Se(0) as Eq. 9a.

$$T_{mh} = 4[Se^0]N_a \; / \; (d_{Fe(2+)} \; \cdot \; A_s \cdot 10^{18}) \tag{9a}$$

$$\Gamma_{Se} = [Se^0] \; / \; A_s \tag{9b}$$

where $[Se^0]$ is the number of moles of Se^0 atoms reduced from Se(IV) on the magnetite surface, multiplied by 4 to account for 4 Fe^{2+} atoms oxidized for every Se(IV) reduced, N_a, Avogadro's number, $d_{Fe(2+)}$, the density of Fe^{2+} atoms in the magnetite structure (atoms nm^{-3}), and A_S, the magnetite surface area ($m^2\ g^{-1}$) multiplied by 10^{18} to convert m^2 to nm^2. $[Se^0]$ is calculated from a CV curve in Fig. 2.2 (pH 6.0 and 10 mM [Se]) using the same conditions for quantification 1 in section 4.1 resulting in an approximated

thickness of maghemite is 5.4 Å, which is on the order of magnitude of the one estimated in a previous study on Cr(VI) reduction catalyzed by magnetite (1 to 2.4 nm) (Peterson et al., 1997). The surface coverage of Se(0) (Γ_{Se}) is evaluated, according to Eq. 9b, for the same CV curve (pH 6.0 and 10 mM [Se]) and is 0.30 nmol·cm^{-2}. This corresponds to 15 % coverage (0.15 ML) of the theoretical surface coverage for a metal monolayer (ML) on a substrate (2 nmol·cm^{-2}) (Gerischer and Tobias, 1978; Beni et al., 2004). These estimated values imply that, in aqueous systems, the surface oxidation of unreacted magnetite particles may catalyze reaction pathways of selenite reduction as observed in this study, coupled with electron supply from the formation of an oxidized layer that is a few to tens of Å thick. The catalytic ability of magnetite would likely degrade over time as the mineral surface is passivated by reaction products (Peterson et al., 1997; Ruiz et al., 2000).

In the experiments presented here, a high concentration of Se(IV) (1 to 25 mM) was required to differentiate the electrical signal of selenium species from the large background current of magnetite. This high selenium content may be one reason for the dominance of elemental selenium as a reduction product. Ferrous iron can be generated from magnetite dissolution at very reducing conditions (section 3.1.1) and may play a role in the preservation of selenium species Se(-I) or Se(-II) as solid phases. Ferroselite ($FeSe_2$) is a stable compound of iron and selenium and is found in metal deposits bearing iron sulfides with high selenium content (Howard, 1977). The coexistence of elemental selenium and iron selenides with structures similar to FeSe and Fe_7Se_8 were found when a batch reaction of selenite with magnetite nanoparticles was maintained longer than the timescale of this study (Scheinost and Charlet, 2008). Therefore, in reducing environments where reactive iron is abundant, negative oxidation states of selenium are expected to be common.

5. CONCLUSIONS

In this study, electrochemical techniques are used to evaluate possible redox processes catalyzed by magnetite over a range of experimental conditions (Eh 1.09 to -0.77 V or 0.85 to -1.0 V *vs*. Ag/AgCl; pH 4.0 to 9.5). Biselenite ($HSeO_3^-$) can act as a redox-sensitive species under those conditions. Reaction pathways catalyzed by magnetite involving reduction of selenite and oxidation of reduced products are identified from the electrochemical and spectroscopic measurements. A soluble selenium oxyanion, Se(IV), is transformed into Se(0) or Se(-II) on the magnetite surface as it encounters reducing conditions (Eh = -0.27 V). Se(0) is directly deposited on the mineral substrate whereas adsorbed Se(-II) can undergo a subsequent comproportionation reaction with Se(IV) in solution to form Se(0). These reduced species can be remobilized to Se(IV) if exposed to oxidizing conditions (Eh = +0.44 V). Formation of soluble Se(VI) from oxidation of the lower valence forms may be mediated by magnetite, but since this study focuses on solid-state processes, no spectroscopic evidence is available for further oxidation in solution. The pH-dependence of the redox transformation of selenium may become significant in the microporous structure of soils or sediments due to a pH gradient formed at the particle-solution interface and the gradient between different pores with little tortuosity when pH changes are induced by redox processes. This is particularly true when compared with the redox transformation in the solution phase where a more homogeneous distribution of Eh and pH values is found. The retention of selenium on the mineral substrate by abiotic reduction is energetically and kinetically facilitated at low redox potentials. From chronoamperometry measurements, the kinetics of the retention mechanism is characterized mainly by the simultaneous nucleation and growth of elemental selenium (*i.e.*, progressive nucleation) under ambient temperature and highly reducing conditions (Eh < –0.47 V). The XPS analysis on the potential-stepped magnetite electrodes implies that once

deposited on magnetite, remobilization of elemental selenium to soluble species would be partially irreversible and kinetically retarded. Therefore, magnetite can act not only as a catalyst for redox reactions of selenium but also as a substrate to retain selenium in an immobilized form. These findings demonstrate that the effect of natural minerals on the thermodynamics and kinetics of electron transfer is an important factor in predicting selenium mobility and reactivity in sediments and natural waters.

Acknowledgements

The authors are grateful for the support from the U.S. National Science Foundation, Division of Earth Sciences, Grant No. EAR-1223976. Y.K. acknowledges support from Samsung Scholarship.

References

Alanyalioglu M., Demir U. and Shannon C. (2004) Electrochemical formation of Se atomic layers on Au (111) surfaces: the role of adsorbed selenate and selenite. *J. Electroanal. Chem.* **561**, 21-27.

Babu P. K., Lewera A., Chung J. H., Hunger R., Jaegermann W., Alonso-Vante N., Wieckowski A. and Oldfield E. (2007) Selenium becomes metallic in Ru-Se fuel cell catalysts: an EC-NMR and XPS investigation. *J. Am. Chem. Soc.* **129**, 15140-15141.

Bard A. J. and Faulkner L. R. (1980) *Electrochemical methods: fundamentals and applications*. Wiley New York.

Barth J., Grathwohl P., Fowler H., Bellin A., Gerzabek M., Lair G., Barceló D., Petrovic M., Navarro A. and Négrel P. (2009) *Mobility, turnover and storage of pollutants in soils, sediments and waters: Achievements and results of the EU project AquaTerra-A review*, Sustainable Agriculture. Springer, pp. 857-871.

Beni V., Newton H. V., Arrigan D. W., Hill M., Lane W. A. and Mathewson A. (2004) Voltammetric behaviour at gold electrodes immersed in the BCR sequential extraction scheme media: Application of underpotential deposition–stripping voltammetry to determination of copper in soil extracts. *Anal. Chim. Acta* **502**, 195-206.

Bijani S., Schrebler R., Dalchiele E., Gabas M., Martinez L. and Ramos-Barrado J. (2011) Study of the Nucleation and Growth Mechanisms in the Electrodeposition of Micro-and Nanostructured Cu2O Thin Films. *The Journal of Physical Chemistry C* **115**, 21373-21382.

Borch T., Kretzschmar R., Kappler A., Cappellen P. V., Ginder-Vogel M., Voegelin A. and Campbell K. (2009) Biogeochemical redox processes and their impact on contaminant dynamics. *Environ. Sci. Technol.* **44**, 15-23.

Bougouma M., Van Elewyck A., Steichen M., Buess-Herman C. and Doneux T. (2013) Selenium electrochemistry in choline chloride–urea deep eutectic electrolyte. *J. Solid State Electrochem.* **17**, 527-536.

Bruggeman C., Maes A., Vancluysen J. and Vandemussele P. (2005) Selenite reduction in Boom clay: effect of FeS 2, clay minerals and dissolved organic matter. *Environ. Pollut.* **137**, 209-221.

Cachet-Vivier C., Vivier V., Cha C., Nedelec J.-Y. and Yu L. (2001) Electrochemistry of powder material studied by means of the cavity microelectrode (CME). *Electrochim. Acta* **47**, 181-189.

Cha C. S., Li C. M., Yang H. and Liu P. (1994) Powder microelectrodes. *J. Electroanal. Chem.* **368**, 47-54.

Charlet L., Scheinost A., Tournassat C., GrenEche J.-M., Géhin A., Fernández-Martı A., Coudert S., Tisserand D. and Brendle J. (2007) Electron transfer at the mineral/water interface: Selenium reduction by ferrous iron sorbed on clay. *Geochim. Cosmochim. Acta* **71**, 5731-5749.

Gerischer H. and Tobias C. W. (1978) Advances in Electrochemistry and Electrochemical Engineering. Vol. 11. *John Wiley and Sons*, 446.

Golovchak R., Calvez L., Petracovschi E., Bureau B., Savytskii D. and Jain H. (2013) Incorporation of Ga into the structure of Ge–Se glasses. *Mater. Chem. Phys.* **138**, 909-916.

Gorski C. A., Handler R. M., Beard B. L., Pasakarnis T., Johnson C. M. and Scherer M. M. (2012) Fe atom exchange between aqueous Fe2+ and magnetite. *Environ. Sci. Technol.* **46**, 12399-12407.

Grant F. (1985) Aeromagnetics, geology and ore environments, I. Magnetite in igneous, sedimentary and metamorphic rocks: an overview. *Geoexploration* **23**, 303-333.

Grujicic D. and Pesic B. (2002) Electrodeposition of copper: the nucleation mechanisms. *Electrochim. Acta* **47**, 2901-2912.

Hamdadou N., Bernede J. and Khelil A. (2002) Preparation of iron selenide films by selenization technique. *J. Cryst. Growth* **241**, 313-319.

Hölzle M., Retter U. and Kolb D. (1994) The kinetics of structural changes in Cu adlayers on Au (111). *J. Electroanal. Chem.* **371**, 101-109.

Howard J. H. (1977) Geochemistry of selenium: formation of ferroselite and selenium behavior in the vicinity of oxidizing sulfide and uranium deposits. *Geochim. Cosmochim. Acta* **41**, 1665-1678.

Jordan N., Lomenech C., Marmier N., Giffaut E. and Ehrhardt J.-J. (2009) Sorption of selenium(IV) onto magnetite in the presence of silicic acid. *J. Colloid Interface Sci.* **329**, 17-23.

Lai Y., Liu F., Li J., Zhang Z. and Liu Y. (2010) Nucleation and growth of selenium electrodeposition onto tin oxide electrode. *J. Electroanal. Chem.* **639**, 187-192.

Liu X., Fattahi M., Montavon G. and Grambow B. RETENTION OF Se (-II) ONTO PYRITE UNDER REDOX POTENTIAL CONDITIONS. *Mobile Fission and Activation Products in Nuclear Waste Disposal*, 95.

Lovley D. R. (1993) Dissimilatory metal reduction. *Annual Reviews in Microbiology* **47**, 263-290.

Mandale A., Badrinarayanan S., Date S. and Sinha A. (1984) Photoelectron-spectroscopic study of nickel, manganese and cobalt selenides. *J. Electron. Spectrosc. Relat. Phenom.* **33**, 61-72.

Martinez M., Gimenez J., De Pablo J., Rovira M. and Duro L. (2006) Sorption of selenium (IV) and selenium (VI) onto magnetite. *Appl. Surf. Sci.* **252**, 3767-3773.

Missana T., Alonso U., Scheinost A. C., Granizo N. and García-Gutiérrez M. (2009) Selenite retention by nanocrystalline magnetite: Role of adsorption, reduction and dissolution/co-precipitation processes. *Geochim. Cosmochim. Acta* **73**, 6205-6217.

Myneni S., Tokunaga T. K. and Brown G. (1997) Abiotic selenium redox transformations in the presence of Fe (II, III) oxides. *Science* **278**, 1106-1109.

Nurmi J. T., Tratnyek P. G., Sarathy V., Baer D. R., Amonette J. E., Pecher K., Wang C., Linehan J. C., Matson D. W. and Penn R. L. (2005) Characterization and properties of metallic iron nanoparticles: spectroscopy, electrochemistry, and kinetics. *Environ. Sci. Technol.* **39**, 1221-1230.

Öznülüer T. and Demir Ü. (2002) Formation of Bi 2 S 3 thin films on Au (111) by electrochemical atomic layer epitaxy: kinetics of structural changes in the initial monolayers. *J. Electroanal. Chem.* **529**, 34-42.

Peng F. F., Zhang Y. and Gu N. (2008) Size-dependent peroxidase-like catalytic activity of Fe 3 O 4 nanoparticles. *Chin. Chem. Lett.* **19**, 730-733.

Peterson M. L., White A. F., Brown G. E. and Parks G. A. (1997) Surface passivation of magnetite by reaction with aqueous Cr (VI): XAFS and TEM results. *Environ. Sci. Technol.* **31**, 1573-1576.

Renock D., Mueller M., Yuan K., Ewing R. C. and Becker U. (2013) The energetics and kinetics of uranyl reduction on pyrite, hematite, and magnetite surfaces: A powder microelectrode study. *Geochim. Cosmochim. Acta* **118**, 56-71.

Ronov A. and Yaroshevsky A. (1969) Chemical composition of the earth's crust. *Washington DC American Geophysical Union Geophysical Monograph Series* **13**, 37-57.

Rovira M., Giménez J., Martínez M., Martínez-Lladó X., de Pablo J., Marti V. and Duro L. (2008) Sorption of selenium (IV) and selenium (VI) onto natural iron oxides: goethite and hematite. *J. Hazard. Mater.* **150**, 279-284.

Ruiz N., Seal S. and Reinhart D. (2000) Surface chemical reactivity in selected zero-valent iron samples used in groundwater remediation. *J. Hazard. Mater.* **80**, 107-117.

Saji V. S. and Lee C.-W. (2013) Selenium electrochemistry. *RSC Advances* **3**, 10058-10077.

Santos M. C. and Machado S. A. S. (2004) Microgravimetric, rotating ring-disc and voltammetric studies of the underpotential deposition of selenium on polycrystalline platinum electrodes. *J. Electroanal. Chem.* **567**, 203-210.

Scharifker B. and Hills G. (1983) Theoretical and experimental studies of multiple nucleation. *Electrochim. Acta* **28**, 879-889.

Scheinost A. C. and Charlet L. (2008) Selenite reduction by mackinawite, magnetite and siderite: XAS characterization of nanosized redox products. *Environ. Sci. Technol.* **42**, 1984-1989.

Schrebler R., Cury P., Orellana M., Gómez H., Córdova R. and Dalchiele E. (2001) Electrochemical and nanoelectrogravimetric studies of the nucleation and growth mechanisms of rhenium on polycrystalline gold electrode. *Electrochim. Acta* **46**, 4309-4318.

Shenasa M., Sainkar S. and Lichtman D. (1986) XPS study of some selected selenium compounds. *J. Electron. Spectrosc. Relat. Phenom.* **40**, 329-337.

Steponavičius A., Šimkūnaitė D., Valsiūnas I. and Baltrūnas G. (2011) Initial stages of selenium electrodeposition onto glassy car bon electrode. *chemija* **22**.

Stumm W. and Sulzberger B. (1992) The cycling of iron in natural environments: considerations based on laboratory studies of heterogeneous redox processes. *Geochim. Cosmochim. Acta* **56**, 3233-3257.

Tang H., Kitani A. and Shiotani M. (1996) Electrochemical formation of polyaniline in selenic acid. *J. Electrochem. Soc.* **143**, 3079-3082.

Taylor S., Marcano M., Rosso K. and Becker U. (2015) An experimental and ab initio study on the abiotic reduction of uranyl by ferrous iron. *Geochim. Cosmochim. Acta* **156**, 154-172.

Tewari P. and McLean A. (1972) Temperature dependence of point of zero charge of alumina and magnetite. *J. Colloid Interface Sci.* **40**, 267-272.

Vielstich W. and Xia X. (1995) Comments on" Electrochemistry of methanol at low index crystal planes of platinum: an integrated voltammetric and chronoamperometric study". *J. Phys. Chem.* **99**, 10421-10422.

Wagner C., Riggs W., Davis L., Moulder J. and Muilenberg G. (1979) Handbook of XPS. *PerkinElmer, Waltham*.

Wang S.-Y., Ho K.-C., Kuo S.-L. and Wu N.-L. (2006) Investigation on capacitance mechanisms of Fe3O4 electrochemical capacitors. *J. Electrochem. Soc.* **153**, A75-A80.

Wei C., Myung N. and Rajeshwar K. (1994) A combined voltammetry and electrochemical quartz crystal microgravimetry study of the reduction of aqueous Se (IV) at gold. *J. Electroanal. Chem.* **375**, 109-115.

White A. F. and Peterson M. L. (1996) Reduction of aqueous transition metal species on the surfaces of Fe (II)-containing oxides. *Geochim. Cosmochim. Acta* **60**, 3799-3814.

White A. F., Peterson M. L. and Hochella M. F. (1994) Electrochemistry and dissolution kinetics of magnetite and ilmenite. *Geochim. Cosmochim. Acta* **58**, 1859-1875.

Williams K. T. and Byers H. G. (1934) Occurence of Selenium in Pyrites. *Industrial & Engineering Chemistry Analytical Edition* **6**, 296-297.

Wu N.-L., Wang S.-Y., Han C.-Y., Wu D.-S. and Shiue L.-R. (2003) Electrochemical capacitor of magnetite in aqueous electrolytes. *J. Power Sources* **113**, 173-178.

Wu X., Zhang Z., Zhang J., Ju Z., Shen D., Li B., Shan C. and Lu Y. (2007) Structural and electrical characterizations of single tetragonal FeSe on Si substrate. *J. Cryst. Growth* **300**, 483-485.

Yang W., Zhang G., Lu S., Xie J. and Liu Q. (1999) Electrochemical studies of Li/LixMn2O4 by using powder microelectrode. *Solid State Ionics* **121**, 85-89.

Yuan K., Ilton E. S., Antonio M. R., Li Z., Cook P. J. and Becker U. (2015a) Electrochemical and spectroscopic evidence on the one-electron reduction of U (VI) to U (V) on magnetite. *Environ. Sci. Technol.*

Yuan K., Renock D., Ewing R. C. and Becker U. (2015b) Uranium reduction on magnetite: Probing for pentavalent uranium using electrochemical methods. *Geochim. Cosmochim. Acta* **156**, 194-206.

Zuleta M., Bursell M., Björnbom P. and Lundblad A. (2003) Determination of the effective diffusion coefficient of nanoporous carbon by means of a single particle microelectrode technique. *J. Electroanal. Chem.* **549**, 101-108.

Chapter III. Photocatalytic reduction of uranyl: Effects of organic ligands and UV light wavelengths

Abstract

Although previous studies demonstrate the photochemical reduction of uranyl (UO_2^{2+}) in the presence of various organic compounds, the actual role of organic molecules as ligands and electron donors during the photoreaction are poorly understood. In this study, photochemical reduction of uranyl is examined with respect to organic ligands as electron donors and complexing agents, the role of titanium oxide (TiO_2) nanoparticles as photocatalysts, and the influence of UV light irradiation with emission peaks in the UV-A, UV-B, and UV-C ranges. Organic compounds with different binding affinities to uranyl such as acetate, ethylenediaminetetracetate (EDTA), oxalate, and hydroquinone were selected.

Uranyl solutions prepared with one organic compound in a 1:8 molar ratio were irradiated under anoxic and acidic conditions (O_2 < 1 ppm, pH 2.5). Uranyl removal by reduction to UO_2 was better than 70% in the presence of oxalate and acetate, followed by hydroquinone (~ 45 %) and EDTA (~ 10 %). Uranyl removal was nearly constant at the UV-A, UV-B, and UV-C regions in the presence of acetate and oxalate whereas greater removal was observed in the EDTA and hydroquinone solutions exposed to UV-C and UV-A, respectively. These results reveal that uranyl reduction is mediated primarily by TiO_2 nanoparticles and is highly dependent on the electron-donor compound. Addition of acetate enhances the uranyl photoreaction in hydroquinone solution.

Dissolved EDTA species act as good electron donors at limited EDTA concentrations (1:2 to 1:4 uranyl to EDTA ratios) but at higher concentrations (for example, 1:8), uranyl-EDTA complexes such as $[(UO_2^{2+})HEDTA]^-$ compete for the surface sites on the TiO_2 nanoparticles, hindering the photoreduction of uranyl. X-ray photoelectron spectroscopy (XPS) of the dried TiO_2 powder shows that more than 70 % of uranium partitioned into the solid phase is present as reduced forms with oxidation states (V) and (IV). The U4f spectra of the U partitioned to the solid phase from the photoreaction with acetate reveal the predominance of U(IV) over U(V), whereas U(V) is the dominant oxidation state as a result of the photoreduction with EDTA. Our results suggest that formation of uranium-ligand complexes play a critical role in controlling the reactivity of uranyl species and the stability of reduced uranium species in the course of the photoreaction.

1. INTRODUCTION

The uranyl ion (UO_2^{2+}) is the most stable form of uranium with the oxidation number VI in natural settings such as soils and groundwater, and in waste mixtures (for example, in nuclear waste disposal sites). Although the mobility of uranyl can be retarded via sorption onto mineral and solid-waste surfaces as well as secondary mineralization (Yang and Davis, 2000; Kim et al., 2015a), remobilization may occur due to complexation with dissolved ligands, thereby potentially spreading pollution. Ethylenediaminetetracetate (EDTA) is a chelating agent commonly used to increase the solubility of toxic and heavy metal ions including uranium as required for industrial applications such as chemical cleaning and decontamination operations. Oxalate is often found in nuclear waste repositories as it is produced by the decomposition of other organic compounds (Campbell et al., 1994). In addition, oxalic acid naturally occurs as a great source of protons and metal-complexing organic ligands that can make various metals (bio-) available in ecosystems (Gadd, 1999). Since uranyl forms strong complexes with these organics, their interactions are important in evaluating the mobility of uranyl in aqueous systems (Havel et al., 2002).

Because of increase in mobility, uranyl-organic complexes are difficult to treat using conventional techniques (Yang and Davis, 2000). One promising treatment approach is to couple metal reduction with photochemical oxidation of organic contaminants using a mineral catalyst. Anatase, a polymorph of titanium oxide (TiO_2), is known to be a robust and efficient mineral catalyst for such photochemical processes. Oxidation of various organic compounds such as EDTA, methanol, propanol, and acetate have been demonstrated to promote photocatalytic reduction of uranyl using anatase (Chen et al., 1999; Evans et al., 2004; Bonato et al., 2008; Salomone et al., 2015). There is a general consensus that the heterogeneous photoreduction of uranyl is hindered in the presence of dissolved oxygen and that uranyl can be reduced and

precipitated as U(IV). However, the respective roles of organic molecules as ligands and electron donors upon this process have been barely investigated.

Upon the photochemical reduction of uranyl mediated by anatase, irradiation by photons with energies higher than its bandgap is necessary to excite the electron (e^-) from the valence band into the conduction band. As a result, a hole (h^+) is generated in the valence band. In order to overcome the bandgap of anatase (3.2 eV), the wavelength of electromagnetic radiation must be 390 nm or shorter which corresponds to ultraviolet (UV) radiation or photons with even higher energies. Although the majority of studies about uranyl photoreduction using anatase have adopted light sources with the primary emission in the UV-A range (315 to 400 nm), some medium-pressure mercury lamps do not filter contributions of radiations having shorter and longer wavelengths (Salomone et al., 2015). More electrons would overcome the bandgap of semiconductors as the wavelength of UV radiation is shorter. It is questionable whether UV radiation with shorter wavelengths and thus more electron-hole pairs in the anatase catalyst will be either cooperative or inhibitive to uranyl photoreduction. Indeed, selection among different UV types is one of the most important parameters in optimizing photochemical treatments of organic and inorganic contaminants as well (Alaton et al., 2002).

The main objective of this study is to investigate 1) the respective role of organic molecules on complexation and electron donation during heterogeneous photoreduction of uranyl and 2) the dependence of the uranyl photoreduction with various organic molecules on UV wavelength. Four different organic ligands were selected as electron donors: acetate, EDTA, oxalate, and hydroquinone. There are previous studies that used acetate and EDTA as an electron donor for uranyl reduction (Chen et al., 1999; Bonato et al., 2008). To our knowledge, the present study is the first to demonstrate the oxidation of oxalate and hydroquinone as coupled with photocatalytic

uranyl reduction. The three subclass regions of the UV spectrum, UV-A, B, and C, are used to examine how uranyl photoreaction with varying organic ligands responds to these regions of UV light. X-ray photoelectron spectroscopy (XPS) was adopted to obtain direct evidence for U photoreduction as catalyzed by TiO_2. Based on the uranium speciation with the organic ligand, reaction mechanisms and effects of organic ligands and UV wavelengths on photocatalytic reduction of uranyl are discussed.

2. METHODS

2.1. Materials and Reagents

Titanium oxide (TiO_2) nanoparticles (AEROXIDE® TiO_2 P25) were provided by Degussa and used without further purification. P25 consists of aggregated primary particles of anatase and rutile, two polymorphs of titanium oxide, in a weight ratio of 4:1. Particle mean diameter is 21 nm and the specific surface area is 50 m^2/g. Prior to solution preparation, Milli-Q® water (resistivity $\geq$ 18.2 MΩ·cm) was autoclaved in Pyrex® media storage bottles at regular sterilizing conditions (that is, 40 min at 121℃ and 138 kPa). Immediately after, purified N_2 was bubbled into the water through a diffuser for about 60 min while the water cooled from 95 to 40 °C. Glass bottles were then capped air-tight and immediately transferred to a controlled-atmosphere glove box. Stock solutions of uranyl and organic compounds were prepared using uranyl nitrate hexahydrate ($UO_2(NO_3)_2 \cdot 6H_2O$, International Bio-analytical Industries), sodium acetate trihydrate ($NaCH_3COOH \cdot 3H_2O$, Fisher Chemical), disodium EDTA dihydrate ($C_{10}H_{14}N_2Na_2O_8 \cdot 2H_2O$, Fisher Chemical), oxalic acid dihydrate ($C_2H_2O_4 \cdot 2H_2O$, Baker analyze) and hydroquinone ($C_6H_6O_2$, Acros Organics).

2.2. Solution Chemistry and Irradiation Experiments

Experimental settings used in this study are summarized in Table 3. 1. For all experiments, the concentration of uranyl was 0.21 mM while the concentrations of organic compounds were varied from 0.42 to 1.68 mM which correspond to the uranyl to organic compound molar ratio of 1:2 to 1:8. Control experiments were run without titanium oxide catalyst or in darkness (set I and II in Table 3. 1) to explore synergistic effects in the coexistence of the catalyst with the light source (set III). The solutions were initially adjusted to a pH of 2.5 by adding concentrated NaOH or HCl. This value of pH was selected because only a minimal change in pH (< 0.2) occurs after 5hr of the photoreaction in solutions used in this study. After the reaction, the solution was filtered, and the supernatants were collected and analyzed by a Perkin-Elmer ELAN DRC-e inductively coupled plasma mass spectroscopy (ICP-MS). In this study, dissolved uranium measured after the reaction corresponds to the uranyl remaining in solution after adsorption to the solid phase and precipitation as uranium-containing solids.

Table. 3. 1. Summary of solution chemistry and experimental conditions.

Solution chemistry		Remarks
$[U]_{ini}$	0.21 mM	U(VI) : Org. is ranged 1:2 to 1:8
[Org.]	0.42 to 1.68 mM	(Org. is acetate, EDTA, oxalate and hydroquinone)
pH	2.5	
$[O_2]$	Solution degassed	< 1 ppm in atmosphere
Temperature	25 ℃	

Experimental set	Constraints		Main process in uranyl removal
	Irradiation	with Catalyst	
I.	No	Yes	Adsorption
II.	Yes	No	Homogeneous photoreduction
III.	Yes	Yes	Adsorption + photoreduction

For our experimental conditions, aqueous U(VI) species and saturation index with respect to various solid phases were calculated by Visual MINTEQ ver. 3.0 with the Thermo.vdb database (Fig. 3. 1). Speciation of uranyl is variable depending on the dissolved organic ligand and its concentration. Experiments in acidic solutions (pH 2.5 in this study) are valid for our experimental purpose as the possibility of wet precipitation of uranyl solids can be ruled out at such a low pH (Fig. 3. 1). Photocatalytic experiments with TiO_2 suspensions were carried out using an in-house fabricated photoreactor consisting of three vessels nestled inside one another (Fig. 3. 2). The quartz inner vessel is a thimble designed to hold a compact fluorescent bulb (Philips 9 W, G23). This inner vessel is positioned inside a central reaction vessel, which in turn sits inside an outer vessel. The outer vessel holds a thermostatic layer of circulating water controlled by an external water chiller. UV light bulbs providing different wavelength ranges were used: (1) 368 nm emission peak for the UV-A region, (2) 311 nm emission peak for the UV-B region, and (3) 254 nm emission peak for the UV-C region. TiO_2 suspensions (65 mL, $1 gL^{-1}$) were irradiated in an anoxic glovebox (< 1 ppm O_2) with a 10% H in N gas mix.

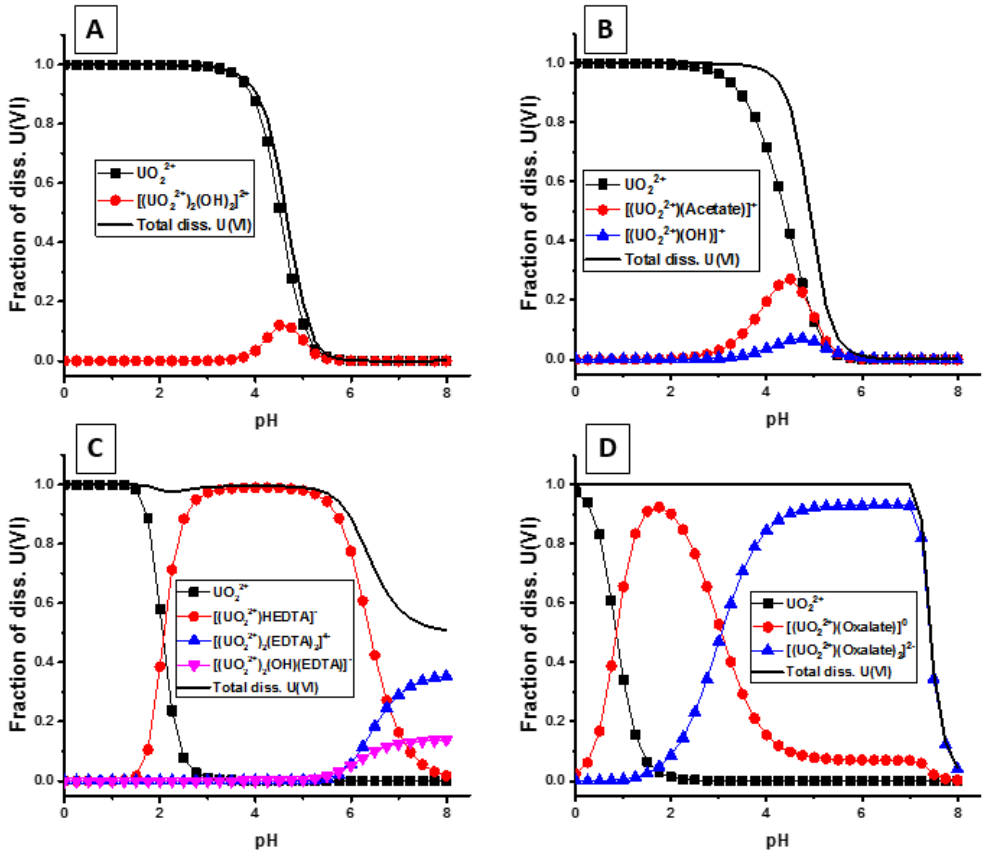

Fig. 3. 1. Speciation of dissolved uranyl (A) as a function of pH (0.21 mM U(VI)), (B) in the presence of 1.68 mM acetate, (C) 1.68 mM EDTA, and (D) 1.68 mM oxalate. Decrease in the total dissolved U(VI) at pH 6 to 10 is mainly due to precipitation of schoepite and U-hydroxides.

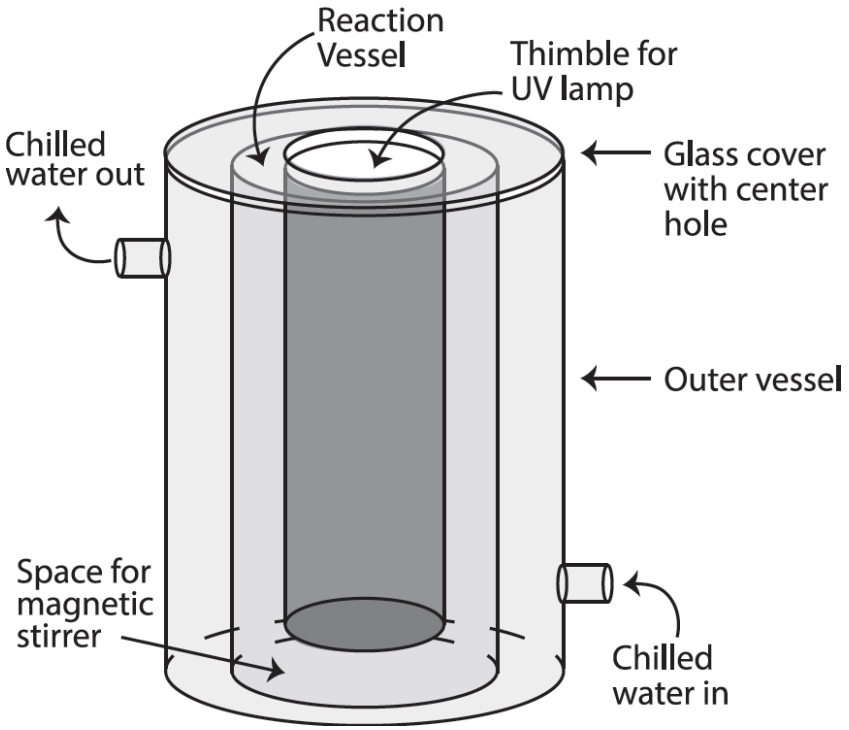

Fig. 3. 2. Illustration of the photoreaction apparatus used in this research. The elongated UV lamp is housed inside the inner quartz thimble in direct contact with the solution to induce photoreactions. Dissolved oxygen can compete with U(VI) for electrons transferred from an electron donor species. To minimize the effect of oxygen, the apparatus is setup in a glove box to maintain anoxic conditions; all solutions are prepared with degassed water. A water chiller outside the glove box is connected to the reaction vessel inside to keep temperature constant during the course of experiments.

2.3. Material Characterization

XPS spectra were collected using an Axis Ultra spectrometer (Kratos Analytical UK). Monochromatic and focused Al Kα radiation (1486.6 eV) was used for the excitation of samples. All measurements were performed in the hybrid mode, which employs both electrostatic and magnetic lenses. The x-ray emission current and anode voltage used during spectra acquisition were 8 mA and 14 keV, respectively. Survey and core scans were acquired at constant pass energies of 160 and 20 eV, respectively. Measurements were performed under vacuum conditions lower than 10^{-8} Torr. All spectra reported were calibrated using the position of the Ti 2p peak (458.7 eV) or the C 1s peak (284.9 eV) for adventitious carbon. Spectra analysis and calibration were performed using the CASA XPS software (version 2.3.16, www.casaxps.com). Caution is needed on XPS analysis for uranium because U(VI) is likely reduced during exposure to the X-ray beam (Ilton et al., 2007). Sequential analyses were taken on the same spot, for each specimen, in order to check for beam-induced reduction as suggested by Ulrich et al. (2009). The specimen with EDTA was stable over the first several spectra whereas oxidation state measurements of the specimens with acetate and the uranyl adsorption sample suggested reduction over time. Fortunately, reduction was found to be systematic and slow. The XPS spectra presented in this work are always the first two scans in each measurement such that the contribution of the beam-induced reduction to the XPS spectra is minimal.

Microscopic morphologies of solid phases before and after the catalytic photoreaction were examined using scanning electron microscopy (SEM, Hitachi, S-4800) equipped with an EDX spectrometer.

2.4. Modeling Molecular Structures of Uranyl-Organic Complexes

Energy optimizations of uranyl-organic complexes were performed using the software package DMol^3 (Local Density Functional Calculations on Molecules) (Delley, 1990). The Perdew-Wang generalized gradient scheme (GGA) was used in combination with ultrasoft pseudopotentials. The GGA scheme was parameterized by the Perdew-Burke-Ernzerhof (PBE) functional (Perdew et al., 1996). The double numeric quality basis set (DNP) and effective core potentials (ECPs) were used for all calculations. The convergence tolerance for energy change, max force, and max displacement were 2×10^{-5} Ha, 0.004 Ha Å^{-1}, and 0.005 Å, respectively. A Fermi smearing of 0.01 Ha to the orbital occupancy was applied to improve computational performance.

The uranyl species of $[(UO_2^{2+})(C_2O_4)]^0$ and $[(UO_2^{2+})HEDTA]^-$ were modeled and their energy-optimized structures are shown in Fig. 3. 3A and B. The initial model of $[(UO_2^{2+})(C_2O_4)]^0$ before optimization was adopted from Tsushima et al. (2010). To our knowledge, there have been no studies reporting the coordination environment of uranyl forming a complex with EDTA. The $EDTA^{4-}$ anion has 4 O atoms belonging to the carboxyl functional group and two N atoms that can form bonds with the central cation during chelation. When modeling chelation with EDTA, having uranyl as a center metal ion is not simple because it has two O atoms that may induce some steric restrictions. Several possible configurations of $[(UO_2^{2+})HEDTA]^-$ were built while considering some important parameters such as H bonding with N and O, and coordination number of UO_2^{2+} from 4 to 6 with the N and O atoms of EDTA. From energy optimization of those configurations tested, one with the lowest energy is presented in Fig. 3. 3B.

3. RESULTS

3.1. Speciation and Adsorption of Uranyl in the Presence of Organic Ligands

Speciation of uranyl in the presence and absence of organic ligands is calculated as a function of pH and presented in Fig. 3. 1. In the absence of organic ligands, the UO_2^{2+} ion is the most dominant uranyl species in acidic solutions (pH < 4.0, Fig. 3. 1A). The total U(VI) concentration of 0.21 mM decreases at pH values above 4.0 due to the formation of uranyl oxyhydroxide solids such as schoepite. In the presence of an organic ligand, uranyl tends to remain in solution and the total dissolved U concentration remains constant over a wider range of pH. Among acetate, EDTA, and oxalate, acetate shows the weakest binding with the UO_2^{2+} ion such that the fraction of the uranyl-acetate complex is calculated to be less than 30 % in acidic conditions (Fig. 3. 1B). The formation of uranyl-ligand complexes plays a critical role in solution chemistry of uranyl with EDTA and oxalate. The fraction of the UO_2^{2+} ion drastically decreases with increasing pH, and the uranyl-ligand complex is the most dominant species at pH above 2.0. $[(UO_2^{2+})HEDTA]^-$ is the dominant uranyl species in the presence of EDTA, while $[(UO_2^{2+})(C_2O_4)]^0$ and $[(UO_2^{2+})(C_2O_4)_2]^{2-}$ are major species in oxalate solutions at pH 2.5 (Fig. 3. 1C and D).

Uranyl removal from solution in the absence of UV radiation is due to adsorption on TiO_2 (Table 3. 1). Uranium uptake by TiO_2 is the highest in uranyl solutions with EDTA (10 %) and acetate (9 %), followed by hydroquinone and oxalate (less than 6 %) (Table 3. 2). Adsorption of uranyl on TiO_2 is largely controlled by the surface charge of the adsorbent (Cerrillos and Ollis, 1998). The point of zero charge of P25 TiO_2 nanoparticles is near pH 4 to 5 (Noh and Schwarz, 1989). This means that the surface of the TiO_2 particles is positively charged at pH 2.5 and thus repulsive to the UO_2^{2+} ion. Such electrostatic interactions between the surface and the adsorbate can be influenced by the organic ligand. The organic ligand can be adsorbed onto the catalyst

thereby reducing the solid surface excess positive charge. Additionally, the charge of the uranyl species can be modified by complexation with the organic ligand, and the resulting uranyl-ligand complexes may be preferentially partitioned into either the solution or the solid phase. For example, the lowest adsorption of uranyl onto TiO_2 is found from solution with oxalate. At pH 2.5, the dominant oxalate species dissolved in solution is monobasic oxalate ($HC_2O_4^-$). The monobasic oxalate anion may have a strong affinity toward the TiO_2 surface and counterbalance the positive charge of the proton-dominated TiO_2 surface site with its negative charge. Such a mechanism would lessen the interaction of the negatively charged species, $[(UO_2^{2+})(C_2O_4)_2]^{2-}$, with the TiO_2 surface. Although $[(UO_2^{2+})(C_2O_4)]^0$ is dominant in solution with oxalate, it might be moderately or least reactive toward the TiO_2 surface due to its neutral charge.

Table. 3. 2. Uranyl removal from solution after reaction in darkness and without TiO_2.

	U(VI) adsorption by TiO_2 (%)	U(VI) removal without TiO_2 (%)		
UV Light	dark	368 nm	311 nm	254 nm
Acetate	9.0	8.9	5.1	3.8
EDTA	10.2	0.0	4.0	1.7
Oxalate	1.3	11.9	12.2	6.1
HydroQ	5.8	8.7	7.3	0.8

Although metal-organic molecules are present in hydrated forms in solution, the water ligands would be the first to be desorbed because they are more weakly bound than the organic complex. Thus, the proportion of dehydrated species would increase toward the surface region where they interact with reactive surfaces of the solid phase and form bonds with the surface functional group. This tendency has been shown for uranium interacting with the TiO_2 surface where uranium of the uranyl molecule forms bonding directly with oxygen on the surface, for example, in the bidentate mode (Perron et al., 2006, see also the excellent review regarding the structures of hydrated uranyl complexes (Kubicki et al., 2009). Here, the molecular structures of uranyl species, $[(UO_2^{2+})(C_2O_4)]^0$ and $[(UO_2^{2+})HEDTA]^-$, were calculated to consider the reactivity of these

molecules upon interaction with the catalyst surface. When a uranyl ion forms a complex with an oxalate anion, the two O atoms of uranyl (axial oxygen in Fig. 3. 3A) are bent and form an O-U-O angle of 166 °. The two O atoms of oxalate are equatorially positioned with respect to the uranyl structure (equatorial oxygen in Fig. 3.3A). The structure of the uranyl molecule shows the U-O_{ax} distance of 1.8 Å and the U-O_{eq} distance of 2.2 Å. These U-O bond distances are approximately the same as previous reports of uranyl-oxalate complexes (Tsushima et al., 2010). In the model of $[(UO_2^{2+})HEDTA]^-$, the angle between the U atom and the axial O atoms are 151 ° and their distance is 1.8 Å (Fig. 3. 3B). The uranyl forms five-fold coordination with three O atoms of the carboxyl functional group and two N atoms and the U-O distance is 2.3 to 2.5 Å and the U-N distance are 2.7 and 2.9 Å. The oxygen bonded with H is farther away from the uranium atom (3.7 Å). The distances between central uranium and the five nearest N and O atoms are close to values reported from previous studies of uranyl-formate complexes (Lucks et al., 2013).

The electrostatic potential of individual complexes are presented in Fig. 3. 3C and D. The negative potential is mainly distributed near the two nonbonding O atoms of $[(UO_2^{2+})(C_2O_4)]^0$ while O atoms that belong to the carboxyl functional group of EDTA are the main location of the negative potential in the molecular structure of $[(UO_2^{2+})HEDTA]^-$. Uranyl accounts for the largest portion of positive potential found in the molecules of these uranyl complexes. Since the surface of the TiO_2 catalyst is proton-dominant at pH 2.5, the electron-rich regions of these molecules where the negative potential is dominant would be reactive to interact with the positively charged surface. It is followed that these uranyl-organic molecules are likely bound to the surface through the ligand when adsorbed. This inference is in good agreement with a previous study suggesting that the S-L-M binding mode where the ligand (L) is located between the surface (S) and the metal ion (M) could explain adsorption behavior of uranyl in the presence of EDTA (Cerrillos and Ollis,

1998). In turn, it is supposed that the interaction between uranyl and the catalysts surface can be largely modified by the presence of the organic ligand.

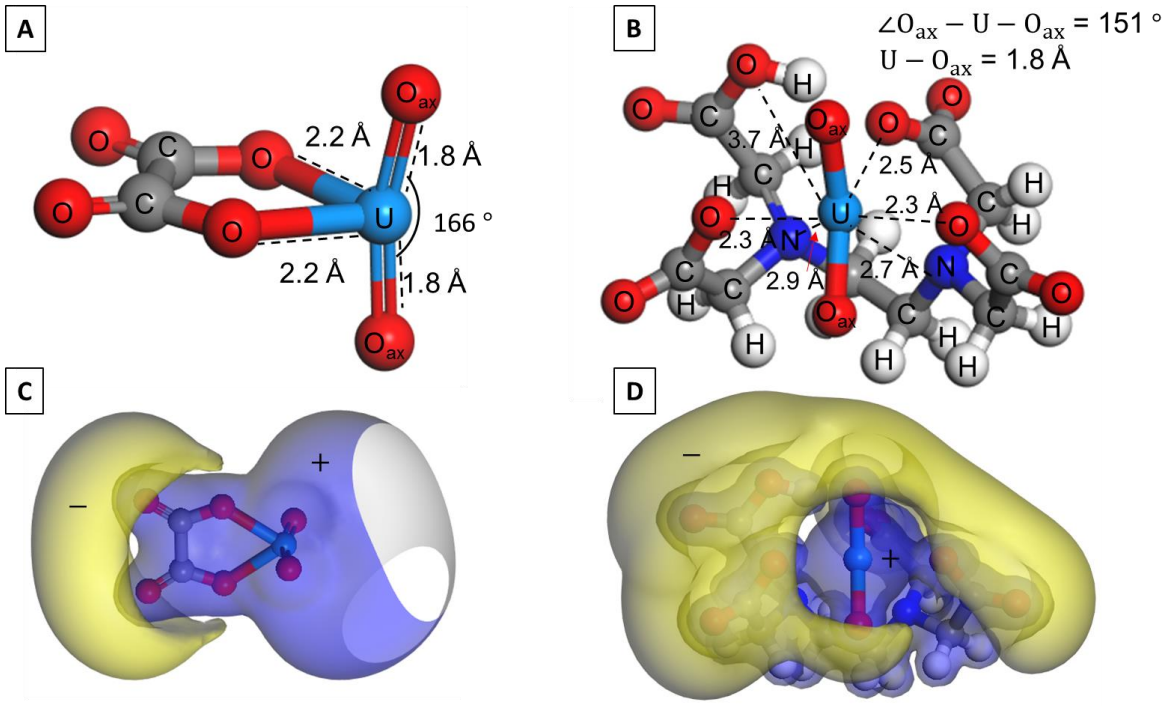

Fig. 3. 3. Energy-optimized structures and electrostatic potential surfaces of $[(UO_2^{2+})(oxalate)]^0$ (A, B) and $[(UO_2^{2+})HEDTA]^-$ (B and D). In Fig. 3. 3C and D, the blue and yellow surfaces represent positive and negative potentials, respectively.

3.2. Macroscopic Evidence of Photocatalytic Uranyl Reduction

Dissolved uranyl can undergo several processes in the presence of UV light and TiO_2 catalyst.

[1] The surface of TiO_2 provides reactive sites where the uranyl molecule can be adsorbed (adsorption).

[2] Uranyl may be reduced by interaction with UV light. The process does not involve catalysis by TiO_2, but possibly the oxidation of a coexisting organic compound (homogeneous photoreduction).

[3] Electrons excited by UV light into the conduction band are transferred to the adsorbed uranyl molecule. This process is coupled with the oxidation of an organic compound that acts as a hole-scavenger (heterogeneous photoreduction).

Experimental sets to estimate the contributions of individual processes are summarized in Table 3. 1 and experimental results are presented in Table 3. 2 and Fig. 3. 4.

At pH 2.5, uranyl removal by TiO_2 without UV light (that is, adsorption) is $\leq$ 10 % in the presence of acetate, oxalate, hydroquinone or EDTA (Table 3. 2). Uranyl removal by photoreaction without TiO_2 particles (that is, homogeneous photoreduction) is less than 10 % for solutions containing acetate, EDTA and hydroquinone, and 6 to 12 % for solution with oxalate depending on the UV region (Table 3. 2). Assuming these two processes were always independent, their maximum contribution would be $\leq$ ~22 % for all possible combinations of organic compound and UV light region. Fig. 3. 4 shows the effect of different UV light wavelengths on uranyl removal from organic compounds solutions in the presence of TiO_2. For solutions containing acetate, oxalate, and hydroquinone, photolytic uranyl removal by TiO_2 is more than 30 % over all UV

regions, 2/3 or more of which can be associated to the influence of the UV source and/or the TiO_2 catalyst.

Among organic molecules tested in this study, the most effective electron donors are acetate and oxalate which show uranium removal of more than 70 % for all the UV lights tested, followed by hydroquinone and EDTA (Fig. 3. 4). There are no significant differences in uranyl removal between the three UV regions when acetate and oxalate are present in solution as an electron donor. Uranyl removal depends highly on the UV light range when uranyl coexists with EDTA and hydroquinone, but dependence on UV wavelength is found contrasting between the latter two compounds. Uranyl removal is the greatest in the UV-A region for solutions containing uranyl and hydroquinone, whereas maximum removal of uranyl from solutions with EDTA occurs in the UV-C region.

Since the organic compounds show different efficiencies as electron donors for uranyl removal (that is, oxalate > acetate > hydroquinone > EDTA), it is worth testing whether the efficiencies of hydroquinone and EDTA are enhanced by adding acetate (or oxalate). The coexistence of acetate and hydroquinone increases uranyl removal by ~15 % whereas uranyl removal with EDTA marginally changes when the same concentration of acetate is added to the solution (Fig. 3. 5A). However, decreasing EDTA concentrations enhances uranyl photoreduction by TiO_2 (Fig. 3. 5B). Uranyl removal increases as the uranyl to EDTA molar ratio increases from 1:8, to 1:4, and to 1:2. This observation suggests that dissolved EDTA species can act as electron donors but hinder the uranyl removal as its concentration reaches certain levels.

These results of uranium solution chemistry show that mechanisms of uranyl photocatalytic reduction can vary depending on the coexisting organic molecule functioning as a ligand and an

electron donor. Specific effects of organic ligands are discussed further in the DISCUSSION section.

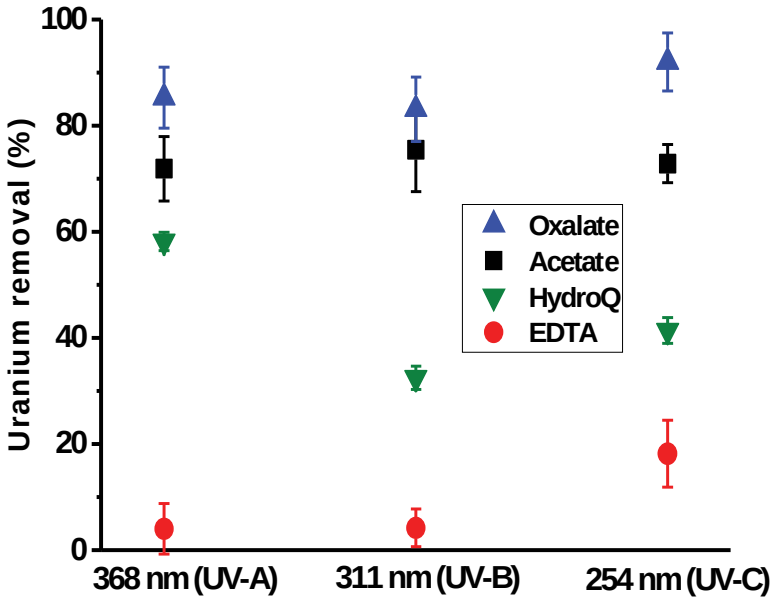

Fig. 3. 4. Uranium removal from solutions containing different organic compounds. $[U(VI)]_{ini}$ = 0.21 mM, $[Org.]_{ini}$ = 1.68 mM, pH = 2.5 and 1g / L of TiO_2. The error bars represent data from replicate experiments.

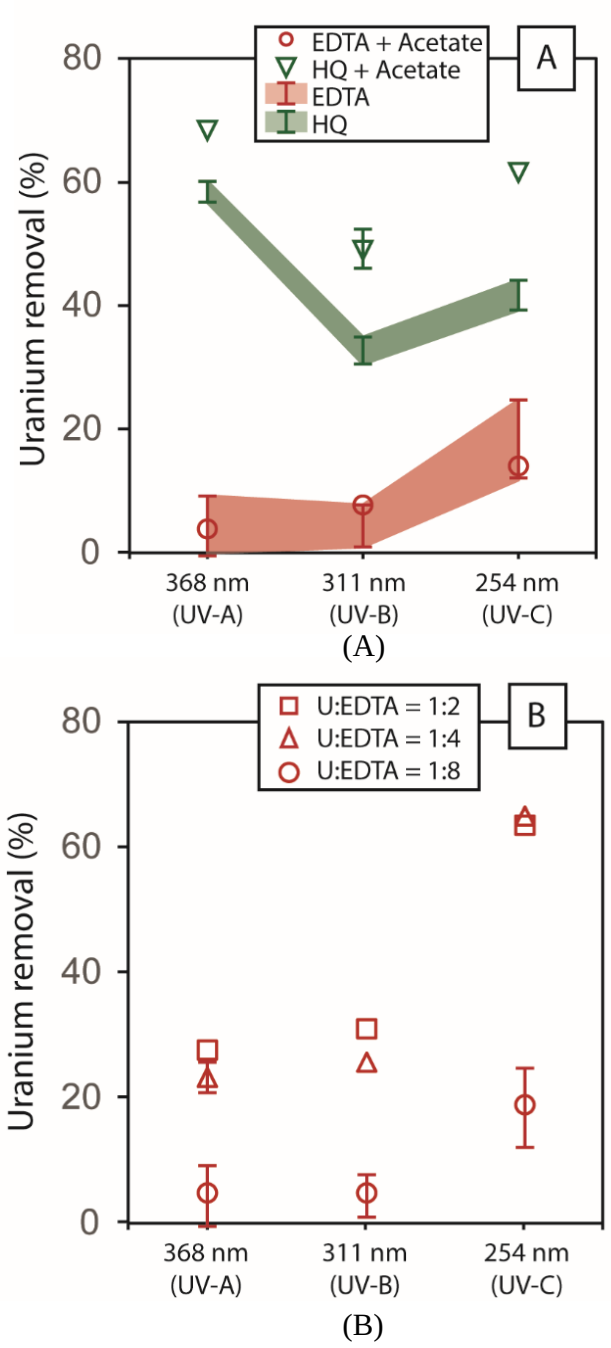

Fig. 3. 5. (A) Effects of adding 1.68 mM acetate on uranium removal from different solutions. Red symbols: 0.21 mM of U(VI) and 1.68 mM of EDTA. Green symbols: hydroquinone. (B) Uranyl removal from solution ($[U(VI)]_{ini}$ = 0.21 mM) with varying concentrations of EDTA (0.42 mM, 0.84 mM, and 1.68 mM). The colored rectangles on Fig. 3. 5A are error bars from replicates. The absence of bars indicate the error is smaller than the symbols.

3.3. Forms of Uranium after Photoreaction with Organics

XPS analysis is performed to measure variation in the oxidation state of uranium as a result of the photoreaction. The binding energies of uranium is analyzed to identify possible forms of uranium in the reacted solid phase such as uranium oxides and uranium-organic complexes.

XPS core scans of the U 4f peaks are presented in Fig. 3. 6. Uranyl nitrate hexahydrate was used as reference material and shows two peaks centered at 382.8 and 393.6 eV, which corresponds to U4f 7/2 and 5/2 spin-orbit split peaks, respectively (data are not shown here). These binding energies are comparable to other reported values of U(VI) in uranyl nitrate hexahydrate (Dash et al., 1999; Froideval et al., 2003). In samples from photoreactions with acetate and EDTA, the U 4f peaks are shifted to lower binding energy by ~2.4 eV (Fig. 3. 6A and B), which is likely indicative of the presence of uranium species with the oxidation states of U(V) and U(IV).

Table. 3. 3. The XPS primary peak positions and the atomic proportions of uranium oxidation states.

U + acetate			
	U(IV)	U(V)	U(VI)
$U4f_{7/2}$	380.3	381.2	382
$U4f_{5/2}$	391.3	392.2	392.8
Atomic proportion	0.50	0.20	0.30
U + EDTA			
	U(IV)	U(V)	U(VI)
$U4f_{7/2}$	380.1	380.5	381.4
$U4f_{5/2}$	390.9	391.4	392.5
Atomic proportion	0.33	0.47	0.20

Distinguishing among the different oxidation states of uranium (IV, V and VI) is not straightforward in samples with mixed oxidation states because the primary peaks lie within 3-4 eV. Notwithstanding, satellite structures that are observed around the primary peaks can be used

to assist in identification of peaks. Specifically, the U(VI) species typically display satellites at around 4 and 10 eV above the primary spin orbit split U4f peaks while satellites that belong to U(IV) and U(V) species tend to appear at ~6 and ~8 eV above, respectively. Based on such relationship between the primary peak and the satellite, we fit three components to the main peaks and satellites of the XPS spectra of uranyl photoreaction with acetate and EDTA to discern uranium species with different oxidation states (Fig. 3. 6). The fitting procedure documented by Ilton and Bagus (2011) is followed in this study. Fitting was performed with characteristic fit parameters being constant, such as the shapes and full width at half maxima (FWHM) of the primary peaks; in addition, the relative ratio of FWHM of the satellite to that of the main peak are identical among peak components with different oxidation states (Ilton and Bagus, 2011). Peak separations between the primary and satellite peaks are found to be 6.0 ± 0.4 and 8.0 ± 0.5 eV, for U(IV) and U(V), respectively (Fig. 3. 6). The fit data confirm that U(IV) and U(V) species result from the uranyl photoreaction with acetate and EDTA. The proportions of U oxidation states were (50%/20%/30% for U(IV)/U(V)/U(VI)) from the acetate solution and (33%/47%/20% for U(IV)/U(V)/U(VI)) from the EDTA one. In other words, in the acetate-containing sample, 70% of U had been reduced by one or two electrons and in the EDTA-containing one, that fraction was 80% (Table 3. 3). The dominant uranium oxidation state is U(IV) in the sample with acetate (50 % in atomic proportion) and U(V) in the sample with EDTA (47 %). The primary peak positions of $U4f_{5/2}$ and $U4f_{7/2}$ for each oxidation state are lowered consistently by 0.2 to 0.8 eV in the sample with EDTA than the one with acetate. These U XPS results suggest that reaction products are not identical between photoreactions with acetate and EDTA.

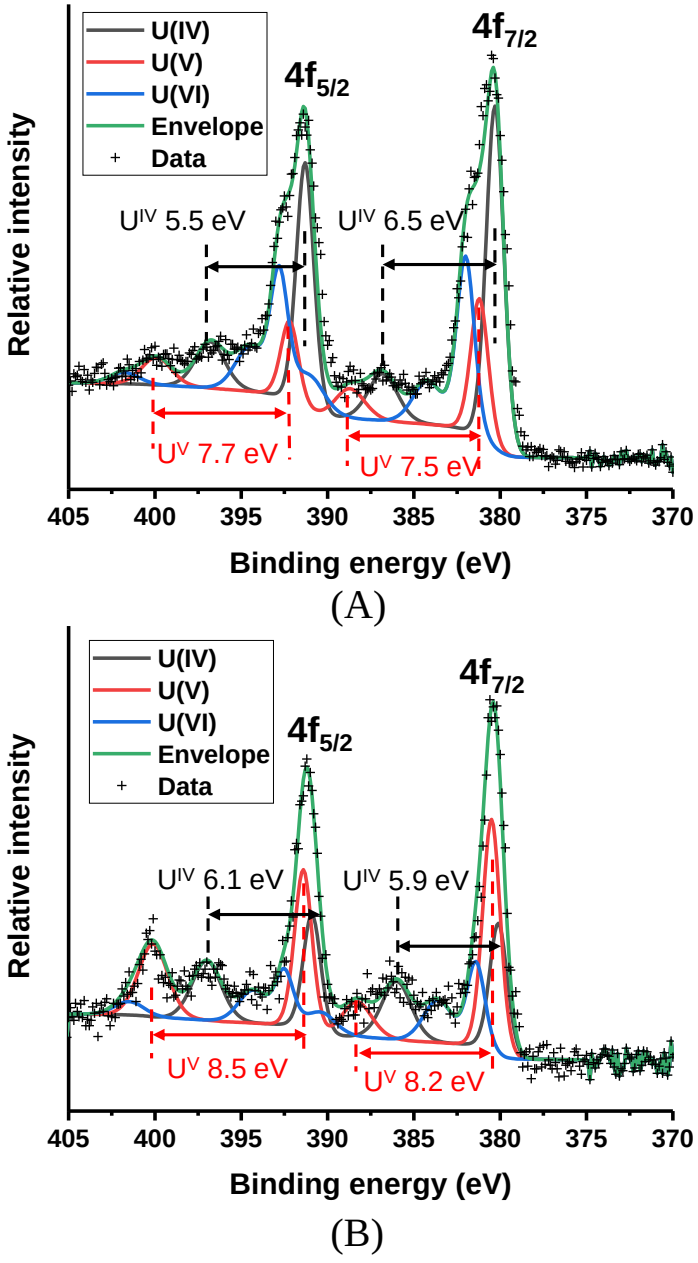

Fig. 3. 6. The fits to the core scans of U 4f orbitals (A) for uranyl photoreduction with acetate (pH 2.5; $[U]_{ini}$ = 0.21 mM and $[acetate]_{ini}$ = 1.68 mM; 5 hr radiation with UV-A) (B) with EDTA (pH 2.5; $[U]_{ini}$ = 0.21 mM and $[EDTA]_{ini}$ = 0.84 mM; 5hr radiation with UV-A).

Previous studies suggest that redox transformation of U(VI) to U(IV) is the dominant process of uranyl photoreduction as catalyzed by TiO_2 and that U(IV) oxides such as UO_2 and UO_{2+x} (x = 0 to 0.25) are the primary product of the process (Chen et al., 1999; Kim et al., 2015b; Salomone et al., 2015). This general conclusion would be the case when the UO_2^{2+} ion is the main reactant to be subject to reduction during the catalytic photoreaction. In solution of pH 2.5 with acetate, the dominant uranium species is the UO_2^{2+} ion (Fig. 3. 1B) and U(IV) species detected in the XPS spectrum is attributed to U(IV) oxides. From SEM measurements, microscopic morphologies of the solid phases are similar before and after the photocatalytic reaction with acetate (Fig. 3. 7). The EDS mapping results show a uniform distribution of uranium in micrometer scales (data not shown here). It is inferred that U(IV) oxides would be in the form of precipitates on the TiO_2 nanoparticle in smaller sizes than the substrate. This inference is consistent with a previous study which reports uniform distributions of uranium precipitates in sub to few nanometer sizes on TiO_2 electrodes after photochemical and electrochemical reduction (Kim et al., 2015b). U(V) dominates over U(IV) in the sample reacted with EDTA (Table 3. 3). The presence of U(IV) could be partially attributed to U(IV) oxide precipitates as similar to photoreaction with acetate. It has been considered that UO_2^{+} is not as stable as UO_2^{2+} and $UO_{2(s)}$ and undergoes a disproportionation reaction to form the latter species (Renock et al., 2013; Yuan et al., 2015b). In solution with EDTA, however, U(VI)-EDTA complexes are dominant over the UO_2^{2+} ion at pH 2.5 (Fig. 3. 1C) and can be reduced to U(V)-EDTA and possibly U(IV)-EDTA without decomplexation (Baker and Sawyer, 1970; Chen et al., 1999). This explanation is also consistent with the XPS results showing lower binding energies of uranium species from photoreaction with EDTA than those with acetate.

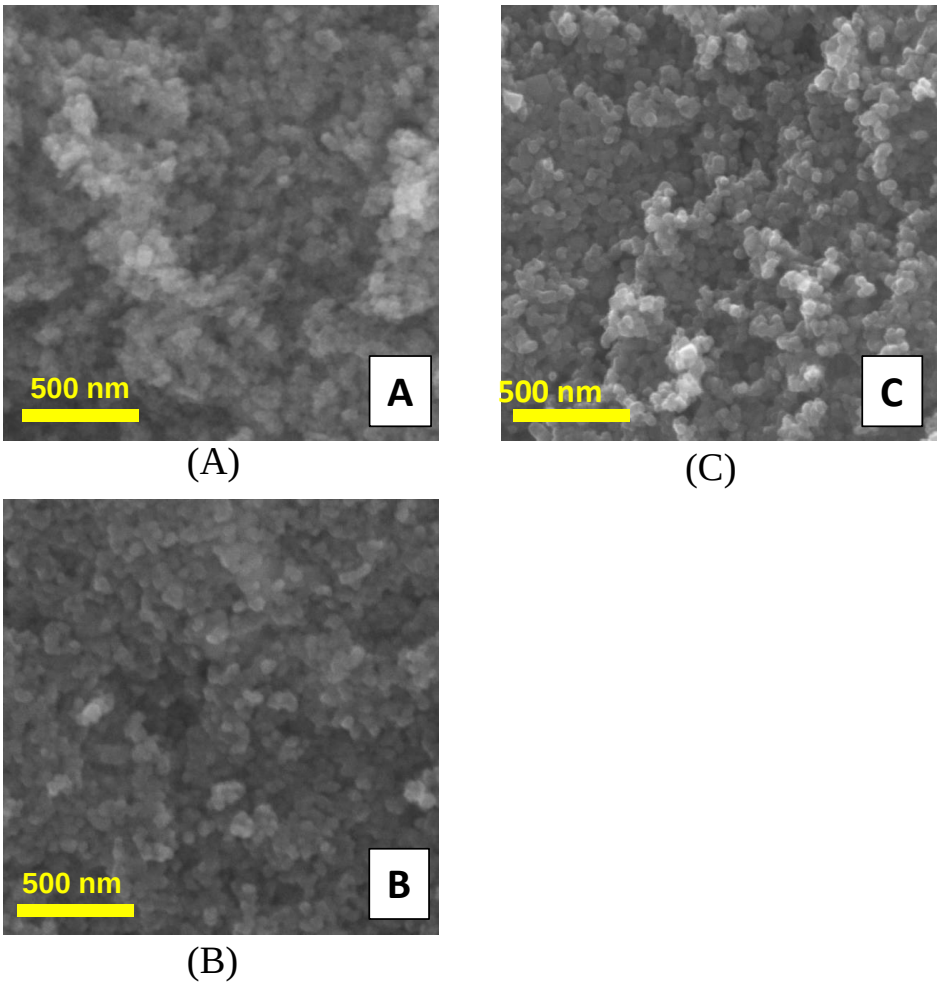

Fig. 3. 7. SEM images of P25 TiO_2 particles. (A) Unreacted samples, and (B) photoreacted samples in solution containing uranyl and acetate and (C) in solution containing uranyl and EDTA.

4. DISCUSSION

4.1. Mechanisms of Photoreduction of Uranyl and Uranyl-Organic Complexes Catalyzed by TiO_2

Our experiments demonstrate the dependency of the uranyl photoreduction with varying organic ligands on the energy of UV light. Uranyl photoreduction mediated by the TiO_2 catalyst proceeds through three sequential steps: (i) the formation of the electron-hole pair by photons; (ii) electron transfer into uranyl species; and (iii) oxidation of organic compound to scavenge the hole. In this section, these individual steps of uranyl photoreduction are examined and reaction mechanisms in relation to complexation with organic ligands and photoexcitation by UV lights are specified.

In our experimental setting, the formation of the electron-hole pair takes place when electrons in the valence band gain energies greater than the band gap of TiO_2 as radiated with UV light. The energy gap between the valence and conduction bands in TiO_2 is 3.2 eV and can be overcome by all UV light regions used in this study as calculated from the energy associated with radiation:

$$E = h\nu \quad (1)$$

where h is the Plank's constant $(6.626 \cdot 10^{-34}\ J \cdot s)$ and ν is the frequency of light (s^{-1}). UV light with shorter wavelengths provides photons with higher energies. This means that some proportion of excited electrons occupy higher energy states in the conduction band that are not available from photoexcitation with longer UV wavelengths (the energy diagram in Fig. 3.8). Whether uranyl species can gain electrons from the conduction band is determined by their relative energies: Electrons are transferred between those energetic states in the conduction band and the electron acceptor, which are at approximately the same energy level (Xu and Schoonen, 2000). The standard electrode potential of reaction between UO_2^{2+} and UO_2^{+} is 0.163 V, and the standard

electrode potential of the uranyl-organic complexes are lower than this value due to the electron-donating ability of organic ligands (Morris, 2002; Kim et al., 2009). In other words, the energy level of the uranyl-organic complex is higher than that of the uranyl ion such that electrons must be excited to higher energetic states in the conduction band to be transferred to the uranyl-organic complex (the energy diagram in Fig. 3. 8). This justification accounts for the trend of uranyl photoreduction with EDTA where uranyl removal is greater by a factor of two or three when photons are sourced from UV-C light than UV-A and B (Fig. 3. 5B). It is found that the uranyl removal with acetate and oxalate is nearly constant with varying the UV wavelength (Fig. 3. 4). Because the uranyl ion is the dominant species in solution with acetate, it is inferred that photons in the UV-A, B and C regions have sufficient energies to excite electrons to energetic states in the conduction band that coincide with the energy level of the uranyl ion. If only the photo flux and energy are the main limiting factor during the uranyl photo reaction, the photoreaction with an organic compound would be the highest at the UV-C region or nearly constant over all UV regions. However, the photoreaction with hydroquinone is lower in the UV-B and UV-C compared to the UV-A region. This observation indicates that there are limiting factors other than the photon flux and energy that influence the uranyl photoreduction with organic compounds. This peculiar trend of the photoreaction with hydroquinone is discussed further in the following section.

After the electron-hole pair is formed by photoexcitation, electrons are transferred to adsorbed uranyl species (eq 2) and the hole (h^+) serves as a mediator to couple uranyl reduction with oxidation of other species (Fig. 3. 8). One such coupled reaction would be water oxidation by the hole (h^+) in the valence band to obtain an OH radical ($OH\cdot$) (eq 3).

$$U(VI\,/\,V) + e_{CB}{}^{-} \rightarrow U(V\,/\,IV) \quad (2)$$

$$H_2O + h_{vB}{}^{+} \rightarrow HO\cdot + H^{+} \quad (3)$$

$OH\cdot$ can undergo self-combination to form hydrogen peroxide (H_2O_2), which in turn produces an oxygen molecule (O_2) as the final product. Although reduced U(V) and U(IV) species are not stable in the presence of h^+, $OH\cdot$, or O_2, organic compounds can scavenge those oxidants, and in doing so, promote uranyl reduction. Organic or inorganic radicals can result from the reaction between the organic compound and the oxidants.

Forouzan et al. (1996) suggested that oxalate undergoes a two-step process of oxidation with an intermediate radical. The first step is to decompose the molecule into CO_2 and the radical anion ($CO_2^{\cdot-}$) (eq 4). In the second step, $CO_2^{\cdot-}$ donates an electron to the metal ion. This suggestion can be applied to our experiments as stated in equations (4) and (5).

$$HC_2O_4^- + h_{vB}^+ \rightarrow CO_2 + CO_2^{\cdot-} + H^+ \quad (4)$$

$$CO_2^{\cdot-} + U(VI/V) \rightarrow CO_2 + U(V/IV) \quad (5)$$

Acetate and EDTA have carboxyl groups (COOH or COO^-) in the structure and react with either the valence band hole or the OH radical to produce organic radicals (eqs 6 and 7).

$$R - CH_2COO^- + h_{vB}^+ \rightarrow R - CH_2COO^{\cdot} \quad (6)$$

$$R - CH_2COO^- + HO^{\cdot} \rightarrow R - CH_2COO^{\cdot} + OH^- \quad (7)$$

The organic radicals undergo further reactions possibly involving water and the valence band hole generating CO_2 and oxidation products (for example, eqs 8 and 9).

$$R - CH_2COO^{\cdot} \rightarrow R - CH_2^{\cdot} + CO_2 \quad (8)$$

$$R - CH_2^{\cdot} + H_2O + h_{vB}^+ \rightarrow RH + CH_2O + H^+ \quad (9)$$

Hydroquinone is the major product of the photocatalytic phenol oxidation mediated by TiO_2 and its oxidation results in the formation of quinone (Sobczyński et al., 1999). Therefore, the

oxidation of hydroquinone to quinone is one likely reaction to be coupled with the photocatalytic reduction of uranium species in solution with hydroquinone.

4.2. Effects of Organic Ligands on Uranyl Photoreduction

The present and previous studies (Madden et al., 1997; Chen et al., 1999) propose that uranyl-ligand complexes are photochemically reactive and reduced to form U(V)-ligand complexes as catalyzed by TiO_2 nanoparticles (Fig. 3. 8A). EDTA and oxalate form strong complexes with uranyl, such as $[(UO_2^{2+})HEDTA]^{-}$, $[(UO_2^{2+})(oxalate)]^{0}$, $[(UO_2^{2+})(oxalate)_2]^{2-}$, and possibly $[(UO_2^{2+})(oxalate)_3]^{4-}$ (see Vallet et al., 2003) and these complexes can be potential species to preserve the oxidation state of U(V) and U(IV) after photochemical reduction of uranyl (Fig. 3. 6 and text). Although the role of organic molecules seems manifest on complexation and redox transformation of uranyl during the photochemical process, their oxidation processes are complicate and are barely known in connection with the uranyl photoreduction. In this section, some of the results are revisited to discuss possible processes that involve organic molecules and influence the uranyl photoreduction.

The process of adsorption is a critical step in the reaction pathway for a reactant to undergo heterogeneous photoreaction. Intriguingly, our data of adsorption and heterogeneous photoreaction in solution with uranyl and the organic ligand show that photocatalytic uranyl removal is not necessarily proportional to uranyl adsorption on the catalyst. For example, adsorption of uranyl on TiO_2 is marginal in the presence of oxalate and no UV radiation. However, for the same suspension, removal of uranyl is maximum under UV radiation. Conversely, the highest adsorption of uranyl is found in solution with EDTA whereas photocatalytic reduction of uranyl is limited in the presence of this organic molecule. These observations indicate that

reactions that do not involve the catalyst (that is, homogeneous reactions) may contribute to the uranyl removal. The oxidation of monobasic oxalate ($HC_2O_4^-$) is mediated by the anatase catalyst (eq 4). The resulting radical anion ($CO_2^{\cdot -}$) is released into solution and reacts with dissolved uranium species (eq 5; Fig. 3. 8B). As a result, one oxalate molecule ion can release two electrons and reduce uranium species via more than one process (eq 2 and 5), which accounts for its highest ability as an electron donor among the four organic ligands tested in this study.

The oxidation of EDTA in the presence of UV irradiation is a source of electrons for uranyl reduction transferred through the TiO_2 catalyst, but uranium removal from solution tends to decrease at high concentrations of EDTA (Fig. 3. 5B). After the electron transfer proceeds, reduced uranium species of U(V) and U(IV) that remain in the form of EDTA complexes can be either released into solution or partitioned onto the catalyst surface (Fig. 3. 8A). The release of reduced uranium species into solution would be enhanced with increasing the EDTA concentration. This explanation is also consistent with the XPS data results of photoreduction with EDTA showing the dominance of U(V) over other U species and lower binding energies of reduced species than those produced from the reaction with acetate (Fig. 3. 6 and text). Another reason for the decrease in uranyl removal at higher EDTA concentrations may be that products of EDTA oxidation precipitate on the surface of TiO_2 while the photoreaction proceeds, such that the catalysis becomes less effective as the reaction proceeds (Fig. 3. 8C). This hypothesis is supported by our macroscopic observation that the TiO_2 catalyst turns dark grey after photoreactions in solution of EDTA with and without dissolved uranyl. The hydrogen molecule (H_2) and ethylenediaminetriacetate (ED3A) can be produced as a result of the photooxidation of acetate and EDTA, respectively, as described in equation (9). ED3A is found to undergo sequential oxidation steps that lead to smaller oxidation products when the reaction system is saturated with the oxygen

molecule (Babay et al., 2001). In case of photoreaction with hydroquinone, quinone can be oxidized further into other intermediates and ultimately CO_2 and H_2O as long as an oxygen supply is not limited during the reaction (Sobczyński et al., 1999). In our experimental settings, however, gaseous oxygen is limited to less than 1 ppm and dissolved oxygen is removed by water boiling above 100 ℃ and sequential degassing by N gas (see the METHODS section). As a result, the oxidation of large organic ligands would not be complete. Such oxidation products could impede further reduction of uranium species mediated by the catalyst. One peculiar trend observed from the reaction with hydroquinone is that heterogeneous uranyl reduction is lower in the UV-B and UV-C compared to the UV-A region (Fig. 3. 4). The heterogeneous photoreduction depends on the production of the electron-hole pair in the catalyst. The production rate of the electron-hole pair increases with increasing UV light energy (Fig. 3. 8). With shorter wavelengths of UV light, not only the process of electron transfer to uranyl species but also the reactions associated with the valence band holes, including the oxidation of organic ligands and the production of strong oxidants, will proceed to a greater extent (eq 3, 4 and 6; Fig. 3. 8D). If the oxidation rate of organic ligands is high enough to scavenge the oxidants produced from the valence band hole, oxidation of reduced uranium can be prevented. In the case where the rate of oxidant production is greater than the rate of electron donation from the organic molecule, however, uranyl reduction is hindered, and reduced uranium species are oxidized by the oxidant. It is possible that limited uranium reduction occurs in the UV-B and -C ranges because the production of oxidant surpasses electron donation from hydroquinone to a larger degree than it does in the UV-A range.

Our preliminary results for uranyl removal in the absence of organic ligands show that uranyl removal with TiO_2 is not significant (< 5%) at pH 2.5 under no UV light, but after 5 hours of irradiation, increases to levels on the order of uranyl removal with EDTA. Salomone and others

(2015) performed uranyl photoreaction experiments in the presence of propanol. They also observed that a certain amount of uranyl is removed from solution in the absence of propanol. Unlike uranyl removal with EDTA, photoreaction without organic ligands produced no grey precipitates under the UV light. This observation suggests that uranyl removal processes differ between solutions with and without organic compounds, and that organic compounds are the primary electron donors to uranyl during the photoreaction with high ratios of organic compound to uranyl as it is suggested in previous related works (Chen et al., 1999; Evans et al., 2004; Bonato et al., 2008; Salomone et al., 2015). It was beyond the scope of our study to address the processes responsible for uranyl removal by irradiated TiO_2 without organic compounds. These mechanisms remain chiefly unidentified and their contribution cannot be completely ruled out from our experimental setting wherein the photodecomposition of dissolved organic ligands are the major contribution to uranyl removal from solution. However, the removal rates without organic ligands are a few times lower than the removal rates with oxalate and acetate, which suggest a limited influence at the time-scale of our experiments. Future research should include specific mechanisms of uranyl removal in the absence of organic electron donors.

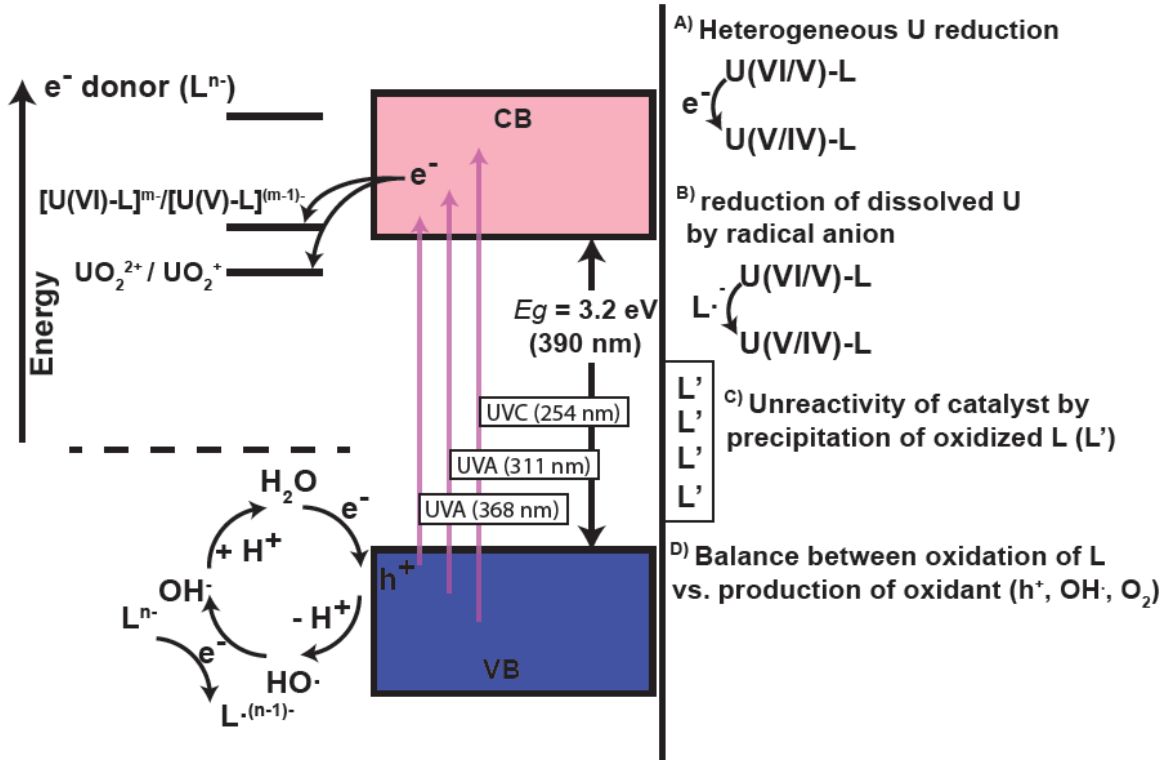

Fig. 3. 8. Simplified energy diagram of the photocatalytic uranyl reduction in the presence of organic electron donors and proposed processes involving organic ligands that can influence the uranyl photoreduction. The results of this study suggest that uranium photoreduction can be mediated not only (A) mineral catalyst but also (B) radical anions such as $CO_2^{\cdot-}$. (C) Precipitation of oxidation products of electron donating organics can hinder further photoreduction of uranyl. (D) Oxidation of organic ligands is essential to promote uranium reduction and its balance with production of oxidants matters with varying the UV wavelength to prevent the reoxidation of reduced uranium species.

5. CONCLUSIONS

This study describes the synergistic interplay between organic ligands (that can provide electrons but also may hinder electron transfer), a catalytic surface, and light in the reduction of uranyl molecules. To our knowledge, the present study is the first to report the dependency of the uranyl photoreduction on the wavelength (or energy) of UV light. Such dependencies are variable depending on organic compounds. Acetate is a good electron donor but does not act as a ligand in our experiments because of its week binding affinity with uranyl. It has been shown that uranyl photoreduction as coupled with oxidation of acetate is nearly independent of UV wavelength. Oxalate is a good electron donor as well as a strong ligand. Uranyl photoreduction with oxalate is strikingly efficient but may result from multiple processes that can be activated by any photons in the UV-A, B, and C spectrum. Electrons in higher energetic states of the conduction band are required to reduce uranyl-EDTA complexes. The production of such electrons can be further promoted by using UV light with shorter wavelengths. Although EDTA acts as an electron donor, increasing EDTA concentrations does not necessarily assist in enhancing uranyl removal from solution. This is probably because solubility of reduced uranium species increases if they form complexes with EDTA. Hydroquinone is found to act as an electron donor, but its electron donation becomes inefficient to leave uranium in reduced forms as the photon energy increases. This result supports the idea that reduced uranium from photoreduction is preserved only when the oxidation of organic molecules proceeds at fast rates to overcome oxidant attacks.

The computational results in this study reveals a significant change in the reactivity of uranyl toward the positively/negatively charged surfaces due to the formation of complexes with organic ligands. Further simulations using DFT calculations are necessary to decipher the exact mechanism of surface adsorption and the process of electron transfer within uranyl-organic complexes upon

interaction with TiO_2. One could potentially adopt time-dependent DFT calculations to simulate the reduction of a uranyl-organic complex during the course of electron injection from the valence band to the conduction band by UV light (for example, Elenewski et al., 2016).

U(V) remains stable upon the photocatalytic reduction with EDTA whereas U(IV) is the dominant species as a result of photoreaction with acetate. Distinct features in uranium redox chemistry between different electron donors are likely the result of the formation of complexes of reduced uranium species with organic ligands. Our results show that specific effects of organic molecules and UV radiation ranges should be considered when performing photocatalytic uranyl reduction. Yuan et al. (2015a) demonstrates that U(V) is more stable and stay on the surface longer than previously believed when it is produced from uranyl reduction mediated by magnetite. Our spectroscopic data suggest that U(V) can be an important reaction intermediate upon photo-induced redox transformation of uranium, especially when its stability can be enhanced by complexation with organic molecules.

The extraction or immobilization of U(VI) is an important pursue. Naturally, it has been primarily addressed in environments where contamination risk is high. Recent events suggest that it would be advisable to expand our understanding of uranium removal to other settings (Schneider et al., 2017). In the marine photic zone, uranium chemistry is largely affected by the presence of carbonate. Uranyl-carbonate complexes in the form of $[UO_2{\cdot}(CO_3)_n]$ (typically, n is 1 to 3) are dominant at neutral and weak basic pH (Djogic et al., 1986). Future studies could be aimed at investigating photoreaction of uranyl carbonate complexes, for example, in the absence and presence of TiO_2. Those attempts will address the extraction of dissolved uranyl from natural seawater or the recovery of accidently discharged radionuclide uranium.

Acknowledgements

The authors are grateful for the support from the U.S. Department of Energy's (DOE) Office of Science, Office of Basic Energy Sciences (BES), Chemical Sciences, Geosciences, & Biosciences (CSGB) Division for the topics of Heavy Element Chemistry and Geoscience (grant number DE-FG02-06ER15783). Y.K. acknowledges support from Samsung Scholarship. Y.K. thanks Thomas Yavaraski for educating to perform ICP-MS and Will Bender for collaborating on the SEM measurement. The authors acknowledge financial support from the University of Michigan College of Engineering and technical support from the Michigan Center for Materials Characterization.

References

Alaton I. A., Balcioglu I. A. and Bahnemann D. W. (2002) Advanced oxidation of a reactive dyebath effluent: comparison of O_3, H_2O_2/UV-C and TiO_2/UV-A processes. *Water Res.* **36**, 1143-1154.

Babay P. A., Emilio C. A., Ferreyra R. E., Gautier E. A., Gettar R. T. and Litter M. I. (2001) Kinetics and mechanisms of EDTA photocatalytic degradation with TiO_2. *Water Sci. Technol.* **44**, 179-186.

Baker B. C. and Sawyer D. T. (1970) Electrochemical studies of the uranium (VI)-ethylenediaminetetraacetic acid complex. *Inorg. Chem.* **9**, 197-204.

Bonato M., Allen G. and Scott T. (2008) Reduction of U (VI) to U (IV) on the surface of TiO_2 anatase nanotubes. *IET Micro & Nano Letters* **3**, 57-61.

Campbell J., Stromatt R., Smith M., Bean R., Jones T. and Strachan D. (1994) Organic analysis at the Hanford nuclear site. *Anal. Chem.* **66**, 1208A-1215A.

Cerrillos C. and Ollis D. F. (1998) Photocatalytic reduction and removal of uranium from a uranium-EDTA solution. *Journal of Advanced Oxidation Technologies* **3**, 167-173.

Chen J., Ollis D. F., Rulkens W. H. and Bruning H. (1999) Photocatalyzed deposition and concentration of soluble uranium (VI) from TiO_2 suspensions. *Colloids and Surfaces A: Physicochemical and Engineering Aspects* **151**, 339-349.

Dash S., Kamruddin M., Bera S., Ajikumar P., Tyagi A., Narasimhan S. and Raj B. (1999) Temperature programmed decomposition of uranyl nitrate hexahydrate. *J. Nucl. Mater.* **264**, 271-282.

Delley B. (1990) An all-electron numerical method for solving the local density functional for polyatomic molecules. *The Journal of Chemical Physics* **92**, 508-517.

Djogic R., Sipos L. and Branica M. (1986) Characterization of uranium (VI) in seawater 1. *Limnology and Oceanography* **31**, 1122-1131.

Elenewski J. E., Cai J. Y., Jiang W. and Chen H. (2016) Functional mode hot electron transfer theory. *The Journal of Physical Chemistry C* **120**, 20579-20587.

Evans C. J., Nicholson G. P., Faith D. A. and Kan M. J. (2004) Photochemical removal of uranium from a phosphate waste solution. *Green Chemistry* **6**, 196-197.

Forouzan F., Richards T. C. and Bard A. J. (1996) Photoinduced reaction at TiO_2 particles. Photodeposition from NiII solutions with oxalate. *J. Phys. Chem.* **100**, 18123-18127.

Froideval A., Del Nero M., Barillon R., Hommet J. and Mignot G. (2003) pH dependence of uranyl retention in a quartz/solution system: an XPS study. *J. Colloid Interface Sci.* **266**, 221-235.

Gadd G. M. (1999) Fungal production of citric and oxalic acid: importance in metal speciation, physiology and biogeochemical processes. *Advances in Microbial Physiology* **41**, 47-92.

Havel J., Soto-Guerrero J. and Lubal P. (2002) Spectrophotometric study of uranyl–oxalate complexation in solution. *Polyhedron* **21**, 1411-1420.

Ilton E. S. and Bagus P. S. (2011) XPS determination of uranium oxidation states. *Surf. Interface Anal.* **43**, 1549-1560.

Ilton E. S., Boily J.-F. and Bagus P. S. (2007) Beam induced reduction of U (VI) during X-ray photoelectron spectroscopy: the utility of the U4f satellite structure for identifying uranium oxidation states in mixed valence uranium oxides. *Surf. Sci.* **601**, 908-916.

Kim D., Duckworth O. W. and Strathmann T. J. (2009) Hydroxamate siderophore-promoted reactions between iron (II) and nitroaromatic groundwater contaminants. *Geochim. Cosmochim. Acta* **73**, 1297-1311.

Kim Y., Seo J., Kang S.-A., Choi S.-G. and Lee Y. J. (2015a) Geochemistry and uranium mineralogy of the black slate in the Okcheon Metamorphic Belt, South Korea. *Geochem. J.* **49**, 443-452.

Kim Y. K., Lee S., Ryu J. and Park H. (2015b) Solar conversion of seawater uranium (VI) using TiO_2 electrodes. *Applied Catalysis B: Environmental* **163**, 584-590.

Kubicki J. D., Halada G. P., Jha P. and Phillips B. L. (2009) Quantum mechanical calculation of aqueuous uranium complexes: carbonate, phosphate, organic and biomolecular species. *Chemistry Central Journal* **3**, 10.

Lucks C., Rossberg A., Tsushima S., Foerstendorf H., Fahmy K. and Bernhard G. (2013) Formic acid interaction with the uranyl (VI) ion: structural and photochemical characterization. *Dalton Trans.* **42**, 13584-13589.

Madden T. H., Datye A. K., Fulton M., Prairie M. R., Majumdar S. A. and Stange B. M. (1997) Oxidation of metal−EDTA complexes by TiO_2 photocatalysis. *Environ. Sci. Technol.* **31**, 3475-3481.

Morris D. E. (2002) Redox energetics and kinetics of uranyl coordination complexes in aqueous solution. *Inorg. Chem.* **41**, 3542-3547.

Noh J. S. and Schwarz J. A. (1989) Estimation of the point of zero charge of simple oxides by mass titration. *J. Colloid Interface Sci.* **130**, 157-164.

Perdew J. P., Burke K. and Ernzerhof M. (1996) Generalized gradient approximation made simple. *Phys. Rev. Lett.* **77**, 3865.

Perron H., Domain C., Roques J., Drot R., Simoni E. and Catalette H. (2006) Periodic density functional theory investigation of the uranyl ion sorption on the TiO2 rutile (110) face. *Inorg. Chem.* **45**, 6568-6570.

Renock D., Mueller M., Yuan K., Ewing R. C. and Becker U. (2013) The energetics and kinetics of uranyl reduction on pyrite, hematite, and magnetite surfaces: A powder microelectrode study. *Geochim. Cosmochim. Acta* **118**, 56-71.

Salomone V. N., Meichtry J. M., Zampieri G. and Litter M. I. (2015) New insights in the heterogeneous photocatalytic removal of U (VI) in aqueous solution in the presence of 2-propanol. *Chem. Eng. J.* **261**, 27-35.

Schneider S., Bister S., Christl M., Hori M., Shozugawa K., Synal H.-A., Steinhauser G. and Walther C. (2017) Radionuclide pollution inside the Fukushima Daiichi Exclusion Zone, Part 2: Forensic search for the "forgotten" contaminants uranium-236 and Plutonium. *Appl. Geochem.* **85**, 194-200.

Sobczyński A., Duczmal Ł. and Dobosz A. (1999) Photocatalysis by illuminated titania: oxidation of hydroquinone and p-benzoquinone. *Monatshefte für Chemie/Chemical Monthly* **130**, 377-384.

Tsushima S., Brendler V. and Fahmy K. (2010) Aqueous coordination chemistry and photochemistry of uranyl (VI) oxalate revisited: a density functional theory study. *Dalton Trans.* **39**, 10953-10958.

Ulrich K.-U., Ilton E. S., Veeramani H., Sharp J. O., Bernier-Latmani R., Schofield E. J., Bargar J. R. and Giammar D. E. (2009) Comparative dissolution kinetics of biogenic and chemogenic uraninite under oxidizing conditions in the presence of carbonate. *Geochim. Cosmochim. Acta* **73**, 6065-6083.

Vallet V., Moll H., Wahlgren U., Szabó Z. and Grenthe I. (2003) Structure and bonding in solution of dioxouranium (VI) oxalate complexes: Isomers and intramolecular ligand exchange. *Inorg. Chem.* **42**, 1982-1993.

Xu Y. and Schoonen M. A. (2000) The absolute energy positions of conduction and valence bands of selected semiconducting minerals. *Am. Mineral.* **85**, 543-556.

Yang J.-K. and Davis A. P. (2000) Photocatalytic oxidation of Cu (II)− EDTA with illuminated TiO_2: Kinetics. *Environ. Sci. Technol.* **34**, 3789-3795.

Yuan K., Ilton E. S., Antonio M. R., Li Z., Cook P. J. and Becker U. (2015a) Electrochemical and spectroscopic evidence on the one-electron reduction of U (VI) to U (V) on magnetite. *Environ. Sci. Technol.* **49**, 6206-6213.

Yuan K., Renock D., Ewing R. C. and Becker U. (2015b) Uranium reduction on magnetite: Probing for pentavalent uranium using electrochemical methods. *Geochim. Cosmochim. Acta* **156**, 194-206.

Chapter IV. An ab-initio study of the energetics and geometry of sulfide, sulfite and sulfate incorporation into apatite: The thermodynamic basis for using this system as an oxybarometer

Abstract

Despite many studies reporting the presence of S-bearing apatite in igneous and hydrothermal systems, the oxidation states and incorporation mechanisms of S in the apatite structure remain poorly understood. In this study, we use ab-initio calculations to investigate the energetics and geometry of incorporation of S with its oxidation states S^{6+}, S^{4+}, and S^{2-} into the apatite end-members fluor-, chlor-, and hydroxyl-apatite, $[Ca_{10}(PO_4)_6(F,Cl,OH)_2]$. The relative stability of different oxidation states of S in apatite is evaluated by using balanced reaction equations, where the apatite host and a solid S-bearing source phase (e.g., gypsum for S^{6+} and troilite for S^{2-}) are the reactants, and the S-incorporated apatite and an anion sink phase are the products. For the incorporation of S into apatite, coupled substitutions are necessary to compensate for charge imbalance. One possible coupled substitution mechanism involves the replacement of $La^{3+} + PO_4^{3+}$ $\leftrightarrow$ $Ca^{2+} + SO_4^{2-}$. The incorporation of SO_4^{2-} into La- and Na-bearing apatite, $Ca_8NaLa(PO_4)_6(F,Cl,OH)_2$, is energetically favored over the incorporation into La- and Si-bearing apatite, $Ca_9La(PO_4)_5(SiO_4)(F,Cl,OH)_2$ (the difference in incorporation energy (ΔE_{rxn}) is 10.7 kJ/mol). This thermodynamic gain is partially attributed to the electrostatic contribution of Na^+,

and the energetic contribution of La^{+} to the stability of SO_4^{2-} incorporated into the apatite structure. Co-incorporation of SO_4^{2-} and SO_3^{2-} (i.e., replacement of $S^{4+} + S^{6+} \leftrightarrow 2P^{5+}$) is more energetically favored when the lone pair electrons of SO_3^{2-} face towards the anion column site, versus facing away from it.

Full or partial incorporation of S^{2-} is most favorable on the column anion site in the form of $[Ca_{10}(PO_4)_6S]$ and $[Ca_{20}(PO_4)_{12}SX_2)]$, where X = F, Cl, or OH. Sulfide (S^{2-}) completely substitutes for the column ions and is positioned in the anion column at z = 0.5 (half-way between two F sites at z = 1/4 and z = 3/4) in the geometrically optimized structure. The calculated energies for partial incorporation of S^{2-} demonstrate that at an energy minima (i.e., geometrically optimized), S^{2-} is displaced by 1.0-1.75 Å away from the F^{-} position at z = 1/4 or 3/4, and that the probability for S^{2-} to be incorporated into the apatite structure is highest for chlorapatite end-members.

Our results describe energetically feasible incorporation mechanisms for all three oxidations states of S (S^{6+}, S^{4+}, S^{2-}) into apatite, along with structural distortion and concurring electronic structure changes. These observations are consistent with recently published experimental results that demonstrate S^{6+}, S^{4+} and S^{2-} incorporation into apatite, where the ratio of $S^{6+}/\sum S$ in apatite is controlled by oxygen fugacity. The new computational and experimental data provide the basis for using S in apatite as a geochemical proxy to trace variations in the oxidation state in magmatic and magmatic-hydrothermal systems.

1. INTRODUCTION

The apatite group minerals with the general chemical formula [$Ca_{10}(PO_4)_6(F,Cl,OH)_2$] are the most abundant phosphate minerals on Earth (Rakovan and Waychunas, 2013; Harlov, 2015). The diverse chemistry of apatite is related to its flexible structure that can accommodate a large number of cations and anions (Hughes and Rakovan, 2002). The Ca cation sites can be replaced by alkali and transition metals (e.g., Na, K, Mn, Ni, Cu) and rare earth elements (e.g., La, Ce), whereas the major oxyanions such as SiO_4^{4-}, SO_4^{2-}, CO_3^{2-} can occupy the phosphate (PO_4^{3-}) site (Hughes and Rakovan, 2002).

Despite several studies demonstrating the evolution and variation of S recorded in apatite phases from igneous systems (Peng et al., 1997; Streck and Dilles, 1998; Imai, 2002; Parat et al., 2002; Parat and Holtz, 2004; Parat and Holtz, 2005), little is known about the structure and thermodynamic stability of S in apatite. A recent study by Konecke et al. (2017) is the first to confirm qualitatively that variable abundances of S^{6+}, S^{4+}, and S^{2-} are incorporated into apatite that is crystallized from a mafic silicate melt under varying oxygen fugacity (fO_2) conditions. The new experimental data on S redox chemistry in apatite highlight the need for theoretical understanding of the structural incorporation of different S species in apatite.

In this study, the thermodynamics and geometry of S incorporation in the apatite structure were investigated computationally. While common trace element impurities (e.g., Na, Si, rare earth elements, REEs) in natural apatite are taken into account (Hughes et al., 1991), we focus on evaluating some of the most likely scenarios that are in line with experimental observations (e.g., $2P^{5+} \Leftrightarrow S^{6+} + S^{4+}$ and $2(F^-, Cl^-, OH^-) \Leftrightarrow S^{2-}$ + vacancy; Konecke et al., 2017). In order to remain computationally consistent across a chemical equation, all phases considered are solids and are quantum-mechanically modeled at ambient pressure (P) and temperature (T) conditions since

elevated P and T are beyond current possibilities for the applied approach. The relative stability of S with different oxidation states (S^{6+}, S^{4+}, and S^{2-}) in apatite is calculated with reference to common solid source phases for S (e.g., gypsum for SO_4^{2-} and troilite for S^{2-}) and sink phases that accommodate the replaced anions from apatite (e.g., monazite for PO_4^{3-}). This computational approach permits the determination of: [1] the energetic favorability of S incorporation into apatite depending on the occupancy of the column anion or cation impurities favorable for coupled substitution and [2] the electronic structure and structural distortion of the incorporation site upon S incorporation. Based on the results of this study, the potential role of S-in-apatite as a proxy to trace redox in magmatic systems is discussed.

1.1. Previous work

Historically, sulfate (S^{6+}) has been suggested as the only oxidation state of S in the apatite structure (cf. Parat et al., 2011) based on the observation that S-rich (terrestrial) apatite, containing up to 0.8 wt.% S, has been observed in oxidizing (anhydrite-bearing) environments, where sulfate (S^{6+}) and sulfite (S^{4+}) are the dominant (or only) S oxidation states in the melt and fluid, respectively (e.g., Rouse and Dunn, 1982; Liu and Comodi, 1993; Tepper and Kuehner, 1999). Direct evidence for the presence of sulfate in the apatite structure was reported by Paris et al. (2001) who used synchrotron-radiation S *K*-edge micro X-ray absorption near-edge structure (μ−XANES) spectroscopy to document the presence of sulfate in Durango apatite (Lyons, 1988) from the Cerro de Mercado iron oxide-apatite deposits near Durango, Mexico. Their results supported the hypothesis that S is incorporated as S^{6+} into the apatite structure. There are, however, apatite data from reduced systems, where sulfur is present mostly as sulfide (S^{2-}) in the melt (Jugo et al., 2005), which suggest that apatite growing from the melt may incorporate S^{2-}. For instance,

S concentrations in apatite from reduced lunar mare basalts (i.e., the iron-wüstite fO_2 buffer; Sato et al., 1973) exceed 400 μg/g S (Greenwood et al., 2011; Boyce et al., 2014).

Recently, Konecke et al. (2017) provided qualitative evidence for the presence of S^{6+}, S^{4+}, and S^{2-} in apatite. Apatite crystals were grown from a hydrous S-bearing mafic melt at 1,000°C, 300 MPa, and over a broad range of oxygen fugacities ($(\log(fO_2)$ = FMQ to FMQ+3; FMQ = fayalite-magnetite-quartz solid buffer). Those authors used S μ−XANES to document the presence of distinct sulfate S^{6+} (~2482 eV), sulfite S^{4+} (~2478 eV) and sulfide S^{2-} (~2470 eV) in the apatite structure (Fig. 4.1). Specifically, apatite is dominated by S^{6+} with a small contribution of S^{4+} under oxidizing conditions (FMQ+1.2 and +3), whereas S^{2-} is the dominant S oxidation state at more reducing conditions (FMQ). Their results demonstrate that, once calibrated, the S oxidation state in apatite can be a sensitive indicator of variations in oxygen fugacity at redox conditions relevant to arc and MORB settings (e.g., Behrens and Gaillard, 2006). However, the mechanisms and bonding environments of each S oxidation state in apatite remain unknown, and are imperative to the development of a quantitative S-in-apatite oxybarometer.

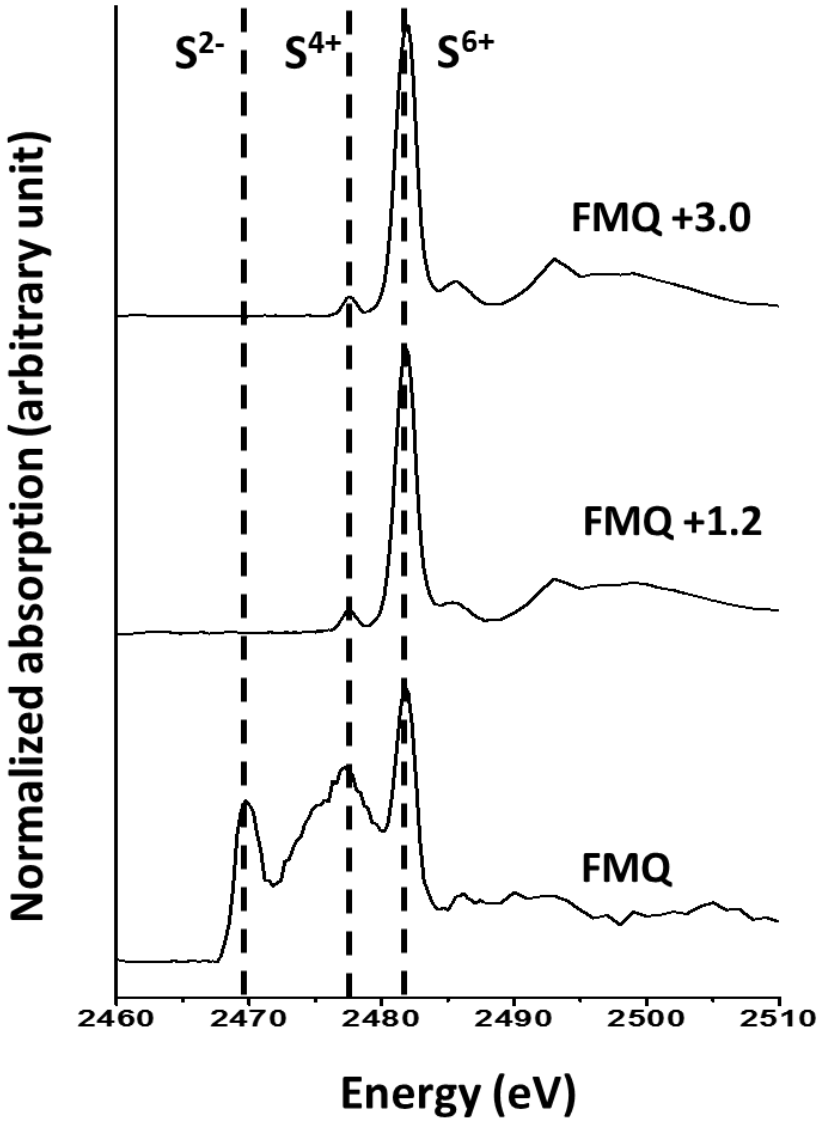

Fig. 4. 1. S XANES analysis of apatite crystallized from a mafic melt at 1,000 ºC, 300 MPa and different fO_2 conditions (modified from Figure 2 in Konecke et al. (2017)).

2. Methods

2.1. Computational parameters

The computational approach adopted in this study is based on density functional theory (DFT) with planewaves representing functions for the overall wave function of upper valence and conduction band electrons (basis functions), while inner valence and core electrons of an atom and their interactions with the valence electrons are approximated by pseudopotentials. The optimization was performed using the quantum-mechanical code CASTEP (Segall et al., 2002). The Perdew-Wang generalized gradient scheme (GGA) was used along with ultrasoft pseudopotentials. The GGA scheme was parameterized by the Perdew–Burke–Ernzerhof functional (Perdew et al., 1996). The energy cutoff for planewave expansion was 400.0 eV and the Brillouin zone was sampled using a k-point separation of 0.05 $Å^{-1}$ according to the Monkhorst-Pack scheme (Monkhorst and Pack, 1976). Self-consistent field cycles were assumed to converge with an energy difference of less than 2.0 $x10^{-6}$ eV/atom. A spin-polarized approach was implemented when the unit cell of a mineral includes atoms with unpaired spins. For example, ferrous iron, (Fe^{2+}) has four 3d unpaired spins in its high-spin state. The electronic contribution of localized unpaired d states to materials properties may be incompletely described using standard DFT approaches. For such cases, a Hubbard U correction was implemented to account for the on-site Coulomb interaction (represented by the parameter, U) and the exchange interaction (J). For this approach, the effective Hubbard U parameter, U_{eff} (= U-J) values, was adopted from previous works studying the Fe 3d states in various silicates (U_{eff} = 2.9 and 4.8; Stackhouse et al., 2010; Hsu et al., 2011) and sulfides (U_{eff} = 2.0; Rohrbach et al., 2003).

2.2. Incorporation energy calculation

The reaction equation of S-incorporation consists of a pure (i.e., end-member) and impure (i.e., trace elements-bearing) apatite in the form of host apatite ($apatite_{host}$) and S-incorporated apatite ($apatite_{S\text{-}incorporated}$), respectively. Accordingly, appropriate solid sources for S ($source_i$) and sinks for ions replaced in the mineral host ($sink_i$) were selected to maintain stoichiometry. A host apatite phase and sources for S in different oxidation states are reactants while S-incorporated apatite and sinks for anions being released from the apatite host are products. The general equation for this approach takes the form:

$$apatite_{host} + \sum_{i=1}^{n} a_i \, source_i \leftrightarrow apatite_{S-incorporated} + \sum_{i=1}^{m} b_i \, sink_i \quad (1).$$

The incorporation reactions are balanced to involve one atom of S on both sides of the equation such that the calculated reaction energy (E_{rxn}) is defined as the energy required to incorporate one mole of S in an apatite host phase (unless otherwise stated). In addition, this setup allows for a consistent quantum-mechanical treatment; i.e., using the same computational parameters throughout the equation, which is crucial to obtain reliable energetic data.

The process of element incorporation into a mineral involves providing an ion from a medium such as a solid source, liquid, or gas phase and releasing another ion from the host phase into that medium. Therefore, the role of a medium, where an incorporation reaction occurs, can be important for computationally simulating incorporation energies into the mineral phase in geological systems. Examples for incorporation using solid sources and sinks can be found in Shuller et al. (2013) and Shuller-Nickles et al. (2014). The atomistic assessment for hydrated ions incorporated into host minerals is rather complicated and computationally difficult, as it involves a series of reaction equations that have to be combined to handle species of different characters (hydrated vs. vacuum, charged vs. neutral, clusters vs. 3D periodic) that can typically not be combined and

computationally treated in one equation using a consistent approach (see, e.g., Walker and Becker, 2015; Smith et al., 2016). Additionally, it is more challenging to take into account the role of magmatic melts or fluids under high pressure and temperature for a quantum-mechanical computational assessment of the incorporation process. Modeling magmatic-hydrothermal systems would require a quantum-mechanical molecular-dynamics model using large unit cells at high P-T conditions that approach or exceed the limits of current computational capability and is beyond the scope of this study. Therefore, all source and sink phases are periodic solids and commonly play a role in accommodating atoms that will be incorporated into and/or liberated from apatite. In order to increase the geological significance of our evaluation, minerals or ionic compounds that occur and are stable in magmatic or hydrothermal environments are selected as sources and sinks for the reaction equations. Once energies of all phases involved in the incorporation equations are computationally attained, reaction energies for each incorporation equation can be calculated using the general approach:

$$\Delta E_{rxn} = \sum E_{prod} - \sum E_{reac} \quad (2)$$

The resulting incorporation reaction energy indicates the stability of the S-incorporated apatite relative to the corresponding host apatite, and the source and sink phases. In addition, the relative stability of various incorporated apatite phases can be compared when common source phases are used. The incorporation energies calculated using CASTEP are well described by Shuller et al. (2013). Energies calculated using CASTEP include contributions from electronic properties such as electronic relaxations and spin-spin interactions. The ΔE_{rxn} evaluated from the CASTEP energies of the reactants and products are in good agreement with enthalpies, for the reason that they are calculated at ambient pressure (VdP = 0). To evaluate ΔG_{rxn}, entropy contributions (e.g.,

vibrational entropies of the solid phases used in our study) must be considered. However, this requires significant computational efforts and is not covered within the scope of this study.

2.3. The structure model of apatite

The initial models for the apatite end-members are adopted from the natural apatite structure, $[Ca_{10}(PO_4)_6(F, OH, Cl)_2]$ ($P6_3/m$; seeHughes et al., 1990; Hughes and Rakovan, 2015), and are depicted in Fig. 4.2 and 4.3. The column anion site [00z] of the apatite structure ($P6_3/m$) is mainly occupied by F^-, OH^-, and Cl^-. Natural apatite end-members are subdivided into fluorapatite $[Ca_5(PO_4)_3F]$, chlorapatite $[Ca_5(PO_4)_3Cl]$, and hydroxylapatite $[Ca_5(PO_4)_3(OH)]$ based on a single occupant of the anion column, but often occur as a solid solution with binary or ternary anion columns (Hughes et al., 1990; Hughes and Rakovan, 2002; Hughes et al., 2016). The column anion site has the potential to accommodate other anions with different radius and/or charge. A well-known example is carbonate (CO_3^{2-}) incorporation into hydroxylapatite, which occurs in both the phosphate and column anion sites (Fleet and Liu, 2007).

There are the two types of Ca sites in the apatite structure, Ca1 and Ca2. The Ca1 type is coordinated to nine O atoms while the Ca2 site is coordinated to six O atoms and one column anion. In the $P6_3/m$ space group, Ca2 atoms form triangles on the planes at z = 1/4 and 3/4. Each of the three Ca atoms at the triangle corners is bonded to the central anion in the [00z] column (Hughes et al., 1990). Fluorine, the smallest of the column anions, lies on the mirror planes at z = 1/4 and 3/4 such that it is located at the center of the Ca triangle (Fig. 4.2a). The OH^- and Cl^- are too large to be positioned in the center of the Ca triangle and are thus displaced above or below the planes. As a result of such displacement, OH^- and Cl^- have multiple possible positions along the anion column in the apatite unit cell. Since all atoms in the apatite structure are given full

atomic occupancy in this study, two positions of Cl^- or OH^- below the planes at z = 1/4 and 3/4 were selected to complete the unit cell formula, $[Ca_{10}(PO_4)_6(F, Cl, OH)_2]$. Using the structural and computational parameters above, a good agreement in the unit cell parameter values was found between calculated and natural end-member apatites (Table 4. 1). The resulting structures are then used to geometrically optimize the host and S-substituted apatite models.

Table 4. 1. Lattice parameters for natural and calculated (CASTEP) apatite.

	a (Å)	*c* (Å)	z value[b] of (F, Cl, OH)
Fluorapatite			
Calculated	9.469	6.894	0.2500
Natural[a]	9.397	6.878	0.2500
Deviation (%)	0.76	0.22	
Chlorapatite			
Calculated	9.525	6.895	0.4379
Natural[a]	9.598	6.776	0.4323
Deviation (%)	0.76	1.76	
Hydroxylapatite			
Calculated	9.763	6.757	0.2128
Natural[a]	9.417	6.875	0.1979
Deviation (%)	3.68	1.71	

Notes: [a] Hughes and Rakovan (2002) [b] The z value of anion column position (0, 0, z).

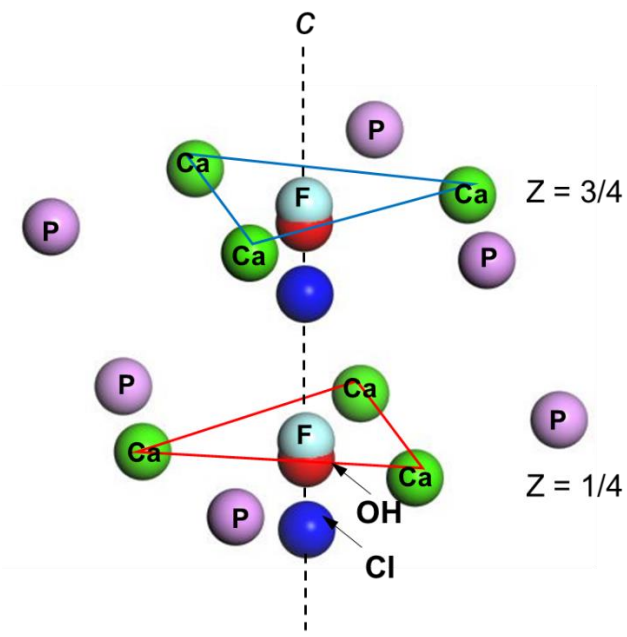

(A)

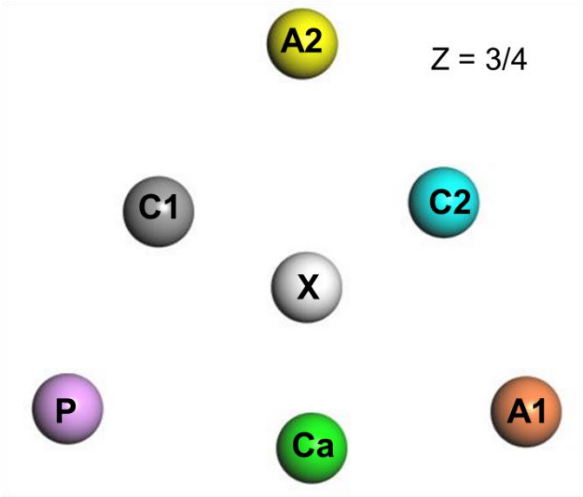

(B)

Fig. 4. 2. (A) The anion column anion site and the nearest Ca (Ca2) and P atoms in the hexagonal apatite structure viewed parallel to the c-axis. (B) The coordination environment of X (= F, OH, Cl) on the plane of z = 3/4 in the host or S^{6+}-incorporated apatite where A1 = P or Si, A2 = P or S, C1 = Ca or Na and C2 = Ca or La. Atoms Ca, C1 and C2 form triangles, where the corners are Ca2 sites. In both (A) and (B), oxygen atoms are omitted.

2.4. Sulfur replacement mechanisms in S-bearing apatite

An important step in the incorporation energy calculations is to identify replacement mechanisms that may play a critical role in hosting S in natural apatite. All mechanisms tested in this study are based on previous reports of natural and experimentally produced apatite.

2.4.1. Sulfate mechanisms

It has been suggested that the P site is the most likely location where substitution of SO_4^{2-} occurs in the apatite structure (Streck and Dilles, 1998; Pan and Fleet, 2002; Parat et al., 2011), where possible replacement mechanisms include:

$$P^{5+} + Ca^{2+} \leftrightarrow S^{6+} + Na^{+} \quad (3)$$

$$2P^{5+} \leftrightarrow S^{6+} + Si^{4+} \quad (4)$$

In the current study, all calculations for SO_4^{2-} substitution are based on replacement mechanisms (3) and (4). We used geologically relevant solid source and sink phases for the calculations. For instance, anhydrite ($CaSO_4$) commonly coexists with S-rich apatite in oxidized magmatic systems (Baker and Rutherford, 1996b; Streck and Dilles, 1998) and, thus, is a geologically relevant candidate as a source phase for SO_4^{2-}.

Moreover, in oxidized magma, Na^+ (replacing Ca^{2+}) and SiO_4^{4-} (replacing PO_4^{3-}) can be concomitant ions for S^{6+} incorporation in apatite to maintain charge neutrality (Eq. 3 and 4). In addition, rare earth elements (REE^{3+}) can substitute for Ca^{2+} in the apatite structure via the coupled substitutions $REE^{3+} + Si^{4+} \leftrightarrow Ca^{2+} + P^{5+}$ and $REE^{3+} + Na^{+} \leftrightarrow 2Ca^{2+}$ (Hughes et al., 1991; Pan and Fleet, 2002). Hughes et al. (1991) reported a total REE^{3+} concentration range of 2 to 16 wt% in REE-bearing apatite samples and a good linear correlation between $[Na^+ + Si^{4+}]$ vs. $[\sum REE^{3+}]$ (~1:1 atomic ratio), which can be well explained by the coupled substitutions reactions above.

Streck and Dilles (1998) reported variations in the S content in apatite, reaching up to 0.56 wt% S in apatite from the Yerington batholith (Nevada), and a strong correlation between [Si^{4+}+Na^{+}-$\sum REE^{3+}$] vs [S^{6+}] (~1:1 atomic ratio), which supports the coupled substitution of Si^{4+} and Na^{+} with S^{6+} and/or REE^{3+}. Based on these considerations, La-bearing apatite is selected as the host apatite phase, which incorporates SO_4^{2-} in the structure. Two distinct cases involving La-bearing apatite, $[Ca_8NaLa][(PO_4)_6]X_2$ and $[Ca_9La][(PO_4)_5(SiO_4)]X_2$, are evaluated individually, and the effects of Na^{+} and Si^{4+} on incorporating SO_4^{2-} into apatite are discussed in detail. La-monazite ($LaPO_4$), which commonly occurs as a P-bearing accessory mineral in igneous rocks (Foerster, 1998), is selected as a mineral sink phase for PO_4^{3-} being replaced by SO_4^{2-} in order to account the formation of La-bearing apatite.

In models of $apatite_{host}$ (S-free) and $apatite_{S\text{-}incorporated}$, Na^{+} and La^{3+} are positioned on the Ca2 atomic sites at the mirror plane at z = 3/4 and one of the three PO_4^{3-} sites nearest to the column anion is replaced by SiO_4^{4-} or SO_4^{2-} (Fig. 4.2b).

2.4.2. Sulfate-sulfite mechanisms

A recent study identified the co-existence of S^{4+} and S^{6+} in natural and experimentally produced apatite and suggested a possible coupled substitution mechanism involving the replacement of two phosphate atoms by SO_4^{2-} and SO_3^{2-} via the coupled substitution (Konecke et al. 2017):

$$2P^{5+} \leftrightarrow S^{6+} + S^{4+} \quad (5)$$

Based on this observation, a possible mechanism of co-incorporation of S^{4+} and S^{6+} into fluor-, chlor-, and hydroxylapatite is examined by balancing an incorporation reaction equation in combination with the nickel-nickel oxide (ΔNNO) oxygen fugacity buffer. A Na- and Si-bearing apatite, $[Ca_7La_2Na][(PO_4)_5(SiO_4)](F, Cl, OH)_2$, is selected as the host phase. Anhydrite and La-

monazite are used as source and sink phases, respectively. In models of *apatite*$_{S\text{-}incorporated}$, one of the three nearest phosphate sites at the mirror plane at z = 1/4 and 3/4 to the anion column is replaced by SO_3^{2-} and SO_4^{2-}, respectively (Fig. 2 and 3a).

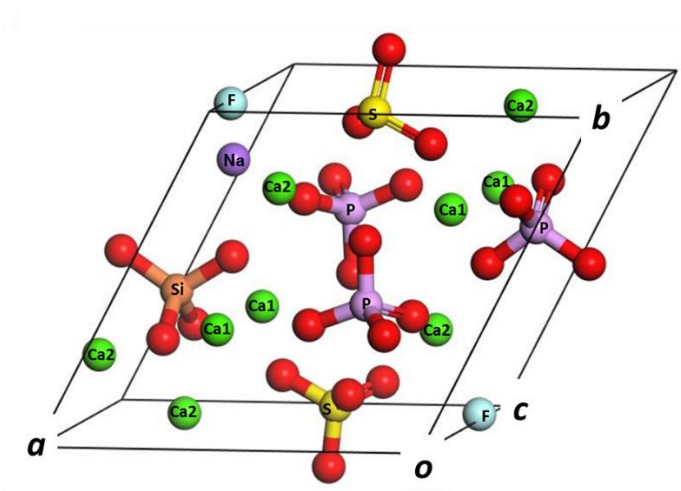

(A)

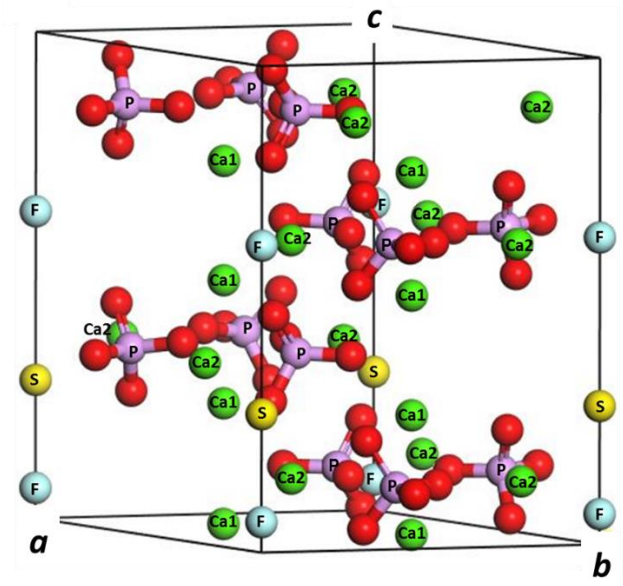

(B)

Fig. 4. 3. Examples of S-incorporated apatite models. (A) The unit cell of SO_4^{2-}- and SO_3^{2-}-incorporated fluorapatite, $Ca_9Na(PO_4)_3(SiO_4)(SO_4)(SO_3)F_2$ and (B) the 1×1×2 supercell of S^{2-}-incorporated apatite, $Ca_{20}(PO_4)_{12}SF_2$.

2.4.3. Sulfide mechanisms

Henning et al. (2000) used single crystal X-ray diffraction to determine the structure of experimentally produced S^{2-}-bearing apatite in the form $Ca_{10}(PO_4)_6S$, and report that S occupies the anion column consistent with the following coupled substitution (Eq. 6).

$$2(F, Cl, OH)^- \leftrightarrow S^{2-} + \text{vacancy} \quad (6)$$

Hence, a testable scenario for the incorporation of S^{2-} into the anion column in apatite involves FeS (troilite) and Na_2S as solid S^{2-} sources and is based on the affinity of Fe^{2+} and Na^+ for S^{2-} in geological processes (Burns and Fyfe, 1966; Fiege et al., 2015). When F^- and Cl^- in apatite are replaced by S^{2-} from these sources, metal fluorides and chlorides are produced as a solid sink. To consider OH^- released from apatite, the metamorphic amphibole grunerite, $[Fe_7Si_8O_{22}(OH)_2]$, is selected as a sink phase and ferrosilite ($FeSiO_3$) and quartz (SiO_2) are added as reactants to balance the composition of grunerite. Grunerite, as a key amphibole end-member, possesses a broad stability field in the simple system of FeO-SiO_2-H_2O (Lattard and Evans, 1992). Thermodynamic equilibria between grunerite and other Fe-silicates, such as ferrosilite and fayalite, have been adopted as a tool to estimate temperature, pressure, and H_2O activity in metamorphic, hydrothermal, and volcanic systems (e.g., Lattard and Evans, 1992; Elliott, 2001). This makes it a suitable phase to investigate magmatic and magmatic-hydrothermal scenarios.

When building initial models (i.e., ones subjected to geometry optimization), S^{2-} replaces two F^-, Cl^-, or OH^- anions in fluor-, chlor- or hydroxylapatite (Eq. 6). Once placed in the column, S^{2-} can be re-positioned to any unoccupied position of the column during the course of the geometry optimization. The optimization algorithm finds local minima in the energy landscape adjusting the lattice parameters and the coordinates of each atom in the initial model. Therefore, it is important to ensure an energetic or geometric variation in the optimization result as the initial

position of S^{2-} varies in the anion column. The position of F^-, Cl^- and OH^- in the apatite anion column (i.e., (0 0 z) calculated from the end-member apatite; see Table 4. 1) is selected as the position of S^{2-} in the initial models. Where necessary, S^{2-} is referred to as $S(F, Cl, OH)_{ini}$, when a position near the anion column is chosen as the initial S^{2-} position replacing F^-, Cl^-, or OH^- anions. For this type of replacement, full incorporation of S^{2-} in apatite is considered in the form of $Ca_{10}(PO_4)_6S$. Moreover, we considered the partial incorporation of S^{2-} in the 1×1×2 supercell of apatite in the form of $Ca_{20}(PO_4)_{12}S(F, OH \text{ or } Cl)_2$ (Fig. 4.3b). Notably, in the supercell, a S^{2-} atom is located between two of column anions such that the optimized positions of the column anions are the result of S^{2-} interacting with surrounding F^-, Cl^-, or OH^- anions. The calculated reaction energy defines the energy required for the incorporation of one S^{2-} ion in the 1×1×2 supercell of apatite.

2.5. Computational scopes and errors

In a computational study like this, the sources of errors have more of a systematic character and less of a random one as they occur in experimental studies. One source of variability is the computational parameters, such as density functionals, pseudopotentials, as well a quantity and types of basis functions. Testing all parameters for the examples used in this study would increase the computational effort by at least an order of magnitude. Therefore, testing can be done only with a limited number of examples and computational parameters. We found a significant cancellation of error within one thermodynamic reaction equation, which is expected, as all computational parameters have to be consistent within such an equation.

More important than such parameter testing is a good understanding of the limitations of the model setup. This includes the structural model setup with a limited-sized unit cell, which

increases the relative concentration of the incorporated species, as well as the decision to use selected solid source and sink phases. All of these decisions have been made to model geologically relevant scenarios in reasonable computation times. Our approach is suitable to learn about the thermodynamic stability with respect to references, and the atomic and electronic structure of mineral phases. The thermodynamic energies of incorporation are relative quantities that would change by choosing different sink/source phases or transitioning to dynamic hydrothermal fluids, whereas the results for the electronic/atomic structure of incorporation would remain unaffected.

3. RESULTS

3.1. Incorporation energy and geometry: Sulfate (SO_4^{2-})

The reaction equations and energies for S^{6+} incorporation into La-apatite phases are presented in Table 4. 2. In the equations, charge imbalance of La^{3+} in place of Ca^{2+} is compensated by coupled substitution with Na^{+} or Si^{4+} in the apatite structure. Incorporation energies calculated from the Na-bearing apatite phases are lower than those of the Si-bearing phases for all tested scenarios. In the Na-bearing system, the lowest incorporation energy is found in fluorapatite, followed by chlorapatite and hydroxylapatite. Energy differences between those are relatively small (3 to 6 kJ/mol). In the Si-bearing apatite, the incorporation of S^{6+} into chlorapatite is energetically more favored than the incorporation into fluorapatite and hydroxylapatite (by 10.4 kJ/mol).

Table 4. 2. Reaction equations and energies of incorporation of S^{6+} and co-incorporation of S^{4+} with S^{6+} into apatite.

Incorporation reaction	ΔE_{rxn} (kJ/mol)		
S^{6+}-incorporation into La-bearing apatite	X = F	Cl	OH
Na-bearing: $[Ca_8NaLa][(PO_4)_6]X_2 + CaSO_4 \leftrightarrow [Ca_9Na][(PO_4)_5(SO_4)]X_2 + LaPO_4$	-1.74	1.16	4.34
Si-bearing: $[Ca_9La][(PO_4)_5(SiO_4)]X_2 + CaSO_4 \leftrightarrow [Ca_{10}][(PO_4)_4(SiO_4)(SO_4)]X_2 + LaPO_4$	15.44	5.02	15.44
S^{4+}, S^{6+}-incorporation into La-bearing apatite	X = F	Cl	OH
$[Ca_7La_2Na][(PO_4)_5(SiO_4)](F, Cl, OH)_2 + 2CaSO_4 + Ni \leftrightarrow [Ca_9Na][(PO_4)_3(SiO_4)(SO_4)(SO_3)](F, Cl, OH)_2 + 2LaPO_4 + NiO$			
A-type S^{4+}	117.71	95.52	117.71
B-type S^{4+}	132.19	111.92	131.22

The unit cell volume is changed as a function of cell parameters and, thus, can be indicative of the net effect of replacing phosphate by SO_4^{2-} in the optimized structure. The cell volumes of S-incorporated apatite phases are presented in Table 4. 3. Exchange of $P^{5+} + Ca^{2+} \leftrightarrow S^{6+} + Na^{+}$ and of $2P^{5+} \leftrightarrow S^{6+} + S^{4+}$ in the unit cell of fluor-, chlor-, and hydroxylapatite leads to a volume expansion by 3 to 5 and 6 to 8 $\mathring{A}^3$, respectively. The ionic radius of 4-coordinated S^{6+} (0.12 Å) is smaller than that of P^{5+} (0.17 Å; Shannon, 1976). Thus, the volume expansion by the coupled exchanges should be mainly due to the larger ionic size of Na^{+} compared to Ca^{2+}, and Si^{4+} compared to P^{5+}. Cations occupying the Ca2 site are 7-coordinated, and the size of 7-coordinated Na^{+} and Ca^{2+} are approximately 1.12 and 1.06 Å, respectively. The 4-coordinated Si^{4+} is 0.26 Å and thus its occupancy in place of P^{5+} would lead to a volume expansion of the unit cell. Although, accounting for less than 1.4 % of the unit cell volume, such a variation in the unit cell volume shows a monotonic increase with increasing column anion size ($Cl^{-} > OH^{-} > F^{-}$) in the S^{6+} incorporated Si-bearing apatite series.

Table 4. 3. Summary of geometric parameters for SO_4^{2-}-incorporated apatite phases.

Optimized structure	Cell volume (Å^3)	X-S distance [a] (Å)	O-S-O angle [a] (degree)
Fluorapatite			
S, Na-bearing	538.9	3.68	107.9
S, Si-bearing	541.1	3.55	107.6
End-member	535.3	3.64	107.2
Chorapatite			
S, Na-bearing	563.7	4.02	108.3
S, Si-bearing	568.4	3.92	108.2
End-member	560.6	3.97	107.7
Hydroxylapatite			
S, Na-bearing	545.9	3.73	108.2
S, Si-bearing	547.6	3.61	108.4
End-member	541.8	3.67	107.6

Notes: [a] For the apatite end-members, (F^-, Cl^-, or OH^-)-S distance and O-S-O angle is measured for P in place of S.

In the optimized S^{6+} incorporated Na- and Si-bearing apatite phases, bond lengths and angles measured from incorporated SO_4^{2-} molecules are similar to reported values for the SO_4^{2-} molecule (109.5°and 1.49 Å) with a maximum deviation of 2.7° and 0.02 Å. The nearest PO_4^{3-} and SO_4^{2-} to the column site have two O atoms displaced above and below the planes at z = 1/4 and 3/4 while the other two O atoms are placed on the planes (Fig. 4.4a). The former two O atoms face toward S on the (0 0 z) column anion such that their positions may be more susceptible to the property of the column ion than the latter two. The angle formed between the S center and the column-oriented O atoms (O-S-O) are presented in Fig. 4.4a and Table 4. 3. In the S^{6+} incorporated Na-bearing apatite series, the O-S-O angle tends to increase with increasing column anion size from 107.9° to

108.4 ° whereas the O-P-O angle in fluorapatite changes from 107.2 ° (X = F) to 107.7 ° in chlorapatite (Table 4.3).

3.2. Incorporation energy and geometry: Sulfate (SO_4^{2-}) and sulfite (SO_3^{2-})

The reaction equations and energies for co-incorporation of sulfite (S^{4+}) with sulfate (S^{6+}) into La-bearing fluor-, chlor-, and hydroxylapatite are presented in Table 4.2. In the reaction, La-monazite ($LaPO_4$) is used as a sink phase to accommodate phosphate released from the host apatite. Solid nickel ($Ni_{(s)}$) is introduced to play a role as an oxygen buffer to take up one O atom of the sulfate SO_4^{2-} molecule forming a sulfite SO_3^{2-} molecule (reduction of S^{6+} to S^{4+}). The molecular geometry of SO_3^{2-} is a trigonal pyramid with a lone pair of electrons at one corner. As mentioned above, two of the four PO_4^{3-} (or SO_4^{2-}) O atoms are displaced from the planes at z = 1/4 and face toward the (0 0 z) anion column. The other two are placed on the plane and face away from the column (Fig. 4.4a). In building a model for SO_3^{2-} replacing PO_4^{3-}, one of either the former two or the latter two O atoms is replaced by a lone pair of electrons (Fig. 4.4b and c). In Fig. 4.4 and Table 4. 2, the two cases are labeled A-type and B-type SO_3^{2-}, respectively.

The incorporation energy is the lowest in chlorapatite compared to fluorapatite and hydroxylapatite, and the energy difference between the former and the latter two are 19 kJ/(1 mol SO_3^{2-} + 1 mol SO_4^{2-}) and 22 kJ/(1 mol SO_3^{2-} + 1 mol SO_4^{2-}), respectively (Table 4. 2). The orientation of the SO_3^{2-} loan pair influences the stability of the incorporated apatite. Lower incorporation energy is found for A-type SO_3^{2-}-incorporated apatite when compared to B-type SO_3^{2-}-incorporated apatite (the energy difference is 14 to 16 kJ/(1 mol SO_3^{2-} + 1 mol SO_4^{2-}) for each apatite end-member). Thus, the co-incorporation mechanism of sulfate and A-type sulfite is energetically more likely than the mechanism involving B-type sulfite.

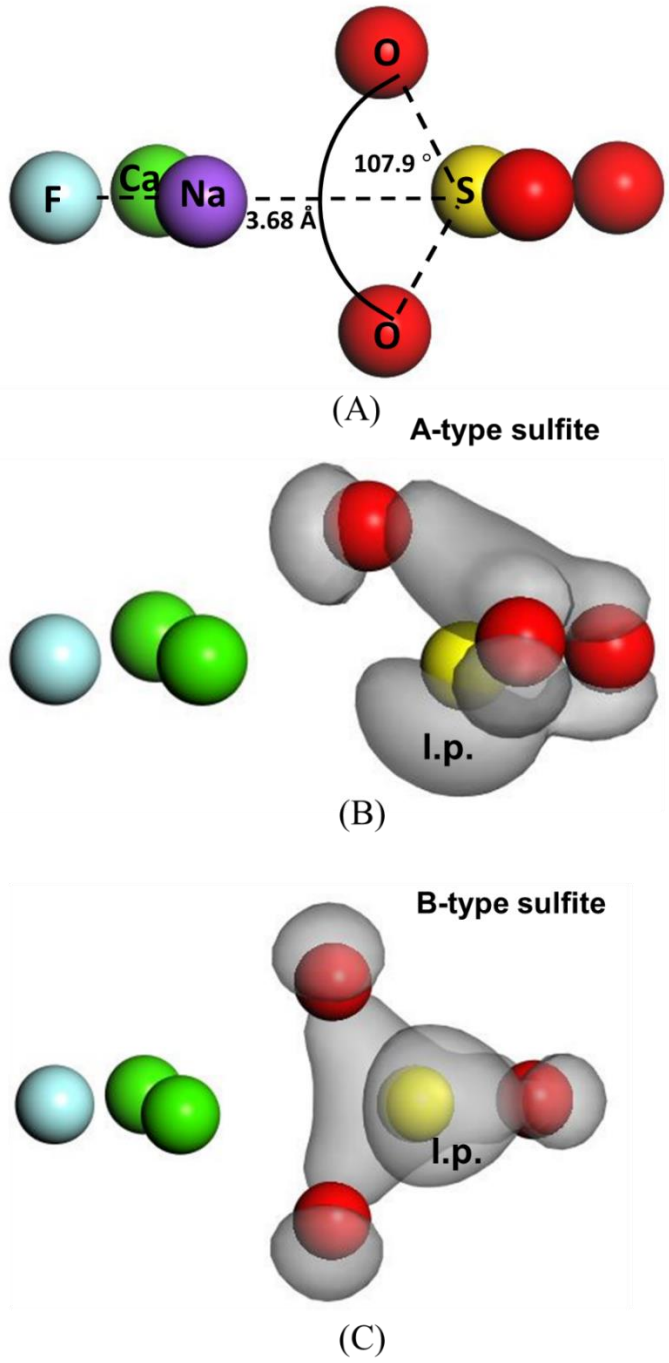

Fig. 4. 4. Atomistic-level view of (A) SO_4^{2-} near the F column in S^{6+}-incorporated Na-bearing apatite and (B) A-type and (C) B-type SO_3^{2-} near the F column in S^{6+} and S^{4+} co-incorporated apatite. Orbital contours for SO_3^{2-} are shown to indicate the lone pair (l.p.) electrons and S-O bonding (see text for more details).

Table 4. 4. Summary of geometric parameters for SO_4^{2-} and SO_3^{2-} incorporated apatite.

Optimized structure	Cell volume ($Å^3$)	X-S^{6+} distance (Å)	X-S^{6+} distance (Å)	z [a] of S^{4+}	z [a] of S^{6+}
Fluorapatite					
Incorporation of					
A-type SO_3^{2-}	542.3	3.63	3.61	0.2230	0.7507
B-type SO_3^{2-}	543.9	3.68	3.68	0.2500	0.7500
Chlorapatite					
A-type SO_3^{2-}	570.4	3.75	3.85	0.2204	0.7502
B-type SO_3^{2-}	574.5	3.97	3.94	0.2462	0.7503
Hydroxylapatite					
A-type SO_3^{2-}	548.5	3.67	3.64	0.2186	0.7461
B-type SO_3^{2-}	551.7	3.73	3.74	0.2432	0.7533

Notes: [a] The z value of fractional coordination (x, y, z)

In the optimized S-incorporated apatite phases, bond lengths and angles measured from the incorporated SO_3^{2-} molecules are in good agreement with previous reported values (104.3° and 1.53 Å) (Andersen and Lindqvist, 1984). The cell volumes and distances between S^{4+} and F^-, Cl^-, or OH^- in optimized S-incorporated apatite phases are presented in Table 4. 4. Larger cell volumes are found for B-type SO_3^{2-}-incorporated apatite when compared to A-type SO_3^{2-}-incorporated apatite. B-type SO_3^{2-}-incorporated apatite has 0.05 to 0.2 Å longer (F, Cl, OH)–S^{4+} and (F, Cl, OH)–S^{6+} distances than A-type SO_3^{2-} apatite. The cell volume results coincide with the (F, Cl, OH)–S distance variation in the sense that the longer atomic distance generally contributes to the larger cell volume of the mineral. The calculated z fractional coordinate of the S center of SO_4^{2-} is barely displaced from the plane at Z = 3/4 (< 0.03 Å). The S atom of A-type SO_3^{2-} is displaced ~0.2 Å from the plane at Z = 1/4 whereas the B-type SO_3^{2-} deviates by less than 0.05 Å from the same plane.

3.3. Incorporation energy and geometry: Sulfide (S^{2-})

The equations and calculated energies of reactions for S^{2-} incorporation into fluor-, chlor-, and hydroxylapatite in the Fe-S and Na-S, and Fe-Si-S systems are presented in Table 4. 5. Lattice parameters of the initial and optimized S^{2-} incorporated apatite structures are summarized in Table 4. 6. The calculated reaction energies for S^{2-} incorporation are highly dependent on selected source and sink phases. Energies calculated by using Fe-bearing phases (Fe-S system) are higher than incorporation energies calculated using Na-bearing phases (Na-S system). This effect arises from the higher stability of troilite (FeS) used as a source phase relative to Fe-bearing sink phase solids than the stability of Na_2S relative to Na sink phases. However, in a given system, where source phases and/or sink phases are fixed, the stability of S-incorporated apatite phases can be evaluated relative to host apatite phases. In case of hydroxylapatite, since Si-bearing minerals are used as source phases in addition to FeS, the stability of apatite phases is not comparable between the Fe-S and Fe-Si-S systems. Full incorporation of S^{2-} into the Cl site (denoted by $S(Cl)_{ini}$ in Table 4. 5) of chlorapatite is more stable than into the F site ($S(F)_{ini}$) of fluorapatite. The calculated incorporation energy difference between fluorapatite and chlorapatite is 256 and 265 kJ/mol in the Fe-S and Na-S systems, respectively. Full incorporation of S^{2-} into the hydroxylapatite structure achieves appreciable stability relative to Fe-silicates (-71.9 kJ/mol; Table 4. 5).

The optimized structures of fully S^{2-} incorporated apatite are compared with a previous study of synthetic sulfoapatite, $[Ca_{10}(PO_4)_6S]$ (Henning et al., 2000; Table 4. 6). Calculated cell parameters are in good agreement with the measured parameters. In the optimized structure of S^{2-} full incorporation, the position of S^{2-} is at z = 0.5018 and 0.5004 in the hydroxylapatite and chlorapatite structures, respectively and at z = 0.75 in the fluorapatite structure where F^- is replaced by S^{2-} in the initial model.

Table 4. 5. Reaction equations and energies of S^{2-} full and partial incorporation into apatite.

	ΔE_{rxn} (kJ/mol)		
	Column geometry of S^{2-}		
Fe-S system	$S(F)_{ini}$	$S(Cl)_{ini}$	$S(OH)_{ini}$
Full incorporation			
$Ca_{10}(PO_4)_6F_2 + FeS \leftrightarrow Ca_{10}(PO_4)_6(S) + FeF_2$	362.02 (232.83)[a)]	—	—
$Ca_{10}(PO_4)_6Cl_2 + FeS \leftrightarrow Ca_{10}(PO_4)_6(S) + FeCl_2$	—	105.11	—
Partial incorporation			
$Ca_{20}(PO_4)_{12}F_4 + FeS \leftrightarrow Ca_{20}(PO_4)_{12}(S)F_2 + FeF_2$	399.53	343.37	344.21
$Ca_{20}(PO_4)_{12}Cl_4 + FeS \leftrightarrow Ca_{20}(PO_4)_{12}(S)Cl_2 + FeCl_2$	101.77	97.10	102.83
Na-S system			
Full incorporation			
$Ca_{10}(PO_4)_6F_2 + Na_2S \leftrightarrow Ca_{10}(PO_4)_6(S) + 2NaF_2$	203.76 (74.59)[a)]	—	—
$Ca_{10}(PO_4)_6Cl_2 + Na_2S \leftrightarrow Ca_{10}(PO_4)_6(S) + 2NaCl$	—	-61.32	—
Partial incorporation			
$Ca_{20}(PO_4)_{12}F_4 + Na_2S \leftrightarrow Ca_{20}(PO_4)_{12}(S)F_2 + 2NaF_2$	241.27	185.11	185.95
$Ca_{20}(PO_4)_{12}Cl_4 + Na_2S \leftrightarrow Ca_{20}(PO_4)_{12}(S)Cl_2 + 2NaCl$	-64.66	-69.33	-63.60
Fe-Si-S system			
Full incorporation			
$Ca_{10}(PO_4)_6(OH)_2 + FeS + 6FeSiO_3 + 2SiO_2 \leftrightarrow Ca_{10}(PO_4)_6(S) + Fe_7Si_8O_{22}(OH)_2$			-71.86
Partial incorporation			
$Ca_{20}(PO_4)_{12}(OH)_4 + FeS + 6FeSiO_3 + 2SiO_2 \leftrightarrow Ca_{20}(PO_4)_{12}(S)(OH)_2 + Fe_7Si_8O_{22}(OH)_2$	58.35	40.97	46.84

Notes: [a] The calculated incorporation energy S^{2-} in fluorapatite when initially positioned at (0, 0, 0.7).

When located at (0, 0, 0.70) in the initial model of fluorapatite, however, S^{2-} is relaxed to the position at z = 0.5 during geometry optimization, resulting in the incorporation energy lower than one having S^{2-} at z = 0.75 (the energy difference of 129 kJ/mol) (Table 4. 5 and 6). This indicates

that S^{2-} in the F^- position (z =1/4 or 3/4, at the center of the Ca triangle) is metastable for S^{2-} larger than F^-, and (0, 0, 0.5) is the most likely position of column anion S^{2-} in sulfoapatite, $[Ca_{10}(PO_4)_6S]$. This result is in good agreement with experimental data for synthetic sulfoapatite (z = 0.5) (Henning et al., 2000).

Lower reaction energies are found in cases of partial incorporation into chlorapatite when compared to those of fluorapatite (Table 4. 5). The incorporation energy also depends on where S^{2-} is incorporated in the anion column of the initial model structure (denoted by $(F, Cl, OH)_{ini}$ in Table 4. 6). Upon the partial incorporation into fluorapatite, incorporation of S^{2-} on a F^- position ($S(F)_{ini}$) is less stable than S^{2-} on Cl^- and OH^- positions ($S(Cl)_{ini}$ and $S(OH)_{ini}$) (energy difference of 55 to 56 kJ/mol). When partially incorporated into chlorapatite, the dependence of the S stability on the column position is relatively lower and leads to energy differences between $S(F, Cl, OH)_{ini}$ less than 6 kJ/mol. From these results, one can infer that the probability of S^{2-} being incorporated into apatite is enhanced when S^{2-} is partitioned into the Cl-bearing apatite structure or when Cl^- coexists with S^{2-} in the anion column site. Upon partial substitution of S^{2-} in hydroxylapatite, the stability of incorporated S^{2-} is higher at the Cl or OH site relative to the F site. Column anion positions in the optimized structures of partially S^{2-} substituted apatite are depicted in Fig. 4.5. The anion column S is located at z = 0.57 in the optimized structure of fluorapatite when S^{2-} is initially positioned at the Cl^- or OH^- site (denoted by $(F, Cl, OH)_{ini}$ in Table 4. 6). The minimum energy configurations are found when the position of S^{2-} is (0, 0, 0.61) in the hydroxylapatite structure. The anion column S^{2-} is positioned at z = 0.51 in S^{2-} incorporated chlorapatite, regardless of its initial position. Interaction with surrounding column anions is an important factor that determines the position of S^{2-}. In the anion column environment tested here where S is located between two anions–i.e. F^-, Cl^-, or OH^-, at or near z = 1/4 and 5/4 (with respect to the initial 1×1×1 unit cell) in

the 1×1×2 supercell (Fig. 4.5) –the lowest-energy configuration shows that S^{2-} in the anion column is located at z = 0.50 to 0.61. The presence of S^{2-} in the anion column results in displacing the remaining F^-, Cl^-, or OH^- above or below the planes at z = 1/4.

Table 4. 6. The cell and lattice parameters of initial and optimized configurations of S^{2-} fully and partially incorporated apatite.

		Full incorporation			Partial incorporation
Optimized structure	z^b of $(F, Cl, OH)_{ini}$	*a* (Å)	*b* (Å)	z^c of S^{2-}	z^c of S^{2-}
S-apatite (experiment)[a]		9.462	6.834	0.5	
S in the fluorapatite structure	0.25 and 0.75	9.825	6.739	0.7500 (0.5016)[d]	0.57
Deviation (%)		3.84	1.39		
S in the chlorapatite structure	0.062 and 0.562	9.566	6.843	0.5018	0.51
Deviation (%)		1.10	0.13		
S in the hydroxyapatite structure	0.213 and 0.713	9.542	6.859	0.5004	0.61
Deviation (%)		0.85	0.36		

Notes: [a] *Henning et al. (2000)*

[b] The z value of column anion position (0, 0, z) used in the initial S^{2-} incorporation models. In the models, (F, Cl, OH) at or near the mirror plane at z = ¾ is replaced by S^{2-}.

[c] The z value of S^{2-} position (0, 0, z) in the lowest-energy configurations. See Figure 5 for details.

[d] The optimized position of S^{2-} in fluorapatite when initially positioned at (0, 0, 0.7).

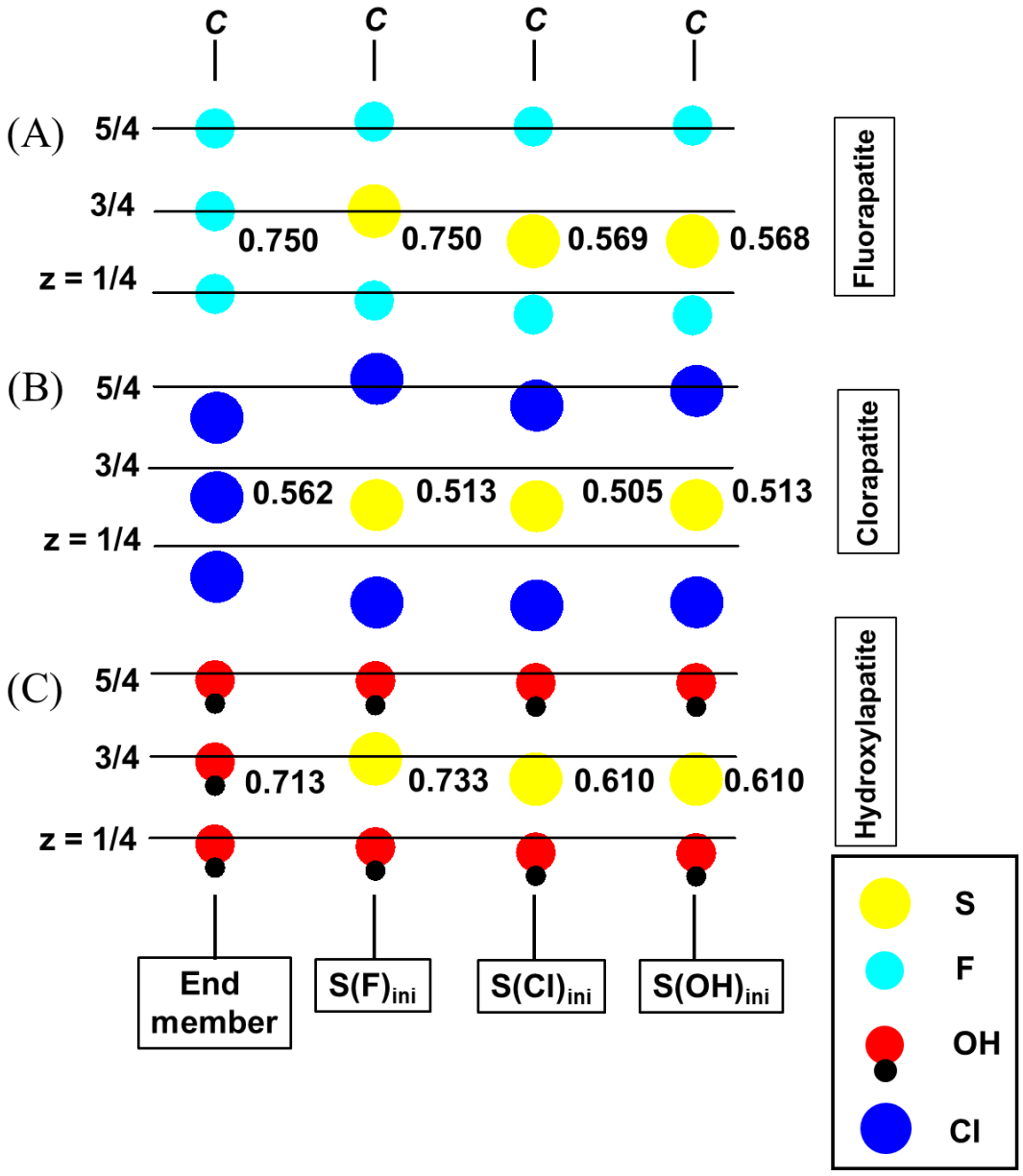

Fig. 4. 5. The optimized positions of column anions in hexagonal end-member and partially S^{2-}-incorporated apatite in the 1×1×2 supercell. (A) fluorapatite (B) chlorapatite and (C) hydroxylapatite systems are depicted respectively. The anion (F^-, Cl^- or OH^-) dominating the column with the position of S^{2-} in the initial model is labeled at the tail of c axis. The fractional coordinate of z (with respect to the unit cell) in the optimized structure is presented for S at or near z = 3/4. Note that the column anion site at z = 7/4 (coordinate with respect to the original 1×1×1 unit cell, not shown) is vacant in the supercell whose zero charge is compensated with a charge of 2- from S.

4. DISCUSSION

4.1. Effects of impurities on sulfate (SO_4^{2-}) incorporation in apatite

Generally, higher reaction energies result from stable reactants or unstable products. Therefore, the lower S^{6+} incorporation energies observed for the La-Na-bearing apatite when compared to La-Si-bearing apatite (Table 4. 2) indicate that (i) the La-Si-bearing host apatite is more stable than La-Na-bearing host apatite or (ii) that S^{6+} incorporation into apatite becomes energetically more stable when SO_4^{2-} is coordinated with Na^+ and PO_4^{3-} than with Ca^{2+} and SiO_4^{4-}. The incorporation energies of La^{3+} and Na^+ versus La^{3+} and Si^{4+} into apatite were calculated in order to consider the stability of the impure apatite hosting S oxidation states relative to the pure end-member fluor-, chlor-, and hydroxylapatite (Table 4. 7). Incorporation energies of La^{3+} and Na^+ into apatite are higher than those of La^{3+} and Si^{4+} into apatite for fluorapatite and hydroxylapatite. Hence, scenario (i) may be favored for fluorapatite and hydroxylapatite. Scenario (ii) can be evaluated using linear combinations of equations for S^{6+} incorporation into La^{3+}-bearing apatite (Table 4. 2) and for La^{3+} incorporation into end-member apatite (Table 4. 7). The incorporation energies of S^{6+} and Na^+-bearing apatite are lower than those of S^{6+} and Si^{4+}-bearing apatite for all apatite end-members, which supports scenario (ii). In addition, comparison between equations for S^{6+} incorporation into host apatite phases (Table 4. 2 and 7) suggests that incorporation of SO_4^{2-} into La-bearing apatite may be energetically more favorable than the incorporation into the end-member fluor-, chlor-, and hydroxylapatite.

Table 4. 7. Reaction equations and energies of La^{3+}- and S^{6+}-incorporation into end-member apatite.

	ΔE_{rxn} (kJ/mol)		
La^{3+}-incorporation into end-member apatite	X = F	Cl	OH
La^{3+} and Na^{+}: $Ca_{10}(PO_4)_6X_2 + 1/3Na_3PO_4 + LaPO_4 \leftrightarrow [Ca_8NaLa][(PO_4)_6]X_2 + 2/3Ca_3(PO_4)_2$	91.28	68.12	77.29
La^{3+} and Si^{4+}: $Ca_{10}(PO_4)_6X_2 + Ca_2SiO_4 + LaPO_4 \leftrightarrow [Ca_9La][(PO_4)_5(SiO_4)]X_2 + Ca_3(PO_4)_2$	75.45	69.76	70.72
S^{6+}-incorporation into end-member apatite	X = F	Cl	OH
S^{6+} and Na^{+}: $Ca_{10}(PO_4)_6X_2 + 1/3Na_3PO_4 + CaSO_4 \leftrightarrow [Ca_9Na][(PO_4)_5(SO_4)]X_2 + 2/3Ca_3(PO_4)_2$	89.54	69.28	81.63
S^{6+} and Si^{4+}: $Ca_{10}(PO_4)_6X_2 + Ca_2SiO_4 + CaSO_4 \leftrightarrow [Ca_{10}][(PO_4)_4(SiO_4)(SO_4)]X_2 + Ca_3(PO_4)_2$	90.89	74.78	86.16

Since replacements of Ca^{2+} and PO_4^{3-} by other ions (Na^{+}, La^{3+}, SiO_4^{4-} and SO_4^{2-}) are made at the nearest position to the column anions (F, Cl, OH) in all models tested, it is expected that energy differences between the apatite phases used as reactants and products arise mainly from chemical or structural environments on the column anion sites (Fig. 4.2). In this regard, the first and second possibilities above ((i) and (ii)) can be understood in terms of interatomic interaction. In host and S-incorporated apatite, the Ca triangle that surrounds the column anion has one or two Ca2 atoms replaced by Na^{+} or La^{3+} (Fig. 4.2b). Cations positioned at the triangle corners are electrostatically repelled from each other and attracted to the column anion and surrounding phosphate and other oxyanions. The Coulomb energy between the interacting ions is defined in a classical manner such that the energy is proportional to the product of the charges of the two ions, q_i and q_j, and increases inversely with the distance between the two, r_{ij}. When multiple atoms are present in a system, the Coulomb energy is defined as Equation 7.

$$E_{coulomb} = \frac{e^2}{4\pi\varepsilon_0}\sum_{i>j}\frac{q_i q_j}{r_{ij}} \quad (7)$$

Here, the Coulomb force of the cations in a triangle and the surrounding anions is balanced by two contributions: (i) repulsion between the cations and (ii) interaction of the triangle cations with the surrounding anions that stabilize the triangular structure. A higher repulsive force is exerted on the triangle structure when La^{3+} is located at a corner of the triangle than when Na^{+} or Ca^{2+} is there. In this case, the effect of La^{3+} ion can be counteracted by coexistence with SiO_4^{4-} that makes the triangle less unstable. That is, the attractive coulombic force between cations and SiO_4^{4-} with a 4- charge is stronger than the force exerted by PO_4^{3-} with a 3- charge. This indicates that La-bearing apatite phases can be stabilized by coexisting with silicate ions (the first possibility above). On the other hand, the presence of Na^{+} or SiO_4^{4-} near SO_4^{2-} can make a large contribution to the stability of S^{6+}-incorporated phases. Na^{+} is electrically less attractive to SO_4^{2-} than Ca^{2+} while SiO_4^{4-} is more repulsive to SO_4^{2-} than PO_4^{3-}. This means that electrical interaction of SO_4^{2-} with Na^{+} or SiO_4^{4-} alone does not increase the stability of incorporated SO_4^{2-}. However, Na^{+} on the Ca2 site and SiO_4^{4-} on a neighboring phosphate site both can contribute to energy lowering of the anion column triangle. Na^{+} occupying the Ca2 site has a lower repulsive force than Ca^{2+}, which lowers the instability of the triangular arrangement by cation-cation repulsion. The presence of a neighboring silicate anion will counteract the repulsive force between the triangle Ca^{2+} ions. However the effect of SiO_4^{4-} on Ca^{2+} ions will be less than the case of La^{3+} included in the host apatite phase. The net effect of these contributions might enable some of the S-incorporated apatite phases to be more stable in the coexistence with Na^{+} than with Si^{4+} (the second possibility).

The effect of the anion column on S^{6+} incorporation into La-bearing apatite can be manifested in the Si-bearing apatite system, as demonstrated by the calculated incorporation energies (Table 4. 2). The incorporation energy is lower in chloroapatite compared to fluorapatite and hydroxylapatite. The lowest incorporation energy for S^{6+} and Si^{4+} into end-member apatite is found

for chlorapatite (Table 4. 7). The repulsive force between column anion Cl^- and SO_4^{2-} is one possible contribution to the stability of S^{6+}-incorporated Cl-apatite. In the optimized S-incorporated apatite, the center-to-center distance is 3.55 Å between F^- and S^{6+}, 3.92 Å between Cl^- and S^{6+} and 3.61 Å between OH^- and S^{6+} (Table 4. 3). Therefore, chlorapatite is expected to experience the smallest repulsive force between the column anion (Cl^-) and SO_4^{2-}.

4.2. Sulfide (S^{2-}) site stability in the apatite structure

The incorporation energy of S^{2-} into apatite is closely correlated with the optimized structure of S-bearing apatite. In S^{2-} full incorporation, the incorporation energy of S^{2-} positioned at z = 0.5 is lower than that of S^{2-} at 0.75 (Table 4. 5 and 6). The anion column site at z = 0.75 and 0.25 is surrounded by three Ca2 atoms but its site occupancy is limited for anions bigger than F^- (Fig. 4.2a). The occupancy of S^{2-} at (0, 0, 0.75) leads to the expansion of the column triangle with a Ca-Ca distance of 4.47 Å that is 4.02 Å in the F^- occupancy. Such structural alteration by S on the F site can largely contribute to relatively higher incorporation energy than S^{2-} incorporation on the Cl^- site. In cases of partial substitution, relatively high incorporation energies are calculated for optimized cells with S^{2-} replacing two F^- anions (Fig. 4.5 and Table 4. 5). Partial incorporation of S^{2-} into the F^- site in fluorapatite and hydroxylapatite results in an increase in the Ca-Ca distance in the anion column triangle at z = 3/4 by 10.2 and 7.6 %, respectively. This is the expected result due to the ionic size difference between S^{2-} and F^-. It is inferred that the substitution of S^{2-} in the F^- site in the apatite structure is energetically and geometrically unfavorable. In contrast, full or partial substitution of S^{2-} into fluor-, chlor-, or hydroxylapatite results in relatively low incorporation energies when S^{2-} is positioned in the Cl^- and OH^- site. In the lowest-energy configurations for the partial substitution, the predicted position of the S^{2-} ion in fluor-, chlor- and

hydroxylapatite are 1 to 1.75 Å displaced from the mirror plane at z = 1/4 or 3/4 (Fig. 4.5 and Table 4. 6), which is close to the Cl^- site in the natural apatite structure (0.1823 displacement in the z value from the mirror planes; Table 4. 1). These results suggest that the Cl^- site can be one of the energetically stable sites for S^{2-} incorporation in the apatite structure.

The stability of an incorporating or substituting ion in an atomic site of a mineral structure can be explained on the basis of the Goldschmidt's substitution rules, which states that the "native" ions in a given site are more likely to be substituted by foreign ions with a similar radius, charge, and ionic nature (e.g., chemical hardness and electronegativity; Klein and Dutrow, 2002). According to these criteria, S^{2-} substituting in the column anion site has an acceptable charge difference of one unit. The radius difference is a paramount factor that influences substitution of S^{2-} in apatite. The reported ionic radii of F^-, Cl^-, and S^{2-} are 1.33, 1.81, and 1.84 Å, respectively (Shannon, 1976). The ionic radius of S^{2-} is very close to that of Cl^- (difference by 1.6 %) whereas there is an appreciable difference in ionic radius between S^{2-} and F^- anions by 27.7 %. This indicates that incorporation of S^{2-} in the F^- site is either unlikely or quite limited. In addition, S^{2-} is similar in its chemical nature to Cl^-. The chemical hardness of S^{2-} is classified as a soft base, which gives rise to its affinity with various soft transition metals such as Fe^{2+}, Cu^+, and Hg^{2+} in geological processes, e.g., ore-formation (Pearson, 1968). Chlorine is chemically soft and less electronegative than F^-. Such chemical similarities between S^{2-} and Cl^- may contribute to affinity of the two anions in apatite.

4.3. Future work

As H_2S in a silicate melt is deprotonated, S^{2-} may be partitioned into mineral phases as either S^{2-} or HS^-. The possibility of HS^- incorporation into apatite was not determined in this study since

the results of Henning et al. (2000) already indicate that S^{2-} may be the favored S species, but future work should examine whether HS^- can also be an important component in the anion column site as it may behave like OH^-. Moreover, examination by quantum-mechanical molecular dynamics (MD) may enable evaluation of the energy and structure of periodic solids (e.g., minerals) under high pressure or temperature (Segall et al., 2002). Recent studies have successfully demonstrated applications of ab-initio MD approaches for evaluating hydrothermal reactions involving molecular or aqueous species (e.g., Sherman, 2007; Mei et al., 2013). To our knowledge, however, the published literature is currently lacking studies applying MD tools to incorporation into minerals under magmatic-hydrothermal conditions. In this regard, treatment of high pressure and temperature dynamics (with or without H_2O) on S-bearing apatite should be the subject of future studies.

We highlight that the interpretation of S behavior in this study is based on the traditional paradigm that SO_4^{2-} and S^{2-} are the only relevant S species in silicate melts (Baker and Rutherford, 1996a); however, this assumption has been challenged by the discovery of the S radical ions (e.g., S_2^-, S_3^-) in hydrothermal fluids and silicate melts (Winther et al., 1998; Jacquemet et al., 2014; Pokrovski and Dubessy, 2015) and by the possible presence of (un-quenchable) S^{4+} in silicate melts (Métrich et al., 2009). Therefore, it is important to consider the role of various S species and oxidation states in geological fluids and melts when S-bearing phases (e.g., apatite) that are subject to high temperatures and pressures are investigated in future studies.

5. Implications

The crystallographic characteristics and energetic stability of the S-incorporated apatite structure varies depending on the S oxidation state in apatite and can be significantly influenced by [A] the neighboring column anion (F^-, Cl^-, or OH^-), [B] potential pre-existing substitutions for Ca^{2+} and P^{5+} (e.g., La^{3+}, Na^+, Si^{4+}) and [C] the molecular geometry and orientation of S oxyanions in the structure.

Sulfide (S^{2-}) occupancy in the anion column site (S^{2-} + vacancy) in the apatite structure is a likely mechanism in reduced geological systems. Of the model configurations tested, the scenarios with S^{2-} accommodated in the chlorapatite structure and with S^{2-} positioned closely to Cl^- in the anion column in chlorapatite are most energetically plausible. In most natural systems, however, F^-, Cl^-, and OH^- are the three major column anions in apatite, while S is a trace element in apatite, independent of its oxidation state (< 1 wt% S; Parat et al., 2011; Konecke et al., 2017). Thus, the presence of S^{2-} in natural apatite is probably not limited to chloroapatite or Cl-rich apatite. The thermodynamic advantage of S^{2-} in the Cl site may play a role in determining the S content in apatite that forms under Cl- and S-rich reduced environments. This is consistent with the positive correlation between Cl and S contents found from lunar apatite (Boyce et al., 2014) and the XANES-determined presence of S^{2-} in apatite crystallized from a mafic melt under reducing redox conditions (Konecke et al., 2017).

The results for oxidized sulfur species (S^{4+}, S^{6+}) presented in this study indicate that there are more energetic or geometric constraints (e.g., the orientation of the S lone pair electrons) on SO_3^{2-} incorporation into the apatite structure than on SO_4^{2-} incorporation. The data from this study and Konecke et al. (2017) support the hypothesis that the substitution of SO_3^{2-} into apatite is relatively minor, but appreciable if coexisting with SO_4^{2-} in apatite formed under oxidizing conditions.

The abundance and relative proportions of S^{2-}, S^{4+} and S^{6} in geologic systems is a function of oxygen fugacity (fO_2), and recorded directly in the S chemistry of apatite (Konecke et al., 2017). The modeling of S oxidation stated in the apatite structure in this study, combined with the experimental results reported by Konecke et al., 2017, implies that the oxidation state of S-in-apatite has the potential to serve as a geochemical proxy to probe the fO_2 of magmatic and hydrothermal systems.

Acknowledgments

Y.K. acknowledges support from Samsung Scholarship. A.F. and A.C.S. acknowledge the U.S. National Science Foundation EAR Grant #1524394. B.A.K. acknowledges support from Rackham Graduate School (UM) and a Society of Economic Geologists Student Research Grant. Finally, we thank J. Rakovan, G. Pokrovski, D. Harlov, and one anonymous reviewer for their constructive reviews, and are grateful for the editorial handling of F. Nestola.

References

Andersen L. and Lindqvist O. (1984) Neutron diffraction refinement of magnesium sulfite hexahydrate, $MgSO_3$. $6H_2O$. *Acta Crystallogr. Sect. C: Cryst. Struct. Commun.* **40**, 584-586.

Baker L. and Rutherford M. J. (1996a) Sulfur diffusion in rhyolite melts. *Contrib. Mineral. Petrol.* **123**, 335-344.

Baker L. L. and Rutherford M. J. (1996b) Crystallisation of anhydrite-bearing magmas. *Geological Society of America Special Papers* **315**, 243-250.

Behrens H. and Gaillard F. (2006) Geochemical aspects of melts: volatiles and redox behavior. *Elements* **2**, 275-280.

Boyce J., Tomlinson S., McCubbin F., Greenwood J. and Treiman A. (2014) The lunar apatite paradox. *Science* **344**, 400-402.

Burns R. and Fyfe W. (1966) Distribution of elements in geological processes. *Chem. Geol.* **1**, 49-56.

Elliott B. (2001) Crystallization conditions of the Wiborg rapakivi batholith, SE Finland: an evaluation of amphibole and biotite mineral chemistry. *Mineralogy and Petrology* **72**, 305-324.

Fiege A., Holtz F., Behrens H., Mandeville C. W., Shimizu N., Crede L. S. and Goettlicher J. (2015) Experimental investigation of the S and S-isotope distribution between H 2 O–S±Cl fluids and basaltic melts during decompression. *Chem. Geol.* **393**, 36-54.

Fleet M. E. and Liu X. (2007) Coupled substitution of type A and B carbonate in sodium-bearing apatite. *Biomaterials* **28**, 916-926.

Foerster H.-J. (1998) The chemical composition of REE-Y-Th-U-rich accessory minerals in peraluminous granites of the Erzgebirge-Fichtelgebirge region, Germany, Part I: The monazite-(Ce)-brabantite solid solution series. *Am. Mineral.* **83**, 259-272.

Greenwood J. P., Itoh S., Sakamoto N., Warren P., Taylor L. and Yurimoto H. (2011) Hydrogen isotope ratios in lunar rocks indicate delivery of cometary water to the Moon. *Nature Geoscience* **4**, 79.

Harlov D. E. (2015) Apatite: a fingerprint for metasomatic processes. *Elements* **11**, 171-176.

Henning P., Adolfsson E. and Grins J. (2000) The chalcogenide phosphate apatites $Ca_{10}(PO_4)_6S$, $Sr_{10}(PO_4)_6S$, $Ba_{10}(PO_4)_6S$ and $Ca_{10}(PO_4)_6Se$. *Zeitschrift für Kristallographie International journal for structural, physical, and chemical aspects of crystalline materials* **215**, 226.

Hsu H., Blaha P., Cococcioni M. and Wentzcovitch R. M. (2011) Spin-state crossover and hyperfine interactions of ferric iron in $MgSiO_3$ perovskite. *Phys. Rev. Lett.* **106**, 118501.

Hughes J. M., Cameron M. and Crowley K. D. (1990) Crystal structures of natural ternary apatites; solid solution in the $Ca_5(PO_4)_3X$ (X= F, OH, Cl) system. *Am. Mineral.* **75**, 295-304.

Hughes J. M., Cameron M. and Mariano A. N. (1991) Rare-earth-element ordering and structural variations in natural rare-earth'bearing apatites. *Am. Mineral.* **76**, I165-1173.

Hughes J. M., Harlov D., Kelly S. R., Rakovan J. and Wilke M. (2016) Solid solution in the apatite OH-Cl binary system: Compositional dependence of solid-solution mechanisms in calcium phosphate apatites along the Cl-OH binary. *Am. Mineral.* **101**, 1783-1791.

Hughes J. M. and Rakovan J. (2002) The crystal structure of apatite, $Ca_5(PO_4)_3(F, OH, Cl)$. *Rev. Mineral. Geochem.* **48**, 1-12.

Hughes J. M. and Rakovan J. F. (2015) Structurally robust, chemically diverse: apatite and apatite supergroup minerals. *Elements* **11**, 165-170.

Imai A. (2002) Metallogenesis of porphyry Cu deposits of the western Luzon arc, Philippines: K-Ar ages, SO3 contents of microphenocrystic apatite and significance of intrusive rocks. *Resource Geology* **52**, 147-161.

Jacquemet N., Guillaume D., Zwick A. and Pokrovski G. S. (2014) In situ Raman spectroscopy identification of the $S\bar{3}$ ion in S-rich hydrothermal fluids from synthetic fluid inclusions. *Am. Mineral.* **99**, 1109-1118.

Jugo P. J., Luth R. W. and Richards J. P. (2005) Experimental data on the speciation of sulfur as a function of oxygen fugacity in basaltic melts. *Geochim. Cosmochim. Acta* **69**, 497-503.

Klein C. and Dutrow B. (2002) *Manual of mineral science (manual of mineralogy)*. John Wiley.

Konecke B. A., Fiege A., Simon A. C., Parat F. and Stechern A. (2017) Co-variability of S6+, S4+, and $S2^-$ in apatite as a function of oxidation state: Implications for a new oxybarometer. *Am. Mineral.* **102**, 548-557.

Lattard D. and Evans B. W. (1992) New experiments on the stability of grunerite. *Eur. J. Mineral.* **4**, 219-238.

Liu Y. and Comodi P. (1993) Some aspects of the crystal-chemistry of apatites. *Mineral. Mag.* **57**, 709-720.

Lyons J. I. (1988) Volcanogenic iron oxide deposits, Cerro de Mercado and vicinity, Durango. *Econ. Geol.* **83**, 1886-1906.

Mei Y., Sherman D. M., Liu W. and Brugger J. (2013) Complexation of gold in S 3−-rich hydrothermal fluids: Evidence from ab-initio molecular dynamics simulations. *Chem. Geol.* **347**, 34-42.

Métrich N., Berry A. J., O'Neill H. S. C. and Susini J. (2009) The oxidation state of sulfur in synthetic and natural glasses determined by X-ray absorption spectroscopy. *Geochim. Cosmochim. Acta* **73**, 2382-2399.

Monkhorst H. J. and Pack J. D. (1976) Special points for Brillouin-zone integrations. *Phys. Rev. B* **13**, 5188.

Pan Y. and Fleet M. E. (2002) Compositions of the apatite-group minerals: substitution mechanisms and controlling factors. *Rev. Mineral. Geochem.* **48**, 13-49.

Parat F., Dungan M. A. and Streck M. J. (2002) Anhydrite, pyrrhotite, and sulfur-rich apatite: tracing the sulfur evolution of an Oligocene andesite (Eagle Mountain, CO, USA). *Lithos* **64**, 63-75.

Parat F. and Holtz F. (2004) Sulfur partitioning between apatite and melt and effect of sulfur on apatite solubility at oxidizing conditions. *Contrib. Mineral. Petrol.* **147**, 201-212.

Parat F. and Holtz F. (2005) Sulfur partition coefficient between apatite and rhyolite: the role of bulk S content. *Contrib. Mineral. Petrol.* **150**, 643-651.

Parat F., Holtz F. and Streck M. J. (2011) Sulfur-bearing magmatic accessory minerals. *Rev. Mineral. Geochem.* **73**, 285-314.

Paris E., Giuli G., Carroll M. R. and Davoli I. (2001) The valence and speciation of sulfur in glasses by X-ray absorption spectroscopy. *Can. Mineral.* **39**, 331-339.

Pearson R. G. (1968) Hard and soft acids and bases, HSAB, part 1: Fundamental principles. *J. Chem. Educ.* **45**, 581.

Peng G., Luhr J. F. and McGee J. J. (1997) Factors controlling sulfur concentrations in volcanic apatite. *Am. Mineral.* **82**, 1210-1224.

Perdew J. P., Burke K. and Ernzerhof M. (1996) Generalized gradient approximation made simple. *Phys. Rev. Lett.* **77**, 3865.

Pokrovski G. S. and Dubessy J. (2015) Stability and abundance of the trisulfur radical ion in hydrothermal fluids. *Earth. Planet. Sci. Lett.* **411**, 298-309.

Rakovan J. and Waychunas G. (2013) Apatite—The Great Pretender. Mineral Monographs 17.

Rohrbach A., Hafner J. and Kresse G. (2003) Electronic correlation effects in transition-metal sulfides. *J. Phys.: Condens. Matter* **15**, 979.

Rouse R. C. and Dunn P. J. (1982) A contribution to the crystal chemistry of ellestadite and the silicate sulfate apatites. *Am. Mineral.* **67**, 90-96.

Sato M., Hickling N. and McLane J. E. (1973) Oxygen fugacity values of Apollo 12, 14, and 15 lunar samples and reduced state of lunar magmas, Lunar and Planetary Science Conference Proceedings, **p.** 1061.

Segall M., Lindan P. J., Probert M. a., Pickard C., Hasnip P., Clark S. and Payne M. (2002) First-principles simulation: ideas, illustrations and the CASTEP code. *J. Phys.: Condens. Matter* **14**, 2717.

Shannon R. t. (1976) Revised effective ionic radii and systematic studies of interatomic distances in halides and chalcogenides. *Acta Crystallographica Section A: Crystal Physics, Diffraction, Theoretical and General Crystallography* **32**, 751-767.

Sherman D. M. (2007) Complexation of Cu+ in hydrothermal NaCl brines: ab initio molecular dynamics and energetics. *Geochim. Cosmochim. Acta* **71**, 714-722.

Shuller-Nickles L. C., Bender W. M., Walker S. M. and Becker U. (2014) Quantum-mechanical methods for quantifying incorporation of contaminants in proximal minerals. *Minerals* **4**, 690-715.

Shuller L. C., Ewing R. C. and Becker U. (2013) Np-incorporation into uranyl phases: A quantum–mechanical evaluation. *J. Nucl. Mater.* **434**, 440-450.

Smith F. N., Um W., Taylor C. D., Kim D.-S., Schweiger M. J. and Kruger A. A. (2016) Computational Investigation of Technetium (IV) Incorporation into Inverse Spinels: Magnetite (Fe_3O_4) and Trevorite ($NiFe_2O_4$). *Environ. Sci. Technol.* **50**, 5216-5224.

Stackhouse S., Stixrude L. and Karki B. B. (2010) Determination of the high-pressure properties of fayalite from first-principles calculations. *Earth. Planet. Sci. Lett.* **289**, 449-456.

Streck M. J. and Dilles J. H. (1998) Sulfur evolution of oxidized arc magmas as recorded in apatite from a porphyry copper batholith. *Geology* **26**, 523-526.

Tepper J. H. and Kuehner S. M. (1999) Complex zoning in apatite from the Idaho batholith: A record of magma mixing and intracrystalline trace element diffusion. *Am. Mineral.* **84**, 581-595.

Walker S. M. and Becker U. (2015) Uranyl (VI) and neptunyl (V) incorporation in carbonate and sulfate minerals: Insight from first-principles. *Geochim. Cosmochim. Acta* **161**, 19-35.

Winther K. T., Watson E. B. and Korenowski G. M. (1998) Magmatic sulfur compounds and sulfur diffusion in albite melt at 1 GPa and 1300–1500 C. *Am. Mineral.* **83**, 1141-1151.

Chapter V. Thermodynamic mixing properties of alunite supergroup minerals: Quantum-mechanical modeling and thermodynamic analysis of sulfate, chromate, selenate, phosphate, and arsenate solid solutions, as well as uranyl incorporation

Abstract

In various geological settings, alunite supergroup minerals including the end members alunite [$KAl_3(SO_4)_2(OH)_6$] and jarosite [$KFe_3(SO_4)_2(OH)_6$] occur in extensive solid solution on the cation and anion sites, enabling them to accommodate a variety of elements. Jarosite is known for scavenging heavy metals on the K site (e.g., Pb in solid solution between jarosite and plumbojarosite) in acid mine drainage settings, while both jarosite and alunite can be important in controlling toxic anions such as selenate, chromate, or arsenate. However, there is no thermodynamic information on the solubility of these important cations and anions as a function of temperature, in part because this information is difficult to obtain experimentally. In this study, thermodynamic mixing properties of sulfate-chromate (S-Cr) and sulfate-selenate (S-Se) solid solution and of sulfate-phosphate-arsenate (S-P-As) solid solutions in alunite supergroup minerals are investigated based on quantum-mechanical modeling and statistical thermodynamic analysis.

S-Cr and S-Se solid solutions in alunite and jarosite are due to the mixing of anions with equivalent charges on the sulfate site. The enthalpy of mixing (ΔH_{mix}) is lowest at 0 K (-273 ℃) and increases

with increasing temperature; it also depends on the arrangement of atoms on the sulfate site (i.e., atomic ordering). ΔH_{mix} is almost constant at -70 ℃ and higher temperatures. These findings imply that S-Cr and S-Se solid solutions tend to be complete at room temperature and no ordering is acquired at or above ambient conditions. The Gibbs free energy of mixing (ΔG_{mix}) indicates that the jarosite structure is more flexible to accommodate chromate and selenate at the sulfate site than the alunite structure and that complete solid solution can be formed between jarosite and both Se- and Cr-analogues at temperatures above -80 ℃. Along with the energetic data of uranyl (UO_2^{2+}) incorporation into jarosite-type minerals showing that uranyl could be potentially associated with the formation of Pb-bearing jarosite, our modeling results of solid solutions in jarosite and alunite demonstrate the critical role of alunite supergroup minerals in controlling toxic elements for long-term immobilization.

S-P-As solid solution is also explored between alunite family minerals [$DAl_3(TO_4)_2(OH, H_2O)_6$] (D is K^+, Na^+ or Ca^{2+}; TO_4 is SO_4^{2-}, PO_4^{3-} or AsO_4^{3-}). The energetic barrier (as indicated by the maximum ΔH_{mix}) for mixing between ions with different charges (i.e., S-P and As-S solid solution; ~2 to 3 kJ/mol of exchangeable atoms) is higher by a factor of two or three compared to anions with the equal charge (P-As solid solution; 1 to 1.5 kJ/mol of exchangeable atoms). Below 700 °C, ternary S-P-As mixing over a range of compositions in ternary space having alunite, crandallite [$CaAl_3(PO_4)_6(OH)_5(H_2O)$], and arsenocrandallite [$CaAl_3(AsO_4)_6(OH)_5(H_2O)$] as end members shows large miscibility gaps at compositions close to the ratio of S:P:As = 4:1:1 and 1:1:1 at the TO_4 site. Ternary S-P-As mixing between woodhouseite, arsenowoodhouseite, and one of alunite and natroalunite shows that arsenate is more compatible with sulfate in natroalunite than sulfate in alunite whereas substitution of sulfate with phosphate is energetically more favorable in alunite than natroalunite. Our computed phase diagrams of S-P-As mixing suggest

that binary solid solutions between pairs of sulfate, phosphate and arsenate in alunite family minerals scarcely occur below 100 °C, is limited at temperatures from 100 to 300 °C and become extensive or complete above 300 °C.

1. INTRODUCTION

The alunite mineral supergroup has the general formula of $DG_3(TO_4)_2(OH, H_2O)_6$ (Dutrizac and Jambor, 2000). The D sites are occupied by monovalent, divalent, or trivalent cations, G is mainly Al^{3+} or Fe^{3+}, and TO_4 can be SO_4^{2+}, AsO_4^{3-}, PO_4^{3-}, or CrO_4^{2+}. Jarosite [(K, Na)$Fe_3(SO_4)_2(OH)_6$] and alunite [(K, Na)$Al_3(SO_4)_2(OH)_6$] are two representative minerals of the alunite supergroup and their occurrences are predominant in acidic aqueous and subsoil environments. A variety of metal cations including lead, copper, and zinc can substitute for K^+ and Na^+ in these minerals (Hochella Jr et al., 1999; Hochella Jr et al., 2005). The flexible structure of jarosite and alunite can also host anions other than sulfate such as chromate, selenate, arsenate, and phosphate and is important in controlling the mobility of these toxic elements associated with the oxidation of sulfide and chromite ores. While the alkali ions replacement has been extensively studied, the thermodynamic understanding of solid solution forms between anions in alunite supergroup minerals has not been well established (Stoffregen et al., 2000).

Although subdivision of the supergroup minerals can be variable, classification based on the occupant of the atomic sites is widely accepted (Jambor, 1999; Dutrizac and Jambor, 2000; Stoffregen et al., 2000). With regards to the occupancy of the G site, the supergroup can be subdivided into the jarosite (Fe rich) or alunite (Al rich) family. Further subdivision can be made based on the dominant anion at the TO_4 site. Minerals with the predominance (≥ 75 %) of SO_4^{2+} belong to the alunite group, and minerals with the predominance of PO_4^{3+} and AsO_4^{3+} are classified into the crandallite and arsenocrandallite group, respectively (Fig. 5. 1).

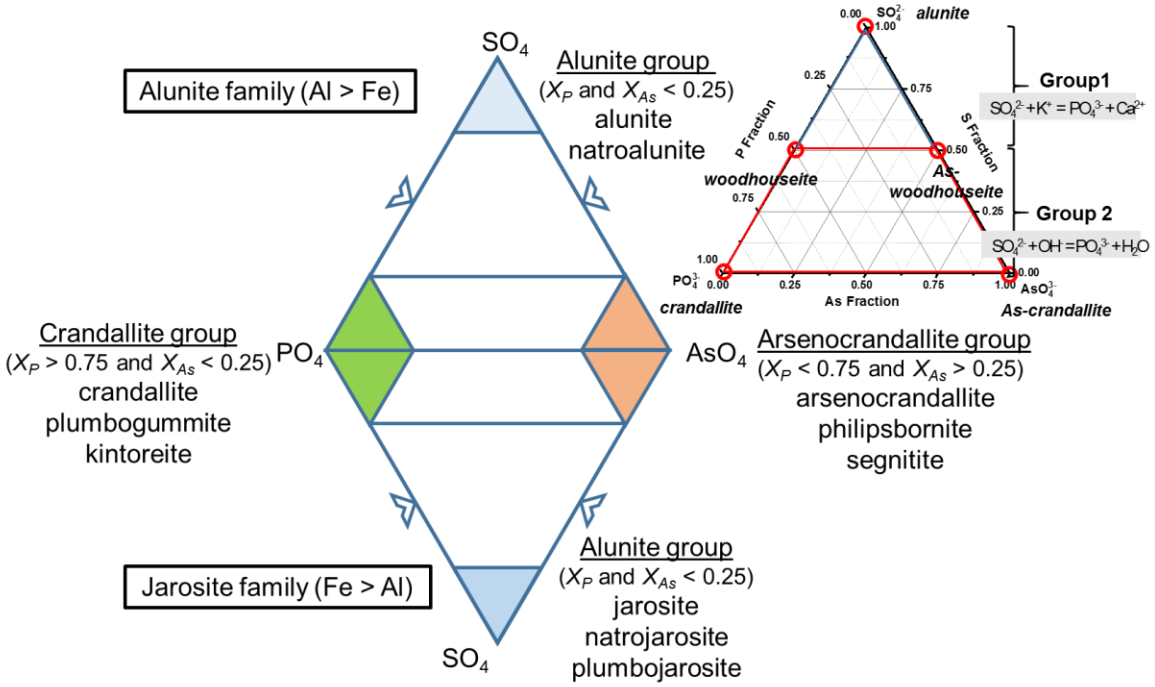

Fig. 5. 1. Classification of the alunite supergroup members with some examples of each subgroup. The lines inside the diagram show the TO4 compositional limits with respect to the molar fraction of phosphate (XP) and arsenate (XAs) (modified from Jambor, 1999). Inlet: Alunite family minerals studied in this study with two substitution mechanisms needed for mixing between those minerals.

Jarosite has been mostly considered a supergene mineral whereas its occurrence as a hypogene mineral is reported but rare relative to alunite (Dutrizac and Jambor, 2000; Stoffregen et al., 2000). Recently, there has been an increasing awareness that the discovery of jarosite on Mars may be evidence of chemical weathering processes under relevant martian conditions (Madden et al., 2004; Morris et al., 2004). Oxidation of sulfide ores gives rise to acidic sulfate-rich environments where alkali elements such as K^+ and Na^+ can be released from weathering of aluminosilicates (e.g., clay minerals). As a result, sulfate minerals such as alkali-dominant jarosite can be precipitated as a secondary phase. Jarosite or natrojarosite, $[NaFe_3(SO_4)_2(OH)_6]$, is precipitated depending on the relative proportion of Na/K in solutions, but the formation of natrojarosite

requires a fairly high Na/K ratio due to the greater thermodynamic stability of K-rich jarosite minerals (Dutrizac and Jambor, 2000). Also, jarosite- and natrojarosite-bearing soils are widespread in association with soil acidification (pH 3 to 4) including marine sediments with pyrite and mine tailings. Jarosite is stable as a mineral phase at acidic pH (typically pH < 3 where the D site can also be occupied by H_3O^+), but can be dissolved and transformed into other Fe-bearing minerals such as goethite in neutral and alkaline solutions. The stability of alunite supergroup mineral species is important in environmental studies of mineral deposits and of waste materials from mining and mineral processing because its formation and dissolution are related to the release of a variety of potential contaminants into aqueous and subsoil environments (Hochella Jr et al., 1999; Becker and Gasharova, 2001; Hochella Jr et al., 2005). Concentrations of toxic elements are high in oxidation regions of sulfide and chromite mines where jarosite formation is accompanied by the production of sulfate and protons. The flexible structure of jarosite makes it an important scavenger mineral for heavy metals (e.g., Pb^{2+}, Cu^{2+}, Cd^{2+}, Zn^{2+}) at the D site and anions other than sulfate such as chromate, selenate and arsenate at the TO_4 site. In such settings, solid solution in the jarosite structure where contaminants occupy the cation or anion site over a range of fraction is likely to form and is an important factor in evaluating the mobility of contaminants (Schindler and Hochella Jr, 2015; Schindler et al., 2016). One such discovery is reported by Baron et al. (1996) that Cr-equivalent jarosite [$KFe_3(CrO_4)_2(OH)_6$] has been identified in chromium contaminated soils. A follow-up experimental study by Baron and Palmer (2002) demonstrates the formation of extensive solid solution between sulfate and chromate, [$KFe_3((Cr_xS_{(1-x)})O_4)_2(OH)_6$] ($x$ being between 0 and 1). Another relevant finding is that Se-substituted jarosite, [$KFe_3((Se_xS_{(1-x)})O_4)_2(OH)_6$] can be prepared by precipitation from aqueous solution and jarosite and Se-analogue form a nearly ideal solid solution series (Dutrizac et al., 1981). It has been experimentally

demonstrated that some lanthanide and actinide elements such as Sc, Y, and U (as uranyl) could be potentially hosted in jarosite-type minerals (Dutrizac and Chen, 2009). Although its formation is not as common as jarosite in the oxidized region of sulfide ores and acid mine drainage, alunite can accommodate a variety of contaminants due to its flexible structure. Therefore, alunite has been suggested as a potential host mineral that can incorporate toxic elements for long-term immobilization (Kolitsch and Pring, 2001).

Alunite occurs in various geologic settings including sedimentary, hydrothermal, and metamorphic rocks. The formation of natural alunite occurs at different temperatures including ambient (< 100 °C) for near-surface environments, higher temperatures (e.g., ~200 to 300 °C) such as hydrothermal settings, and temperatures up to ~ 500 °C for some instances of intermediate-grade metamorphism (Alpers and Brimhall, 1988; Stoffregen and Alpers, 1992; Stoffregen et al., 2000). The morphology and size of alunite tend to be dependent on the formation temperature (Stoffregen and Alpers, 1992; Stoffregen et al., 2000). Blade-shaped crystals or coarse vein grains of alunite may occur in sizes of a few millimeters in hot springs (~ 200 to 300 °C), whereas fine-grained alunite (few μm in size) is often found within veinlets or sediments that occur at lower temperatures. The formation temperature is also considered an important factor in determining the degree of solid solution in alunite. Substitution of sulfate for phosphate (PO_4^{2-}) occurs in natural alunite formed in magmatic-hydrothermal deposits (Allibone et al., 1995). This substitution is proportional to divalent cations such as Ca^{2+}, Sr^{2+}, and Ba^{2+} that replace K^+ (or Na^+ in natroalunite) in the mineral structure which supports the replacement mechanism of $SO_4^{2-} + K^+ \leftrightarrow PO_4^{3-} + Ca^{2+}$. Only a limited degree of such coupled substitution is observed from magmatic-related hypogene alunite formed at temperatures below 300 °C, although solid solution is inferred to be more

extensive at higher temperatures (Stoffregen et al., 2000). Due to similar sizes and trivalent charges of phosphate and arsenate (P-O and As-O distances, ~1.5 and ~1.6 Å in the molecular geometry), the substitution of sulfate for arsenate (AsO_4^{2-}) is expected to be comparable with the substitution for phosphate and thus seems possible to be observed at high temperatures. In this sense, the effect of formation temperature on the S-As-P solid solution in alunite is important for understanding the compositional variation observed in natural alunite (Novak et al., 1994; Allibone et al., 1995; Ripp and Kanakin, 1998). Although the S-As-P solid solution is among the most notable solid solutions formed in the alunite supergroup, little experimental or theoretical work has been done for solid solutions related to phosphate or arsenate at the TO_4 site (Dutrizac and Jambor, 2000).

In this study, the thermodynamic properties of the solid solution series at the TO_4 site of the alunite supergroup mineral are investigated using quantum-mechanical modeling and statistical thermodynamic analysis. This study focuses on two important groups of solid solutions: 1) the S-Cr and S-Se solid solutions formed in the alunite and jarosite structures 2) the S-P-As solid solution series including crandallite, arsenocrandallite, and alunite (or natroalunite) as end members. In addition, the energetics of incorporation of uranyl (UO_2^{2+}) and lead (Pb^{2+}) is investigated on the basis of the solid-state and aqueous reactions to expand our understanding of jarosite-type minerals as a potential scavenger of heavy metals. Prior to DFT calculation, possible configurations of ion arrangements within each solid solution are created to represent intermediate compositions between the end-member species. Quantum-mechanical modeling applied to these configurations reveals the corresponding excess energy of configurations with respect to a physical mixing of end-members. From these results, the enthalpy of mixing can be derived using statistical thermodynamic analysis and assuming a Boltzmann distribution of energies. Thermodynamic integration then allows for the derivation of Gibbs free energies and configurational entropies of

mixing for respective solid solution series. Vibrational entropies, as derived in Becker and Pollok (2002) that described Al^{3+}/Fe^{3+} replacement, are not within the scope of this study because this study is quantum-mechanics based and full vibrational analysis of all compositions and structures would have been computationally expensive. This computational and statistical thermodynamic evaluation allows for the determination of (1) phase stability and the degree of solid solution as a function of composition and temperature and (2) possible ordering effects (by atomic arrangement in the mineral structure) and mixing properties (e.g., ideality and randomness of mixing) upon the formation of solid solution. Such a theoretical approach enables the derivation of equilibrium properties as a function of temperature and is, therefore, a tool to predict if, e.g., certain solid solutions will have a tendency to exsolve at a long-term time scale. This work is the first to evaluate the extent to which solid solutions between alunite supergroup minerals occur (i.e., the solid solution limit) as a function of temperature. In the discussion section, our computed data are revisited and are found to be consistent with previous experimental and field observations on alunite supergroup minerals. The thermodynamic data derived from this study suggest the significance of solid solution formation of alunite supergroup minerals over a wide range of temperature in various geochemical systems. The data support the idea that jarosite can accommodate foreign ions even at extremely low temperatures and thus be indicative of aqeous and biological processes on the Mars surface. Our modeling results provide some thermodynamic bases for evaluating the critical role of jarosite, alunite, and crandallite in controlling toxic elements for long-term immobilization in aqueous and subsoil environments and for using the mixing properties of alunite family minerals as an indicator for the equilibrium temperature of their formations in magmatic-hydrothermal systems.

2. Methods

2.1. Computational methods

The computational approach adopted in this study is based on density functional theory (DFT) where planewaves represent functions for the overall wave function and the core electrons of an atom and their interactions with the valence electrons are approximate to pseudopotentials. The optimization was performed using the quantum-mechanical (QM) code CASTEP (Segall et al., 2002). The Perdew-Wang generalized gradient scheme (GGA) was used along with ultrasoft pseudopotentials (Perdew et al., 1996). An energy cutoff for planewave expansion was chosen to be 400.0 eV and the Brillouin zone was sampled using a 3 × 3 × 1 k-point grid according to the Monkhorst-Pack scheme (Monkhorst and Pack, 1976). Self-consistent field cycles were assumed to converge with an energy difference of less than 2.0×10^{-6} eV/atom. A spin-polarized approach was implemented in cases of the jarosite solid solution series containing Fe^{3+} to enable the five unpaired spins in the Fe 3d orbital to adopt the lowest-energy configuration. All calculations were performed with the primitive unit cell (P1, no symmetry restrictions). By using these computational parameters, a good agreement is found between calculated and experimental cell parameters of alunite supergroup minerals (Table 5. 1).

Table 5. 1. Lattice parameters of natural and calculated (CASTEP) alunite supergroup minerals

	Calculated		Experiment		Deviation (%)		Reference
	a (Å)	c (Å)	a (Å)	c (Å)	a (Å)	c (Å)	
Jarosite	7.4	17.4	7.3	17.1	2.2	2.0	Mills et al. (2013)
Cr-equv. jarosite	7.5	17.8	7.4	17.8	1.5	0.1	Cudennec et al. (1980)
Se-equv. jarosite	7.5	18.0	7.4	17.4	1.8	3.2	Dutrizac et al. (1981)
Alunite	7.1	17.6	7.0	17.3	1.3	1.9	Zema et al. (2012)
natroalunite	7.1	17.0	7.0	16.9	0.9	0.6	Okada et al. (1982)
Cr-equv. alunite	7.2	18.1	7.1	17.8	1.1	1.8	Cudennec et al. (1980)
Se-equv. alunite	7.1	17.9	–	–	–	–	–
crandallite	7.2	16.2	7.0	16.2	2.1	0.0	Blount (1974)
arsenocrandallite	7.2	16.7	7.1	17.3	1.9	3.1	Lengauer et al. (1994)
woodhousite	7.0	16.4	7.0	16.2	1.0	1.0	Kato (1971)

2.2. The structure model of the alunite group mineral

As structural models, the unit cells of alunite, natroalunite, and jarosite ($R\bar{3}m$) were chosen, with three $KAl_3(SO_4)_2(OH)_6$, $NaAl_3(SO_4)_2(OH)_6$ and $KFe_3(SO_4)_2(OH)_6$ formula units (Z = 3, 78 atoms), respectively (Fig. 5. 2). The unit cell contains six exchangeable TO_4 anion sites (labelled T1 to T6 in Fig. 5. 2A) and three exchangeable D cation sites. O atoms at the O1 and O2 sites belong to TO_4 and the O atom of the hydroxide anion (OH^-) occupies the O3 site (Fig. 5. 2A). The H atom of the hydroxide anion forms hydrogen bonds with adjacent O atoms such that it is oriented toward the nearest O1 or O2 site. Prior to full energy optimization using DFT calculation, possible configurations were created by replacing S at the TO_4 site with other elements including Cr, Se, P and As, and replacing Na and K at the D site with Ca as necessary to comprise solid solution compositions of interest. Each solid solution configuration represents one solid solution state with a certain atomic arrangement in the structure. The internal energy change (ΔE_n^{α}) is calculated for

every single state of solid solution and statistical thermodynamic analysis is undertaken to calculate thermodynamic quantities of mixing as described in section 2.3 .

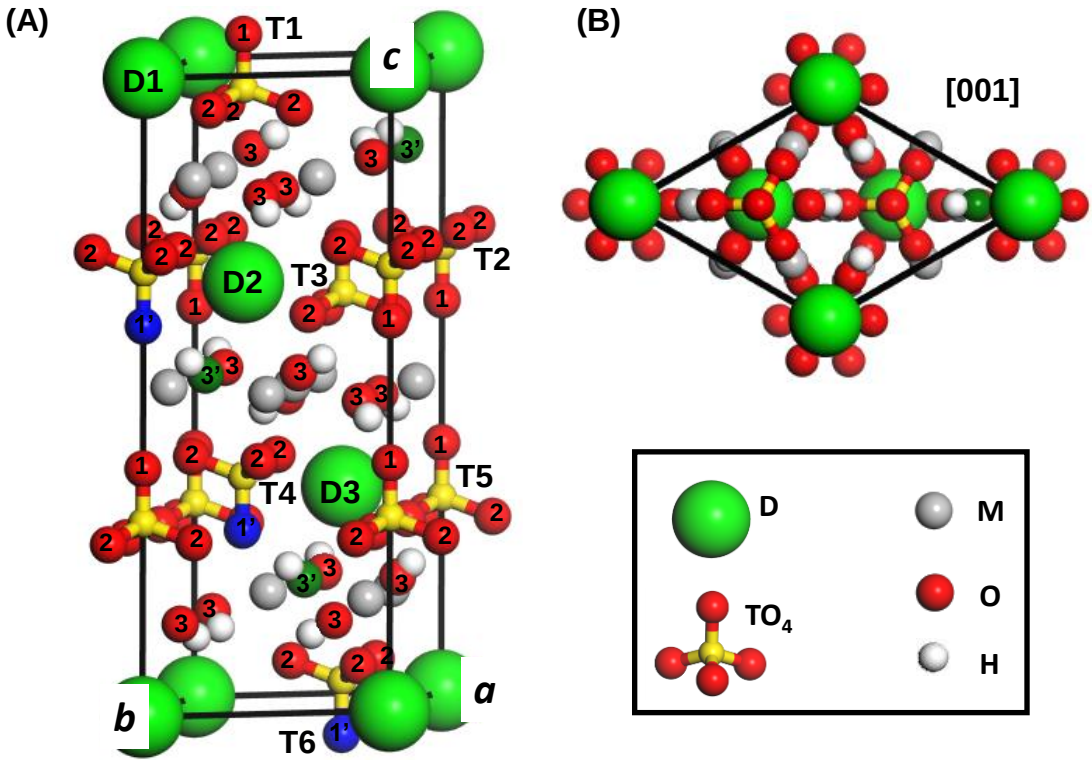

Fig. 5. 2. Different views on the bulk structure of the alunite supergroup mineral used in this study. (A) The view in [110] direction and (B) in [001] direction. In (A), the D and TO4 sites are labeled D1 to D3 and T1 to T6, respectively. The O atoms (red ball) are labeled 1, 2 and 3 to stand for the O1, O2 and O3 sites, respectively. The oxygen atoms labeled 1' and 3' (green and blue balls) represent oxygen sites at which water molecules are positioned in model configurations of phosphate- or arsenate-bearing minerals (O3') and their nearest O1 sites (O1').

Binary mixing between CrO_4^{2-} and SO_4^{2-} and between SeO_4^{2-} and SO_4^{2-} is simulated using the structure of alunite and jarosite having sulfate as the main anion. The six exchangeable sites allow for the generation of 36 symmetry-unique configurations which represent seven solid solution compositions (molar fraction of Cr or Se at the S site = 0, 1/6, 1/3, 1/2, 2/3, 5/6 and 1).

In order to investigate thermodynamic properties of the S-P-As solid solution in alunite family minerals, alunite and natroalunite are selected as the end member species for SO_4^{2-}, crandallite and arsenocrandallite as the end member species for PO_4^{3-} and AsO_4^{3-}, respectively (Fig. 5. 1). The S-P-As solid solution includes three subseries of the binary mixing system, namely, S-P, S-As and P-As solid solutions. No charge compensation is necessary upon the P-As solid solution whereas the S-P and S-As solid solutions are based on mixing between two anions with different charges, sulfate, and one of phosphate and arsenate. The charge imbalance at the TO_4 site must be compensated by another substitution at the D or OH site. This can lead to two replacement mechanisms

$$\text{Mech. 1: } SO_4^{2-} + D^{n+} \leftrightarrow PO_4^{3-} \left(\text{or } AsO_4^{3-}\right) + D^{(n+1)+} \quad (1)$$

$$\text{Mech. 2: } SO_4^{2-} + OH^- \leftrightarrow PO_4^{3-} \left(\text{or } AsO_4^{3-}\right) + H_2O. \quad (2)$$

Depending on the sulfate-bearing end member (alunite or natroalunite) involved in the S-P and S-As solid solution, Eq. 1 (Mech. 1) can be specified into

$$\text{Mech. 1 (K): } SO_4^{2-} + K^+ \leftrightarrow PO_4^{3-} \left(\text{or } AsO_4^{3-}\right) + Ca^{2+} \quad \text{(in alunite)} \quad (3)$$

$$\text{Mech. 1 (Na): } SO_4^{2-} + Na^+ \leftrightarrow PO_4^{3-} \left(\text{or } AsO_4^{3-}\right) + Ca^{2+} \quad \text{(in natroalunite).} \quad (4)$$

In the alunite family subgroup, alunite, crandallite, and arsenocrandallite are mineral species in which the TO_4 site is fully occupied by one of sulfate, phosphate, and arsenate, respectively. The coupled substitution of $SO_4^{2-} + K^+/Na^+ \leftrightarrow PO_4^{3-}$ (or AsO_4^{3-}) + Ca^{2+} at the sulfate site of alunite and natroalunite yields two end members, woodhouseite [$CaAl_3(PO_4)(SO_4)(OH)_6$], and arsenowoodhouseite [$CaAl_3(PO_4)(AsO_4)(OH)_6$]. The fractions of P ($X_P$) and As ($X_{As}$) are one half in the latter two mineral species and another substitution of $SO_4^{2-} + OH^- \leftrightarrow PO_4^{3-}$ (or AsO_4^{3-}) + H_2O is needed to examine S-P-As mixing involving crandallite [$CaAl_3(PO_4)_2(OH)_5(H_2O)$] and

arsenocrandallite [$CaAl_3(AsO_4)_2(OH)_5(H_2O)$] (Fig. 5. 1). Therefore, the S-P-As mixing is examined with two groups of end members individually (see the inlet in Fig. 5. 1): one group has woodhouseite and arsenowoodhousite and one of alunite and natroalunite, which accounts for the variation in the S fraction (X_S) between 0 and 0.5 and another group comprises woodhousite, arsenowoodhouseite, crandallite and arsenocrandallite, ones with $X_S = 0.5$ or 1. In the initial model configurations of crandallite and arsenocrandallite (Z = 3 formula units), there are three Ca^{2+} cations and three H_2O molecules that can be used to test Mech. 1 and 2, respectively. The arrangement of three exchangeable atoms at the D or OH site produces eight possible configurations of solid solution that represent four compositions (X_P or X_{As} = 0, 1/6, 1/3 and 1/2 for solid solutions between alunite / natroalunite and woodhouseite / arsenowoodhouseite; X_P or X_{As} = 1/2, 2/3, 5/6 and 1 for solid solutions between woodhouseite / arsenowoodhouseite and crandallite / arsenocrandallite) for respective mixing mechanisms. In building model configurations for intermediate compositions, three exchangeable TO_4 sites (T1, T3 and T5) are selected for testing Mech. 1 in which sulfate and one of phosphate and arsenate replace one another, and the nearest D site (D1 to D3) is occupied by K^+, Na^+ or Ca^{2+}. For Mech. 2, TO_4 sites, T2, T4 and T6, are chosen for the anions to occupy while the nearest O3 site to phosphate or arsenate (labeled O3' in Fig. 5. 2A) is occupied by H_2O.

2.3. Statistical thermodynamic analysis of solid solution

The goal of this section is to formulate thermodynamic variables of a solid solution system using energies calculated from quantum mechanical modeling. The formulation is mainly based on statistical thermodynamic principles. If the energy of a system in a particular state *n* (= 1, 2,

3···) is E_n, then according to the Boltzmann distribution, the probability p_n of that state is given by

$$p_n = \frac{\exp(-\frac{E_n}{K_B T})}{\sum_n \exp(-\frac{E_n}{K_B T})} = \frac{\exp(-\frac{E_n}{K_B T})}{Q} . \quad (5)$$

where K_B is the Boltzmann constant and $T$is the temperature of the system. The denominator, $Q = \sum_n \exp(-\frac{E_n}{K_B T})$, is called the canonical partition function for the system and the key to statistical mechanics because it can be used to calculate all the thermodynamic properties of the system.

The internal energy (E_n) of a macroscopic system with a certain number of possible microscopic states n (= 1, 2, 3···) can be identified with the mean energy calculated as

$$E = \frac{\sum_n E_n \exp(-\frac{E_n}{K_B T})}{\sum_n \exp(-\frac{E_n}{K_B T})} . \quad (6)$$

Equation (6) can be described as the mean of the energy where the individual energy (E_n) of a specific configuration (n) is weighted by its probability to occur (i.e., by its Boltzmann factor).

The Helmholtz free energy of a system (F) is proportional to the canonical partition function and is calculated as

$$F = -K_B T \ln\left[\sum_n \exp\left(-\frac{E_n}{K_B T}\right)\right] = -K_B T \ln Q . \quad (7)$$

Given that a solution is a homogeneous mixture of two or more substances in gas, liquid, solid, or ionic states, the molar enthalpy (H) and Gibbs free energy (G) of a solution phase α read as

$$H = \sum_i X_i \bar{H}_i^{\alpha} + \Delta H_{mix} \quad (8)$$

$$G = \sum_i X_i \mu_i^{\alpha} + \Delta G_{mix} \quad (9)$$

where X_i is the molar fraction of component i, $\overline{H_i^\alpha}$ and μ_i^α are the partial molar enthalpy and chemical potential of α with respect to component i, respectively, and ΔH_{mix} and ΔG_{mix} are the enthalpy and Gibbs free energy of mixing, respectively. For the binary mixing system, end member mineral phase A and B form solid solution phase α = $A_xB_{(1-x)}$ (x is the molar fraction of A between 0 and 1) and the generalized reaction equation can be expressed as

$$xA + (1 - x)B = A_xB_{(1-x)}. \quad (10)$$

The electronic energies of model configurations are calculated from the quantum-mechanical modeling using CASTEP and used to calculate the reaction energy of this balanced equation. Our calculations are formally for the ground state of a model configuration, and the calculated reaction energy is equivalent to the internal energy change (ΔE_n^α) upon the process of mixing (e.g., Feng et al., 2006; Shuller et al., 2013). The enthalpy change upon the formation of solid solution is related to the internal energy and can be expressed as

$$\Delta H_n^\alpha = \Delta E_n^\alpha + p\Delta V \quad (11)$$

where ΔV is the volume change and p is the pressure. In a solid, the volume change is quite small, and the internal energy is large relative to the value of $p\Delta V$ under the atmospheric pressure (Shigemi and Wada, 2004). Therefore, the enthalpy change can be computed from the internal energy change. In the same manner, the Gibbs free energy change is evaluated directly by determining the Helmholtz free energy (Eq. 12).

$$\Delta G_n^\alpha = \Delta F_n^\alpha + p\Delta V \quad (12)$$

Specifically, in the binary mixing system, these thermodynamic quantities of solid solution phase α at a given composition, x, and temperature, T can be formulated using Eq. 6 to 9 as follows:

$$\Delta H_{mix}(x,T) = H(x,T) - [xH_A(T) + (1-x)H_B(T)] = \frac{\sum_n \Delta E_n \cdot \exp(-\frac{\Delta E_n^{\alpha}}{K_B T})}{\sum_n \exp(-\frac{\Delta E_n^{\alpha}}{K_B T})}$$

(13)

$$\Delta G_{mix}(x,T) = G(x,T) - [xG_A(T) + (1-x)G_B(T)] =$$

$$-K_B T \ln[\sum_n \exp\left(-\frac{\Delta E_n^{\alpha}}{K_B T}\right)]. \qquad (14)$$

ΔG at arbitrary temperature T_1, $\Delta G(T_1)$ can be numerically calculated from the thermodynamic relations $H = \frac{\partial(G/T)}{\partial(1/T)}$ and $\Delta H = \frac{\partial(\Delta G/T)}{\partial(1/T)}$, thus

$$\frac{\Delta G(x,T_1)}{T_1} = \lim_{T\to\infty}\left[\frac{\Delta G(x,T)}{T}\right] + \int_{T_1}^{\infty} \frac{\Delta H(x,T)}{T^2}\, dT$$

(15)

$$\lim_{T\to\infty}[\Delta G(x,T)/T] = \lim_{T\to\infty}\left[-k_B \ln \sum_i \exp\left(-\frac{\Delta E_i}{K_B T}\right)\right] = -k_B \ln \Omega$$

(16)

where Ω is the number of distinguishable microscopic states corresponding to a macroscopic state of a system. For random mixing of species K and L (i.e., simple binary mixing), the number of ways that n_K of K and n_L of L are distributed over the total of N (= n_K + n_L) sites is given by

$$\Omega = \frac{N!}{n_K! n_L!}. \qquad (17)$$

If the magnitude of N is on the order of 10^{23} or Avogadro's number, the definition of entropy leads to Sterling's approximation for large N (i.e., $\ln N! \approx N \ln N - N$),

$$S = k_B \ln \Omega \cong N k_B \left[\frac{n_K}{N} \ln \frac{N}{n_K} + \frac{n_L}{N} \ln \frac{N}{n_L}\right] = -R(X_K \ln X_K + X_L \ln X_L) \qquad (18)$$

where *R* is the gas constant. This entropy is called the point entropy and is a function of the number of energy-equivalent ways of arranging atoms on the available lattice sites (i.e., random mixing) (Ganguly and Saxena, 2012). For a hypothetical or real solution in which energy of configurations is dependent on the way of arranging atoms at the sites (i.e., ordering), correction is needed to consider the deviation of the corresponding mixing from random mixing (Eq. 19).

Combining Eq. 15 to 18 gives rise to molar Gibbs free energy of mixing defined as

$$\Delta G_{mix}(x,\ T) = \underbrace{RT\ [x \ln x + (1-x)\ln(1-x)]}_{contribution\ of\ random\ mixing} \quad + \quad \underbrace{T \cdot \int_T^{\infty} \frac{\Delta H_{mix}\,(\mathrm{x,T})}{T^2}\, dT}_{contribution\ of\ ordering}. \tag{19}$$

One important principle applied in this study is that a solid solution is randomly mixed in its ideal state. If a solid solution is ideal, there is no significant energy change involved in the rearrangement of ions on a given site. Non-ideal solid solutions are not randomly mixed because energy of the solid solution system is dependent on the arrangement of atoms. This principle has been successfully applied to explain solid solutions for several examples of natural minerals described by Ganguly and Saxena (2012). For binary mixing systems it follows that the Gibbs free energy of mixing in ideal solution reads as

$$\Delta G_{mix}^{ideal}(x,T) = RT\ [x \ln x + (1-x)\ln(1-x)]$$

. (20)

The difference between a thermodynamic property of a solution (real or hypothetical one) and the corresponding ideal solution property is defined as an excess thermodynamic property (Ganguly and Saxena, 2012). From Eq. 19 and 20, the excess Gibbs free energy is expressed as

$$\Delta G_{mix}^{xs}(x,T) = \Delta G_{mix}(x,T) - \Delta G_{mix}^{ideal}(x,T) = T \cdot \int_T^{\infty} \frac{\Delta H_{mix}\,(\mathrm{x},\tau)}{\tau^2}\, d\tau. \tag{21}$$

Therefore, the Gibbs free energy of mixing is the sum of the Gibbs free energy of mixing in ideal solution (the first term on the right side of Eq. 19) and the excess Gibbs free energy of mixing (the second term). Ideality and randomness of mixing in solid solution will be discussed further in section 4.1. Once the molar Gibbs free energy and enthalpy of mixing are obtained, calculating the molar entropy of mixing is straightforward (Eq. 22)

$$\Delta S_{mix} = \frac{\Delta H_{mix} - \Delta G_{mix}}{T}. \quad (22)$$

2.4. Evaluation of incorporation energy

The method and background of computational evaluation of incorporation energy based on the solid-state reaction are well documented in the literature (Walker and Becker, 2015; Kim et al., 2017). Briefly, the reaction equation of U-incorporation into jarosite consists of a pure (i.e., end member) and impure (i.e., trace-element bearing) jarosite in the form of host and U-incorporated jarosite. Accordingly, appropriate solid sources for U and sinks for ions replaced in the mineral host are selected to maintain stoichiometry. In Table 5. 2, end member potassium jarosite and plumbojarosite, and Pb-bearing jarosite (Pb:K = 1:1) are host minerals to accommodate the uranyl ion (UO_2^{2+}) that is sourced from uranyl chloride (UO_2Cl_2). The equation is balanced by the U-incorporated jarosite and the chloride sink phases such as cotunnite ($PbCl_2$) and sylvite (KCl) that are products as a result of incorporation. Once the energies of all phases involved in the incorporation equations are computationally constrained, the reaction energies of the respective incorporation equations can be calculated using the general approach:

$$\Delta E_{rxn} = \sum E_{prod} - \sum E_{reac}. \quad (23)$$

The resulting incorporation reaction energy indicates the stability of the S-incorporated jarosite relative to the corresponding host jarosite and the source and sink phases. The relative stability of various incorporated phases can be compared when common source phases are used (Kim et al., 2017). One computational approach documented by Walker and Becker (2015) is adopted in this study to evaluate the incorporation energy of the hydrated uranyl ion into potassium and plumbojarosite phases. The atomistic assessment for hydrated ions incorporated into mineral phases involves a series of reaction equations that have to be combined to constraint species with different characters (hydrated vs. vacuum, charged vs. neutral, clusters vs. 3D periodic). The overall balanced equation involves the host and U-incorporated jarosite phases and the hydrated UO_2^{2+}, Pb^{2+} or K^+ ions in place of the corresponding source and sink solid phases (Table 5. 2, V to VIII).

Table 5. 2. Reaction equations and energies of incorporation of UO_2^{2+} and Pb^{2+} into jarosite group minerals.

	Incorporation reaction (solid source and sink phases)							ΔE (kJ/mol)
I.	$KPbFe_9(SO_4)_6(OH)_{18(s)}$ Pb-bearing jarosite	+	$UO_2Cl_{2(s)}$	↔	$K(UO_2)Fe_9(SO_4)_6(OH)_{18(s)}$	+	$PbCl_{2(s)}$	-14
II.	$Pb_3Fe_{18}(SO_4)_{12}(OH)_{36(S)}$ plumbojarosite	+	$UO_2Cl_{2(s)}$	↔	$Pb_2(UO_2)Fe_{18}(SO_4)_{12}(OH)_{36(S)}$	+	$PbCl_{2(s)}$	99
III.	$K_3Fe_9(SO_4)_6(OH)_{18(s)}$ potassium jarosite	+	$UO_2Cl_{2(s)}$	↔	$K(UO_2)Fe_9(SO_4)_6(OH)_{18(s)}$	+	$2KCl_{(S)}$	59
IV.	$K_3Fe_9(SO_4)_6(OH)_{18(s)}$ potassium jarosite	+	$PbCl_{2(S)}$	↔	$KPbFe_9(SO_4)_6(OH)_{18(S)}$	+	$2KCl_{(S)}$	72
	Incorporation reaction (aqueous source and sink phases)							ΔE (kJ/mol)
V.	$KPbFe_9(SO_4)_6(OH)_{18(s)}$ Pb-bearing jarosite	+	$UO_2^{2+}{}_{(aq)}$	↔	$K(UO_2)(SO_4)_6(OH)_{18(s)}$	+	$Pb^{2+}{}_{(aq)}$	-95
VI.	$Pb_3Fe_{18}(SO_4)_{12}(OH)_{36(S)}$ plumbojarosite	+	$UO_2^{2+}{}_{(aq)}$	↔	$Pb_2(UO_2)Fe_{18}(SO_4)_{12}(OH)_{36(S)}$	+	$Pb^{2+}{}_{(aq)}$	18
VII.	$K_3Fe_9(SO_4)_6(OH)_{18(s)}$ potassium jarosite	+	$UO_2^{2+}{}_{(aq)}$	↔	$K(UO_2)(SO_4)_6(OH)_{18(s)}$	+	$2K^{+}{}_{(aq)}$	107
VIII.	$K_3Fe_9(SO_4)_6(OH)_{18(s)}$ potassium jarosite	+	$Pb^{2+}{}_{(aq)}$	↔	$KPbFe_9(SO_4)_6(OH)_{18(S)}$	+	$2K^{+}{}_{(aq)}$	202

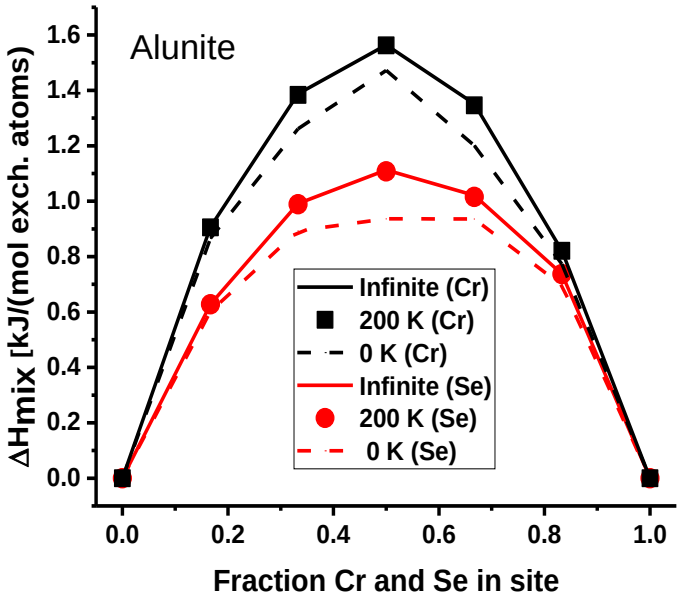

(A)

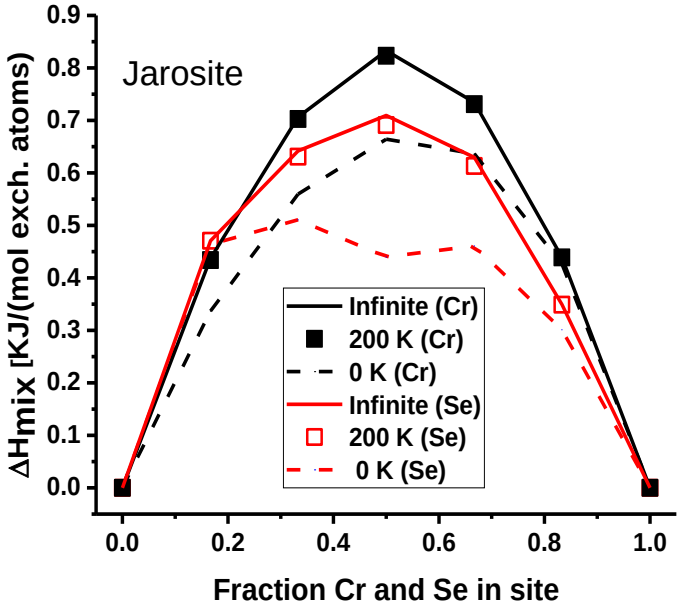

(B)

Fig. 5. 3. The enthalpy of mixing as a function of temperature (A) for Cr and Se at the sulfate site in alunite and (B) in jarosite.

3. RESULTS

3.1. S-Se, S-Cr, and P-As Mixing at the TO_4 site

In Fig. 5. 3, the enthalpies of mixing (ΔH_{mix}) for Cr and Se in alunite and jarosite are presented with respect to the molar fraction of Cr or Se (Cr/(Cr+S) or Se/(Se+S)). The curve of ΔH_{mix} at 0 K represents the lowest energy states of solid solution as a function of molar fraction. The mixing enthalpy increases with temperature as the probability of solid solution states with higher energy increases (Eq. 5). There is a local minimum at 1:1 ratio on the 0 K enthalpy curve of Se mixing in jarosite, which indicates the energetic contribution of ordering of S, and Se (see section 4.1). There are minimal differences of ΔH_{mix} between 200 K and higher temperatures (< 0.02 kJmol^{-1}) for all four solid solution series in alunite and jarosite. The highest enthalpy of mixing is found at a 1:1 ratio of Cr to S and of Se to S for enthalpy curves of 200 K and higher temperatures.

The Gibbs free energy of mixing is numerically calculated using Eq. 19 and presented in Fig. 5. 4. The data are plotted for the discrete values of Cr or Se molar fraction and corresponding fitted curves are added for the temperatures of interest. The curve fitting is based on the Margules formulation. Specifically, excess Gibbs free energy (ΔG^{xs}) is calculated by evaluating Eq. 21 and fitted to Margules functions for binary mixing as described by Ganguly and Saxena (2012) (Eq. 24).

$$\Delta G^{xs} = (W_B^G X_A + W_A^G X_B) X_A X_B \tag{24}$$

where W_A^G and W_B^G are referred to as Margules parameters and X_A and X_B (X_A + X_B = 1 for the binary system) are the molar fraction of mineral species A (alunite or jarosite) and B (Cr- or Se-analogue). Therefore, fitted curves are formulated from the combination of Eq. 19 and 24 as

$$\Delta G_{mix}(x,T) = RT\,[x \ln x + (1-x)\ln(1-x)] + x(1-x)[W_{\mathrm{B}}^G x + W_{\mathrm{A}}^G (1-x)] \tag{25}$$

where x is the molar fraction of Cr or Se. Excess Gibbs free energy (ΔG^{xs}) is a function of temperature, so W_A^G and W_B^G are evaluated for respective temperatures and the root mean square deviation (RMSD) between calculated and fitted molar Gibbs free energies (ΔG_{mix}) is less than 0.04 kJ/mol of exchangeable atoms (Fig. 5. 4).

The Gibbs free energy of mixing for Cr and Se in alunite and jarosite shows distinct patterns as temperature changes. At low temperatures (< ~150 K for jarosite and < ~250 K for alunite), there are two local minima, at molar fractions greater and less than 0.5, respectively, and there is a region of the positive Gibbs free energy of mixing between these minima. As it goes to intermediate temperatures, two local minima exist, but the free energy of mixing is negative over an entire range of molar fraction. At high temperatures (> ~ 200 K for jarosite and > ~350 K for alunite), the Gibbs free energy of mixing is of negative values with one global minimum approximately at a molar fraction of 0.5.

The enthalpy and Gibbs free energy of mixing for the solid solution between crandallite and arsenocrandallite (the P-As solid solution) are presented in Fig. 5. 5. At low temperatures, the mixing enthalpy curve is asymmetric due to atomic ordering at a As:P ratio of 2:1 (see section 4.1) but becomes symmetric at temperatures above 200 K. Transition from the Gibbs free energy curve with two local minima (potential exsolution for x values between the minima) to the one with one global minimum (complete mixing) occurs at temperatures between 300 and 500 K.

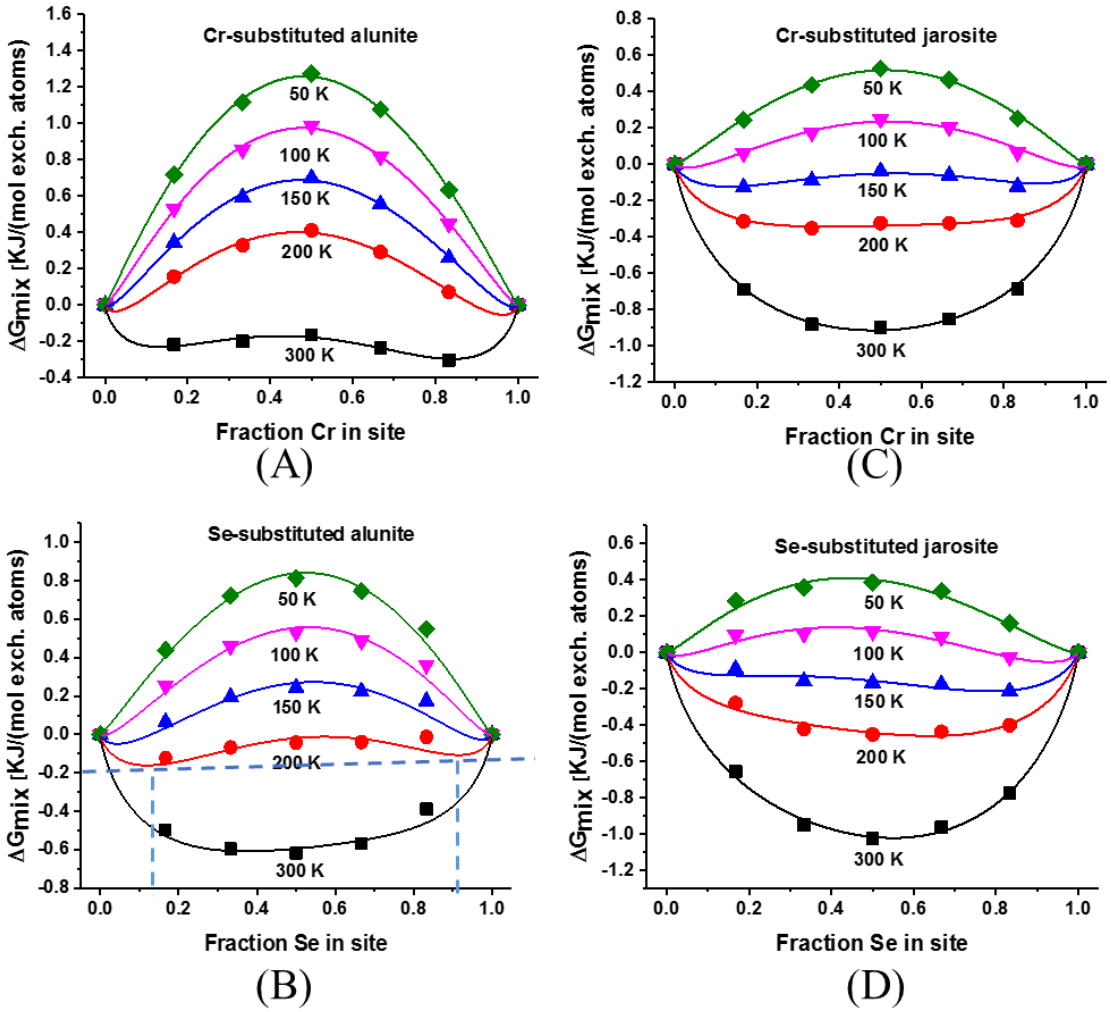

Fig. 5. 4. The Gibbs free energy of mixing as a function of temperature (A) for Cr and (B) Se at the sulfate site in alunite and (C) for Cr and (D) Se at the sulfate site in jarosite. In Fig. 4 B, the common tangent touches the free energy curve derived at 200 K where the Se fraction in Se-substituted alunite is 0.13 and 0.91 (see text for more details).

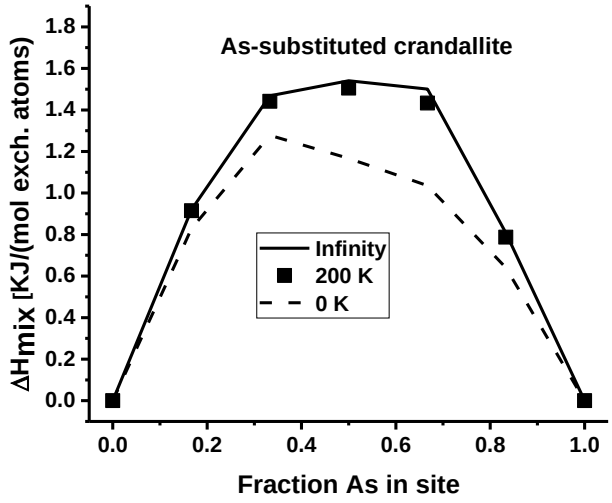

(A)

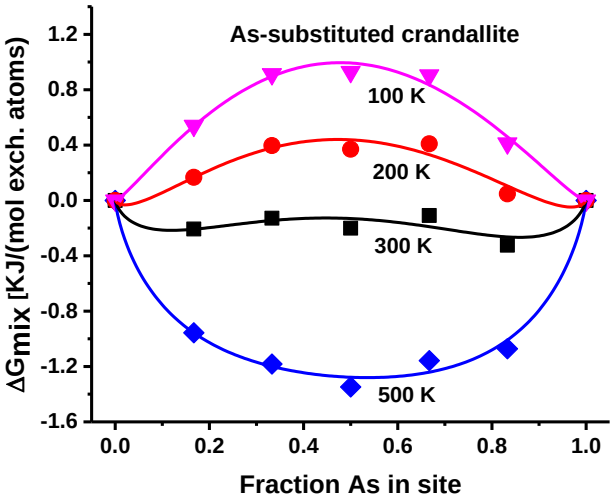

(B)

Fig. 5. 5. (A) The enthalpy of mixing and (B) Gibbs free energy of mixing as a function of temperature for As-P solid solution having crandallite and arsenocrandallite as end member minerals.

3.2. The limit of solid solution in alunite and jarosite as a function of temperature

The molar Gibbs free energy of mixing, $\Delta G_{mix}(x, T)$ is a measure of whether homogeneous mixing prevails over exsolution in the system with a given composition and temperature, that is to say, the spontaneity of homogeneous mixing. In the patterns of the Gibbs free energy shown from mixing between two anions with equivalent charges (Fig. 5. 4 and 5B), positive energy of mixing means the absence of solid solution at a certain range of temperature and composition. There are two local minima at low and intermediate temperatures, which indicate the miscibility gap upon mixing between the two end member minerals. The miscibility gap is overcome at high temperatures by the contribution of the point entropy multiplied by $(-T)$ (Eq. 20) such that solid solution occurs over the whole range of composition. One possible approach to quantity the degree of binary solid solution as a function of composition and temperature is to apply the common tangent rule and derive phase diagrams (Reich and Becker, 2006; Shuller et al., 2011). For a brief illustration, in Fig. 5. 4 B, the common tangent touches the free energy curve of Se-substituted alunite of 200 K at Se fractions of 0.13 and 0.91 that represent equilibrium phases for mixing systems with intermediate compositions. For a given composition ranging between the Se fractions of 0.13 and 0.91, the Gibbs free energies of the solid solution phase is higher than that of the mechanical mixture of the two equilibrium phases that has the same bulk composition. As a result, at equilibrium, the system will undergo exsolution to those phases and forms a miscibility gap. On the Gibbs free energy curve of 300 K with the global minimum, the solid solution phase of an arbitrary composition has lower Gibbs free energy of mixing than all possible mixtures of two phases that have the same bulk composition such that no miscibility gap appears at that temperature.

Phase diagrams for solid solution of Cr and Se in alunite and jarosite are derived using the common tangent method as a function of temperature and composition (Fig. 5. 6). There are (theoretical) miscibility gaps for S-Cr and S-Se solid solution in jarosite at temperatures below 190 K. S-Cr and S-Se solid solutions in alunite form miscibility gaps at temperatures below 360 K and 270 K, respectively. It is inferred that the structure of jarosite is more flexible to accommodate Cr and Se at the S site compared to the structure of alunite and that at temperatures below 100 ℃, selenate has higher compatibility for the sulfate site in alunite and jarosite compared to chromate. Our calculation results are consistent with experimental reports that extensive solid solutions between jarosite and its chromate analogue and between jarosite and its selenite analogue are formed from aqueous solutions of ~ 95 ℃ (Dutrizac et al., 1981; Baron and Palmer, 2002)

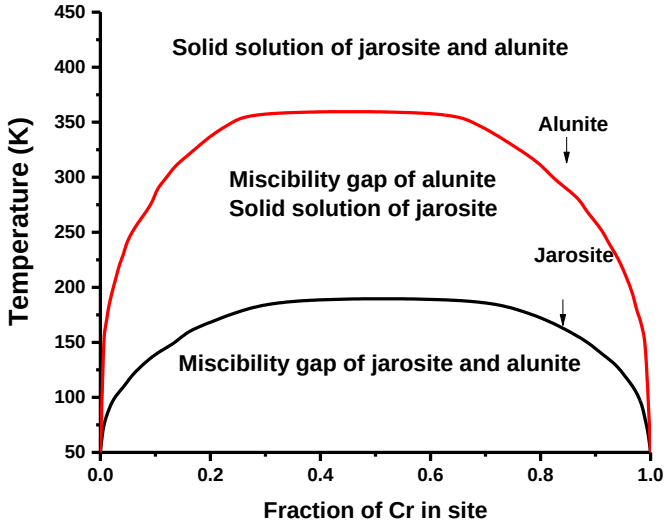

(A)

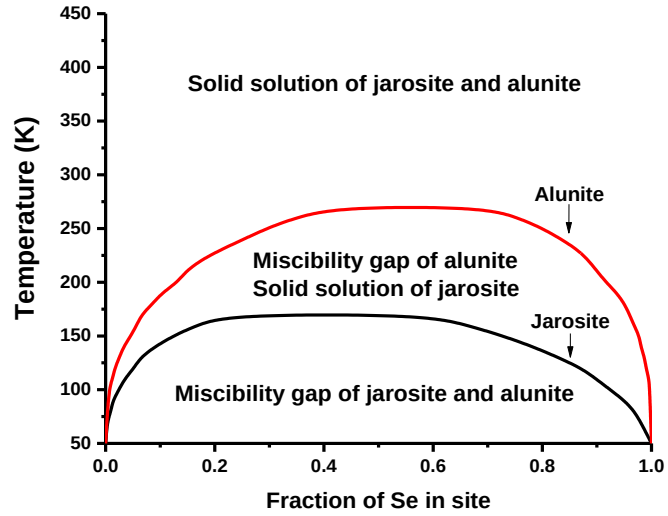

(B)

Fig. 5. 6. Phase diagrams as a function of temperature and composition for (A) S-Cr and (B) S-Se solid solution in alunite and jarosite. The labels in the diagrams indicate regions where a solid solution or miscibility gap of is stable in the structure of alunite and jarosite.

3.3. The S-P-As solid solution in alunite-group minerals

The thermodynamic properties and the phase equilibria of the S-P-As ternary mixing in alunite family minerals are derived by plotting energetic data on ternary diagrams. Our modeling results of S-P and S-As solid solutions are limited to estimate atomic ordering (see section 4.1). A small number (eight) of relevant configurations can be built using the unit cell adopted in this study due to the high number of solid solutions tested in this study and the high number of atoms in the conventional unit cell. The use of larger supercells that allow for more configurations would have been computationally intensive and prohibitive. In section 4.1, it is concluded that the degree of randomness in atomic arrangement increases with increasing temperature and thus the contribution of ordering to the Gibbs free energy is marginal at high temperatures. Therefore, it is assumed that S-P and S-As mixing are ideal without ordering effects for high temperatures (≥ 300 K). One can generate phase diagrams for these solid solution series using the point entropy of mixing and the Margules model applied to the enthalpy of mixing over high-temperature ranges.

The enthalpy of mixing between three mineral phases, α, β and γ can be expressed as the sum of Margules functions for their binary systems and ternary interaction parameters as follows:

$$\Delta H_{mix} = \left(W_B^{\alpha\beta} x_\alpha + W_A^{\alpha\beta} x_\beta\right) x_\alpha x_\beta + \left(W_B^{\beta\gamma} x_\beta + W_A^{\beta\gamma} x_\gamma\right) x_\beta x_\gamma + \left(W_B^{\gamma\alpha} x_\gamma + W_A^{\gamma\alpha} x_\alpha\right) x_\gamma x_\alpha + W_C^{\alpha\beta\gamma} x_\alpha x_\beta x_\gamma \quad (26)$$

where x_α, x_β, and x_γ are the fractions of phase α, β and γ in the ternary system and $x_\alpha + x_\beta + x_\gamma = 1$. The first three cubic polynomial functions with parameter W_A and W_B account for binary mixing systems between α and β, β and γ, and γ and α solid solutions. The last term with parameter W_C takes into account ternary interaction within possible ternay complexes (Ganguly and Saxena, 2012). In order to examine the effects of temperature on the thermodynamics of ternary solid

solution, Gibbs free energies are calculated with varying temperatures based on the ideal mixing of three components whose entropy is expressed as:

$$\Delta S_{mix}^{ideal}(x,T) = -R\left[x_\alpha \ln x_\alpha + x_\beta \ln x_\beta + x_\gamma \ln x_\gamma\right] \quad (27)$$

Once Gibbs free energies are derived as a function of temperature, ternary phase diagrams are constructed using the convex hull method to determine the equilibrium assemblages (a.k.a. convex envelope method; e.g,, Connolly and Kerrick, 1987; Connolly, 1990; Lee et al., 1992; de Capitani and Petrakakis, 2010). The convex hull describes the minimum energy bounding surface that lies everywhere at or below the Gibbs energy surface in composition space. It thus represents the equilibrium system as a single phase or combination of phases that minimizes the energy for a given bulk composition. Therefore it replaces the tangents that connect minima of the ΔG_{mix} curve in a binary system when generalizing to a multi-component system. The first step is to evaluate the Gibbs free energy of mixing at temperatures of interest over a discrete set of points in ternary composition space (e.g., Fig. 5. 7C and D). Then the smallest convex set that contains all points of Gibbs free energy as a function of compositions is defined as the convex hull. A point on the surface represents a composition where a solid solution occurs in equilibrium, whereas a point that lies above the hull indicates a composition at which the mixture of exsolution phases has lower Gibbs free energy than the corresponding homogeneous phase. Based on this convex hull method, a miscibility gap is located in regions of composition space where Gibbs free energy surface is curved upwards (see the concave regions in Fig. 5. 7C and D).

The ternary diagram of the enthalpy of S-P-As mixing between alunite, woodhouseite, and arsenowoodhouseite is presented in Fig. 5. 7A. The enthalpies of mixing between alunite and woodhouseite and between alunite and arsenowoodhouseite are relatively higher than mixing between woodhouseite and arsenowoodhouseite. The former two binary systems are of exchange

between sulfate and the trivalent anions at the TO_4 site and the latter one is of exchange between phosphate and arsenate. Such energetic barriers to exchange anions with different charges lower the probability of forming solid solution as compositions get close to the point where the mole fraction ratio of alunite, woodhouseite, and arsenowoodhouseite is 1:1:1 (that is, the ratio of S:P:As at the TO_4 site = 4:1:1). In the S-P-As mixing with natroalunite, the enthalpy of mixing between natroalunite and woodhouseite is higher than mixing between natroalunite and arsenowoodhouseite (Fig. 5. 7B). The maximum enthalpy is located where the mole fraction ratio of natroalunite, woodhouseite, and arsenowoodhouseite is 2:2:1 (S:P:As = 7:2:1). A quantitative analysis on ternary solid solution is provided from the Gibbs free energies (Fig. 5. 7C and D) and phase diagrams (Fig. 5. 8). At temperatures below 400 K, solid solution is limited to compositions close to the end member species, alunite, woodhouseite, arsenowoodhouseite, and natroalunite (Fig. 5. 8). Large miscibility gaps are predicted below 600 K where the molar fraction of phosphate (X_P) and arsenate (X_{As}) at the TO_4 site are more than 10 % in alunite and where the molar fraction of sulfate (X_S) is more than 60 % in woodhouseite and arsenowoodhouseite (Fig. 5. 8A). At temperatures above 600 K, the formation of solid solution prevails between alunite and woodhouseite and between woodhouseite and arsenowoodhouseite. At temperatures below 1000 K, the miscibility gap gradually diminishes as temperature increases yet excludes the possibility of extensive S-As substitution in arsenowoodhouseite and of the formation of solid solution phases with compositions close to S:P:As = 4:1:1. The ternary mixing involving natroalunite (as the end member with X_S = 1) forms solid solution over a wider range of compositions compared to the mixing involving alunite (Fig. 5. 8B). The miscibility gaps with varying temperatures are centered at the ratio of S:P:As = 7:2:1 where the enthalpy of mixing is the highest (Fig. 5. 7B) and indicate that solid solution is fairly limited between natroalunite and woodhouseite below 800 K. The

miscibility gap region decreases with increasing temperature and the formation of complete ternary solid solution between natroalunite, woodhouseite and arsenowoodhouseite is achieved at 900 K.

The energetic quantities and phase stabilities of S-P-As mixing based on the substitution mechanism of $SO_4^{2-} + OH^- \leftrightarrow PO_4^{3-}$ (or AsO_4^{3-}) + H_2O over the region of compositions with X_S from 0.5 to 1 and of $SO_4^{2-} + K^+ \leftrightarrow PO_4^{3-}$ (or AsO_4^{3-}) + Ca^{2+} over the region with X_S from 0 to 0.5 are presented in Fig. 5. 9. These variations in sulfate fraction at the TO_4 site encompass the entire range of compositions in the alunite family group involving alunite, woodhouseite, arsenowoodhouseite, crandallite and arsenocrandallite. At temperatures above 450 K, positive enthalpies and negative Gibbs free energies of mixing dominate over the entire range of composition (Fig. 5. 9A and B). At temperatures below 1000 K, there are large miscibility gaps at compositions close to S:P:As = 4:1:1 upon the substitution of $SO_4^{2-} + K^+ \leftrightarrow PO_4^{3-}$ (or AsO_4^{3-}) + Ca^{2+} and at compositions near S:P:As = 1:1:1 upon the substitution of $SO_4^{2-} + OH^- \leftrightarrow PO_4^{3-}$ (or AsO_4^{3-}) + H_2O. The computed phase diagram predicts the formation of small miscibility gaps that shrink with increasing temperature, yielding near-complete solid solutions above 700K over compositional ranges between alunite and woodhouseite, woodhouseite and arsenowoodhouseite, and crandallite and arsenocrandallite.

In summary, substitution of $SO_4^{2-} + K^+ \leftrightarrow PO_4^{3-} + Ca^{2+}$ and of $PO_4^{3-} \leftrightarrow AsO_4^{3-}$ would be important mechanisms in forming solid solution of alunite family minerals over a range of temperature between 400 and 900 K (~ 130 to 630 ℃). Arsenate is more exchangeable with sulfate in natroalunite than sulfate in alunite, therefore solid solution phases between natroalunite and arsenowoodhouseite are predicted to be stable in experimental or natural settings of their formation. In section 4.3, some of the computed results of the S-P-As solid solution are revisited and discussed to demonstrate how they support observations from natural alunite family minerals

and the potential role of this ternary mixing as an indicator for the equilibrium temperature at which alunite phases are formed.

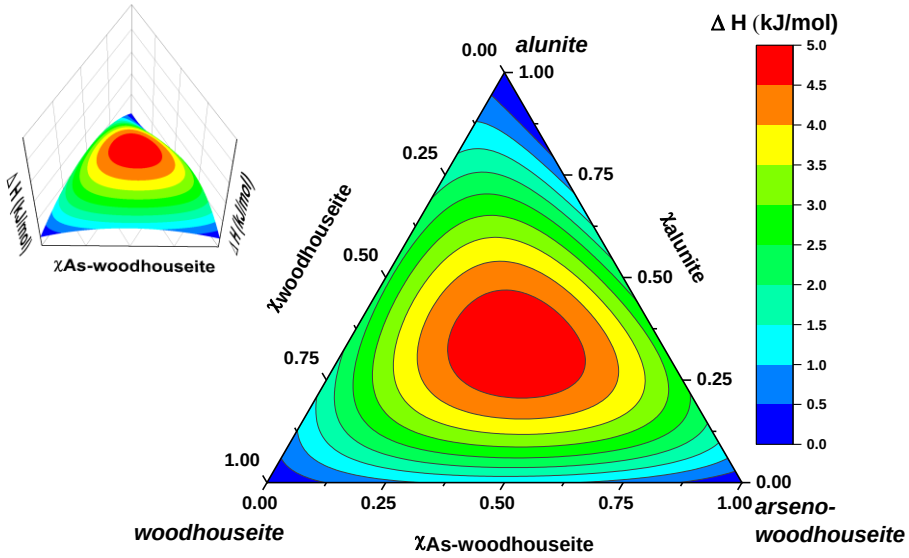

(A)

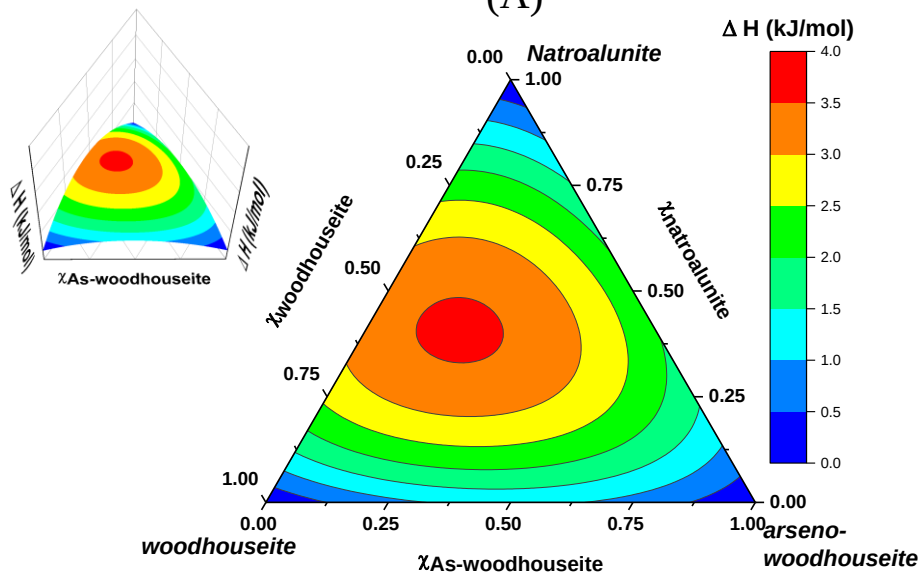

(B)

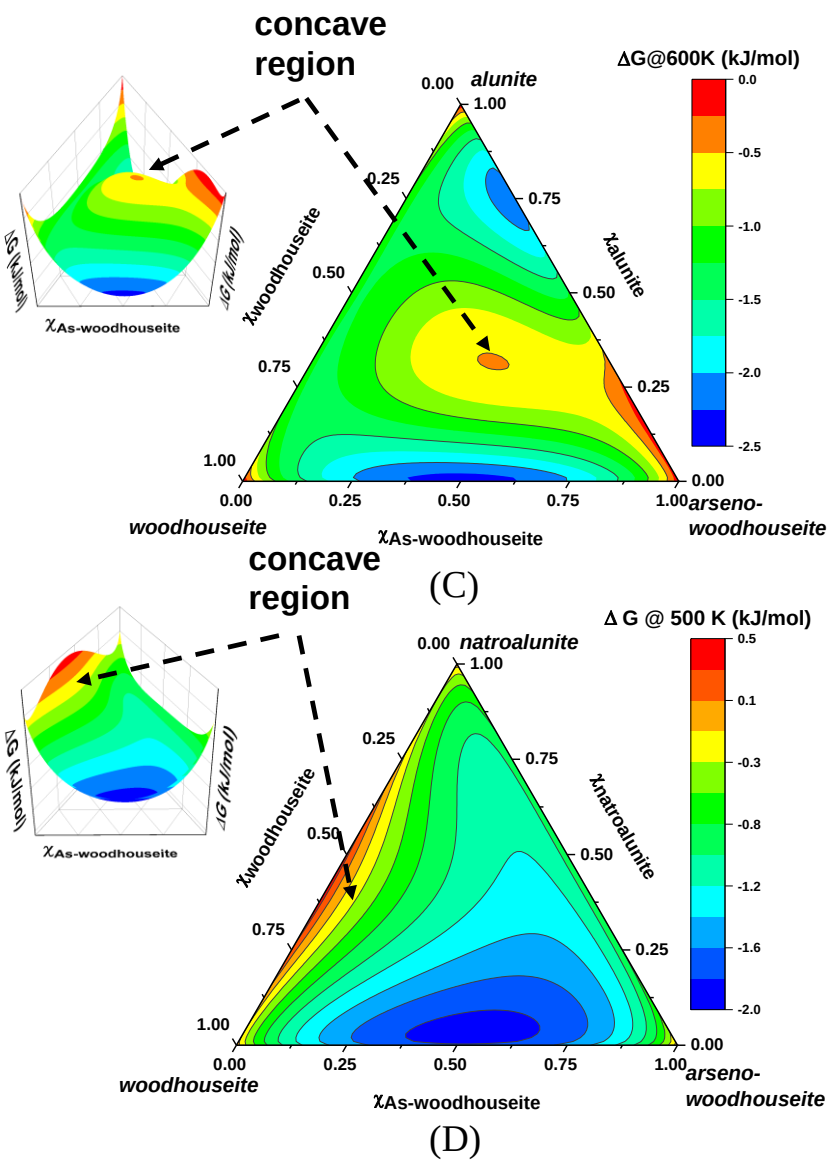

Fig. 5. 7. Enthalpies and Gibbs free energies of ternary mixing between woodhouseite, arsenowoodhouseite and (A, C) one of alunite and (C, D) natroalunite. The ternary energy diagrams are presented in 2-dimensional space as well as in 3-dimensional space (smaller ones).

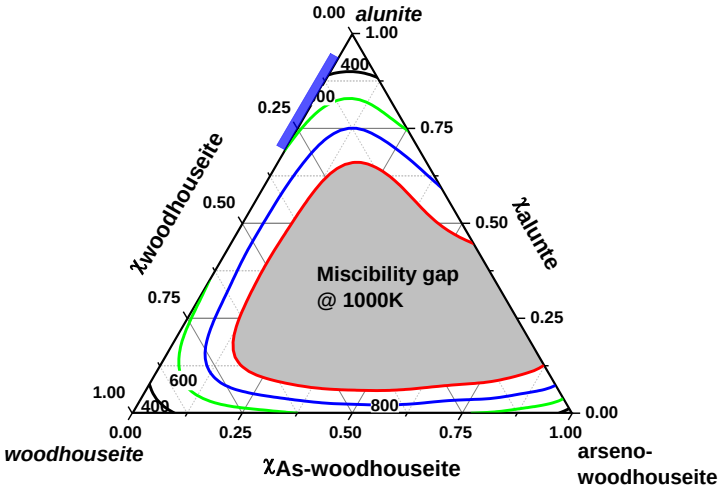

(A)

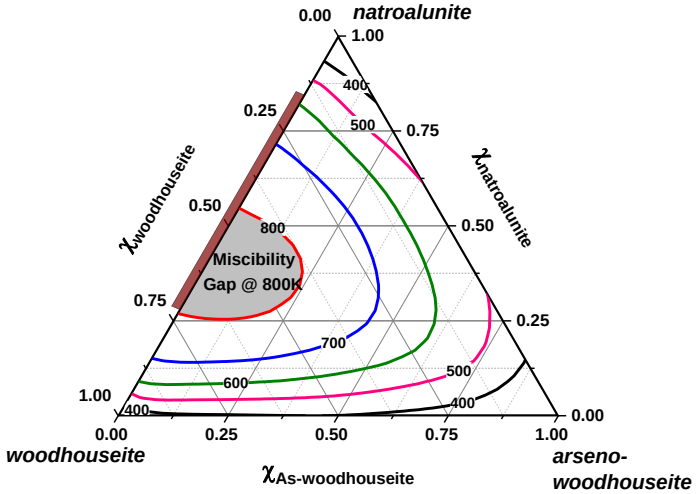

(B)

Fig. 5. 8. Phase diagrams of ternary mixing between woodhouseite, arsenowoodhouseite and one of (A) alunite and (B) natroalunite. The blue belt in 8A and brown belt in 8B represent the ranges of solid solution between alunite and woodhousite (Ripp and Kanakin, 1998; Ripp et al., 1998) and between natroalnite and woodhouseite (Wise, 1975) observed from natural alunite family minerals.

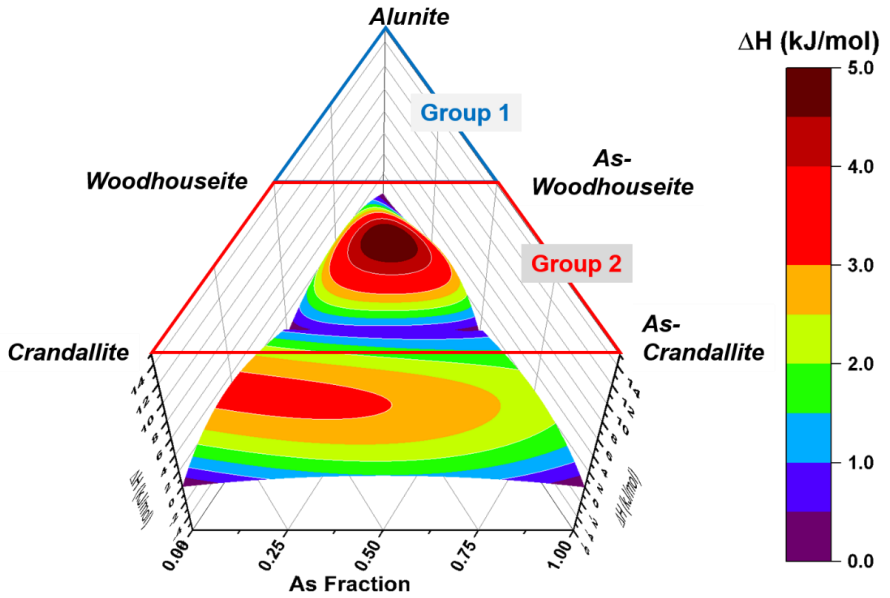
Alunite
Group 1
Woodhouseite
As-
Woodhouseite
Group 2
Crandallite
As-
Crandallite
ΔH (kJ/mol)
5.0
4.0
3.0
2.0
1.0
0.0
0.00
0.25
0.50
0.75
1.00
As Fraction

(A)

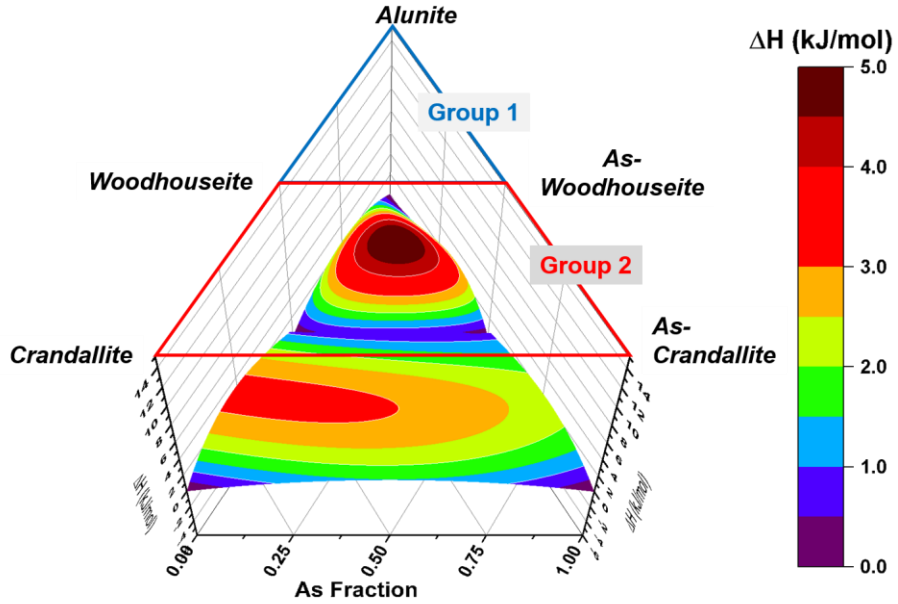
Alunite
Group 1
Woodhouseite
As-
Woodhouseite
Group 2
Crandallite
As-
Crandallite
ΔH (kJ/mol)
5.0
4.0
3.0
2.0
1.0
0.0
0.00
0.25
0.50
0.75
1.00
As Fraction

(B)

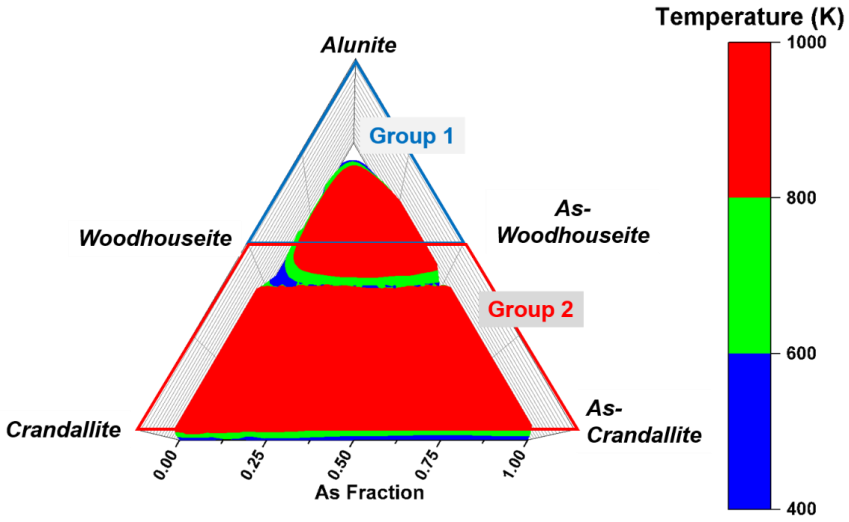

(C)

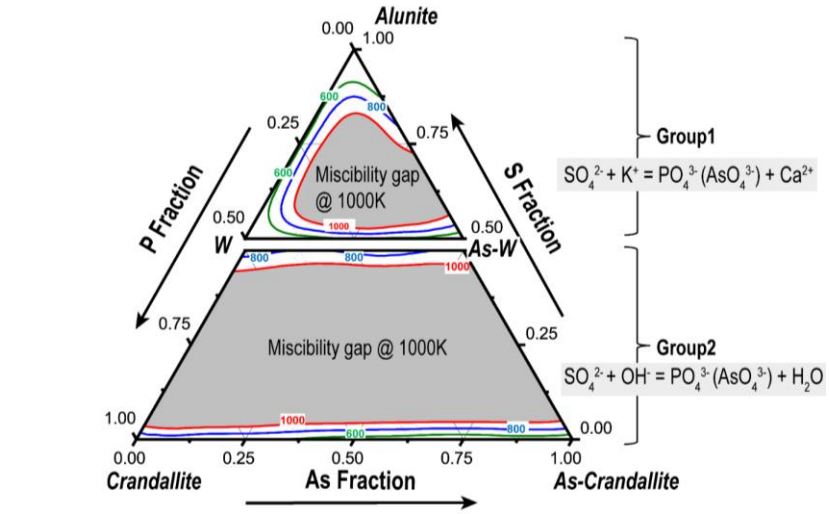

(D)

Fig. 5. 9. Ternary diagrams of S-P-As solid solution having alunite, woodhouseite, arsenowoodhouseite, crandallite, and arsenocrandallite at each corner (A) for the enthalpy and (B) Gibbs free energy of mixing and (C) phase diagrams in 3-dimensional and (D) 2-dimensional space. The two defined ternary systems (Group 1 and 2) are based on the two substitution mechanisms between alunite family minerals (Eq. 1 to 4; inlet in Fig. 1) over the compositional ranges, XS ≤ 0.5 and 0.5 ≤ XS, respectively.

3.4. Incorporation of uranyl and lead into the jarosite structure

The reaction equations and energies for UO_2^{2+} incorporation into end member potassium- and plumbojarosite and Pb-bearing jarosite are presented in Table 5. 2. When using solid source and sink phases, the lowest incorporation energy is calculated from Pb-bearing jarosite (here replacing Pb^{2+} by UO_2^{2+} is exothermic) followed by end member potassium- and plumbojarosite. If the source for uranyl is a hydrated ion from aqueous solution (and the sink for K^+ or Pb^{2+} is water), plumbojarosite is more favorable as a host mineral than potassium jarosite, yet remains less energetically stable relative to Pb-bearing jarosite. The energetic preference of UO_2^{2+} replacing Pb^{2+} in Pb-bearing jarosite is mainly due to the instability of Pb-bearing jarosite relative to the end member jarosite. The calculated energy for incorporation of Pb^{2+} into potassium jarosite is 72 and 202 kJ/mol on the setting of solid phases and hydration, respectively (Table 5. 2. IV and VIII), which accounts for extra energy required to incorporate uranyl into potassium jarosite in place of Pb-bearing jarosite.

The energy-optimized geometry of uranyl and lead incorporated in the jarosite structure is shown in Fig. 5. 10. Both the uranyl and lead ions are coordinated with oxygen atoms nearby. The lead ion is surrounded by eight oxygen atoms at the O3 and O2 sites. The distances from Pb to the O3 site are 2.6 and 2.9 Å while the corresponding distance is 2.8 Å in potassium jarosite. These different Pb-O3 distances in Pb-incorporated jarosite are due to the vacancy at the TO_4 site when one Pb^{2+} ion replaces two K^+ ions. The coordination environments of lead and uranyl in jarosite are similar, but the U-O distances vary from 1.8 Å, similar to the original uranyl distance, to 3.0 Å. In Fig. 5. 10A, the nearest six oxygen atoms and their distances with center U are denoted. These interatomic distances resemble the coordination environment of uranyl-ligand complexes that have two axial oxygen atoms at about 1.8 Å distance and equatorial oxygen atoms at 2.4 to

2.7 Å distances (Guilbaud and Wipff, 1993; Lucks et al., 2013). This result indicates good compatibility of uranyl at the D site and intimate bonds being formed between uranyl and surrounding ions in the jarosite structure.

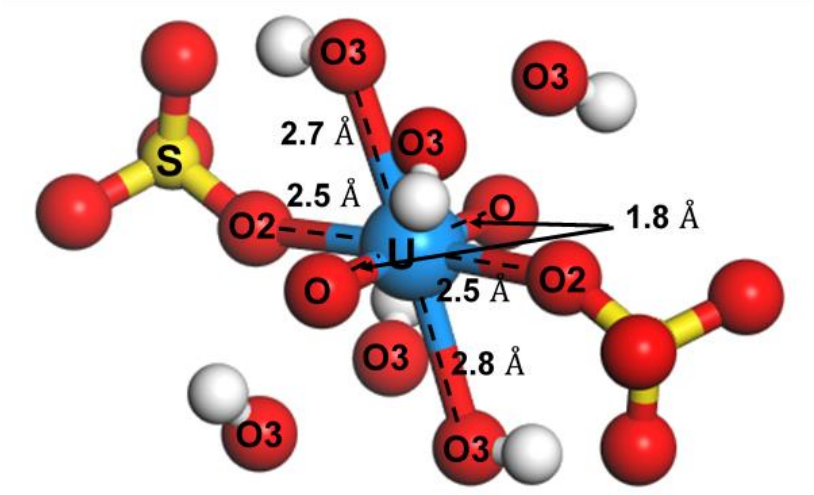

(A)

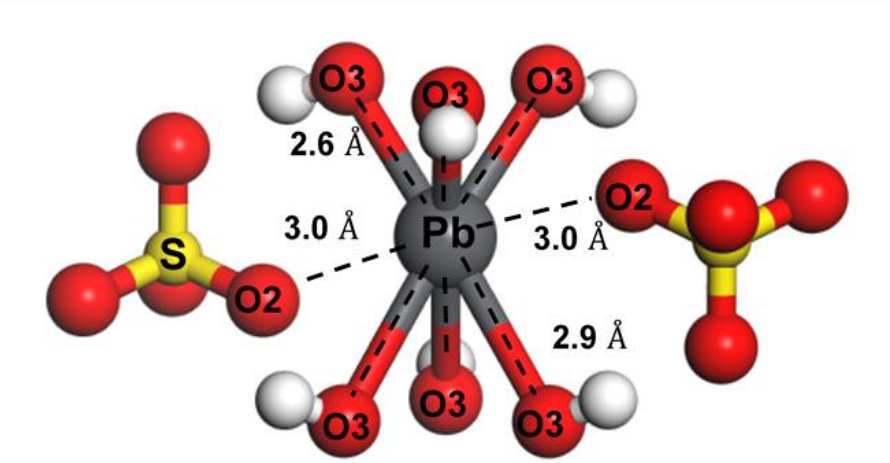

(B)

Fig. 5. 10. Energy-optimized structures of (A) UO_2^{2+} and (B) Pb^{2+} at the D site and their coordination environments in the jarosite structure.

3.5. Protonation of phosphate and arsenate in crandallite and arsenocrandallite

In this study, crandallite and arsenocrandallite are tentatively assumed to have structural water molecules at the O3 site in order to maintain charge neutrality (Mech. 2 in Eq. 2). This means the presence of "extra" protons in their structures (here, "extra" means the existence of protons other than H atoms belonging to OH^- anions at the O3 site). To date, however, the occupancy of extra protons in crandallite and arsenocrandallite is not fully understood. There are two possibilities to accommodate extra protons in the structure: 1) phosphate or arsenate is protonated or 2) a proton bonds with hydroxide to form a water molecule. Although some previous works adopted the chemical formula of $[CaAl_3(PO_4)_2(OH)_5(H_2O)]$ for crandallite and of $[CaAl_3(AsO_4)_2(OH)_5(H_2O)]$ for arsenocrandallite, which support the second possibility unintentionally (e.g., Jambor, 1999; Dutrizac and Jambor, 2000), little work has been done to address the position of excess proton in crandallite and arsenocrandallite. To our knowledge, a study by Blount (1974) that explains the crystal structure of crandallite is the only relevant study that has addressed this aspect thus far. A piece of evidence to support the first possibility is found from the lowest energy configuration of crandallite and arsenocrandallite obtained from quantum mechanical modeling in this study.

In the initial model configuration of crandallite and arsenocrandallite, three of the TO_4 sites (T2, T4 and T6 whose O1 sites are labelled O1' in Fig. 5. 2A) were selected to accommodate phosphate or arsenate, and the nearest O3 site (labelled O3') is replaced by the water molecule to complete the chemical formula of $CaAl_3(XO_4)_2(OH)_5(H_2O)$ where X = P or As. The energy minimization calculation by CASTEP predicts the lowest energy configuration of these minerals in which the phosphate and arsenate molecule are protonated as a result of the dissociation of the water molecule (Fig. 5. 11). The distances between the O1' and O3' sites are 2.7 Å in both crandallite and arsenocrandallite (Fig. 5. 11B and C). In the energy -optimized structure of

crandallite and arsenocrandallite, the proton dissociated from the water molecule (H1' in Fig. 5. 11) is closer to the O1' site (the distance, $\overline{O1'H1'}$ is 1.0 Å) than the O3' site ($\overline{O3'H1'}$ is 1.7 Å) and the sum of these distances are approximately equal to the distance between the O1' and O3' sites ($\overline{O1'O3'}$ = 2.7 Å). The angles between the O1', H1', and O3' atoms (∠O1'-H1'-O3') are 161° in crandallite and 168° in arsenocrandallite, which are close to 180°. These geometric relations prove that the H1' atom is positioned nearly on the linear line between the O1' and O3' sites. The single point energy (these are quantum-mechanical calculations without automatic subsequent geometry optimization) of crandallite and arsenocrandallite is calculated as a function of the distance $\overline{O1'H1'}$ while the H1' atom remains positioned on the linear line between O1' and O3' (Fig. 5. 12). The minimum energy is found at $\overline{O1'H1'}$ of 1 Å and the energy increases as the H1' atom gets closer to the O3' atom. $\overline{O1'H1'}$ of 1.7 Å corresponds to the initial model configuration used for energy optimization where the water molecule coexists with phosphate or arsenate without protonation. The energy lowering by the transition of $\overline{O1'H1'}$ from 1.7 to 1.0 Å is on the order of 50 kJ/mol in both crandallite and arsenocrandallite (Fig. 5. 12). It follows that phosphate in the protonated form (HPO_4^{2-}) is energetically more favorable relative to deprotonated phosphate (PO_4^{3-}) with an adjacent water molecule at the O3 site (instead of OH^-) in these minerals. Blount (1974) characterized natural crandallite and suggested the chemical formula of $[CaAl_3(OH)_6(PO_3(O_{1/2}(OH)_{1/2})_2]$ based on X-ray diffraction and infrared spectroscopic results. Specifically, it was found from their study that H atoms can only be present at one half of the O1 sites, and the O2 sites are not likely to hold the H atom but forms the edge of the Ca polyhedron. Our modeling result supports their finding from natural crandallite and predicts that in the crandallite and arsenocrandallite structures, half the O1 sites are occupied by protonated phosphate

or phosphate that is present in the form of HPO_4^- or $HAsO_4^-$, and suggests the chemical formula of $[CaAl_3XO_4(HXO_4)(OH)_6]$ (X = P and As) for these minerals.

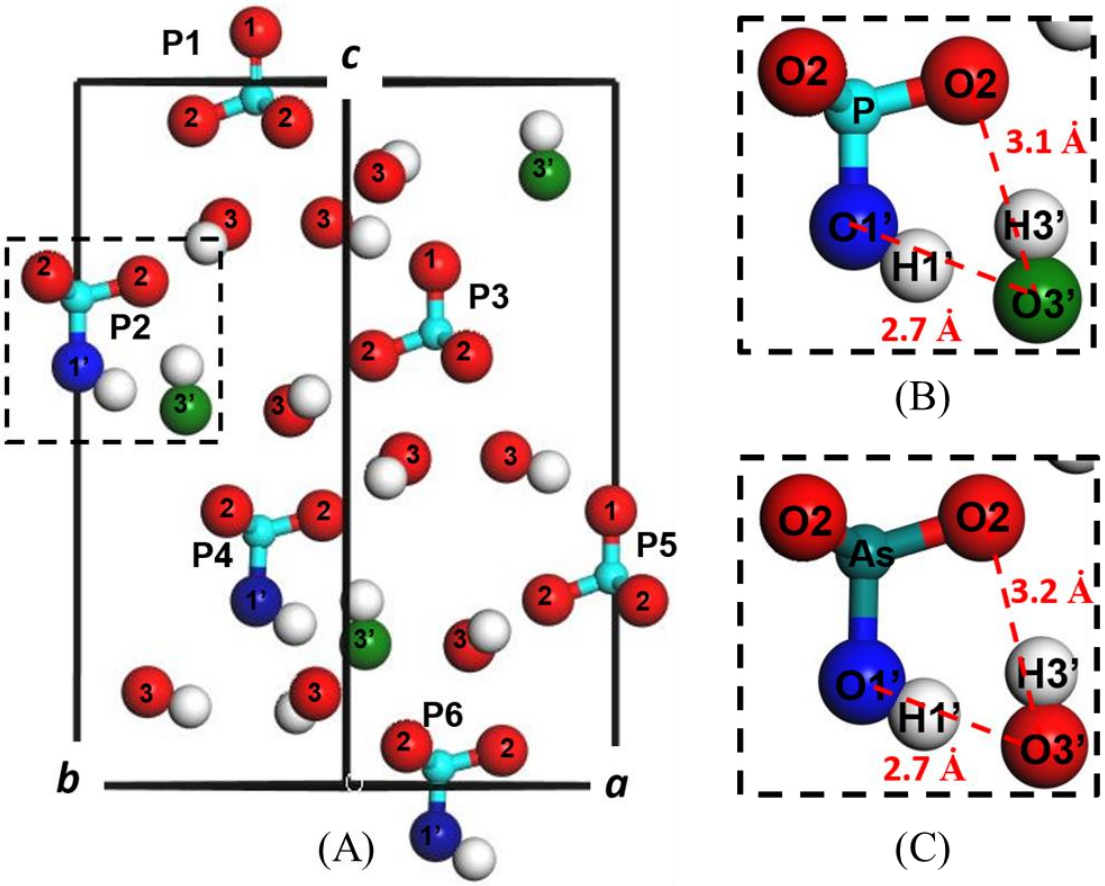

Fig. 5. 11. The lowest-energy configuration (after energy optimization) (A) of crandallite, (B) protonated phosphate and hydroxide in crandallite (the magnified view of the dotted square in (A)) and (C) protonated arsenate and hydroxide in arsenocrandallite.

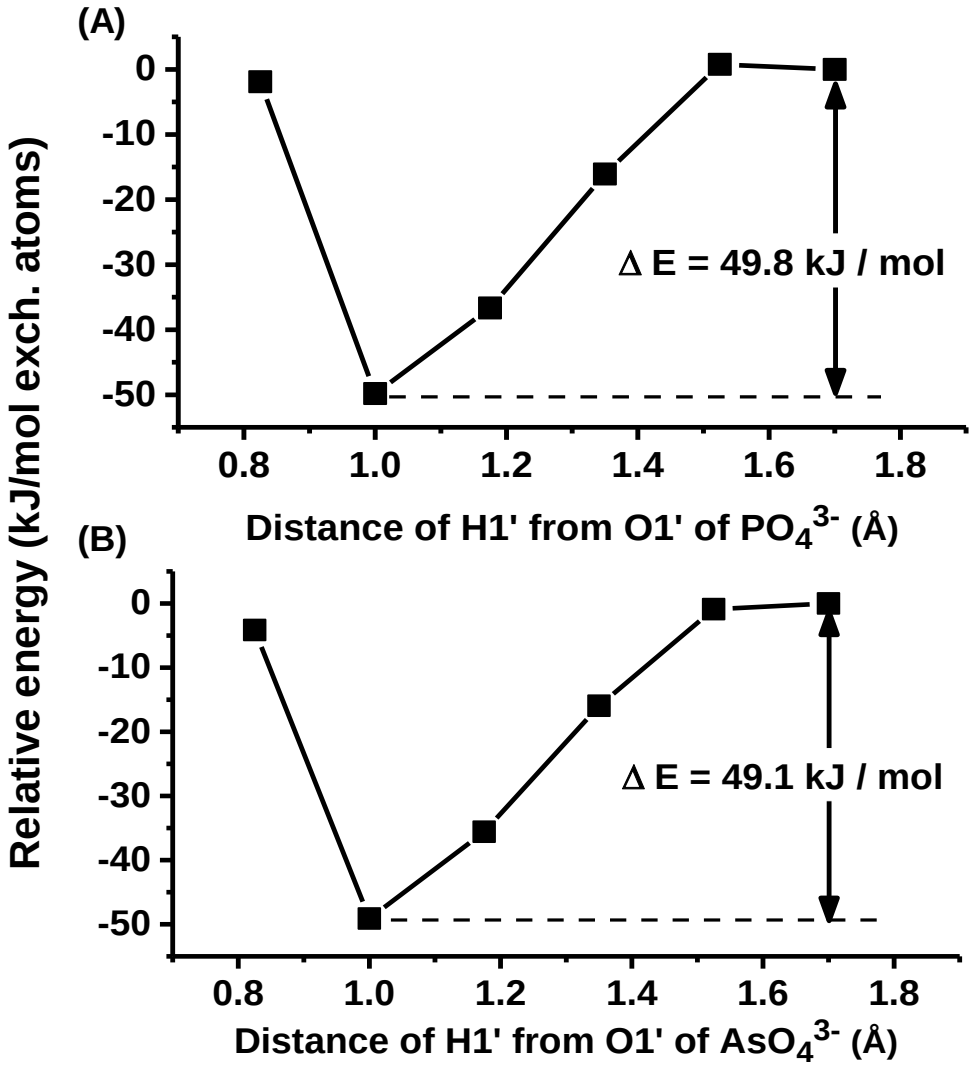

Fig. 5. 12. The single point energy of (A) crandallite and (B) arsenocrandallite as a function of the position of H1’ atom on the linear line between the O1’and O3’ atoms (as labeled in Fig. 11).

4. Discussion

4.1. Ideality and randomness of mixing in solid solution

The activity of a component in solution is a function of its concentration and expressed as

$$a_i = \overline{X}_i \overline{\gamma}_i \tag{28}$$

where $\overline{X}_i$ is an appropriate function of the concentration (e.g., molar fraction) of the component *i* in the solution and $\overline{\gamma}_i$ is the corresponding activity coefficient (Ganguly and Saxena, 2012). A solution is defined to be ideal when $\overline{\gamma}_i$ = 1 for all components. The Gibbs free energy of mixing is a function of the concentration and the activity coefficient according to

$$\Delta G_{mix}(x,T) = RT \sum_i \bar{X}_i \ln(\bar{X}_i \overline{\gamma}_i), \tag{29}$$

and for the binary mixing between mineral species A and B,

$$\Delta G_{mix}(x,T) = RT\,[x \ln(x\overline{\gamma_A}) + (1-x)\ln((1-x)\overline{\gamma_B})]. \tag{30}$$

The Gibbs free energy of mixing in ideal solution (i.e., $\overline{\gamma}_i$ = 1) reads as

$$\Delta G_{mix}^{ideal}(x,T) = RT \sum_i \bar{X}_i \ln \overline{X}_i\,, \tag{31}$$

and for a binary system, this equation corresponds to Eq. 20.

In mixing between the two anions with equal charges (i.e., S-Cr, S-Se and P-As solid solutions), the positive Gibbs free energy of mixing at low temperatures arises mainly from the contribution of the positive enthalpy of mixing (Fig. 5. 4 and 5, here, the positive values are fairly small compared to many other solid solutions) which is indicative of non-ideal solid solutions. At high temperatures, the Gibbs free energy of mixing shows the global minimum near a molar fraction of 0.5 which resembles the point entropy multiplied by $(-T)$ (Eq. 20). In the expression of the Gibbs free energy of mixing derived in this study (Eq. 19), the contribution of random mixing is

equivalent to the Gibbs free energy of mixing in ideal solution (Eq. 20) and increases (relative to the contribution of ordering) as temperature increases such that $\Delta G_{mix}(x,T) \cong \Delta G_{mix}^{ideal}(x,T)$ for high temperatures. From comparing Eq. 20 and 30, it fallows that the activity coefficient $\overline{\gamma_1}$ and $\overline{\gamma_2}$ go toward unity with increasing temperature. That is, the degree of the solid solution being ideal (i.e., ideality) increases with temperature.

A statistical thermodynamic assumption for a randomly mixed solution is that configurations of the solution are equally probable at a given composition (Ganguly and Saxena, 2012). The probability of configurations whose ensemble form a Boltzmann distribution (Eq. 5) dictates that the arrangement of atoms with lower energy has the higher probability to take place. Accordingly, in random mixing at finite temperature, configurations of solid solution at a given composition are supposed to have equivalent energies. The randomness of mixing can be characterized by the entropy of mixing, ΔS_{mix} (Eq. 17 and 18). The computed results of solid solution in the alunite supergroup mineral show non-randomness of mixing between two divalent (S-Cr and S-Se solutions) and between trivalent anions (P-As solid solutions) at low temperatures. For example, in Fig. 5. 13A, the entropy of mixing at 25 K for S-Cr and S-Se solid solutions in alunite and jarosite is lower than the point entropy (Eq. 18), indicating non-randomness of mixing in these solid solutions. The trend of $\Delta S_{mix}(x,T)$ as a function of temperature for Se-substituted jarosite is presented in Fig. 5. 13B. There is a local minimum of $\Delta S_{mix}(x,T)$ at an intermediate composition (Se to S ratio of 1:1 in jarosite) when the temperature is as low as 25 K. Such a local minimum is not found for temperatures above 50 K, while the solid solution achieves good consistency with the point entropy (Eq. 18) at temperature above 200 K. That is, the system is approximately in randomly mixed states as temperature increases. At lower temperatures, the preference of atoms to occupy exchangeable sites in certain arrangements (i.e., ordering) decreases the degree of

randomness in mixing and thus lower the entropy of mixing. The contribution of high-energy configurations to the canonical partition function (Eq. 5) increases with increasing temperature and so does the degree of randomness.

Such atomic ordering also explains the local minimum at the intermediate composition upon the ΔH_{mix} curves for Se-substituted jarosite (Fig. 5. 3B). The enthalpy of mixing at 0 K represents the lowest energy state of solid solution (Fig. 5. 3) because at 0 K, the probability of states with higher energy becomes infinitely small relative to that of the lowest energy state (Eq. 5). The atomic arrangement of Se and S in Se-substituted jarosite that gives the lowest energy is S-Se-S-Se-S-Se and the one with the second lowest energy is S-Se-S-Se-Se-S for the six exchangeable sulfate sites along the [001] direction (T1 to T6 in Fig. 5. 2A). It is inferred that energy lowering arises from the interaction between S and Se when they are positioned in the alternating pattern (i.e., repeating of S-Se units). When temperature increases, the probability of high-energy configurations increases and so does the enthalpy of mixing (Eq. 6 and 13). In random mixing, all configurations have equal probabilities, and, thus the internal energy of mixing is independent of ordering such that $\Delta H_{mix}(x,T)$ is constant with varying temperatures. The results of mixing between anions with equivalent charges (i.e., in Cr-S, Se-S, and As-P solid solutions) show that $\Delta H_{mix}(x,T)$ is nearly constant at high temperatures (Fig. 5. 3 and 5). This means that these solid solution systems tend to move toward random mixing as temperature increases.

The excess entropy of mixing, ΔS_{mix}^{xs}, can be an indicator for the degree of randomness in solid solutions. From Eq. 21 and the definition of the Gibbs free energy ($G = H - TS$), the excess entropy can be expressed as

$$\Delta S_{mix}^{xs}(x,T) = \Delta S_{mix}(x,T) - \Delta S_{mix}^{ideal}(x,T) = \left(\frac{1}{T}\right) \cdot \left[\Delta H_{mix}(x,T) - T \cdot \int_{T}^{\infty} \frac{\Delta H_{mix}(x,\tau)}{\tau^2} d\tau \right] \quad (32)$$

where τ is the variable of temperature. In non-random mixing, ΔH_{mix} increases with increasing temperature such that $\Delta H_{mix}(x,\tau) > \Delta H_{mix}(x,T)$ for any $\tau > T$, and thus

$$0 = \left(\frac{1}{T}\right) \cdot \left[\Delta H_{mix}(x,T) - T \cdot \Delta H_{mix}(x,T) \cdot \int_{T}^{\infty} \frac{1}{\tau^2} d\tau \right] > \Delta S_{mix}^{xs}(x,T) \quad (33)$$

In random mixing, $\Delta H_{mix}(x,\tau)$ is independent of temperature, and thus $\Delta S_{mix}^{xs}(x,T) = 0$. These derivations verify that the value of $\Delta S_{mix}^{xs}(x,T)$ is negative for non-random mixing and zero for random mixing. In Fig. 5. 13B, $\Delta S_{mix}^{xs}(x,T)$ for Se-substituted jarosite is negative at all temperatures but converges to zero as temperature increases above 100 K. That means that random mixing can be expected at any environmentally relevant condition at or above room temperature, which is consistent with the interpretations on randomness from enthalpy and entropy of mixing as described above.

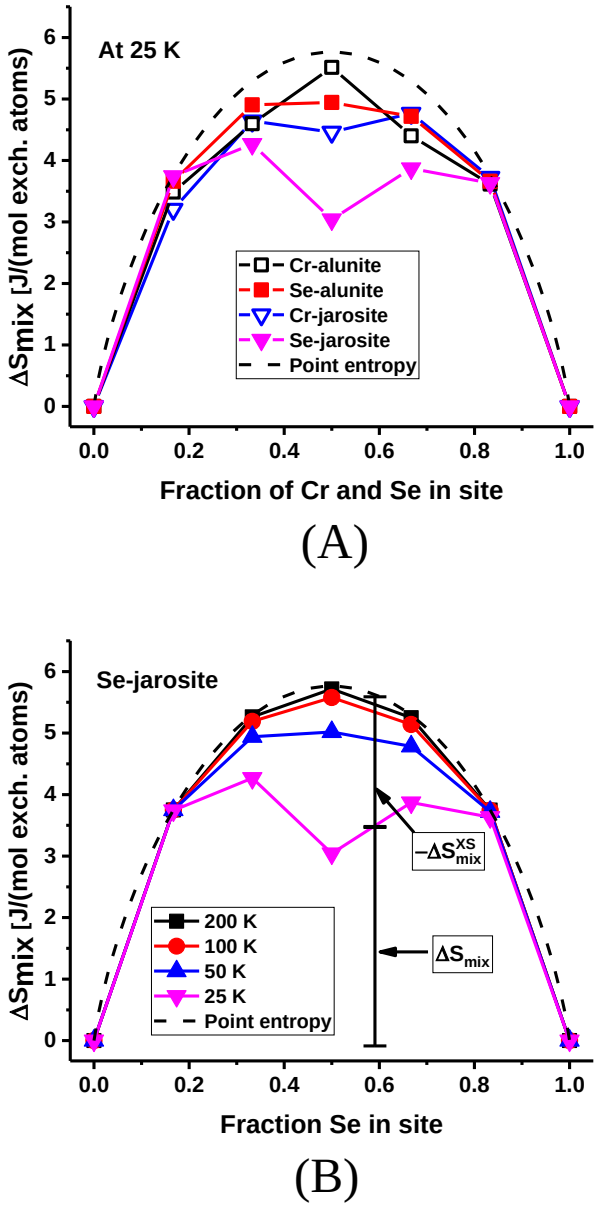

Fig. 5. 13. The entropy of mixing (A) for S-Se and S-Cr solid solution series in alunite and jarosite at 25 K and (B) for S-Se solid solution in jarosite as a function of temperature. For theoretical equilibration below 100 K, $\Delta S_{mix}^{xs}(x,T)$ is negative (i.e., significantly below the point entropy of random mixing shown by the dashed line) and only in this temperature range, ordering would occur.

4.2. Solid solution and incorporation into alunite supergroup minerals

The principal factors that determine the degree of solid solution in a mineral structure are 1) the relative sizes and the charges of the ions involved in the substitution 2) temperature and pressure 3) the availability of ions where solid solution occurs (Klein et al., 2007). Ions with equivalent charges are likely to substitute one another if their radius differences are small. Therefore, substitutions between phosphate and arsenate (P-O and As-O distances are ~1.5 and 1.6 Å, respectively), and between sulfate and selenate (or chromate) (S-O, Se-O, and Cr-O distances are ~1.5, 1.7, and 1.7 Å, respectively) are likely in the alunite supergroup. The positive enthalpies of the S-P and S-As solid solutions are greater than those of the S-Cr, S-Se, and P-As solid solutions (Fig. 5. 3, 5 and 7), which is indicative of greater energetic unfavorability for mixing between anions with different charges, and therefore, a greater tendency for exsolution. Despite similar sizes of phosphate, arsenate, and sulfate, the coupled substitution that requires another substitution at the D and O3 site may cause more structural alteration and thus energetic unfavorability (e.g., Kim et al., 2017). Under high-temperature conditions, such an energetic disadvantage can be overcome to form S-P-As solid solution (Fig. 5. 7 to 9). Our computed ternary phase diagrams of solid solution between alunite family minerals show large miscibility gaps where all the molar fractions of S, P, and As at the TO_4 site are greater than 10 % (Fig. 5. 9). However, a wide range of mixing between these end members is predicted when one of the fractions of S, P, and As at the TO_4 site is less than 10 %. Mixing is assumed binary solid solutions where the sum of two of the S, P and As fractions is greater than 90 %. It is predicted from our computed data that binary S-P, P-As, and As-P solid solutions in alunite minerals scarcely occur below 100 °C, are stable over a certain range of compositions at temperatures from 100 to 300 °C, and become extensive or complete above 300 °C (Fig. 5. 8).

Our computational data show that there are thermodynamic barriers (~50 to 100 kJ/mol in case of reactions having solid chlorides; ~100 to 200 kJ/mol in case of hydration) to incorporate Pb and U in end member jarosite species (Table 5. 2). This result is consistent with experimental reports for the preferential incorporation of K^+ over Pb^{2+} and UO_2^{2+} in the jarosite structure (Dutrizac, 2008; Dutrizac and Chen, 2009). Plumbojarosite is found as a weathering product of lead sulfide deposits or as a byproduct of hydrometallurgical processes to recover metals such as Zn, Cu and Ag. Because of the thermodynamic stability of K^+ in jarosite, plumbojarosite rarely occurs as end member species but readily forms a solid solution with potassium jarosite. (Szymanski, 1985; Basciano and Peterson, 2010). Therefore, in natural environments or hydrometallurgical processes, the common forms of Pb in association with jarosite potentially include Pb-incorporated jarosite (Pb < K in the composition) and K-bearing plumbojarosite (Pb > K). Incorporation reactions of Pb^{2+} and UO_2^{2+} into jarosite are cooperative because of lowering in the energy barrier by substituting UO_2^{2+} for Pb^{2+} in Pb-bearing jarosite (Table 5. 2). In this sense, Pb and U could be associated with the formation of jarosite in the form of co-incorporation at the D site of the structure.

4.3. Theoretical predictions versus experimental and field observations on alunite supergroup minerals

Our computed data show that at temperatures between 0 and 100 ℃, chromate and selenate are highly compatible in jarosite and complete solid solution between jarosite and one of its chromate and selenate analogues is thermodynamically stable. This result is consistent with experimental observations on the formation of jarosite-type minerals. Baron and Palmer (2002) have demonstrated that in aqueous solutions with varying Cr/S ratios at 95℃, jarosite forms extensive

solid solution between sulfate and chromate in the form of $[KFe_3((Cr_xS_{(1-x)})O_4)_2(OH)_6]$ (x being between 0 and 1). Similarly, Dutrizac et al. (1981) reported a continuous variation in the fraction of Se at the S site (between 0 and 1) in jarosite phases produced from solutions containing sulfate and selenate at 95 to 100 ℃, $[KFe_3((Se_xS_{(1-x)})O_4)_2(OH)_6]$. Our data from modeling predict that chromate and selenate substitute for sulfate in jarosite more readily than they do for sulfate in alunite. Based on the lowest temperature above which complete solid solution forms (Fig. 5. 6), the compatibility of Cr and Se in jarosite and alunite is inferred to increase in the order of Se in jarosite (-100 ℃) > Cr in jarosite (-80 ℃) > Se in alunite (0 ℃) > Cr in alunite (90 ℃). Substitution of arsenate for phosphate in crandallite is estimated to become extensive and complete at temperatures between 150 and 250 °C (Fig. 5. 5). Besides the energetic data of uranyl (UO_2^{2+}) incorporation into jarosite-type minerals showing that uranyl could be potentially associated with the formation of Pb-bearing jarosite (section 4.2), our modeling results of solid solutions in jarosite, alunite, and crandallite contribute to the thermodynamic data necessary for evaluating the critical role of alunite supergroup minerals in controlling toxic elements for long-term immobilization.

Since the discovery of jarosite on Mars (Madden et al., 2004), the physical and chemical properties of jarosite have received increasing attention. For example, the surface temperature of Mars can be as low as -120 ℃ (Smith et al., 2004) and it has been suggested that jarosite is thermodynamically stable under most present-day Martian surface temperatures (Navrotsky et al., 2005). Since jarosite can incorporate various foreign ions and molecules in the structure, it can be an indicator of aqeous and biological processes on Earth and Mars (Kotler et al., 2008). The stability of solid solution in jarosite as a function of temperature is computed in this study and the resulting phase diagrams show that once they form, Cr- and Se-substituted jarosite can be stable

without exsolution over Mars' surface temperatures. In turn, this result supports that the mineral chemistry of jarosite may substantiate geoloical events on Mars such as weathering and alteration.

This work includes the first geochemical application that combines quantum-mechanical calculations, statistical thermodynamic analysis, and the complex hull method to derive ternary phase diagrams of S-P-As solid solution between alunite family minerals. How do the quantum mechanical predictions of this study compare to observations from natural alunite family minerals? Data reported by Ripp and Kanakin (1998) and Ripp et al. (1998) suggested extensive solid solution between natroalunite and woodhouseite from metamorphosed high aluminum rocks of the Ichetui occurrence in the Transbaikal region, Russia. These compositions of the solid solution correspond to the molar proportion of woodhouseite between 0.15 and 0.72, which our computed phase diagram (Fig. 5. 8B) predicts is stable at equilibration temperatures above 530 ℃. This thermal constraint is consistent with the metamorphic temperature (520 to 600℃) estimated from the Ichetui occurrence (Ripp and Kanakin, 1998). Likewise, the solid solution between alunite and woodhouseite reported by Wise (1975) shows the molar fraction of woodhouseite ranging from 0.07 to 0.3 which is estimated to occur above 330 ℃ (Fig. 5. 8A). This temperature may have been achieved in hypogene fluids where these solid-solution phases were produced (Wise, 1975). In the magmatic hydrothermal Au-Ag deposit at the Temora Mine, Australia, quartz-rich advanced argillic alteration assemblages show a nearly continuous variation between end member alunite (or natroalunite) and woodhouseite, supporting the coupled substitution mechanism of $(Na^{+}, K^{+}) + SO_4^{2-} \leftrightarrow Ca^{2+} + PO_4^{3-}$ (Allibone et al., 1995). Based on the analysis of phase relations, these alteration assemblages were estimated to form at a temperature of 275 °C. A relevant inference proposed by Stoffregen et al. (2000) who examined data from various deposits is that the formation of coupled substitution between phosphate (or arsenate) and sulfate in hypogene alunite seems

limited at temperatures below 300 °C but is more extensive at higher temperatures. Therefore, our results of quantum mechanical predictions are consistent with these observations and inferences from natural alunite family minerals. Availability of phosphate and arsenate can be another limiting factor in determining the degree of solid solution in alunite. If phosphate or arsenate were depleted in a system, the incorporation of P or As into alunite would be limited even in cases where the formation temperature is sufficiently high to form a wide range of solid solution. In magmatic-hydrothermal systems where phosphate or arsenate is the major anions to form an alunite supergroup mineral as well as sulfate, a degree of solid solution in alunite may serve as a semi-quantitative indicator for the equilibrium temperature at which alunite phases are formed and stable in the system.

In our modeling, the calcium cation (Ca^{2+}) is set to be the main anion at the D site to compensate the charge difference between sulfate and phosphate (or arsenate). In natural minerals of the supergroup, however, other cations (e.g., Sr^{2+}, Ba^{2+} and Pb^{2+}) are also known to occupy the D site along with Ca^{2+} or to form their own mineral phases that belong to the crandallite or arsenocrandallite group (Fig. 5. 1) (Allibone et al., 1995; Schwab et al., 2004; Hikov et al., 2010). In particular, the presence of Pb^{2+} may have a cooperative effect on incorporation of phosphate or arsenate into alunite and jarosite. It is worth to note that nearly complete S-P-As solid solution has been well documented for Pb-dominant minerals of the supergroup (Jambor, 1999) (a few mineral names are listed in Fig. 5. 1). One important question is whether thermodynamic properties of mixing between sulfate and phosphate (or arsenate) are dependent on which cation occupies the D site. Determining the effect of the D site cation on S-P-As solid solution will be the subject of future computational studies.

5. Conclusions

In this study, solid solution series in the alunite supergroup are simulated based on first-principle calculations. A statistical thermodynamic model, based on energetic-weighting of a collection of simulated atomic arrangements, is formulated to evaluate thermodynamic mixing properties of solid solutions. In the binary solid solution, ideality and randomness increase with increasing temperature and transition from ordering to random anion arrangement in this supergroup is typically achieved at temperatures below room temperature. The results of the ternary solid solution (derived from the assumption of ideal mixing) are in good agreement with the solubility of sulfate, phosphate and arsenate observed from natural alunite group minerals.

At the tetrahedral TO_4 site of the alunite supergroup, mixing between sulfate (or phosphate) and another anion with the equivalent charge such as chromate and selenate (arsenate for phosphate) is thermodynamically possible even at low temperatures (< 100 °C). Chromate, selenate, and arsenate occur as trace elements in contaminated soils or oxidized mine-tailing sites. In such low-temperature environments, therefore, the concentration of dissolved Cr, Se, and As can be largely controlled by the formation of solid solutions in host minerals including alunite, jarosite, and crandallite. Incorporation of uranyl at the D site of jarosite would be limited in the jarosite structure when competing with K^+ for that site, yet substitution of UO_2^{2+} for other cations in the structure, such as Pb^{2+}, is found to be energetically possible.

Mixing between ions with different charges (either phosphate or arsenate substituting for sulfate) in the alunite supergroup is examined having woodhouseite and arsenowoodhouseite or crandallite and arsenocrandallite as end member minerals for phosphate and arsenate. The energetic barrier to mixing (reflected by the peak enthalpy of mixing) is higher by a factor of two or three compared to mixing between anions with equal charges and can be overcome as

temperature rises. Substitution of phosphate and arsenate for sulfate in alunite and natroalunite is found to be fairly limited (X_P and $X_{As} < 0.05$) at room temperature but is more extensive ($0.1 < X_P < 0.2$ and $0.1 < X_{As} < 0.5$) at temperatures between 130 and 330 °C. Complete solid solutions between woodhouseite and one of alunite and natroalunite and between arsenowoodhouseite and natroalunite are achieved over a range of temperature between 330 and 630 °C.

Acknowledgements

The authors are grateful for the support from the U.S. Department of Energy's (DOE) Office of Science, 464 Office of Basic Energy Sciences (BES), Chemical Sciences, Geosciences, & Biosciences (CSGB) Division 465 for the topics of Heavy Element Chemistry and Geoscience (grant number DE-FG02-06ER15783). Y.K. acknowledges support from Samsung Scholarship. A.S.W. acknowledges the Turner Postdoctoral Fellowship for supporting involvement in this work. We thank anonymous reviewers for their constructive reviews and are grateful for the editorial handling of A. B. Kersting.

References

Allibone A. H., Cordery G. R., Morrison G. W., Jaireth S. and Lindhorst J. W. (1995) Synchronous advanced argillic alteration and deformation in a shear zone-hosted magmatic hydrothermal Au-Ag deposit at the Temora (Gidginburg) Mine, New South Wales, Australia. *Econ. Geol.* **90**, 1570-1603.

Alpers C. N. and Brimhall G. H. (1988) Middle Miocene climatic change in the Atacama Desert, northern Chile: Evidence from supergene mineralization at La Escondida. *Geol. Soc. Am. Bull.* **100**, 1640-1656.

Baron D. and Palmer C. D. (2002) Solid-solution aqueous-solution reactions between jarosite ($KFe_3(SO_4)_2(OH)_6$) and its chromate analog. *Geochim. Cosmochim. Acta* **66**, 2841-2853.

Baron D., Palmer C. D. and Stanley J. T. (1996) Identification of two Iiron−chromate precipitates in a Cr (VI)-contaminated soil. *Environ. Sci. Technol.* **30**, 964-968.

Basciano L. C. and Peterson R. C. (2010) A crystallographic study of the incomplete solid-solution between plumbojarosite and jarosite. *Can. Mineral.* **48**, 651-659.

Becker U. and Gasharova B. (2001) AFM observations and simulations of jarosite growth at the molecular scale: probing the basis for the incorporation of foreign ions into jarosite as a storage mineral. *Phys. Chem. Miner.* **28**, 545-556.

Becker U. and Pollok K. (2002) Molecular simulations of interfacial and thermodynamic mixing properties of grossular–andradite garnets. *Phys. Chem. Miner.* **29**, 52-64.

Blount A. M. (1974) Crystal-structure of crandallite. *Am. Mineral.* **59**, 41-47.

Connolly J. (1990) Multivariable phase diagrams: an. *algorithm based on generalized thermodynamics. Am J Sci* **290**, 666-718.

Connolly J. and Kerrick D. (1987) An algorithm and computer program for calculating composition phase diagrams. *Calphad* **11**, 1-55.

Cudennec Y., Riou A., Bonnin A. and Caillet P. (1980) Etudes cristallographiques et infrarouges d'hydroxychromates de fer et d'aluminium de structure alunite. *Rev. Chim. Minér.* **17**, 158-167.

de Capitani C. and Petrakakis K. (2010) The computation of equilibrium assemblage diagrams with Theriak/Domino software. *Am. Mineral.* **95**, 1006-1016.

Dutrizac J. (2008) Factors affecting the precipitation of potassium jarosite in sulfate and chloride media. *Metall. Mater. Trans. B* **39**, 771-783.

Dutrizac J. and Chen T. (2009) The behaviour of scandium, yttrium and uranium during jarosite precipitation. *Hydrometallurgy* **98**, 128-135.

Dutrizac J., Dinardo O. and Kaiman S. (1981) Selenate analogues of jarosite-type compounds. *Hydrometallurgy* **6**, 327-337.

Dutrizac J. E. and Jambor J. L. (2000) Jarosites and their application in hydrometallurgy. *Rev. Mineral. Geochem.* **40**, 405-452.

Feng J., Grochala W., Jaroń T., Hoffmann R., Bergara A. and Ashcroft N. (2006) Structures and potential superconductivity in SiH_4 at high pressure: En route to "metallic hydrogen". *Phys. Rev. Lett.* **96**, 017006.

Ganguly J. and Saxena S. K. (2012) *Mixtures and mineral reactions*. Springer Science & Business Media.

Guilbaud P. and Wipff G. (1993) Hydration of uranyl (UO_2^{2+}) cation and its nitrate ion and 18-crown-6 adducts studied by molecular dynamics simulations. *J. Phys. Chem.* **97**, 5685-5692.

Hikov A., Lerouge C. and Velinova N. (2010) Geochemistry of alunite group minerals in advanced argillic altered rocks from the Asarel porphyry copper deposit, Central Srednogorie. *Rev. Bulg. Geol. Soc* **71**, 133-148.

Hochella Jr M. F., Moore J. N., Golla U. and Putnis A. (1999) A TEM study of samples from acid mine drainage systems: Metal-mineral association with implications for transport. *Geochim. Cosmochim. Acta* **63**, 3395-3406.

Hochella Jr M. F., Moore J. N., Putnis C. V., Putnis A., Kasama T. and Eberl D. D. (2005) Direct observation of heavy metal-mineral association from the Clark Fork River Superfund Complex: Implications for metal transport and bioavailability. *Geochim. Cosmochim. Acta* **69**, 1651-1663.

Jambor J. L. (1999) Nomenclature of the alunite supergroup. *Can. Mineral.* **37**, 1323-1341.

Kato T. (1971) The crystal structures of goyazite and woodhouseite. *Neu. Jb. Mineral., Mh.*, 241-247.

Kim Y., Konecke B., Fiege A., Simon A. and Becker U. (2017) An ab-initio study of the energetics and geometry of sulfide, sulfite, and sulfate incorporation into apatite: The thermodynamic basis for using this system as an oxybarometer. *Am. Mineral.* **102**, 1646-1656.

Klein C., Dutrow B. and Dana J. D. (2007) *The 23rd edition of the manual of mineral science:(after James D. Dana).*

Kolitsch U. and Pring A. (2001) Crystal chemistry of the crandallite, beudantite and alunite groups: a review and evaluation of the suitability as storage materials for toxic metals. *J. Mineral. Petro. Sci.* **96**, 67-78.

Kotler J. M., Hinman N. W., Yan B., Stoner D. L. and Scott J. R. (2008) Glycine identification in natural jarosites using laser desorption Fourier transform mass spectrometry: Implications for the search for life on Mars. *Astrobiology* **8**, 253-266.

Lee D., Choy J. and Lee J. (1992) Computer generation of binary and ternary phase diagrams via a convex hull method. *J. Phase Equilib.* **13**, 365-372.

Lengauer C., Giester G. and Irran E. (1994) $KCr_3(SO_4)_2(OH)_6$: Synthesis, characterization, powder diffraction data, and structure refinement by the Rietveld technique and a compilation of alunite-type compounds. *Powder Diffr.* **9**, 265-271.

Lucks C., Rossberg A., Tsushima S., Foerstendorf H., Fahmy K. and Bernhard G. (2013) Formic acid interaction with the uranyl (VI) ion: structural and photochemical characterization. *Dalton Trans.* **42**, 13584-13589.

Madden M. E., Bodnar R. and Rimstidt J. (2004) Jarosite as an indicator of water-limited chemical weathering on Mars. *Nature* **431**, 821.

Mills S. J., Nestola F., Kahlenberg V., Christy A. G., Hejny C. and Redhammer G. J. (2013) Looking for jarosite on Mars: The low-temperature crystal structure of jarosite. *Am. Mineral.* **98**, 1966-1971.

Monkhorst H. J. and Pack J. D. (1976) Special points for Brillouin-zone integrations. *Phys. Rev. B* **13**, 5188.

Morris R. V., Squyres S., Arvidson R., Bell III J., Christensen P., Gorevan S., Herkenhoff K., Klingelhöfer G., Rieder R. and Farrand W. (2004) A first look at the mineralogy and geochemistry of the MER-B landing site in Meridiani Planum, Lunar and Planetary Science Conference.

Navrotsky A., Forray F. L. and Drouet C. (2005) Jarosite stability on Mars. *Icarus* **176**, 250-253.

Novak F., Jansa J. and Prachar I. (1994) Classification and nomenclature of alunite-jarosite and related mineral groups. *Vestnık Ceského geol. stava* **69**, 453À479.

Okada K., Hirabayashi J. and Ossaka J. (1982) Crystal-structure of natroalunite and crystal-chemistry of the alunite group. *Neu. Jb. Mineral., Mh.*, 534-540.

Perdew J. P., Burke K. and Ernzerhof M. (1996) Generalized gradient approximation made simple. *Phys. Rev. Lett.* **77**, 3865.

Reich M. and Becker U. (2006) First-principles calculations of the thermodynamic mixing properties of arsenic incorporation into pyrite and marcasite. *Chem. Geol.* **225**, 278-290.

Ripp G. and Kanakin S. (1998) Phosphate minerals in the metamorphosed high-alumina rocks of the Ichetui occurrence, Transbaikal region, Doklady earth sciences. Springer, **pp**. 233-235.

Ripp G., Kanakin S. and Shcherbakova M. (1998) Phosphate mineralization in metamorphosed high-alumina rocks of the Ichetuyskoye ore occurrence. *Zapiski Vseross. Mineral. Obshch.* **127**, 98-108.

Schindler M. and Hochella Jr M. F. (2015) Soil memory in mineral surface coatings: Environmental processes recorded at the nanoscale. *Geology* **43**, 415-418.

Schindler M., Lanteigne S., McDonald A. M. and Hochella Jr M. F. (2016) Evidence of Cu-and Ni-bearing surface precipitates and adsorption complexes in remediated soils at the nanoscale: a TEM, micro-Raman, and laser-ablation ICP-MS study of mineral surface coatings. *Can. Mineral.* **54**, 285-309.

Schwab R., Pimpl T., Schukow H., Stolle A. and Breitinger D. (2004) Compounds of the crandallite-type: Synthesis, properties and thermodynamic data of pure crandallite and woodhouseite. *Neu. Jb. Mineral., Mh.* **2004**, 385-409.

Segall M., Lindan P. J., Probert M. a., Pickard C., Hasnip P. J., Clark S. and Payne M. (2002) First-principles simulation: ideas, illustrations and the CASTEP code. *J. Phys.: Condens. Matter* **14**, 2717.

Shigemi A. and Wada T. (2004) Enthalpy of formation of various phases and formation energy of point defects in perovskite-type $NaNbO_3$ by first-principles calculation. *Jpn. J. Appl. Phys.* **43**, 6793.

Shuller L. C., Ewing R. C. and Becker U. (2011) Thermodynamic properties of $ThxU_{1-x}O_2$ ($0< x< 1$) based on quantum–mechanical calculations and Monte-Carlo simulations. *J. Nucl. Mater.* **412**, 13-21.

Shuller L. C., Ewing R. C. and Becker U. (2013) Np-incorporation into uranyl phases: A quantum–mechanical evaluation. *J. Nucl. Mater.* **434**, 440-450.

Smith M. D., Wolff M. J., Lemmon M. T., Spanovich N., Banfield D., Budney C. J., Clancy R. T., Ghosh A., Landis G. A. and Smith P. (2004) First atmospheric science results from the Mars Exploration Rovers Mini-TES. *Science* **306**, 1750-1753.

Stoffregen R. E. and Alpers C. N. (1992) Observations on the unit-cell dimensions, H_2O contents, and 6D values of natural and synthetic alunite. *Am. Mineral.* **77**, 1092-1098.

Stoffregen R. E., Alpers C. N. and Jambor J. L. (2000) Alunite-jarosite crystallography, thermodynamics, and geochronology. *Rev. Mineral. Geochem.* **40**, 453-479.

Szymanski J. T. (1985) The crystal structure of plumbojarosite $Pb[Fe_3(SO_4)_2(OH)_6]_2$. *Can. Mineral.* **23**, 659-668.

Walker S. M. and Becker U. (2015) Uranyl (VI) and neptunyl (V) incorporation in carbonate and sulfate minerals: Insight from first-principles. *Geochim. Cosmochim. Acta* **161**, 19-35.

Wise W. (1975) Solid solution between the alunite, woodhouseite, and crandallite mineral series. *Neu. Jb. Mineral., Mh.* **1975**, 540-545.

Zema M., Callegari A., Tarantino S., Gasparini E. and Ghigna P. (2012) Thermal expansion of alunite up to dehydroxylation and collapse of the crystal structure. *Mineral. Mag.* **76**, 613-623.

Chapter VI. Conclusions

The purpose of this chapter is to revisit the experimental and computational methods developed in this dissertation and suggest some considerations on their applications to future research along with examples of ongoing but not completed projects.

The research presented in this dissertation sheds light on the role of naturally-occurring minerals in catalyzing redox reactions of trace elements in the environment, and in providing process-specific parameters such as the redox state and the equilibrium temperature upon the process of their crystallization in geological systems. The redox-catalytic properties of metal oxides, such as magnetite and anatase, have been examined with respect to environmentally relevant chemical parameters such as pH, Eh, and the presence of organic ligands, oxidants, and reductants. The energetics and temperature dependence of ionic substitution in minerals have been characterized which further the understanding of the mineralization of chemical elements in magmatic, hydrothermal, and metamorphic settings. In these environments, knowing the thermodynamic, structural, and atomistic properties of foreign elements in host minerals can form the basis of using elemental incorporation and their respective oxidation state as redox and thermal proxies.

This dissertation research has developed experimental and spectroscopic approaches that characterize mechanisms and kinetics of abiotic redox transformation of trace elements mediated by metal oxides. The novel electrochemical setup that involves the use of powdered mineral as the

working electrode (described in Chapter II) allows to measure the redox kinetics of natural minerals and allows for identifying reaction mechanisms mediated by minerals as a function of pH and Eh. The combination of such electrochemical setup with the microscopic capabilities of atomic force microscopy (EC-AFM) allows one to visualize and characterize the progress of a metal reduction/precipitation reaction mediated by semiconducting minerals in-situ and in real time. While typically the standard reduction potential is only adjusted for pH (thermodynamics of redox transition), the influence of complexations and adsorption is barely addressed in the literature. The combined usage of quantum-mechanical modeling of the thermodynamic cycle, cyclic voltammetry, and EC-AFM creates a detailed quantitative molecular and atomistic approach that leads to theoretical understanding out of the interpretation of electrochemical peak shifts (Cook et al., 2017, in rev., Gebarski and Becker, 2019, in prep.). Similarly, the calculation of electron transfer rates and the comparison of these rates with peak heights of cyclic voltammograms of cyclic voltammetry experiments (Cook et al., 2017, in rev.) provide a more fundamental understanding of redox kinetics.

One application of EC-AFM is an ongoing project to identify and quantify reaction mechanisms and kinetics of the uranyl reduction and nucleation mediated by magnetite and ilmenite (Kim and Becker, 2019, in prep). The spectroscopic and electrochemical data of this work suggest that reduction of uranyl-organic complexes can be facilitated by the catalysis of Fe-bearing minerals. The mechanism proposed is that the uranyl-organic bonding breaks upon interaction with the mineral surface whereby the Fe-organic bonding is more favorable, and uranyl can be reduced to pentavalent uranium species.

The main achievement of computational approaches described in Chapters IV and V is to understand the energetics and structural distortion of foreign-element incorporation into mineral

hosts based on atomistic modeling approaches. These approaches are highly useful in deriving a thermodynamic basis describing the stability of incorporation and solid solution phases in a geologic system of interest. The critical step is to establish the solid-state and aqueous-state reactions that include reactant and product phases that occur and are stable in a corresponding system. In case of solid solution formation, selection of reactants in an equation of binary and ternary mixing should be limited to naturally occurring end member minerals. Exceptions include ordered structures with intermediate compositions that have higher stability than a pure mixture of end member minerals. For example, ordering of Mg and Ca atoms gives rise to the higher stability of dolomite (enthalpy of mixing < 0) relative to a 1:1 mixture of calcite and magnesite. A follow-up study regarding S redox in apatite addresses the stability of disulfide (S_2^{2-}) positioned at the column anion site in the apatite structure (Kim et al., 2019, prep). Good examples of solid-state sources of disulfide for incorporation into apatite are pyrite (FeS_2) and sodium disulfide (Na_2S_2). These compounds contain sulfur species in the form of the hypothesized incorporated species (that is, disulfide) and they represent compositions of iron- and sodium-rich magmatic melts. Thermodynamic analysis for mixing properties, as described in Chapter V, provides a computational framework to investigate binary and ternary sold solution series. The computational procedure developed in Chapter V is being used to evaluate the amount of disulfide incorporation into apatite (Kim et al., 2019, prep) to predict the stability and equilibrium compositions of solid solution phases as a function of temperature. Chapter V includes examples of natural minerals with compositions corresponding to binary solid solution between woodhouseite and alunite (or natroalunite), which is in good agreement with our computed phase diagrams. Calibration of the computational results with experimental data (e.g., from calorimetric measurements) is, however, difficult because experimental data and field observations are not sufficiently available to cover

the whole range of these binary and ternary solid solutions. This is due to calorimetric measurements of ternary systems being difficult to obtain and time-consuming, and equilibrium is often not reached in systems of slow reaction kinetics. Further studies gauge the computational procedure of this dissertation to well-known examples of solid solution series (e.g., orthoclase-albite-anorthite). The reaction energy evaluated from the internal energies of the reactants and products is in good agreement with enthalpy, because in a solid, the volume change is quite small ($p\Delta V \approx 0$). To evaluate ΔG_{rxn}, vibrational entropy contributions (e.g., obtained from phonon calculations on periodic solid phases) must be considered. This requires significant computational effort. In the ongoing project on disulfide incorporation in apatite (Kim et al., 2019, prep), phonon calculations are performed for selected reaction equations, and the applicability of the combined quantum-mechanical and statistical-thermodynamic approach is demonstrated for deriving thermodynamics of chemical substitution in minerals.

Overall, the research approaches established in this dissertation bridge experiments, field observations, and computational modeling for the evaluation of geochemical reactions involving semiconducting minerals as redox catalyst and the stability and redox states of chemical species in different host minerals. The scope of application of these research approaches for future research will encompass processes in near-surface environments as well has aspects of high-temperature geochemical systems.

References

Cook P., Yuan K., Kim Y., Marcano M. C. and Becker U. (2017, in rev.) Electrochemical and spectroscopic investigations of redox reactions between aqueous selenium species and galena surfaces in acidic conditions. *Geochim. Cosmochim. Acta*.

Gebarski B. and Becker U. (2019, in prep.) Electrochemical analysis of the kinetics of oxidation/reduction reactions of the peroxide-containing mineral studtite in comparison to uranyl peroxide clusters (U_{60}). *Radiochimica Acta*.

Kim Y. and Becker U. (2019, in prep) Imaging the reduction of uranyl on Fe-bearing minerals surfaces using in situ electrochemical AFM. *ACS Earth and Space Science*.

Kim Y., Konecke B., Fiege A., Simon A. and Becker U. (2019, prep) An ab-initio study of the energetics and geometry of disulfide and bisulfide incorporation into apatite. *Am. Mineral.*